Studying the Extragalactic Background Light with the second Cosmic Infrared Background ExpeRiment, CIBER-2

Thesis by
Alicia Lanz

In Partial Fulfillment of the Requirements for the
degree of
Doctor of Philosophy

Caltech

CALIFORNIA INSTITUTE OF TECHNOLOGY
Pasadena, California

2018
Defended May 8, 2018

© 2018

Alicia Lanz
ORCID: 0000-0003-2565-1558

iii

ACKNOWLEDGEMENTS

First and foremost, thank you to my family, who fully supported me leaving my promising engineering career to go back to school to follow my childhood dreams of understanding the universe. Thank you to John, my husband, who supported me unequivocally with time, encouragement, childcare, and camaraderie. Thank you to my daughters, who put up with chaos so their mother could be the best mother she can, which includes being a scientist as well as a mom. Juliette and Marian, I hope you see that with hard work, good people, and perseverance, you too can build lives where your wildest dreams come true. Thank you to my mother, Elaine, who supported me in so many ways over the years, who helped me remember to celebrate success big and small, always had great advice for navigating the difficult times, and who gave of her time and treasure so I could study the biggest questions in the universe. Thank you my brother for being a wonderful and adventurous uncle and chef. Thank you my uncle, Edward, for introducing me to the stars at Joshua tree as child and following up with science fiction filled with wormholes and quantum gravity and questioning authority. Thank you to my in-laws, Dan and Liz, for your time spent caring for the kids so I could go to school. Thank you to the whole, giant, extended family for all your time and support and dinners and wine over the years. It really does take a village to complete a degree while raising children; thank you all for helping that become a reality.

Thank you to my friends. Thank you to my non-academic friends who listened to talks about which they understood little, and who provided good company and relaxation. Thank you to my academic friends who accompanied me through the maze of graduate study and helped me become a better person and a better scientist along the way. Allison Strom, Gina Duggan, Natalie Schaal, Jason Pollack, and Abhilash Mishra, thank you for your friendship and companionship as we learned to be the best community leaders we could be. Sabrina Stierwalt, Abigail Crites, Gwen Rudie, and Becky Tucker, thank you for setting a bar of existing in the world as rigorous, caring, authentic scientists to whom I could aspire, and for mentorship and fun times along the way. Bade Uzgil and Yun-Ting Chen, thank you for helping me understand the mathematics of Fourier transforms and power spectra in all their representations.

Thank you to the Caltech Graduate Student Council, who elected me as their Chair for the 2016-17 academic year, an experience which helped me find my community,

Kathy Dennison, for running ObsCos behind the scenes, and for underscoring the importance of family in all situations. Thank to Sheri Stoll, for helping with all the administrative details and bringing beauty and art into Cahill.

Thank you again to my own slice of the Caltech community; your support and encouragement were vital to me these last few years. I am so grateful to have achieved my highest goal of a physics PhD, and I could not have accomplished this alone. I now look forward to a new set of scientific goals and an expanding circle of family, friends, and community.

ABSTRACT

Fluctuations in the extragalactic background light trace emission from the entire history of galaxy formation, including emission from early luminous sources prior to the reionization of the universe. The formation of the first luminous objects represents an important transition in the evolution of the universe from its smooth initial state to the clumpy, highly ordered state observable today. However, these objects are faint and diffuse and not well studied; direct observations of their emission are needed to constrain current numerical simulations of the nonlinear evolution of the early universe. A number of recent near-infrared measurements show excess spatial power at large angular scales inconsistent with models of $z < 5$ emission from galaxies. These measurements have been interpreted as arising from either redshifted emission of early luminous objects, such as stellar and quasar emission from the epoch of reionization, or the combined intra-halo light from stars thrown out of more recent galaxies during merging activity at lower redshifts. Though astrophysically distinct, both interpretations arise from faint, low surface brightness source populations that are difficult to detect except by statistical approaches using careful observations with suitable instruments. The key to determining the source of these background anisotropies will be wide-field imaging measurements spanning multiple bands from the optical to the near-infrared.

The Cosmic Infrared Background ExpeRiment 2 (CIBER-2) will measure spatial anisotropies in the extragalactic infrared background caused by cosmological structure using six broad spectral bands. The experiment uses three 2048 x 2048 Hawaii-2RG near-infrared arrays in three cameras coupled to a single 28.5 cm telescope housed in a reusable sounding rocket-borne payload. A small portion of each array will also be combined with a linear-variable filter to make absolute measurements of the spectrum of the extragalactic background with high spatial resolution for deep subtraction of Galactic starlight. The large field of view and multiple spectral bands make CIBER-2 unique in its sensitivity to fluctuations predicted by models of lower limits on the luminosity of the first stars and galaxies and in its ability to distinguish between primordial and foreground anisotropies. This work encompasses the scientific motivation for CIBER-2 and describes details of the instrument design and verification prior to flight.

TABLE OF CONTENTS

LIST OF ILLUSTRATIONS

LIST OF TABLES

INTRODUCTION

Experimental physics is a unique interplay between theory, instrument design, and data. Observational cosmology, while not strictly experimental in the traditional sense, involves design of sophisticated equipment to measure theorized cosmological and astrophysical signals. The second Cosmic Infrared Background ExpeRiment, CIBER-2, fits squarely within this tradition; CIBER-2 is a specially designed imaging and spectroscopic camera designed to identify and measureemission from the earliest luminous objects in the universe. The specific design of the instrument is tailored to the theorized prediction of the emission of these primordial luminous objects. My thesis work has been to understand the theorized prediction of this emission and fabricate and integrate the CIBER-2 instrument. In doing so, I have been trained in how to think about instrument design in the context of modern questions of observational cosmology.

Chapter 1 describes the background physics of luminous objects in the universe, with a focus on the cosmological influences of this emission and the means of identifying and measuring such emission. Section 1.1 describes the physics of the early universe within the cosmological framework of the Λ-CDM model. Special attention is paid to how each cosmological epoch or event impacts the formation and emission of the first luminous objects. Section 1.2 describes the Extragalactic Background Light (EBL), which comprises the total astrophysical emission throughout cosmic history, and by definition includes emission from the first faint and diffuse luminous objects. Measurement of the absolute intensity of the EBL is described and early results are summarized alongside a brief mention of constraints provided by complimentary methodologies. Section 1.3 describes EBL spatial fluctuations, which provide an alternate means of probing the EBL by looking at statistical properties of the underlying spatial structure of EBL emission. The mathematics of this approach are described, followed by a description of the underlying physics of formation of early luminous objects. This section also provides a detailed description of signal discrimination and foreground exposition, as well as a summary of inputs to the models used for astrophysical interpretation of the results. Recent results are summarized, with special attention paid to the first Cosmic Infrared Background ExpeRiment, CIBER-1. Finally, this chapter pulls together the lessons learned from measurements of both EBL absolute intensity and spatial fluctuations to motivate the design of a next-generation EBL measurement instrument.

Chapter 2 describes the design of the CIBER-2 instrument. Section 2.1 briefly summarizes the CIBER-2 instrument. Section 2.2 motivates the high level instrument design based upon the science questions of interest. Section 2.3 describes the detailed design, and Section 2.4 brings the component descriptions together for a full instrument summary.

Chapter 3 describes the verification of the CIBER-2 instrument. Section 3.1 discusses the determination of readiness for scientific deployment of an instrument in relation to the original science goals. Section 3.2 describes the testing and test equipment needed for instrument characterization. Section 3.4 describes testing of individual subsystems. Section 3.4 describes the environmental testing CIBER-2 must undergo. Section 3.5 synthesizes the previous tests for verification of the overall instrument.

Chapter 4 describes the planned flight for CIBER-2 science observation. Section 4.1 describes the complete sounding rocket payload, beyond just the CIBER-2 instrument. Section 4.2 describes the intended flight profile. Section 4.3 describes the observing strategy. Section 4.4 describes the preliminary data reduction of the observations, to be followed by complete data analysis.

The appendices include a detailed description of the mechanical subsystems that make up the CIBER-2 instrument in Appendix A, and a set of mechanical drawing of the CIBER-2 focal plane assembly in Appendix B.

In total, this thesis describes the scientific motivation for and process of design and development and planned testing of the CIBER-2 EBL fluctuations imaging instrument.

C h a p t e r   1

EXTRAGALACTIC BACKGROUND LIGHT AND LARGE SCALE STRUCTURE IN THE UNIVERSE

1.1   Overview of the Cosmological History of the Universe

The formation of the first luminous objects in the universe represents an important transition in the evolution of the universe from its smooth initial state to the clumpy, highly ordered state observable today [1]. The earliest galaxies arose from the growth of linear density fluctuations that emerged from quantum fluctuations present in the very early universe. The early evolution of the underlying density fluctuations can be described analytically and confirmed by observations of a specific radiative background, the Cosmic Microwave Background. In contrast to the analytical description appropriate for evolving linear density fields with small perturbations, the first bound objects represent the transition from linear to nonlinear structure formation and must be simulated numerically. Observations of a different radiative background, the Extragalactic Background Light, are needed to constrain current numerical simulations of this nonlinear evolution.

The standard model of cosmology provides an observationally verified description of the origin and evolution of the early universe. Taken together, the mathematical formalism provided by General Relativity and the physics of gravity as the defining force on cosmological scales provide the framework for this dynamical description of the universe.

This cosmological formalism suggests the origin of the universe in a singularity known as the Big Bang, followed by a rapid expansion of spacetime that seeds the universe with inhomogeneities responsible for the distribution of matter observable in the large scale structure of the universe at present times. Primordial nucleosynthesis describes the formation of particles immediately following the inflationary period, which remain in thermal equilibrium with radiation in a hot plasma for a duration. As the universe expands and cools, different types of matter decouple from equilibrium and began evolving on different trajectories. The decoupling of photons from neutral hydrogen atoms releases a relic radiation background observable today as the Cosmic Microwave Background that places important constraints of the value of cosmological parameters. The coalescing of cold dark matter into gravitational

wells at the sites of initial instabilities provides a strong gravitational attractor for baryons as the universe continues to expand, eventually allowing the formation of bound, luminous objects with emission visible today.

These early objects are difficult to observe directly with existing technologies, as they are faint, distant, and surrounded by opaque neutral hydrogen. Observations of these objects are important to constrain numerical simulations and physical understanding of this key transition point in the evolution of the early universe. The collected emission of early luminous sources is present in the extragalactic background radiation, with peak emission from this early period observable at infrared wavelengths today. This section goes through the cosmological standard model, highlighting key events and parameters that shape the formation of the first luminous objects and form the basis for the large scale structure of the universe at present times.

1.1.1 Modern Cosmology Formulation

Cosmology combines theory with observational data to reconstruct the origin and evolution of the universe, from a singular point to the highly structured matter distribution observable today. Observations of cosmologically significant quantities confirm that the early universe is expanding, and is homogenous and isotropic, while significant structure is observable at late times: the cosmic microwave background is smoothly isotropic and homogeneous, with only small fluctuations present, in contrast to galaxies at late times which are clustered along a cosmic web. The framework of general relativity makes it possible to study the growth of large-scale structure in an expanding universe by studying gravitational instability acting on small initial perturbations.

This study of the origin and evolution of the universe relies on the concepts of the metric and geodesic, and applies Einstein's equations to a specific metric in order to relate the parameters of the metric to the energy density of the universe. Conditions in the early universe can be described by applying these concepts to the homogenous universe, and the formation of structure in the universe can be studied by applying the same concepts to a perturbed universe, leading to a statistical description of the highly ordered universe observable today.

Following the formalism developed by Carroll [11] [98], spacetime can be described by an isotropic and homogenous manifold, $\mathcal{M}$. Isotropy requires the universe to look the same in all directions, while homogeny requires the universe to look the

same at every point. As time is observed to have a specific direction, the manifold $\mathcal{M}$ can be separated into space and time domains.

Metrics constrain geodesics, and thus can be thought of describing the relationship between two unique points in spacetime: the metric tensor $g_{\nu\mu}$ relates the four-vector x^μ to a proper interval, ds^2. We define the comoving coordinates x^μ, x^ν of the manifold such that $\mu, \nu \to \{0, 1, 2, 3\}$ with $dx^0 = dt$ reserved for the timelike coordinate, and dx^i for the spacelike coordinates. Metrics operate on vectors to produce a scalar; the action of the metric on two vectors is to produce an inner product. In terms of physical intuition, a freely-falling particle follows a geodesic in spacetime, and the metric describes this relationship.

The isotropy and homogeneity requirements motivate a metric for a maximally symmetric space on a manifold:

$$ds^2 = g_{\mu\nu}dx^\mu dx^\nu = -dt^2 + a^2(t)d\sigma^2, \tag{1.1}$$

where t is a timelike coordinate, units are defined such that the speed of light is set to unity ($c = 1$), and $d\sigma^2$ is the metric on the physical submanifold. This proper interval holds true for expanding spacetimes, with the time-dependent expansion factor parameterized by a coefficient $a(t)$. Selection of a two-sphere as the form of the physical sub-manifold reduces the metric to the most general spatially homogenous and isotropic metric, known as the Robertson-Walker metric:

$$ds^2 = -dt^2 + a^2(t)\Big(\frac{dr^2}{1 - kr^2} + r^2(d\theta^2 + sin^2\theta d\phi^2)\Big). \tag{1.2}$$

where r, θ, ϕ are intervals of distance in spherical coordinates and k is a constant describing the curvature of the universe with values of $+1, 0, -1$ corresponding to positive curvature, flatness, or negative curvature, respectively.

Einstein's field equations govern how a metric responds to energy and momentum. Put another way, they encode the effects of force of gravity directly into the metric tensor. They also determine the behavior of the scale factor, $a(t)$. The tensor form of Einstein's equations for general relativity can be derived from the action principle, using a Hilbert action and Lagrange density, and expressed as

$$G_{\mu\nu} \equiv R_{\mu\nu} - \frac{1}{2}Rg_{\mu\nu} = 8\pi G T_{\mu\nu}, \tag{1.3}$$

where $G_{\mu\nu}$ is the Einstein tensor, $R_{\mu\nu}$ is the Ricci curvature tensor, R is the Ricci scalar, $g_{\mu\nu}$ is the metric tensor, G is Newton's gravitational constant, and $T_{\mu\nu}$ is

the energy-momentum tensor. Note that the cosmological constant, Λ, originally introduced by Einstein to describe a static universe, is not expressly indicated in this equation, and is instead included in the formulation of the energy-momentum tensor.

A common form for the energy-momentum tensor $T_{\mu\nu}$ is that of a perfect fluid,

$$T_{\mu\nu} = (\rho + p)U_\mu U_\nu + p g_{\mu\nu}, \tag{1.4}$$

where U_μ is the fluid four-velocity, ρ is the energy density in the rest frame of the fluid and p is the pressure, also in the rest frame. This pressure is isotropic to be consistent with the RW metric.

Assuming a preferred reference frame in which the expansion of the universe is isotropic, Einstein's general relativistic field equations can be used to determine k and $a(t)$ through the Friedmann equations. These equations are obtained by calculation of the Christoffel symbols $\Gamma^\alpha_{\mu\nu}$, the non-zero Ricci tensor components $R_{\mu\nu}$, and the Ricci scalar R. Einstein's equations can then be solved for two cases, a time component G_{00} and a space component G_{ij}, to obtain the set of two Friedmann equations. The first equation is a constraint equation that defines the time derivative of the the scale factor, $\dot{a}$, in terms of the energy density, $\sum \rho_i$, and curvature, k:

$$H^2 \equiv \left(\frac{\dot{a}}{a}\right)^2 = \frac{8\pi G}{3} \sum_i \rho_i - \frac{k}{a^2}. \tag{1.5}$$

The second Friedmann equation is an acceleration equation that defines the second time derivative scale factor, $\ddot{a}$, in terms of the energy density, $\sum \rho_i$, pressure, $\sum p_i$, and curvature, k:

$$\left(\frac{\ddot{a}}{a}\right) = -\frac{4\pi G}{3} \sum_i \left(\rho_i + 3p_i\right) \tag{1.6}$$

where G is Newton's gravitational constant.

Importantly, the Friedmann equations show the general behavior of physical realizations of a simplified universe across its time evolution. To aid in the physical intuition associated with these mathematical solutions, the Friedmann equations allow the definition of many parameters used to describe the state and time evolution of the universe. To begin, it is first useful to look into the relationship between density and pressure of matter in the early universe, and to consider simplified implications.

From the Friedmann equations, many cosmological parameters can be defined. The *Hubble parameter*, H, describes the rate of expansion of the universe:

$$H = \frac{\dot{a}}{a}. \tag{1.7}$$

At present, $H = H_0$ where H_0 is the Hubble constant. The Hubble parameter describes how fast the most distant galaxies, at a distance of d, are receding from observations centered at the Earth by invoking Hubble's law, $v \simeq Hd$.

The density of the universe can be parameterized in a physically intuitive form by writing the Friedmann equations as

$$\Omega - 1 = \frac{k}{H^2 a^2}. \tag{1.8}$$

where Ω is a new quantity: the density parameter of the universe. Rearranging in terms of this parameter, Ω,

$$\Omega_{total} = \frac{8\pi G}{3H^2}\rho = \frac{\rho}{\rho_c}. \tag{1.9}$$

Then ρ_c is the critical energy density of a universe for which the spatial sections are flat ($k = 1$):

$$\rho_c = \frac{3H^2}{8\pi G}. \tag{1.10}$$

The density parameter thus determines which Robertson-Walker geometry describes this universe, and must be determined observationally. Note the total energy density in the universe is related to local geometry:

$$\Omega_{total} > 1 \Leftrightarrow k = +1 \qquad\qquad \Leftrightarrow \text{closed} \tag{1.11}$$

$$\Omega_{total} = 1 \Leftrightarrow k = 0 \qquad\qquad \Leftrightarrow \text{flat} \tag{1.12}$$

$$\Omega_{total} < 1 \Leftrightarrow k = -1 \qquad\qquad \Leftrightarrow \text{open.} \tag{1.13}$$

Observations select the $k = 0$ case indicating a flat local geometry [50], and this assumption will be followed in the remainder of this chapter.

Similarly, fractional energy densities for each component can be defined as

$$\Omega_i = \frac{\rho_i}{\rho_c}. \tag{1.14}$$

These components include the energy density of matter, Ω_m, the energy density of radiation, Ω_r, and the energy density of the cosmological constant, Ω_Λ.

The Friedmann equation is often expressed in terms of the collected density parameters:

$$\left(\frac{H}{H_0}\right)^2 = \Omega_r a^{-4} + \Omega_m a^{-3} + \Omega_k a^{-2} + \Omega_\Lambda \tag{1.15}$$

where $\Omega_k = 1 - \Omega_{total}$ is the curvature energy density and the expansion coefficient at the present time is $a(t_0) = 1$.

The evolution of the energy density of the universe can be described using fields coupled to the metric described by Einstein's field equations and the Friedmann equations. These are assumed to evolve linearly in time against a smooth, expanding background. Structure in the universe is described by perturbations around this smooth background. A full treatment requires perturbation of these fields, and of the metric and Einstein's equations [18]. However, inside the horizon, a Newtonian approximation allows for development of physical intuition that aids in the interpretation of the general relativistic results. The following discussion of the evolution of perturbed scalar fields and the emerging structure is largely discussed in Newtonian terms of energy conservation, continuity, and Poisson's equations for brevity.

Introducing energy conservation demonstrates that the expansion of the universe leads to local changes in the energy density, as evident from applying an energy conservation equation to the Friedmann equations (Equations 1.5 and 1.6). In general relativity, energy conservation requires the covariant divergence of the energy-momentum tensor to have a zero value:

$$\nabla_\mu T^{\mu\nu} = 0. \tag{1.16}$$

Applied to the energy momentum tensor for a perfect fluid expressed in the FRW metric, an energy conservation equation results that depends only the pressure, density, and Hubble parameter:

$$\dot{\rho} + 3H(\rho + p) = 0. \tag{1.17}$$

This equation indicates that the expansion of the universe (indicated by H) leads to changes in local energy density, interchanging energy between matter and spacetime geometry.

In order to solve the Friedmann equations to better understand the evolution of the universe, assumptions about the relationship of pressure and energy density are needed. Modeling the matter and energy in the universe as a perfect fluid (any fluid which is isotropic in its rest frame) allows for relating the density and pressure through conservation of energy and continuity equations,

$$\rho(a) \propto \frac{1}{a(t)^{3(1+w)}}, \tag{1.18}$$

where w is a constant independent of time, such that $w \neq w(t)$. A simple equation of state, $p = w\rho$, allows evaluation of the energy density of matter: $\rho \sim a^{-3}$ in the case of a *matter dominated* universe. An alternative case is the *radiation dominated*

universe, with an equation of state of $p = \frac{1}{3}\rho$ and corresponding the energy density of radiation $\rho \sim a^{-4}$. This latter case represents the universe at early times. Finally, assuming a cosmological constant, an equation of state for a perfect fluid in this case is $p = -\rho = \frac{\Lambda}{8\pi G}$ with $w = -1$. Note the lack of dependence on a scale factor a in this case.

Observing the effects of the geodesic on a single particle with an energy-momentum four-vector $p_\alpha = (E, \vec{p})$ leads to the conclusion that the energy of a particle decreases with the expansion of the universe as $E \propto \frac{1}{a}$. This leads to the concept of redshift, where the observed wavelength of a photon λ_{obs} is longer than the emitted wavelength λ_{em}:

$$\frac{\lambda_{em}}{\lambda_{obs}} = \frac{a_{obs}}{a_{em}}. \tag{1.19}$$

For observations made today, the observed scale factor is normalized to unity by convention, $a_{obs} = a_0 = 1$, and so $\frac{\lambda_{em}}{\lambda_{obs}} = \frac{1}{a_{em}}$. This change can be characterized as the fractional change in wavelength between the observed and emitted photon wavelengths as

$$z \equiv \frac{\lambda_{obs} - \lambda_{em}}{\lambda_{em}}. \tag{1.20}$$

Considering observations today with the scale factor again normalized to unity, then the expansion scale of the universe at the time of photon emission can be determined as $z = \frac{1}{a} - 1$. Rearranging,

$$1 + z = \frac{1}{a}, \quad a = \frac{1}{1+z}. \tag{1.21}$$

A Robertson-Walker metric whose scale factor satisfies Friedmann's equations is called a Friedmann-Lemaître-Robertson-Walker metric. The cosmological standard model assets the universe at large is described by such a metric and characterized by four parameters $\Omega_{m,0}$, $\Omega_{r,0}$, Ω_Λ, and H_0. Taken together, this formalism defines a concordance cosmology often referred to as ΛCDM. This is a cosmology dominated by gravity on large scales, described by a metric and Einstein's equations, and assumed to be largely homogenous and isotropic. Solutions to the cosmological equations of motion (the Friedmann equations) provide descriptions of the origin and evolution of the early universe, constrained by various assumptions and approximations. These statistical predictions of density distributions guide predictions of structure formation and estimations of observable emission once inhomogeneities are introduced. Physical interpretations of these equations of motion are grouped into historically important epochs in the evolution of the universe in the following sections.

1.1.2 Early moments: Big Bang and Inflation

Big Bang. The history of the universe begins 13.6 billion years ago with the Big Bang [90, 18, 11]. Assuming a flat universe ($k = 0$) consistent with observational evidence, and a constant equation of state parameter w, the first Friedmann equation, Equation 1.5, has an exact solution:

$$a(t) = a_0 \left(\frac{t}{t_0} \right)^{2/3(1+w)}.$$
(1.22)

The scale factor at the present time is a_0.

Analysis of the rate of change of the scale factor, $a(t)$, from the Friedmann Equations shows that the expansion of the universe is slowing: $\ddot{a} < 0$. Observations of galaxies show the universe to be expanding, so $\dot{a} > 0$. Taken together, these indicate the universe is currently decelerating, and must have expanded more quickly in the past. Integrating the Friedmann equations to the time of $a = 0$ produces a singularity, which is interpreted as the "creation of the universe from a singular state" [11]. This event is colloquially referred to as the *Big Bang*. The energy density of the universe must also be asymptotically increasing as $t \to 0$, although our current physics framework does not describe this regime well.
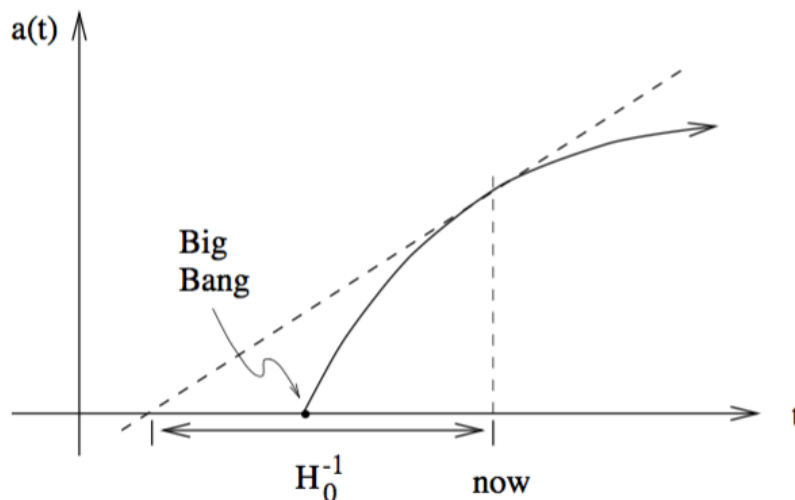
Figure 1.1: Qualitative representation of integration of the Friedmann equations with a singularity at $a = 0$. The scale factor of the expanding universe, $a(t)$, as described by the Friedmann equations, is shown as a function of time, t. The solid curve intersects with $a = 0$ before the time $t = 0$, an event referred to as the Big Bang. *Figure credit: Carroll (1997).*

Inflation. The Big Bang was immediately followed ($t \sim 10^{-40}$) by a period of rapid expansion referred to as the Epoch of Inflation that writes quantum fluctuations present during the Big Bang onto the sky [90, 18, 11], seeding an otherwise isotropic universe with inhomogeneities that later give rise to stars and galaxies. This theory was initially postulated to resolve issues with the Big Bang model (fine-tuning/flatness, isotropy/horizon, relics), but provided a mechanism to expand quantum fluctuations to horizon scales and thus provide a means for inhomogeneities that later give rise to structure.

A popular and important theory of inflation involves a slowly-rolling potential [98]. For matter modeled by a homogenous scalar field ϕ with potential energy V, the field behaves as a perfect fluid with well defined density and pressure. For a potential V with a flat slope, solutions to the equation of motion result in fields ϕ which are nearly constant in space and only slowly changing with time. This slowly-rolling scalar field has an energy density of $\rho_\phi \approx V(\phi) \approx$ constant. Under these slow-roll approximations, the scalar field equation of motion becomes

$$\dot{\phi} \approx -\frac{V'(\phi)}{3H} \tag{1.23}$$

and the Friedmann equation becomes

$$H^2 \approx \frac{8\pi G}{3}V(\phi) \tag{1.24}$$

where the prime indicates a derivative with respect to the scalar field ϕ.

Because inflaton fluctuations $\delta\phi_k$ are scale-independent, inflaton fluctuations can be related to density fluctuations:

$$\delta\rho = \frac{dV}{d\phi}\delta\phi. \tag{1.25}$$

This means inflation produces density perturbations on every scale, with amplitudes nearly the same for each wavenumber. Observations of the amplitudes of the perturbations provides information about the energy scales of inflation. For a potential V that changes gradually, the spectrum of the fluctuations is

$$A_S^2(k) \sim \left.\frac{V^3}{M_p^6(V')^2}\right|_{k=aH} \tag{1.26}$$

where the quantity $V^3/(V')^2$ is to be evaluated at the moment when the physical scale of the perturbation $\lambda = ak$ is equal to the Hubble radius (H^{-1}), indicated by

$k = aH$. Here, the reduced Planck mass, $M_p \sim 10^{18}$ GeV is used as an analog for energy density. The spectrum $A_S^2(K)$ describes *scalar* fluctuations in the metric.

Inflationary scalar fluctuations are adiabatic, which results in correlations between the fluctuations in the densities of radiation with those of all types of matter. The Gaussianity of these inflationary fluctuations also means that the Fourier modes describing fluctuations at different scales are uncorrelated. The assumptions of adiabatic and Gaussian fluctuations have been verified with current observations of the CMB, discussed in more detail later in this section.

Additionally, tensor perturbations in the metric are generated, with the spectrum

$$A_T^2(k) \sim \left. \frac{V}{M_p^4} \right|_{k=aH}. \tag{1.27}$$

These tensor fluctuations can be observed as gravitational waves, and they also affect the polarization of the photons that make up the CMB.

The slow-roll model of inflation, although simplistic, provides a general description of how the universe rapidly expands after the Big Bang in such a way that initial quantum fluctuations give rise to density perturbations governing the evolution of matter in the universe and the formation of the first luminous objects.

Primordial Nucleosynthesis. Following inflation, the universe is a hot, dense plasma dominated by relativistic particles [90, 18, 11]. At this point in the evolution of the universe, baryons, cold dark matter, cosmological constant or curvature terms play no role. While the temperature of this plasma decreases below 1 MeV, weak interactions are no longer in equilibrium and interactions of this force become so infrequent that the resulting particles are said to *freeze out* and protons and neutrons are able to exist as distinct particles, with a ratio of 1:7 neutrons to protons. As the temperature decreases below 100 keV, primordial nucleosynthesis begins. The light elements are produced: ^{4}He, ^{3}He, deuterium (^{2}H), and ^{7}Li. Predictions of relative abundances of each species depend on assumptions of cosmological parameters and are confirmed by observational evidence. These light elements largely comprise the baryonic matter that go on to become gravitationally bound in regions of matter overdensity and become the first luminous sources. The available elements constrain the chemistry of early stellar nuclear synthesis.

1.1.3 Recombination and the Cosmic Microwave Background

Primordial nucleosynthesis is followed by a period of subatomic particle-photon collisions, until the universe expands and cools enough for neutral hydrogen atoms to form and decouple from photons during Recombination [90, 18, 11]. This occurred approximately 400,000 years after the Big Bang, at a redshift of $z \sim 1100$. Although originally emitted at optical wavelengths with an energy of 13.6 eV, this so-called Surface of Last Scattering has been redshifted to millimeter wavelengths ($\sim 400 - 3000 \ \mu$m) with a peak temperature of 2.725 K. This radiative background is referred to as the Cosmic Microwave Background (CMB).

The CMB is a blackbody spectrum that demonstrates almost perfect isotropy [90, 18, 11]. The small deviations from isotropy provide a wealth of information about the early universe, confirming the cosmological model described in previous sections. The observable location and amplitude of these fluctuations in the CMB provide constraints on the values of cosmological parameters in the universe.

At early times, following Primordial Nucleosynthesis, the universe remains a hot, dense plasma characterized as the *radiation-dominated* era. The temperature of the universe was hot enough to ionize hydrogen atoms and photons were tightly coupled to matter, rendering the universe opaque. As the universe expands, photons redshift to lower energies where sufficient numbers of photons no longer maintain the energy for ionization. At this point, protons and electrons form stable neutral hydrogen atoms, no longer in thermal equilibrium with the ionizing photons. The atoms decouple or freeze out from the plasma, which occurs for any particle species when the interaction rate Γ drops below the expansion rate of the universe ($\Gamma \ll H$). The universe becomes transparent to the decoupled photons which now free-steam through the universe, and the universe transitions to the *matter-dominated* epoch.

As the photons were previously in thermal equilibrium with the hot plasma, they are released with a blackbody distribution, where for a temperature T, the energy flux in the frequency range $[\nu, \nu + d\nu]$ is described by the Planck distribution

$$P(\nu, T)d\nu = 8\pi T \left(\frac{\nu}{c}\right)^3 \frac{1}{e^{h\nu/kT} - 1} d\nu \qquad (1.28)$$

where h is Planck's constant and k is the Boltzmann constant. As the wavelengths of photons change with the expansion of the universe, the blackbody spectrum maintains it shape while it is translated to lower temperatures, with $T \propto 1/a$. Note a similar event happened at higher temperatures ($\sim 1 MeV$) as neutrinos decoupled

from the plasma, resulting in a free steaming neutrino background with an observable temperature at late time of ~ 2 K, which is a topic of active research.

The small deviations from a perfectly isotropic blackbody spectrum provide important information about cosmological parameters and events[1]. These deviations are measured as fluctuations ΔT against a constant background T by analysis of the power spectrum of the background. This requires decomposing the signal into spherical harmonics as

$$\frac{\Delta T}{T} = \sum_{\ell m} a_{\ell m} Y_{\ell m}(\theta, \phi) \tag{1.29}$$

where $a_{\ell m}$ are the expansion coefficients and θ and ϕ are spherical polar angles on the sky. The power spectrum is then expressed as the ensemble average of the squared value of the coefficients,

$$C_\ell = \langle |a_{\ell m}|^2 \rangle, \tag{1.30}$$

and generally expressed with a normalizing convention as $\ell(\ell+1)C_\ell/2\pi$. Additional details of power spectrum analysis are developed later in Section 1.3.1. A canonical plot of the CMB temperature auto-spectrum is shown in Figure 1.2.

Inflationary fluctuations are directly related to the CMB fluctuations [18, 11]. The instabilities present at the end of inflation correspond to over and under densities of matter, which affects the local environment of photons released at Recombination by altering the local gravitational potential ϕ, causing slight anisotropies in the energy distributions of the photons as they are redshifted out of these local potentials prior to free-streaming. The maximum fluctuation occurs at a scale where matter has had sufficient time to collapse but not time to oscillate and equilibrate with the surrounding plasma. In this way, *the temperature anisotropies observable in the CMB contain information about the conditions that later gave rise to structure in the universe*. Importantly, measurements of the CMB are the only source of direct measurements of the early universe, but nonetheless contain a wealth of information to verify analytical and numerical predictions of the early evolution of the matter-radiation field.

The total energy density of the universe, Ω_{total}, can also be deduced from CMB anisotropies. The location of the maximum fluctuation provides the size of the horizon, R, at Recombination, where $R \sim H_{CMB}^{-1}$. WMAP observations show the

---

[1]Measurement of these anisotropies have initiated the era of precision cosmology that has revolutionized the field in the last two decades.
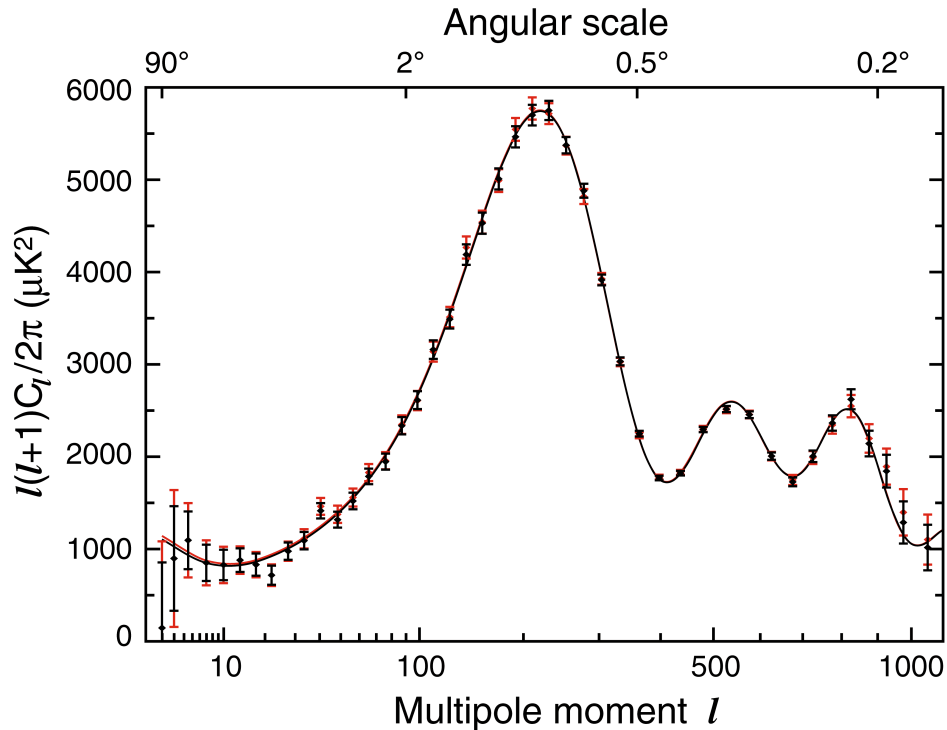
Figure 1.2: CMB power-spectrum from WMAP, at wavelengths of 3.2-13 mm. Image credit WMAP Science Team and Hinshaw et al. 2013.

location of this peak at $\ell \sim 220$ and a value of $0.98 \leq \Omega_{total} \leq 1.08$, in excellent agreement with predictions for a flat universe, $k = 0$, with $\Omega_{total} = 1$ [36]. The positions and amplitudes of the other peaks in the spectrum provide constraints on many other cosmological parameters in a similar manner, including the defining parameters of the standard model, Ω_m, Ω_r, Ω_Λ, (from power spectrum fits) and H_0 (derived) [36].

The remarkable success of extraction of cosmological information from fluctuations in the radiative background of the CMB emboldens investigation of other radiative backgrounds that posses spatial structure. The power spectrum analysis machinery developed for the CMB has wide application to other astrophysical fluctuations, and provides a basis for analysis of radiative backgrounds that trace the spatial positions of the earliest luminous sources in the universe, as detailed in Section 1.3.

1.1.4 The Cosmic Dark Ages

Neutral hydrogen was the defining feature of the of the next period, often referred to as the Cosmic Dark Ages [90, 18, 11]. Hydrogen, a small amount of helium, and

photons dominated the universe as matter began to coalesce in dark matter halos, forming the first generations of stars, and later galaxies, around 400 million years after the Big Bang.

After photons decoupled, the the photon-baryon fluid became two independent gases, one of photons and the other of neutral hydrogen. The evolution of baryons is dominated by gravitational interactions with other baryons and with dark matter, rather than by collisions with photons. Chronologically, dark matter decoupled from the radiation-particle plasma prior to Recombination, during the radiation-domination era (assuming a non-relativistic Cold Dark Matter (CDM) model). After that point, the dark matter particles evolved in a matter only affected by gravity with the mass density set by the relic abundance.

The distribution of dark matter in the post-recombination universe is assumed to be related to the peaks of density in the primordial density fluid. Initial regions of overdensity continued to accumulate particles through gravitation once that particle species uncoupled and evolved independently of the remaining plasma or fluid. In the cold dark matter model, dark matter decoupled from the remaining photon-baryon fluid and began to accrete in overdense regions, eventually becoming gravitationally bound. These extended sites of dark matter are described as halos, with properties determined by the original primordial density properties. A halo model has been developed that describes the mass and spatial distribution of these dark matter halos, and relates these properties to the underlying overdensities [71, 76]. This canonical model also relates the halo properties to the mass and spatial distribution of baryons and early galaxies, thus proving a connection between the initial density distribution of the universe and the large scale structure of galaxies observable today.

The dark matter halo model formalism predicts clustering statistics of dark matter, and can be extended to predict the clustering statistics of galaxies and anything else associated with dark matter halos [14]. Stemming from analytic models that described galaxy groupings as clusters with a range of masses, halo models developed into a formalism for analytical calculations of dark matter clustering, which can, in turn, be extended to describe (biased) galaxy populations.

The halo model assumes dark matter is grouped into halos, and can be described by a profile of a statistical halo and the relationship to an independent halo. In this way a two-halo model is constructed, described by a two-point correlation function with two terms.

$$\xi_{DM}(r) = \xi_{1h}(r) + \xi_{2h}(r). \tag{1.31}$$

The one-halo term $\xi_{1h}(r)$ is calculated based on mass elements within a single halo. The two-halo term $\xi_{2h}(r)$ considers mass elements in distinct pairs of halos. The one-halo term dominates the correlation function on scales smaller than the virial radii of halos, while the two-halo term dominates the correlation function on scales that exceed the virial radii of the largest halos. The one-halo term accounts for the halo mass function $dn(m)/dm$, the mass density distribution within a halo of mass m, and is normalized to the mean mass density of the universe through a multiplicative factor of $1/\rho_m$. The two-halo term contains the dependence on the dark matter power spectrum from linear perturbation theory, ξ_{DM}^{lin}, through cross-correlation of halos of mass m_1 and m_2 and utilization bias factors b to convert from primordial densities to halo formation:

$$\xi_{2h}(r) \propto \int b_h(m_1) b_h(m_2) \xi_{DM}^{lin}. \tag{1.32}$$

The dark matter power spectrum from linear perturbation theory, ξ_{DM}^{lin}, provides the linkage between analytic, general-relativity based perturbations against a smooth background, and the clumpy dark matter halo distribution that is important for predictions of late-time matter distributions.

Similarly, the halo model can be described by a two-term power spectrum, as the power spectrum is just the Fourier transform of the correlation function (see Section 1.3.1), as

$$P(k) = P^{1h}(k) + P^{2h}(k). \tag{1.33}$$

Use of the power spectrum allows for easier handling of convolution integrals and connects nicely to the power spectrum formalism developed in linear perturbation theory. In this case the two-halo term is directly proportional to the linear power spectrum:

$$P^{2h}(k) \equiv P_{DM}^{lin}(k) \frac{I_m^2}{\rho_M^2}. \tag{1.34}$$

Where I_m^2 represents the Fourier transform of the mean mass density profile of halos of mass m and bias b [108].

Finally, this formalism allows for simulation of the spatial clustering of galaxies at later times in the universe, making use of a Halo Occupation Distribution (HOD) that describes the average spatial distribution of galaxies within halos of a certain mass.

These dark matter halos were the sites of baryon accretion during this epoch of the universe, as the baryons accumulated in the gravitational wells provided by the

dark matter halos, eventually forming gravitationally bound objects that became the earliest stars and galaxies.

1.1.5 Early Galaxy Formation

Large scale structure (e.g. stars, galaxies, dark matter halos) arose from small density perturbations in the early universe [81] [1] [8]. Baryonic matter began accreting on vary small scales in the gravitational wells of dark matter halos, which are understood to have coalesced at earlier time than baryonic matter. Regions with an overdensity of baryonic matter collapsed into small, gravitationally-bound objects. Accretion onto these objects continued; eventually the object density overcame atomic repulsion and thermonuclear reactions began, forming early stars. On larger scales, collections of smaller objects also appear as overdensities, with clusters of stars gathered into galaxies and galaxies arranged into galaxy clusters, usually associated with a host dark matter halo.

Formation of the first bound objects defines the transition period at which linear approximations no longer describe the physical universe. Prior to this point, the evolution of the universe could be described with linear cosmological perturbation theory, where all structures could be understood analytically as small deviations from a perfect homogeneous and isotropic background. However, as nonlinear structures begin to form, the approximations of linearity needed for application of perturbation theory no longer apply, and alternate means of analysis are needed [18]. Study of the first generation of sources at high redshifts provides constraints on the power spectrum of density fluctuations on small scales. The conditions that describe formation of the first generation of stars are completely specified by the primordial power spectrum of Gaussian density fluctuations, the mean density of dark matter, and the initial temperature and density of cosmic gas, the primordial elements created by Big Bang nucleosynthesis, and the lack of dynamically significant magnetic fields [1]. The initial mass function of the first stars is described by this fairly simple set of initial conditions which can be described analytically. Beyond this point, computer simulations are needed to model the collapse of nonlinear structure. Specifically, N-body simulations are often employed to simulate the interactions of this phase of the universe, which are computationally intensive as they model the evolution of billions of particles. These models must take into account specific physics of interactions, which are complicated, ill-constrained by direct observations, and depend on many assumptions. Early luminous objects connect the simple initial universe to the complex, highly-structured universe observable at late times. Direct observations

of emission from these objects is needed to constrain and improve existing models.

To describe the first bound objects, consider the competing effects of gravity and electrostatic repulsion. As gas clouds of baryonic matter accrete to be of order the Jeans length, λ_J,

$$\lambda_J = v_s \left(\frac{\pi}{G\rho}\right)^{\frac{1}{2}}, \tag{1.35}$$

where ρ is the density of matter, G is the gravitational constant, and v_s is the corresponding speed of sound (speed at which a wave propagates through matter), the matter cloud condenses around the initial density perturbation, forming a bound object. Alternatively, this accretion can be measured relative to the Jeans mass, $M_J \propto \rho^{1/2}$ of $\sim 10^4_\odot$ (also known as the Bonner-Ebert mass), at which point gravity overcomes the repulsive pressure forces and the objects become bound by gravity. This is believed to have happened at redshifts of $15 < z < 30$ [87] [8]. Once the universe transitions into a matter-dominated state and neutral hydrogen atoms are able to form, the sound velocity decreases, causing a corresponding decrease in the Jeans length. Thus smaller clouds of matter are able to transition to bound objects after recombination. The underlying speed of sound is heavily dependent on the details of the underlying dark matter distribution, which feeds into the density ρ.

The earliest stellar objects are extremely metal poor and consist entirely of chemicals produced in the Primordial Nucleosynthesis (primarily neutral hydrogen and some helium). These objects are described as Population III stars with zero metallicity (Z ~ 0) [5]. They are assumed to be very massive and have a different main-sequence life cycle than many of the stars observable in the universe at late times; this is demonstrated by three-dimensional numerical simulations which suggest the initial mass functions for these stellar objects had stellar masses $> 100 \; M_\odot$ [8]. These stars have luminosities that are nearly blackbodies. The large mass and luminosity of these stars suggests this population is a significant contributor to background emission in the universe. The initial mass function (IMF) suggested for this population [56] is

$$f(M_*) = M_*^{-1}\left(1 + \frac{M_*}{M_*^c}\right)^{-1.35} \tag{1.36}$$

where the mass range is $3 < M_* < 500 M_\odot$ and M_*^c is a maximum mass at which stars form (masses larger than this limit are assumed to collapse into black holes). The final stellar mass is determined by both the mass of the initial gas cloud and the effects of feedback processes, including cooling.

The life cycles of these early, metal-poor stars are assumed to follow a roughly similar version of the stellar main-sequence. At the end of the stellar lifecycle of

sufficiently massive stars, supernovae generate massive explosions which provide chemical enrichment to the local environment, introducing new elements into the surrounding medium and regulating the formation of the first galaxies [8]. The transition to a new population of stars with slightly higher metallicity (Population II, $Z \sim 1/50\ Z_\odot$) is controlled by the rate of introduction of additional metals into the environment and feedback mechanisms promoting cooling of the expelled supernovae remnants. At some point, a critical metallicity is reached and lower-mass Pop II stars begin to make significant contributions to the emission. The IMF for Pop II stars is a much simpler Salpeter form [25],

$$f(M_*) \propto M_*^{-2.35}. \tag{1.37}$$

As the first stars initially formed in specific overdense regions in dark matter halos, it is not likely they formed at spatial distances small enough to be gravitationally bound into true galaxies [8]. Instead, the first generation of Pop III stars likely formed in isolation, and over time, as dark matter halos and associated baryons increased in density, future generations of a mix of Pop II and III stars and associated low-metallicity gas eventually formed into groupings that meet a consensus definition of galaxies.

Observations of emission from early galaxies at redshifts $z > 6$, prior to the reionization of the universe, are likely to include emission from both Pop II and Pop III stars. Identification of the spatial location of such early galaxies likely does not include identification of the very first generation of stars, as they are expected to be in isolation and may not have enough collective emission (compared to a galaxy) to be identifiable as a source. However, the emission from these first stars is nevertheless present in the radiative background. Observations of emission from early galaxies still plays an important role in constraining the spatial distribution and emission of both populations of early stars and the evolution of baryonic matter overall, and will constrain the power spectrum of density fluctuations on small scales.

1.1.6 Epoch of Reionization

The earliest stars and galaxies formed while the universe was still filled with neutral hydrogen [1, 81, 90]. Emission from these objects ended the Dark Ages by ionizing the neutral hydrogen in the universe and allowing photons of all wavelengths to travel freely. This process is prolonged and the exact details are not well understood, due to the lack of observations from this era. Numerical simulations suggest baryonic matter collapses into luminous objects at redshifts $20 < z < 30$, which emit radiation

with sufficient energy to ionize the neutral hydrogen in the immediate vicinity. However, many ionized atoms will recombine with free electrons, causing no net change in the reionization state of the general area.

Eventually, the distance between stars in galaxies is sufficiently small to allow the overlap of the spherical stellar ionization regions, resulting in ionization of the intergalactic medium (IGM) of the galaxy. The region surrounding the galaxy becomes ionized, and will recombine with free electrons if no other ionized galactic spheres are nearby. The fraction of ionizing radiation ($E > 13.6$ eV) from the galaxies is described by the escape fraction, f_{esc}, and estimated to be $< 10\%$. The high density of the early universe decreases the efficiency of escape. Additionally, uneven distribution of gas within a galaxy (clumping) complicates the ionization process as it increases the likelihood of recombination in overdense regions. The number of ionizations per baryon can be estimated as the product of the efficiency with which baryons are incorporated into stars ($f_{star} = 10\%$), the efficiently with which ionizing radiation escapes to ionize new fronts ($f_{esc} = 10\%$), and the number of ionizing photons produced per baryon in stars (N_γ):

$$N_{ion} \equiv N_\gamma f_{star} f_{esc}. \tag{1.38}$$

For reference, the local stellar IMF with $Z = 1/20 \, Z_\odot$ is $N_\gamma \sim 4000$. The number of ionizing photons per baryons is used to estimate the radius of the ionization region surrounding an object, where $r_{max} \propto N_{ion}^{1/3}$. Recombination decreases this radius. This process of spherical ionization region is repeated again at the scale of a dark matter halo, where the size of the ionized region depends on the mass of the halo. Additionally, other luminous objects such as quasars are expected to contribute to ionization in a similar fashion, likely with a different value of N_γ.

Once the ionized regions surrounding halos begin to overlap, ionization of the entire universe is expected to proceed rapidly. The times of onset and duration of this process are not known. To statistically describe the transition from a neutral universe to a fully ionized universe, models rely on the ionized hydrogen filling factor, Q_{HII}:

$$Q_{HII}(t) = \int_0^t \frac{N_{ion}}{0.76} \frac{dF_{col}}{dt'} e^{F(t',t)} dt' \tag{1.39}$$

where $F(t', t)$ is a function accounting for clumpiness and recombination. Note that even after reionization is complete, small areas of neutral medium remain.

These models demonstrate that star-forming galaxies are capable of ionizing the universe in the described manner between $6 < z < 15$, which is consistent with the

few observations available. Post-reionization, photons of all wavelengths are now generally able to travel freely through the universe. Observations of quasars and optical depth measurements indicate the universe was completely ionized by $z \sim 6$, but few additional details about the process between $7 < z < 30$ are known.

One way in which the transition from pre- to post-reionization manifests is in the spectra of galaxies. Prior to reionization, while the universe is filled with neutral hydrogen, galactic spectra are suppressed at energies below the Lyman break energy due to the ionization of neutral hydrogen ($E > 13.6\,\text{eV}$, $\lambda < 0.0912\,\mu$m). Additional suppression occurs at energies sufficient to excite the neutral hydrogen atoms. After reionization is complete, photons are able to travel freely (in general) and a complete, unsuppressed spectrum is observable. Thus the suppression feature provides an important method for identification of early galaxies. Measurement of the level of unsuppressed emission provides a constraint on the total emission of galaxies prior to reionization. Additionally, identification of the precise wavelength of the suppression feature provides the timing of reionization in the observed area of the sky. The observed wavelength of the break feature, λ_o, is redshifted relative to the emitted wavelength, λ_e, due to the expansion of the universe as $\lambda_o = (1 + z)\lambda_e$, allowing for precise determination of the redshift of completion of reionization. Assuming reionization completion occurs between redshifts of $6 < z < 10$, this feature is shifted from emission in the ultraviolet wavelength range to be observable in the near-infrared wavelength range today.

These early epochs of the the universe are represented by a chronological cartoon in Figure 1.3. In this image, note that time increases to the right and redshift increases to the left.

1.1.7 Modern Galaxies and the Universe We Observe Today

After reionization, the universe is much more similar to the modern-day universe we observe today. The more recent, directly-observable universe has been extensively studied with multiwavelength imaging and spectroscopic surveys, and recent observations over the last two decades have revolutionized the current understanding of galaxy formation and evolution [59].

Astronomy works to observe objects within the visible universe, recording emission limited only by technology and object distance across the entire electromagnetic spectrum. In this way, astronomy focuses on the evolution of the galaxy luminosity
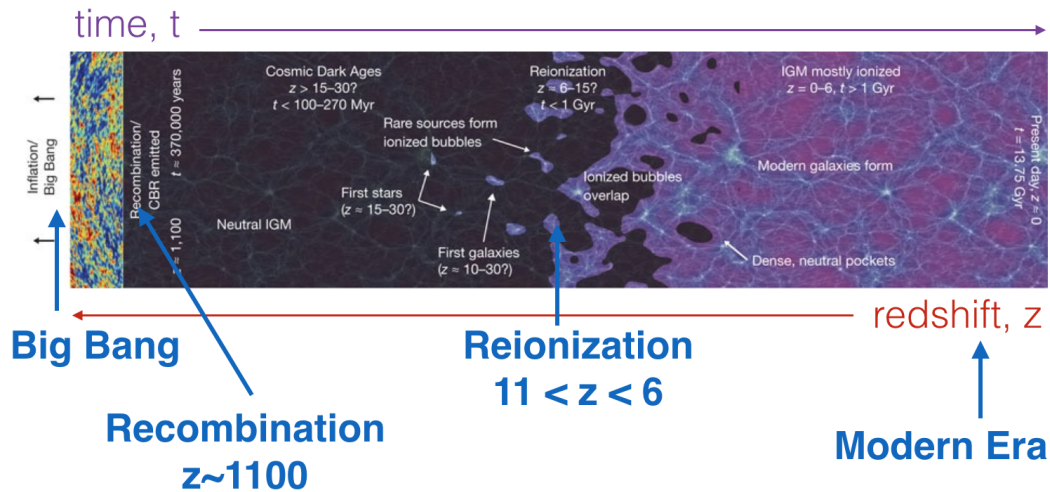
Figure 1.3: Overview of cosmic history from the Big Bang to the present time, with key epochs emphasized.

density and works to generate and empirical description of global star formation and chemical enrichment of the universe [59]. This subsection begins with a focus on the astronomical description of galaxies in late-times, describes the complex industry of extragalactic observations, and situates these modern galaxies in their cosmological context.

Galaxy Properties. The two most important characteristics of galaxies are mass and star formation history. These properties are often inferred from measurement of light, which require stellar population synthesis models for calibration. These models combine physics of stellar evolution with observed spectral energy distributions (SEDs) of galaxies and produce an emergent spectrum for a galaxy with the given properties [59]. It is possible to obtain resolved color-magnitude diagrams of the stellar properties of nearby galaxies, while for more distant galaxies only integrated light can be obtained. Observations of integrated light alone provide an incomplete picture of the contributing properties, as the integrated spectrum is often degenerate between different properties, such as age, metallicity, and dust attenuation. In spite of these limitations, extensive broad and deep galactic surveys have revealed a wealth of information about millions of galaxies out to redshifts of $z \sim 6$. The SED and colors of many galaxies are catalogued along with the observed luminosities and locations. This information is compared to spectral templates to constrain other properties of the galaxies.

The initial mass function (IMF) governs the relation between mass, light, and stellar population age. It controls the ratio of hot, bright stars (which determine the light) to cool, faint stars (which determine the mass), and it describes the luminosity and color evolution of the total stellar population, since stellar masses have different evolutions. The IMF also includes more subtle physics. For example, the IMF affects the time evolution of the integrated stellar mass, which changes as more massive stars lose gas to the ISM via winds or supernovae explosions. Not surprisingly, the IMF is not well constrained by photometric measurements of the integrated light from galaxies. However, for simplicity, the IMF is generally assumed to be universal, with the same shape at all times and in all galaxies. The usual assumption is that the IMF follows a power-law shape described by Salpeter for a finite mass range ($0.1 < M_\odot < 100$),

$$f(M_*) \propto M_*^{-2.35}. \tag{1.40}$$

This obvious oversimplification has ramifications for modeling, and more detailed models or models tailored for specific galaxy populations (such as early, low-metallicity galaxies) adjust the IMF accordingly. Finally, note that the output of the IMF is often described as a mass-to-light ration (M/L).

Star formation histories are determined in many ways, with a popular method using the SEDs and template spectra along with simplifying assumptions that are not likely applicable to an individual galaxy. For recent galaxies with observations in the ultraviolet wavelength band, only the IMF and dust content are needed to provide a good estimate of the instantaneous star-formation rate density because the UV-continuum emission of these galaxies is dominated by short-lived massive stars [59]. This leads to a relationship between star formation rate (SFR, in units of ergs/s/Hz) and UV luminosity ($\mathcal{L}_{UV}$ with units of $M_\odot$/year),

$$\text{SFR} = \mathcal{K}_{UV} \times \mathcal{L}_{UV} \tag{1.41}$$

where $\mathcal{K}_{UV}$ is a factor representing the recent SFH and metal-enrichment history and choice of IMF. Similar relationships hold in other wavelength bands, taking into account other physics as needed (e.g. in the infrared where dust emission plays an important role, the analogous relation has a term to address dust).

The metal enrichment history of the universe can be described by chemical enrichment equations that factor in an initial metallicity Z, a mass fraction of each generation of stars reprocessed back into the interstellar medium (ISM), and the net metal yield (y) of heavy elements dispersed into the ISM or IGM by each generation

of stars [59]. This leads to a total mass density of heavy elements in the ISM/IGM as a product of metallicity and (comoving) density and function of redshift, $Z(z)\rho(z)$. This can be evaluated over cosmic time to trace the mean metallicity of the universe, usually calculated relative to the baryon density. As expected based on the assumption of reprocessing included in the chemical enrichment equations, metallicity increases over time; at the present time the global metallicity is calculated to be $Z_b \simeq 0.09(y/Z_\odot)$, as compared to a redshift of $z \sim 2.5$ when the global metallicity was $Z_b \simeq 0.01(y/Z_\odot)$ [59]. This calculation has weak dependence on the IMF.

Dust also plays a large role in the formation and evolution of stars and galaxies, and are accounted for as much as possible in the models of various galactic parameters. Dust obscures UV emission, and increases observed infrared emission values as the dust typically re-emits radiation in this waveband.

The specific luminosity density at time t of a cosmic stellar population characterized by an star formation rate density $\psi(t)$ and a metal-enrichment law $Z_*(t)$ is given by the convolution integral

$$\rho_\nu = \int_0^t \psi(t-\tau)\mathcal{L}[\tau, Z_*(t-\tau)]d\tau. \tag{1.42}$$

where $\mathcal{L}[\tau, Z_*(t-\tau)]$ is the specific luminosity density radiated per unit initial stellar mass (luminosity mass density) by a simple stellar population (an ensemble of stars formed instantaneously and evolving together) of age τ and metallicity $Z_*(t-\tau)$. Theoretical calculations of the luminosity density depend on many stellar parameters built up by the copious observations of recent times. Comprehensive modeling of star formation histories using data from UV and IR surveys converge upon a consistent picture of the star formation history of the universe, where the star formation rate density has a profile of $\psi(z) \propto (1+z)^{-2.9}$ at $3 \leq z \leq 8$, followed by a peak between redshifts of $z \sim 1.5 - 2$ (at which time the approximate age of the universe was 3.5 Gyr), and concluding with a decline in late-times with a present-day star formation rate density of $\psi(z) \propto (1+z)^{2.7}$. These results indicate that galaxies formed a substantial fraction of their mass by $z < 2$; of order 75% of their total mass. Stars formed in early galaxies with $z > 8$ contribute only 8% of the total stellar mass today. Clearly, this low contribution of stellar mass at early times indicates the luminosity contribution from these sources will also be subdominant and will require careful identification. Additionally, this description of luminosity mass density focuses on stellar emission and ignores emission from

other astrophysical phenomena (dust, active galactic nuclei, quasars and black holes, etc.) which must also be considered in a full treatment of historical cosmic emission.

The Milky Way Galaxy. The Milky Way galaxy is a spiral galaxy characterized by a disk with a stellar distribution such that the density of stars varies exponentially with the vertical height h above or below the disk as $I \propto e^{h/h_{scale}}$. These stars are mapped in the Two Micron All Sky Survey (2MASS), a survey of photometry and astrometry over the entire celestial sphere in the J (1.25 μm), H (1.65 μm), and Ks (2.16 μm) near-infrared photometric bands [94]. 2MASS produced a Point Source Catalog containing 470,992,970 sources, with the sources attributed to Milky Way stars displayed in Figure 1.4. As a spiral galaxy, the Milky Way contains abundant gas, including neutral hydrogen (HI), molecular hydrogen (H_2), ionized hydrogen (HII), and CO (an important tracer molecule) [90]. This gas scatters starlight, generating galactic emission referred to as diffuse Galactic light [7]. Additional dust resides in Earth's solar system in the form of interplanetary dust [102, 47]. These local details provide important foregrounds to consider when making extragalactic observations.

Observations. Over the last few decades, extensive surveys of the visible universe have been carried out in many wavebands. These surveys contain both imaging and spectroscopic data, and many analyses have worked to combine both to provide thorough catalogs of the visible universe with high spatial and redshift coverage. A full review of many surveys can be found in [59] and references therein; here, a few key extragalactic surveys are briefly summarized.

2MASS, briefly mentioned above, was designed to image the large-scale structure of the Milky Way and the local universe. 2MASS has uniformly scanned the entire sky in three near-infrared bands to detect and characterize point sources brighter than about 1 mJy in each band, using two automated 1.3-m telescopes [94].

The Sloan Digital Sky Survey (SDSS) is an extensive survey of approximately one-quarter of the sky from a 2.5-meter telescope at Apache Point Observatory, New Mexico, with an imaging camera and pair of spectrographs. SDSS produced multi-color images and maps containing more than a million galaxies and hundreds of thousands of quasars [104].

The UKIRT Infrared Deep Sky Survey (UKIDSS) is near-infrared counterpart of the
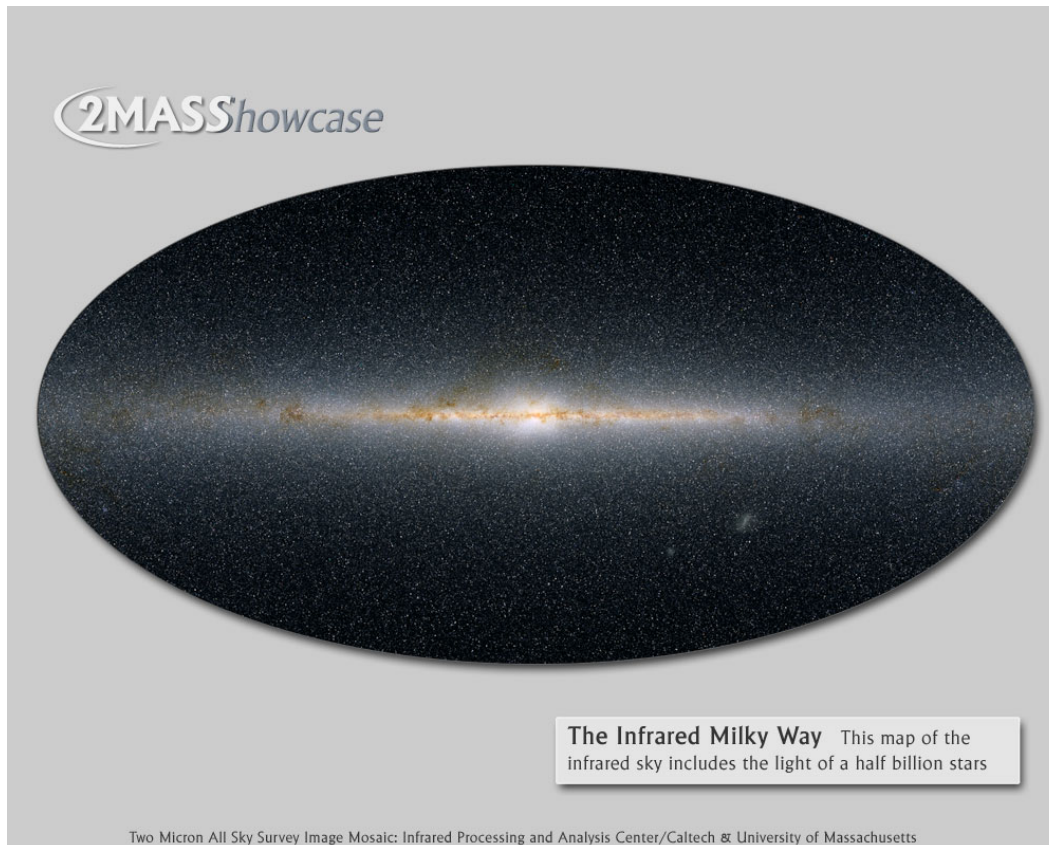
Figure 1.4: Image of the Milky Way galaxy with 2MASS, with over 500,000 stars. Pixel values represent the integrated flux along the line of sight. The light is separated into three color bands corresponding to the near-infrared window that 2MASS observed: blue for J-band (1.2 microns), green for H-band (1.6 microns) and red for K-band (2.2 microns). Image courtesy of IPAC.

Sloan Digital Sky Survey, observing a portion of the sky of several thousand square degrees to deeper magnitudes than 2MASS [57]. It uses the Wide Field Camera (WFCAM) on the 3.8m United Kingdom Infrared Telescope (UKIRT) with ZYJHK filters covering the wavelength range 0.83?2.37 μm at both high and low Galactic latitudes.

The 2dF Galaxy Redshift Survey (2dFGRS) is a major spectroscopic survey of 245,591 objects, mainly galaxies (with redshifts obtained for 221,414 galaxies) over an area of ~1500 square degrees [12]. 2dFGRS was designed to map optically luminous galaxies over a statistically representative volume of the universe in order to characterize the large-scale structure of galaxy distributions.

One important application of extensive galaxy surveys is estimation of the matter-

power spectrum, $P(k)$. The matter power spectrum can be calculated from the Fourier transform of the two-point correlation function of galaxies and complements the wavemodes k accessible with measurements of CMB anisotropies. The spatial separation of large number of galaxies is used to build up the correlation function, which measured the spatial separation between pairs of galaxies. The power spectrum is displayed in Figure 1.5.
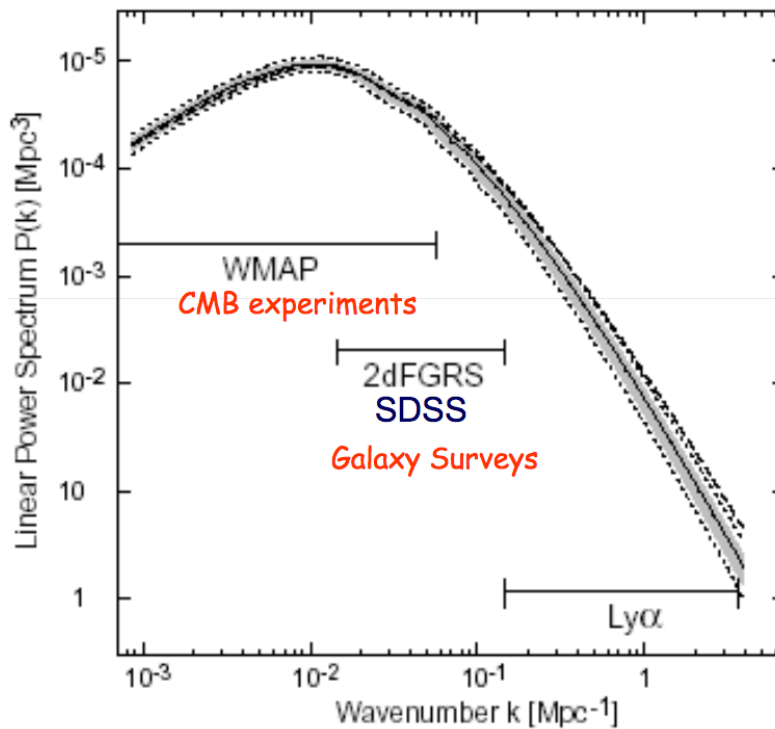
Figure 1.5: The matter-power spectrum, which provides constraints on the spatial distribution and evolution of observable matter in the universe. CMB anisotropy measurements contribute to modes $k < 0.05$, while observations of resolved galaxies contribute to modes $0.01 < k < 0.1$.

The total emission from all observed galaxies (up to $z \sim 5$) has been calculated, as have the spectrum of spatial fluctuations from this population. This provides a reference point for searches of early galaxy emission, as total measurements must exceed the threshold provided by $z < 5$ galaxies. Additionally, these surveys provide a means of treating this more recent emission as foregrounds for earlier galaxy emission, as well as measurements with which predictive models must be consistent.
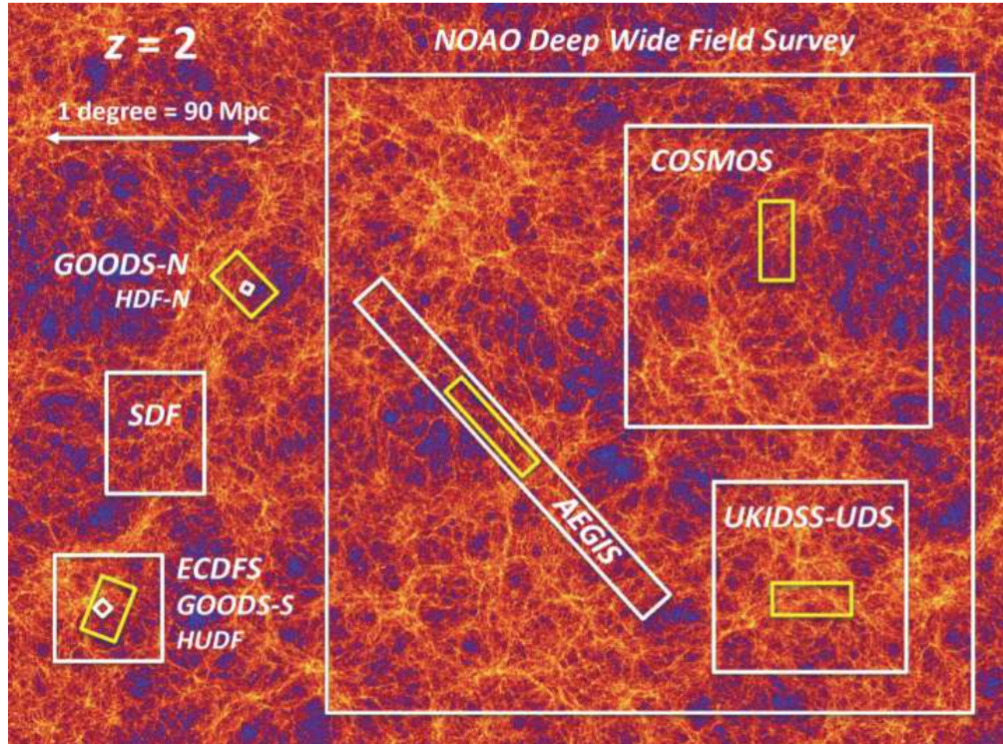
Figure 1.6: Graphical representation of survey area of several important galaxy surveys, including UKIDSS.

Large Scale Structure.   Galaxy properties are determined by the dark matter halos in which they form. In turn, properties of dark matter halos are determined by the density perturbations of the early universe. Analysis of large galaxy surveys provide the information to bridge the gap between these late-time, non-linear processes and the early linear processes, linking the statistical properties of a galaxy population to the properties of the halo in which the population resides. Large surveys provide constraints on the dark matter distribution on large scales, and on galaxy formation models on smaller scales [14].

An additional complexity in the relationship between observable luminous galaxies and the underlying matter distribution is the relationship of galaxy mass distribution to halo mass distribution. The spatial distribution of galaxies does not precisely align with the underlying dark matter distribution, and this offset is measured as a bias factor [37]. This bias is caused by the detailed physics of baryonic accretion which causes the spatial distribution of baryons to differ from the distribution of dark matter. For a density contrast of $\delta = (\rho - \bar{\rho})/\bar{\rho}$ where $\bar{\rho}$ is the mean density at a given scale, the density of galaxies δ_g is a function of the underlaying mass density

δ as $\delta_g = f(\delta)$. For a linear function f, the linear galaxy bias b is then the ratio of the mean overdensity of galaxies to the mean overdensity of mass:

$$b = \frac{\delta_g}{\delta}. \qquad (1.43)$$

It follows that the linear galaxy bias is a function of scale and can be defined as the square root of the ratio of the two-point correlation function of the galaxies relative to the dark matter:

$$b = \left(\frac{\xi_{gal}}{\xi_{DM}}\right)^{\frac{1}{2}} \qquad (1.44)$$

This biasing is easily accommodated by matter distribution simulations that use the two-halo model. This bias can be accounted for in the two-point correlation function or power spectra of dark matter halos and associated galaxies as well, allowing for a means of introducing this information into simulations of structure.

1.1.8 From Cosmology to Large Scale Structure

Early events in the history of the universe set the conditions for later evolution in measurable ways. While the initial universe was large smooth and isotropic, the later universe amplified small anisotropies in density that allowed for gravitational accretion and development of bound and luminous objects that characterize a universe at late times which has much complexity and inhomogeneity on small scales. As the universe expanded and various particle species decoupled from the primordial plasma, different particle species began more independent evolutionary trajectories, with dark matter gravitationally accreting around initial regions of overdensity, photons and baryons decoupling, baryons accreting in gravitational wells in dark matter halos and forming luminous objects that eventually resulted in a metal-enriched, ionized universe. Emission from luminous objects provides a tracer of the history of the later evolution of baryons, and contains information about the earliest luminous stars and galaxies.

1.2 Extragalactic Background Light

The interactions between matter, energy, and spacetime are the cornerstones of cosmology described with the machinery of general relativity, as described in the previous Section. Remarkably, a description of the universe as matter coalescing into gravitational wells generated by initial density fluctuations in the primordial universe allows for a statistical prediction of the spatial distribution of early luminous sources. The detailed distribution and physics of actual sources remains obscured, as there is not much observational data available about these objects and as they

are literally shrouded in neutral hydrogen. As the sources are too far away and faint for individual identification and direct detection with current technologies, alternate means of probing these sources are needed. Success of the study of the diffuse cosmic microwave background suggest a path forward to measure the *collected* emission of these early sources. Photons emitted by these early sources are observable today as part of the extragalactic background light (EBL), a radiative field that comprises all photons emitted by astrophysical sources throughout cosmic history.

This section describes the EBL in detail and discusses methods of measurement of the absolute intensity of this radiative background. It summarizes early measurements and discusses challenges with the measurement of absolute intensity of the extragalactic background light and separation of the contribution of early galaxies.

1.2.1 Extragalactic Background Radiation

The universe is permeated with radiation across all bands of the electromagnetic spectrum. This radiation comes from gravitational and nuclear processes, including both primordial processes from the early evolution of the universe and from the evolution of stars and galaxies during the matter-dominated era. Different physical processes generate photons in different bands. A classic image from Hauser and Dwek [30] compiles measurements across the spectrum to show relative intensities of each background, shown in Figure 1.7.

The highest intensity portion of the spectrum is cosmological in nature; this is the cosmic microwave background radiation generated by the recombination of protons and electrons into neutral hydrogen as described in Section 1.1.3. This radiation is represented by a blackbody spectrum with a temperature of 2.725 K and extends from $\sim 400 - 3000 \ \mu$m.

The background radiation in all other spectral ranges is astrophysical in origin; it is generated by the formation of structure, as stars and galaxies form and evolve. In this work, consistent with [30], the spectral range from ultraviolet (UV) to far infrared (IR) wavelengths is defined as the Extragalactic Background Light (EBL)[2]. This range of the electromagnetic spectrum contains energy with the second-highest intensity (behind the CMB), and is not nearly as precisely measured and characterized (to date) as the CMB. The energy in this range is dominated by emission

---

[2]The infrared portion of the EBL has been referred to in literature as the *cosmic infrared background* (CIB). More recent publications use the more general EBL term and omit reference to the CIB, which is the convention followed here.
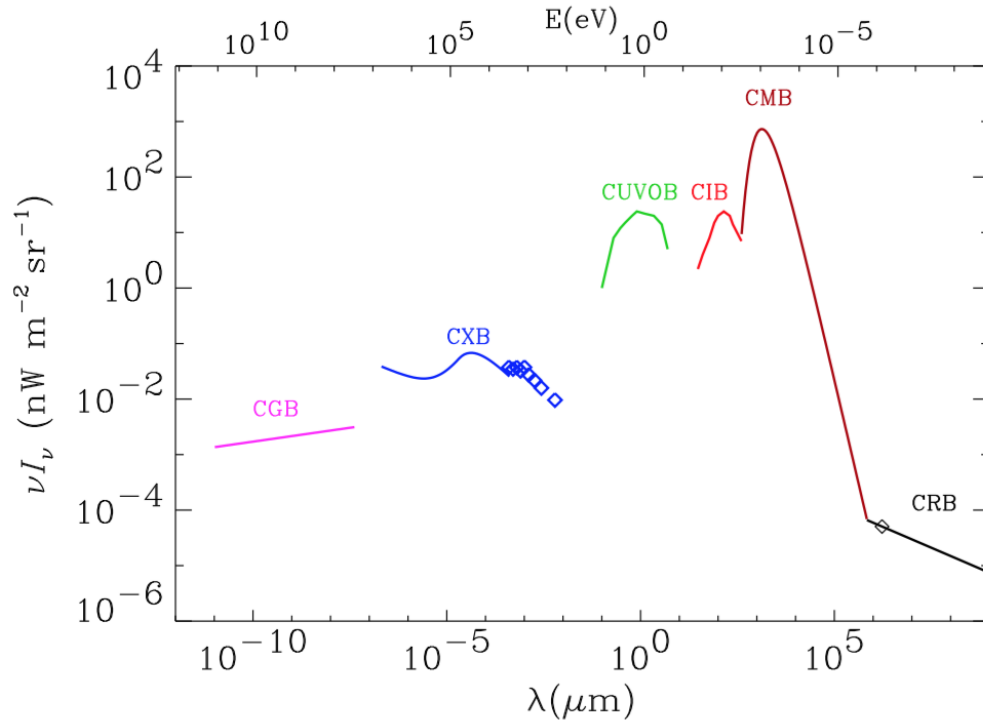
Figure 1.7: From Hauser and Dwek (2001): Spectrum of the cosmic background radiations. Starting at the right hand side of the image, the cosmic radio background (CRB) is represented by a $\nu I_\nu \propto \nu^{0.3}$ spectrum. The dominant radiative background is the cosmic microwave background (CMB), of cosmological origin, shown here as blackbody spectrum at 2.725 K. The UV-optical (CUVOB) and infrared (CIB) backgrounds are schematic representations of the work summarized in the Hauser and Dwek paper [30]. The X-ray background (CXB) is a combination of data and analytical represenations, while the γ-ray background (CGB) is represented by a power law.

from the thermonuclear processes of stars, with additional contributions from dust emission.

The EBL spectral range contains contributions from astrophysical processes from different times throughout cosmic history. More distant objects contribute emission that originated at much earlier times, which is what allows for observation of contributions from early galaxies. Observations of emission thus contain photons from recent objects, such as resolved, $z < 3$ galaxies; diffuse emission from late-time $z < 6$ galaxies, and diffuse emission from early, $z > 6$ galaxies. This is shown schematically in Figure 1.8. Additionally, the EBL contains emission from unresolvable stars outside of traditional galaxy boundaries but within dark matter halos,

collectively referred to as intra-halo light. EBL measurements must make an effort to characterize and distinguish between these different astrophysical contributions.
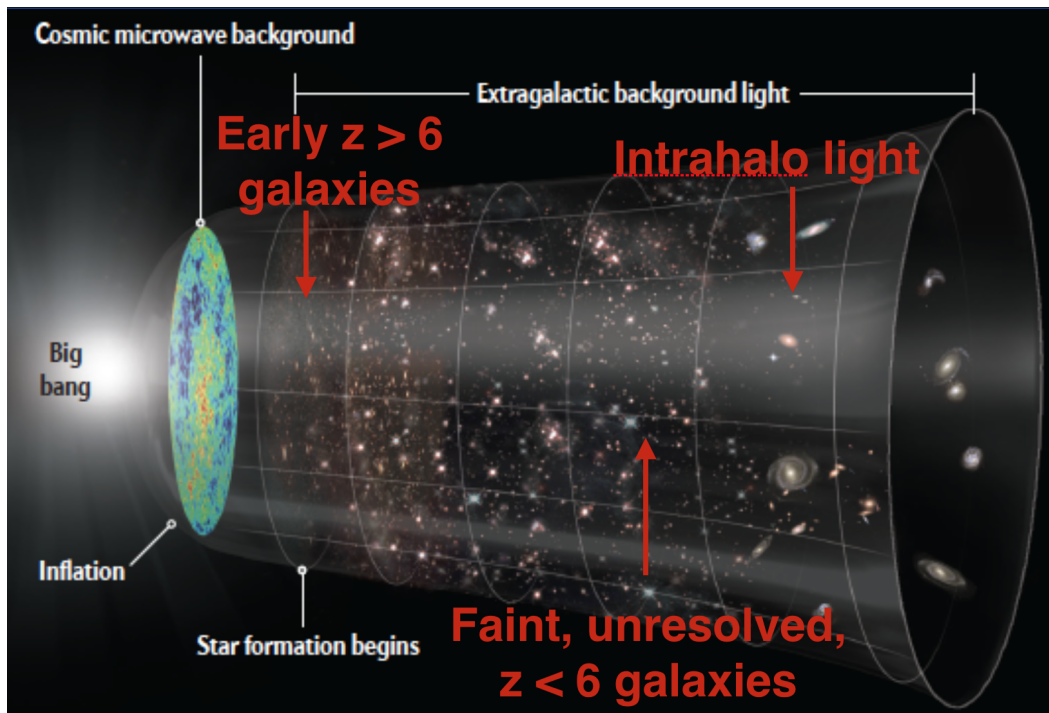
Figure 1.8: Contributions to EBL over cosmic history. The EBL contains photons from stellar thermonuclear processes outside of the Milky Way galaxy, including emission from early and present day galaxies (both resolved and unresolved), and emission from stars outside of traditional galaxy boundaries (collectively described as intrahalo light).

1.2.2 Direct Detection of EBL

The near-infrared EBL has few defining observational characteristics. It has no inherent spatial signature, and instead has complex dependence on multiple factors, such as the character of the luminosity sources, the evolution and history of the sources, the history of dust formation, and the distribution of dust relative to luminous objects [30].

Direct measurements are challenging, both astrophysically and technically. Technically, measurements require accurate signal calibration, usually in the form of a well-calibrated zero flux level reference (e.g. a cold shutter). Other instrument systematics to account for include telescope emission, and measurement systematics such as atmospheric emission, and Earthshine. Astrophysical systematics include signal discrimination, specifically separation of desired EBL signal from other fore-

grounds. Foregrounds are discussed more in detail in Section 1, and include, dust, stars, and $z < 5$ galaxies. Finally, definitive EBL measurements must also show a signal of positive significance, which is also extragalactic and isotropic [30].

The Extragalactic Background Light is traditionally measured as surface brightness, the amount of energy received by a detector of unit area from an incoming solid angle. This type of intensity measurement is indicated by λI_λ with units of nanowatts per meter-squared per steradian, [nW/m^2/sr]. Note the surface brightness can be equated between functions of wavelength or frequency as $\lambda I_\lambda = \nu I_\nu$.

Surface brightness can be converted to common astronomy units of MegaJansky per steradian, [MJy/sr] where 1 MJy = 10^{-20} W/m^2/Hz, as follows:

$$\nu I_\nu \left[\frac{\text{nW}}{\text{m}^2\text{sr}}\right] = \frac{3000}{\lambda[\mu\text{m}]} I_\nu \left[\frac{\text{MJy}}{\text{sr}}\right]. \tag{1.45}$$

Additionally, surface brightness can be related to magnitudes[3] m_i as follows:

$$m_1 - m_2 = -2.5 \log \frac{f_1}{f_2}. \tag{1.46}$$

Finally, this intensity can also be related to the energy density $\epsilon \eta_\epsilon$, where ϵ is the photon energy in electronvolts [eV] and η_ϵ is the photon spectral number density in photons/cm^3/eV,

$$\epsilon \eta_\epsilon \left[\frac{\text{eV}}{\text{cm}^3}\right] = 2.62 \times 10^{-4} \nu I_\nu \left[\frac{\text{nW}}{\text{m}^2\text{sr}}\right]. \tag{1.47}$$

These units are useful for comparison to other methods to constrain the EBL levels expected.

1.2.3 Early Measurements of the Infrared Extragalactic Background

Measurements of the EBL have been made since the early 1980s from a variety of instruments. These measurements identified unknown foregrounds and provided important constraints on expected EBL levels before achieving definitive identification of extragalactic EBL. Contributions to the EBL from early ($z > 6$) sources from the Epoch of Reionization have yet to be confirmed.

1.2.3.1 Sounding Rocket Observations

Sounding rockets provided the first measurements of the infrared EBL, starting in the 1980s [75, 64, 68, 78, 69, 46]. As measurements of the infrared wavelength bands

---

[3]It is important to carefully indicate the magnitude system in use, e.g. AB magnitude or Vega magnitude.

are difficult to make from the surface of the earth due to the brightness of atmospheric emission in this spectral range, some means of getting above the atmosphere was needed, making sounding rockets a natural choice. However, sounding rockets have instrumental systematics that add to the complexity of isolating extragalactic signals from measured observations. Some of the systematic errors introduced by the sounding rocket vehicle include emissions from rocket exhaust, residual atmosphere, and Earthshine. This limited the utility of the early observations to identification of astrophysical foregrounds and EBL upper limits, but paved the way for satellite missions with instruments dedicated to infrared EBL measurements. In spite of these limitations, sounding rockets were successful in establishing upper limits on EBL radiation levels, and underscored the importance of dominant astrophysical foregrounds.

1.2.3.2 Satellite Observations

IRAS. Satellite observations were able to overcome some of the limiting factors of sounding rocket observations, by providing longer integration times and observations with different systematics. The *Infrared Astronomical Satellite (IRAS)*, launched in 1983, provided the first all-sky satellite observations in the infrared. *IRAS* was designed to map discrete sources in the infrared sky at wavelengths of 12, 25, 60, and 100 μm. [77]. *IRAS* measurements identified diffuse emission components in the solar system and Milky Way [31]. Unfortunately, *IRAS* did not contain a zero flux reference, so no definitive NIR EBL measurements were made. Additional satellite measurements would be needed for more definitive EBL measurements.

COBE. The *Cosmic Background Explorer (COBE)* [4] satellite mission provided data for some of the most definitive EBL measurements through the early 2000s. *COBE* included two main instruments, the Diffuse Infrared Background Experiment (DIRBE) [93], and the Far Infrared Absolute Spectrophotometer (FIRAS) [62]. The overall *COBE* mission was designed to facilitate measurements of absolute sky brightness from both instruments, with optimized orbit, scan strategy, and data processing.

The DIRBE instrument was an absolute photometer designed to provide EBL sky maps in ten broad wavelength bands between 1.25 - 240 μm with a $0.7° \times 0.7°$ instantaneous field of view. DIRBE was designed for strong stray light rejection,

and contained a cold chopper and full beam cold shutter for measurements of the zero-point flux offsets. Although all ten wavelength bands were analyzed for EBL contributions, four bands had a signal with positive residuals exceeding 3σ; of these, the 140 and 240 μm bands met the criteria for isotropy. The authors verified the signal was extragalactic in origin and concluded that the EBL was detected at the wavelengths [32, 22]. Upper limits were reported for the observations at other wavelengths. As expected, the largest uncertainty in measurements came from foreground characterization, especially of the interplanetary dust (IPD). DIRBE data was used to develop a detailed dust model [47] still in use today. Additional analyses of the DIRBE data have been done with other models of foregrounds, particularly interplanetary dust and interstellar medium (ISM) contributions, confirming the original results at 140 and 240 μm. More studies worked to account for stellar foregrounds in the Milky Way through use of 2MASS, extending the upper limits to additional wavelengths.

The FIRAS instrument was a Fourier transform spectrometer based on a Michelson interferometer, comparing $7°$-diameter sky brightness measurements to a full beam blackbody calibrator at wavelengths from 100 μm to 1 cm. Preliminary FIRAS data provided measurement of a uniform residual EBL background from 200 μm to 2 mm in excess of foregrounds [85], which was the first tentative EBL identification from *COBE*. Later analysis based on final photometric reduction data [26] used the aforementioned model of interplanetary dust [47] and tested 3 methods of inter-stellar medium accounting to determine a consistent residual isotropic background measurement, consistent with the DIRBE results at 140 and 240 μm [32]. Other analyses of FIRAS data yielded results that did not meet the three standards of proof of positive, extragalactic, isotropic signal [53, 54].

IRTS. The *Infrared Telescope in Space (IRTS)* included an instrument dedicated to the study of the infrared EBL background, the Near Infrared Spectrometer (NIRS), which took measurements for 30 days in 1995 [67]. NIRS is a grating spectrometer with a 8 arcmin square beam and 0.12 μm resolution from 1.4 to 4.0 μm. The NIRS instrument included a cold shutter, providing a zero point flux reference. The NIRS measurements largely agreed with DIRBE measurements at longer wavelengths, but exceeded the NIRS measurements at shorter measurements, rising with a steep slope. A detailed look at the systematic uncertainties could resolve the disagreement in DIRBE and NIRS measurements, particularly in regard to the removal of

interplanetary dust (IPD). Further measurements of the EBL, especially in the NIR, will be important to resolve the DIRBE and NIRS discrepancies.

AKARI. The *AKARI* infrared satellite was designed by the Japan Aerospace Exploration Agency (JAXA) and launched in 2006 [66, 70]. It has a 68.5-cm aperture and two cryogenically-cooled instruments, the Far-Infrared Surveyor (FIS) and Infra-Red Camera (IRC). While the main science goal of *AKARI* was an all-sky survey in the far infrared, it was also available for targeted observations. *AKARI* observations of six fields with the FIS instrument provided measurements of the absolute EBL intensity at four far-infrared wavelengths, 65, 90, 140, and 160 μm [70]. The instantaneous field of view of the two shorter wavelength bands was $30'' \times 30''$ and $50'' \times 50''$ for the two longer wavelength bands; these were imaged as strips then combined in a mosaic image to produce $2° \times 6°$ sky maps of each field. The authors remove resolved galaxies up to specified flux, subtract zodiacal light according to both the Kelsall [47] and Wright [102] models, and correct for galactic cirrus in order to measure the infrared EBL brightness. The resulting measurements were 12.46, 22.33, 20.14, and 13.68 nW/m^2/sr at 65, 90, 140, and 160 μm, respectively. These measurements are consistent with COBE results but above upper limits established by *Spitzer*. The authors interpret this brightness to be due to star forming ultra-luminous infrared galaxies (ULIRGs) at redshifts up to $z \sim 2$.

Hubble Space Telescope. The Hubble Space Telescope includes an imaging and spectroscopy instrument, the Near Infrared Camera and Multi-Object Spectrometer (NICMOS). NICMOS provides imaging capabilities with various filters as well as slitless grism spectroscopy, in the wavelength range 0.8-2.5 μm. Two deep near-infrared NICMOS images of completely uncorrelated regions of the universe, a $50'' \times 50''$ patch of the Hubble Deep Field-North (HDFN) at 1.1 and 1.6 μm, and $144'' \times 144''$ patch of the Hubble Ultra Deep Field (HUDF, called the NICMOS Ultra Deep Field (NUDF) and located in the Chandra Deep Field South) at the same wavelengths, do not demonstrate excess absolute EBL measurements above the expected background. While this measurement records flux between $327 - 461.9$ nW/m^2/sr, after accounting for foregrounds, the analysis determines zero excess flux within the margin of error [97]. This is in conflict with other contemporaneous measurements [42, 45, 70]. The authors attribute the observed emission to faint galaxies at lower redshifts ($z < 7$). Notably, the analysis uses an aggressive ZL model

which subtracts an order of magnitude more ZL from images prior to determining absolute intensity measurements, which they identify as the likely reason for their different measurement and astrophysical interpretation.

1.2.4 Other constraints on the EBL Background

Claimed measurements of the IR EBL must be put in context with other means to constrain EBL estimates. Other emission sources in the universe interact with or contribute to the EBL, so measurements of these sources can be used to constrain direct EBL measurements by placing upper or lower limits on EBL detection claims based on assumptions of the interaction (or contribution) processes. Emission from bright photon sources such as blazars may be attenuated by the EBL, placing upper limits on EBL claims; summed emission from all directly detected galaxies places a lower limit on EBL measurements; the optical depth to electron scattering places limits on the UV-optical background and thus upper limits on the emission from galaxies prior to the completion of reionization ($z > 6$).

1.2.4.1 Gamma-Ray Background

Indirect evidence for the brightness of the infrared EBL background comes from observations of gamma-ray emission from objects known as blazars. Blazars are galaxies with central supermassive black holes emitting gamma rays with extremely high energies in strong jets pointed in the direction of the earth. These emitted gamma rays have energies of trillions of electron volts [TeV], and comparison of the measured blazar spectrum to the predicted spectrum at IR wavelengths can provide a constraint on the EBL in that wavelength band. High energy photons from blazars, γ, collide with EBL background photons, γ_b, to produce an electron-positron pair:

$$\gamma + \gamma_b = e^- + e^+. \tag{1.48}$$

The efficacy of these collisions depends on the interaction cross section of the gamma-ray photons, which peaks sharply at $\sim 1.5 \times 10^{-25}$ cm^{-2} [30]. For a beam of such high energy electrons, the attenuation by the infrared EBL can be strong; the peak interaction cross section occurs when the product of the energies E of the two photons is $E_\gamma E_b \approx 4(m_e c^2)^2 \approx 1$ MeV, corresponding to a gamma-ray photon with energies on the order of $E_\gamma \approx 1.24$ TeV and an EBL photon wavelength of $\lambda_b \approx 1.24$ μm, firmly in the infrared portion of the electromagnetic spectrum.

Constraints on the level of EBL photons providing attenuation are determined by simulation of the blazar spectrum and by the shape of the assumed EBL spectrum.

The general, simple assumption is that the observed gamma-ray flux J_{obs} at energy E_γ is related to the intrinsic source flux from the blazar J_0 exponentially as

$$J_{obs}(E_\gamma) = J_0(E_\gamma)e^{-\tau_{\gamma\gamma}(E_\gamma)}, \qquad (1.49)$$

where $\tau_{\gamma\gamma}$ is the optical depth for the photon-photon interaction, assumed to be proportional to the number density of background photons as $\tau_{\gamma\gamma} \propto n_{\gamma_b}$. Therefore, nearby high-energy sources serve as probes of the intensity of the local infrared EBL. Ground-based Cherenkov telescopes made TeV measurements of blazar energies possible. Cherenkov telescopes are arrays of ground based telescopes that measure cascades of subatomic particles that are the product of the interaction of gamma-rays with the earth's atmosphere. The first Cherenkov arrays in the 1990s detected the blazar Markarian (Mrk) 421. This blazar is estimated to have a low redshift ($z \sim 0.031$) [86] so that it can be used to measure the EBL at late times, in the local universe, without need for corrections due to the expansion of space or evolution of the EBL. These Cherenkov measurements are then combined with direct blazar measurements at other wavelengths to generate an intrinsic blazar spectrum, from which the EBL attenuation and corresponding constraint on EBL level can be calculated. Early applications used the single blazar Mrk 421, measured by the EGRET instrument of the Compton Gamma Ray Observatory satellite, combined with radio data to generate the expected unattenuated blazar spectrum,

This technique has been repeated for a larger number of nearby blazars, identified by the Fermi Gamma Ray telescope, with complimentary spectral data provided by X-ray satellites such as the Chandra X-ray Observatory and XMM-Newton, and combined with optical or radio data when available; recent studies converge on upper limits for EBL intensity of $\lambda F\lambda \sim 12$ nW/m^2/sr [19]. More recent measurements using the High Energy Stereoscopic System (H.E.S.S.) array of Cherenkov telescopes converged on upper limit of $\lambda F\lambda \sim 15 \pm 2$(statistical) ± 3(systematic) nW/m^2/sr [34]. These values are consistent with direct EBL measurements as well as most EBL background levels calculated from fluctuations measurements.

1.2.4.2 Integrated Light from Extragalactic Source Counts

The EBL contains light from all extragalactic sources. This includes light from resolved galaxies. However, light from unresolved galaxies from earlier periods in the history of the universe are of particular interest due to their potential to constrain the physics of star and galaxy formation as well as the transition in the

universe to the growth of non-linear structure. Claims of detection of high redshift ($z > 6$) EBL emission must include total EBL emission that exceeds the level of emission from known galaxies. As explained in section 1, models of the emission history predicted from luminosity functions for galaxies up to redshifts of $z \sim 5$ and consistent with extensive galaxy surveys produce absolute EBL intensities of < 10 nW/m^2/sr for modeled wavelengths between 1.25 and 4.5 μm [33]. This provides an important constraint on astrophysical interpretations of EBL observations; most recent (post-2005) measurements of the EBL intensity and anisotropies exceed these levels.

1.2.5 Optical Depth to Electron Scattering

Measurements of the optical depth to electron scattering from WMAP data also provide constraints on the timing of reionization, as this value accounts for the number of ionizing photons available in the universe as a function of redshift. This value does not directly constrain the EBL level, but can be invoked in models that attempt to reproduce integrated emission from the early universe [17] and used to constrain the total emission from early stellar populations. In this way the astrophysical interpretation of measured EBL can be constrained to require consistency with this optical depth value.

Temperature anisotropies of the CMB can be measured to determine the fraction of CMB photons rescattered during reionization out of the line of sight and re-placed with photons with statistically random temperature fluctuation, effectively suppressing temperature (and polarization) anisotropy of the CMB as $e^{-\tau}$ where τ is the fraction of scattered CMB photons. The WMAP 7-year data put this value at $\tau = 0.088 \pm 0.014$ [50].

1.2.6 Next Steps in EBL Measurement

A handful of surveys of the IR EBL have been completed to date, all from space). Figure 1.9 gathers data from several absolute intensity measurements of the EBL discussed in the preceding sections and plots them relative to one another. All data is shown as the intensity, λI_λ, as a function of wavelength λ in microns [μm]. For comparison, the intensity from known, resolved galaxies out to $z < 5$ is shown as black lines with upward pointing arrows, with the collected intensity of these objects modeled as the thick orange line. Measurements exceed the intensity from local galaxies, which suggests that additional, unresolved objects are contributing to EBL as we hypothesize. However, these measurements do not have particularly

good agreement with each other and trace the brightest local contribution to EBL, foregrounds.
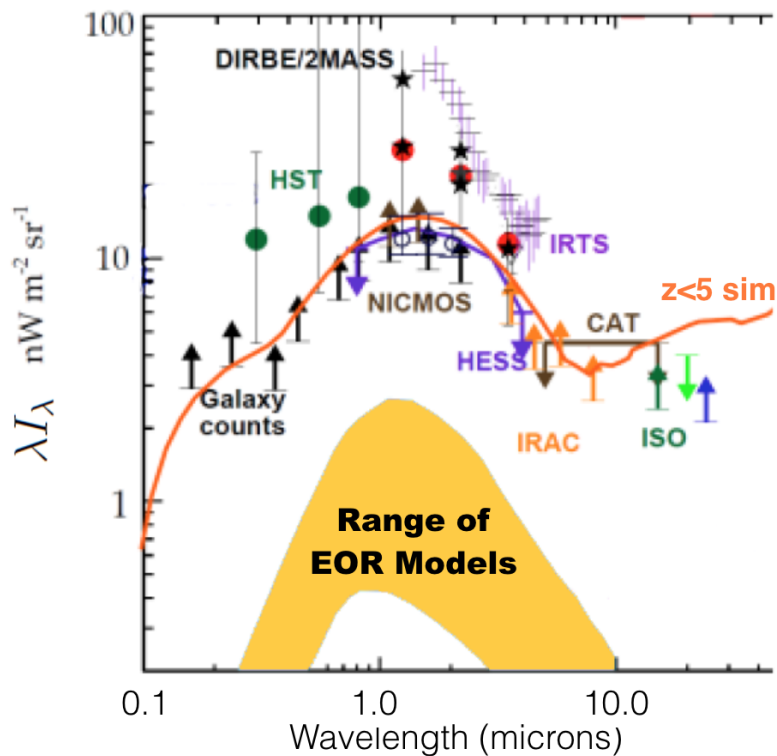
Figure 1.9: Selected EBL measurements shown as intensity, λI_λ, as a function of wavelength λ in microns [μm]. Known, resolved galaxies out to $z < 5$ are shown as black lines with upward pointing arrows, with the collected intensity from $z < 5$ galaxies analytically represented as a solid orange line. Measurements exceed the intensity from local galaxies, which suggests that additional, unresolved objects are contributing to EBL. These measurements are summarized in this work (DIRBE, HST, NICMOS, IRTS, IRAC, ISO), along with EBL constraint data (HESS, CAT). Based on Dole et al 2006.

Direct observation of the mean intensity of the near-infrared EBL with absolute photometry has proven challenging due to bright foregrounds, especially zodiacal light reflected off dust particles in our solar system[30]. Searching for this feature in an absolute measurement is extremely challenging, both astrophysically and technically. Spatial fluctuation measurements are able to discriminate EBL signals from foregrounds by taking advantage of the differing spatial structure of the reionization signal and the foregrounds [30, 42, 15, 17].

1.3 EBL Anisotropies and Intensity Mapping

The earliest galaxies are extremely distant and form a faint and diffuse population. Methods for studying the truly diffuse cosmic microwave background radiation have been very successful in constraining cosmological parameters, and are mature enough to be applied to other diffuse backgrounds with underlying spatial structure. Building on this success, diffuse populations of early galaxies can be studied in much the same manner as the CMB, through analysis of the spatial fluctuations present in the emission. Instead of measuring the absolute intensity of the extragalactic background light, the sky is measured through an intensity map that focuses on the pattern of deviations from an average value over a large range of sky. This method of studying the anisotropy instead of absolute intensity has a large advantage for foreground discrimination.

Anisotropies in the background radiation are characterized by the power spectrum C_ℓ, which is the Fourier transform of the two-dimensional angular correlation function. Anisotropy measurements do not directly measure the absolute level of the EBL, but allow for estimation of the EBL level using well defined models. As a general reference, the power in anisotropies $\delta(\nu I_\nu)$ is a factor of 10 less than the EBL brightness νI_ν [39, 17].

The EBL power spectrum has a unique spatial signature influenced by galactic foregrounds and clustering characteristics of the underlying source population, which contains galactic and stellar contributions from stars and galaxies near enough for direct detection as well as those to faint or too far for direct detection with current technologies, including early galaxies from $z > 6$. The distribution of sources across the field of view determines the power spectrum observed in each field.

Measurements have been made from existing astronomical telescopes, although these instruments were not designed for observations with a large field of view needed for power spectrum analysis. A specialized infrared telescope with a degree scale field of view, the Cosmic Infrared Background ExpeRiment (CIBER-1), flew aboard a sounding rocket and contributed unexpected results that challenge conventional understanding of EBL components. A specialized EBL instrument that leverages success of CIBER-1 is well poised to make substantial contributions to further knowledge of the EBL and its foregrounds. CIBER-2 is such an instrument, and is described in detail in the following chapters.

This section describes the mathematics of EBL power spectra analysis, as well as the underlying physics that go into interpretation of the resulting power spectra. A few

key EBL anisotropy measurements are summarized, with special attention paid to exciting results from CIBER-1, and highlighting lessons learned that would improve future EBL anisotropy experiments.

1.3.1 Mathematics of Intensity Mapping: Power Spectra

Inflation contained an initial power spectrum of density fluctuations, $P_i(k)$, which changes over time as the universe evolves. This initial set of density perturbations gives rise to the distribution of matter at intermediate and late times, which are observable quantities. Linear perturbation theory can be used to understand how this initial density power spectrum is processed over time. The use of linear perturbation analysis naturally gives rise to power spectrum-based observations, productively exploited in CMB observations and more recently applied to observations of radiative backgrounds of early galaxies. The processing of the initial density fluctuations over time is described by a transfer function, T_k.

Theory predicts the statistical properties of cosmological fields, where the quantity of interest here is the matter overdensity $\delta\rho$. Such theory can be constrained by requiring it to reproduce properties of the observable universe, particularly isotropy and homogeneity.

The statistical properties of such fields correspond to mathematical constraints with physical implications. Following the derivation laid out in Dodelson [18], assume a random field $f(\mathbf{x})$ with an ensemble expectation value of zero mean $\langle f(\mathbf{x}) \rangle = 0$, where $\mathbf{x}$ is a comoving spatial position. Requiring a combination of both statistical homogeneity (invariance under translation) and statistical isotropy (invariance under rotation) results in a two-point (real space) correlation function dependent only on the distance between two points:

$$\xi(\mathbf{x}, \mathbf{y}) = \xi(|\mathbf{x} - \mathbf{y}|) \tag{1.50}$$

In Fourier space, with symmetric Fourier conventions, the Fourier transform of the field $f(\mathbf{x})$ becomes

$$f(\mathbf{k}) = \int \frac{d^3\mathbf{x}}{(2\pi)^{2/3}} f(\mathbf{x})e^{-i\mathbf{k}\cdot\mathbf{x}} \text{ and } f(\mathbf{x}) = \int \frac{d^3\mathbf{k}}{(2\pi)^{2/3}} f(\mathbf{k})e^{-i\mathbf{k}\cdot\mathbf{x}}, \tag{1.51}$$

with $f(\mathbf{k}) = f^*(-\mathbf{k})$ for real fields.

Under translations $(\mathbf{x} - \mathbf{a})$, the Fourier transform acquires a phase factor $e^{-i\mathbf{k}\cdot\mathbf{a}}$, so the two-point correlation function becomes

$$\langle f(\mathbf{k})f^*(\mathbf{k}') \rangle = \langle f(\mathbf{k})f^*(\mathbf{k}') \rangle e^{-i\mathbf{k}-\mathbf{k}'\cdot\mathbf{a}} = F(\mathbf{k})\delta(\mathbf{k} - \mathbf{k}') \tag{1.52}$$

where $F(\mathbf{k})$ is a real function. This delta function implies that different Fourier modes are uncorrelated, which has important implications for Gaussian fields. Similarly, invariance of the two-point correlation function under rotations requires $F(\mathbf{k}) = F(k)$ where $k \equiv |\mathbf{k}|$. This allows definition of the power spectrum, $\mathcal{P}_f(k)$, of a homogenous and isotropic field, $f(\mathbf{x})$, by

$$\langle f(\mathbf{k}) f^*(\mathbf{k}') \rangle = \frac{2\pi^2}{k^3} \mathcal{P}_f(k) \delta(\mathbf{k} - \mathbf{k}'). \tag{1.53}$$

Note that the normalization factor $\frac{2\pi^2}{k^3}$ follows convention, and makes $\mathcal{P}_f(k)$ dimensionless as long as $f(\mathbf{x})$ is dimensionless.

The correlation function is the Fourier transform of the power spectrum:

$$\langle f(\mathbf{x}) f(\mathbf{y}) \rangle = \int \frac{d^3\mathbf{k}}{(2\pi)^{2/3}} \frac{d^3\mathbf{k}'}{(2\pi)^{2/3}} \langle f(\mathbf{k}) f^*(\mathbf{k}') \rangle e^{-i\mathbf{k}\cdot\mathbf{x}} e^{-i\mathbf{k}'\cdot\mathbf{y}}$$

$$= \frac{1}{4\pi} \int \frac{dk}{k} \mathcal{P}_f(k) \int d\Omega_k e^{-i\mathbf{k}\cdot(\mathbf{x}-\mathbf{y})}$$

This can then be reduced to a two-dimensional projection on the two-sphere, by taking $\mathbf{x} - \mathbf{y}$ along the z-axis in Fourier space to evaluate the angular integral. Let $\mathbf{k} \cdot (\mathbf{x} - \mathbf{y}) = k|\mathbf{x} - \mathbf{y}|\mu$, so that

$$2\pi \int_{-1}^{1} d\mu \, e^{-i\mathbf{k}|\mathbf{x}-\mathbf{y}|\mu} = 4\pi j_0(k|\mathbf{x} - \mathbf{y}|) \tag{1.54}$$

where $j_0(x) = sin(x)/x$ is a spherical Bessel function of order zero. The simplified correlation function then becomes

$$\xi(\mathbf{x},\mathbf{y}) = \int \frac{dk}{k} \mathcal{P}_f(k) j_0(k|\mathbf{x} - \mathbf{y}|). \tag{1.55}$$

Note that this only depends on $\mathbf{x} - \mathbf{y}$ as required to meet statistical homogeneity and isotropy requirements.

Importantly, the variance of the filed is defined as $\xi(0) = \int d \ln k \mathcal{P}_f(k)$. A power spectrum is said to be scale-invariant if it has a constant $\mathcal{P}_f(k)$. This means its variance receives equal contributions from every decade in k, which becomes important when perturbation theory is applied to the field.

By further requiring a field to be Gaussian in addition to homogenous and isotropic, the probability density function for the field $\mathbf{f}$ is fully specified by the correlation function, with an associated Gaussian Fourier transform of the field, $f(\mathbf{k})$. This

means that the uncorrelated Fourier modes are statistically independent for Gaussian fields, a key feature which is preserved through linear evolution. For Gaussian fluctuations predicted for inflation and early matter distributions, the uncorrelated Fourier modes will remain uncorrelated and statistically independent, a key feature to look for in observations. At later times, non-linear structure formation will destroy Gaussianity on certain scales, consistent with the cosmic web observed today [83]. Note that many active experiments are currently searching for primordial non-Gaussianity [2, 13], though no observations have yet been made.

Additional insight into the power spectrum comes from introducing spherical harmonics at a fixed radius. Spherical harmonics ($Y_{\ell m}$) form a basis for square-integrable functions on the surface of a two-sphere and are solutions to the angular part of Laplace's equation in spherical coordinates

$$f(\hat{\mathbf{n}}) = \sum_{\ell > 0}^{\infty} \sum_{m=-\ell}^{\ell} f_{\ell m} Y_{\ell m}(\hat{\mathbf{n}}) \tag{1.56}$$

where ℓ is an integer ≥ 0 and m and integer with $|m| \leq \ell$. The spherical harmonics are orthonormal over the sphere,

$$\int d\hat{\mathbf{n}} \, Y_{\ell m}(\hat{\mathbf{n}}) \, Y_{\ell m}^*(\hat{\mathbf{n}}) = \delta_{\ell \ell'} \delta_{mm'}. \tag{1.57}$$

The spherical mulitpole coefficients of $f(\hat{\mathbf{n}})$ are

$$f_{\ell m} = \int d\hat{\mathbf{n}} \, Y_{\ell m}^*(\hat{\mathbf{n}}). \tag{1.58}$$

Statistical isotropy then requires that the two-point correlators of $f_{\ell m}$ are

$$\langle f_{\ell m} f_{\ell' m'}^* \rangle = C_\ell \delta_{\ell \ell'} \delta_{mm'}, \tag{1.59}$$

where C_ℓ is the angluar power spectrum of f. The full two-point correlation function then becomes

$$\begin{aligned} \langle f(\hat{\mathbf{n}}) f(\hat{\mathbf{n}}) \rangle &= \sum_{\ell m} \sum_{\ell' m'} \langle f_{\ell m} f_{\ell' m'}^* \rangle Y_{\ell m}(\hat{\mathbf{n}}) Y_{\ell m}^*(\hat{\mathbf{n}}') \\ &= \sum_\ell C_\ell \sum_m Y_{\ell m}(\hat{\mathbf{n}}) Y_{\ell m}^*(\hat{\mathbf{n}}') \\ &= \sum_\ell C_\ell \frac{2\ell + 1}{4\pi} P_\ell(\hat{\mathbf{n}} \cdot \hat{\mathbf{n}}') \\ &= C(\theta). \end{aligned}$$

Here, $\hat{\mathbf{n}} \cdot \hat{\mathbf{n}}' = \cos\theta$ and the sum of products of the $Y_{\ell m}$ is expressed in terms of Legendre polynomials $P_\ell(x)$. Thus the two-point correlation function depends on the angle between two points, consistent with the requirement for statistical isotropy.

The variance of the field is

$$C(0) = \sum_\ell \frac{2\ell + 1}{4\pi} C_\ell \approx \int d\ln\ell \, \frac{\ell(\ell + 1)C_\ell}{2\pi} \tag{1.60}$$

The *angular power spectrum* is generated by restating in terms of the expansion coefficients $f_{\ell m}$, which are the analogues of Fourier coefficients:

$$C(\ell) = \frac{1}{2\ell + 1} \sum_{m=-\ell}^{\ell} |f_{\ell m}|^2. \tag{1.61}$$

Recall this relies on the Gaussianity of the scalar field f for the field to be completely described by the variance of the amplitudes of the multipole components as a function of the ℓ value.

Generally, the angular power spectrum is plotted to emphasize the contribution to the variance per log range in ℓ:

$$f(\ell) = \frac{\ell(\ell + 1)C_\ell}{2\pi}. \tag{1.62}$$

Also, the power spectrum can be obtained from the inversion of the correlation function by orthogonality of Legendre polynomials as

$$C_\ell = 2\pi \int_{-1}^{1} d\cos\theta \, C(\theta) \, P_\ell(\cos\theta). \tag{1.63}$$

The angular power spectrum has wide application to cosmological anisotropy observations, with slightly different formalisms depending on the specific area of study (CMB, EBL, 21-cm emission). This analysis comprises a burgeoning field, *intensity mapping,* with wide applications to the study of large and small scale evolution of the universe. Selection of a specific density field in place of the general field f allows for application of the power spectrum formalism to various cosmological fields.

Photon production traces the underlying density distribution of baryonic matter, with some bias. For observational purposes, the fluctuations of photons (measured as surface brightness λI_λ) can be studied in place of the density fluctuations:

$$\Delta\rho \longrightarrow \Delta(\lambda I_\lambda) \tag{1.64}$$

The same principal applies when utilizing CMB machinery for EBL fluctuations analysis: $\Delta T \longrightarrow \Delta(\lambda I_\lambda)$. This similarity allows application of the mature CMB analysis machinery to EBL fluctutions, with the appropriate substituion of intensity for temperature

$$\Delta T \longrightarrow \Delta(\lambda I_\lambda) \tag{1.65}$$

The variance of the density contrast can be described as a scalar field, which can be in turn decomposed into a linear expansion of real spherical harmonic coefficients $Y_{\ell m}$ as Equation 1.56:

$$f(\theta, \phi) = \sum_{\ell > 0}^{\infty} \sum_{m=-\ell}^{\ell} a_{\ell m} Y_{\ell m}^*(\theta, \phi). \tag{1.66}$$

Note that the CMB power spectrum formalism uses slightly different conventions in the literature, with the field described as a linear expansion of spherical harmonics with coefficients $a_{\ell m}$ in place of $f_{\ell m}$.

With this convention, the angular power spectrum is expressed as:

$$C(\ell) = \frac{1}{2\ell + 1} \sum_{m=-\ell}^{\ell} |a_{\ell m}|^2. \tag{1.67}$$

This power spectrum is still plotted with the normalization convention, $f(\ell) = \frac{\ell(\ell+1)C_\ell}{2\pi}$.

This formalism allows for calculation of Fourier-space maps of sky images. However, artifacts are introduced by the conversion process that must be accounted for in the final science map [106]. The true power spectrum is related to the power spectrum generated from the sky image by a number of conversion factors. First, shot noise present in the power spectrum due to the discrete sampling of the density field must be subtracted from the calculated power spectrum. Any other known, quantifiable sources of noise present (such as instrument noise) must also be subtracted. Additionally, removal of bad or undesired pixels from the original image (known as masking) acts as a window function that mixes modes in the calculated spectrum. This window function needs to be deconvolved from the noise-subtracted spectrum. Finally, the finite volume observed by the telescope beam introduces additional functional dependence that acts as a multiplicative factor and needs to be divided out of the calculated spectrum. These noise and window functions are usually handled explicitly in the Fourier analysis pipeline utilized.

The mathematical formalism summarized here is used in both the generation of models to predict spatial fluctuations from primordial matter distributions and again

in the analysis of observed sky images. Both of these applications are discussed in more detail in the following sections.

1.3.2   Physics of EBL Observables in the Near-Infrared

Early galaxies. The EBL contains contributions from many astrophysical qualities, as illustrated schematically in Figure 1.8. Contributions to the EBL from early, $z > 6$ galaxies are of particular interest, since these galaxies are not well characterized observationally and the value of their intensity in presently unknown. However, they are expected to have a spectral signature distinct from late-type luminous objects as they are likely to be metal poor, demonstrate different thermonuclear processes than late-type stars, and form more massive galaxies with a different evolutionary profile than observed in more recent galaxies. Separating the emission of these early sources from other later astrophysical contributions, such as faint late-type galaxies ($z < 6$) or extragalactic stars outside of traditional galaxy boundaries, both with higher metallicity, requires prediction of hypothetical spectra which can be compared to observations. Fortunately, both the *intensity* and the *spatial distribution* of the emission expected at $z > 6$ contribute to the infrared EBL anisotropies. Each of these can be modeled and compared to observations to constrain the underlying physics of these objects.

Intensity of the total emission from redshifts $z > 6$ is estimated as a combination of early stellar and nebular emission. For completeness, following Fernandez and Komatsu 2006 [25], the intensity can be modeled as the sum of total emission from stars of appropriate metallicity in addition to contributions from Lyman-alpha (Lyα) emission and continuum emission processes. Stellar emission receives contributions from two types of metal-poor stars believed to present in the early universe, as described in Section 1.2: Population III stars that are entirely free of metals (metallicity $Z = 0$), and Population II stars with low metallicity ($Z = 1/50 \, Z_\odot$). Each of these stellar populations have a different stellar parameters, such as initial mass function (IMF), intrinsic bolometric luminosity, effective temperature, main sequence lifetime, and hydrogen photoionization rate. These parameters allow calculation of the total stellar luminosity, assuming a Planck blackbody spectrum with suppression of stellar emission below energies of 13.6 eV (which would be absorbed by the pervasive neutral hydrogen surrounding early stars). This total

luminosity is combined with emission from other nebular sources to generate the luminosity mass density for each population, which is then used to calculate the near-IR background spectral energy distribution and anisotropy power spectrum.

The luminosity mass density is a means of parameterizing the total luminosity as a function of stellar mass at each frequency ν, while taking into account additional contributions to the luminosity beyond stellar emission. Detailed models also include nebular or continuum emission. Lyα emission [92] comes from the decay of the first excited state to the ground state of atomic hydrogen (HI), and is the most luminous spectral emission feature in astrophysical nebulae [80]. Free-free emission (Bremsstrahlung) is caused by a collision between a free electron and an ion and depends largely on the temperature of the surrounding plasma. Free-bound emission occurs during radiative recombination, when a free electron is captured by an ion while emitting a photon and the emitted photon has the energy of the atomic transition. Finally, two photon emission occurs when low-density hydrogen or helium atoms collide with a single free electron, exciting the bound atomic electron to a higher state, which then emits two photons as the atomic electron de-excites. Energy from these processes is combined with energy from stellar emission to determine the luminosity mass density profile for the early background.

As the early universe is not well observed, it is possible that other luminous sources existed in the early universe and contributed to $z > 6$ luminosity. Such objects include direct collapse black holes [105, 9], extremely large black holes formed within early galaxies through suppression of early star formation. Due to their theoretical nature, such objects are not routinely included in predictions of early universe intensity.

Following the formalism developed in Fernandez and Komatsu 2006 [25], the mean luminosity mass density for each each emission source is calculated by integrating over the IMF for each stellar population (II and III). Considering each population separately facilitates accounting of the relative fraction of each stellar population at different redshifts, reflecting the assumption that stars increase in metallicity over time. Additionally, the stellar mass density of each population as a function of redshift is used to to determine the comoving star formation rate density. These densities reflect assumptions about the underlying dark matter distribution and can be varied. Cooray et al 2012 [17] incorporate a two-halo model to more accurately represent the evolution of the linear matter spectrum of the early universe. Finally, the mean luminosity mass density for both stellar populations is combined with the

mean luminosity mass density for the nebular emission to obtain the total luminosity mass density from the stellar nebulae.

Independent measurements of cosmological parameters provide a means of constraining the upper limits of the total stellar nebulae emission used in theoretical EBL models. Cooray et al 2012 [17] estimate the optical depth to electron scattering, τ, for their predicted nebular emission values and compare it to the WMAP 7-year optical depth provided by Komatsu et al 2011 [50], $\tau = 0.088 \pm 0.014$. Consistency with the WMAP measurements signifies that stellar population parameters used in the EBL models are physically plausible.

As per Cooray et al 2012 [17], the *mean infrared EBL intensity* $\nu_{obs}\overline{I}_{\nu_{obs}}$ can be estimated from an integral of the comoving emission of stellar populations II, III, and stellar nebulae over the redshift range of early luminous sources, taken to be $6 < z < 30$:

$$\nu_{obs}\overline{I}_{\nu_{obs}} = \int_{z_{min}}^{z_{max}} dz \frac{c}{H(z)} \frac{\nu_z \overline{j}_\nu(z)}{(1+z)^2}. \tag{1.68}$$

Here, $\overline{j}_\nu(z)$ is a summation of the comoving specific emission coefficients for all emission sources based on the luminosity mass density at frequency ν, c is the speed of light, $H(z)$ is the Hubble parameter as a function of redshift z, and $\nu(z)$ describes the relation of observed and emitted frequencies. Note that peak emission from this population (ultraviolet) is redshifted into the infrared at current observational times as accounted for with the redshift term $\nu(z) = (1+z)\nu_{obs}$. Plots of this emission peak below 1 nw/m^2/sr, with a suppression feature $\sim 1\mu$m reflecting absorption of emission by neutral hydrogen. Higher values are found in the literature when the constraint for agreement with WMAP optical depth is loosened. This type of mean intensity calculation is the source of the swath of estimated intensity for early galaxies on plots of EBL measurements.

The luminosity mass density combines with assumptions about the underlying dark matter halo distribution to generate the *angular cross power spectrum* of the infrared emission at observed frequencies ν and ν' for a multipole ℓ:

$$C_\ell^{\nu\nu'} = \int_{z_{min}}^{z_{max}} dz \left(\frac{d\chi}{dz}\right) \left(\frac{a}{\chi}\right)^2 \overline{j}_\nu(z)\overline{j}_{\nu'}(z) P_{gg}(k, z). \tag{1.69}$$

Here, χ is the comoving angular diameter distance, $a = (1+z)^{-1}$ is the scale factor for the expansion of the universe, $\overline{j}_\nu(z)$ is the mean emission per comoving volume at frequency ν and redshift z. $P_{gg}(k, z)$ is the galaxy power spectrum at

the wavenumber $k = \frac{\ell}{\chi}$ and redshift z, and is based on the dark matter halo distribution. The distribution of galaxies is related to the structure of the underlying dark matter; the dark matter distribution evolved from initial density fluctuations in the early universe and serves as gravitational wells for baryons. As described in Section 1.1, the clustering statistics of dark matter and galaxies can be described by a halo model [82, 76], where the halo profile is fitted by a two-parameter functional form dependent on an inner radius and density related to a virial parameter. This methodology has been successfully reproduced for multiple cosmological scenarios and can be reliably expected to produce repeatable associated baryonic matter distributions through accretion.

Importantly, galaxy clustering measurements are affected by the Poisson fluctuations associated with the shot-noise caused by the finite number of galaxies sampled by the clustering measurement. This shot-noise power spectrum has a distinct shape, independent of multipole ℓ:

$$C_\ell^{\text{shot}} = \int_0^{S_{cut}} dS \, S^2 \frac{dN}{dS}, \tag{1.70}$$

where S is a source flux lower than an upper cut S_{cut} and N is the number of sources. The amplitude of this power spectrum depends on the luminosity mass density for dark matter halos associated with the stellar populations II and III; it traces the luminosity of the sources associated with a dark matter halo making use of the assumption that stellar luminosity is proportional to the halo mass. Note this integral results in a contribution which is proportional to multipole moment ℓ in Fourier space ($C_{ell} \propto \ell$), and at high multipole values (and low angular separation on the sky) this becomes the dominant feature of the power spectrum. At lower multipole values ℓ (larger angular separation), the galaxy clustering term generates a dominant contribution with a flatter shape. This becomes important in signal discrimination, as the power spectrum is affected differently by changes to the number density of galaxies as compared to the spatial distribution of of galaxies, providing insight into the underlying physics.

Reionization Feature. While studying spatial distribution of early galaxies in the EBL, intentional selection of observational wavelength bands allow for collection of additional information about the timing of the reionization of the universe. While the EBL is generally featureless overall, contributions to EBL emission from early ($z > 6$) galaxies show a sharp suppression feature that can be characterized in EBL measurements.

Due to the pervasive neutral hydrogen surrounding the first stars formed prior to the reionization of the universe, all stellar and nebular emission with energies above the ionization energy of neutral hydrogen is absent in observations of the EBL. The single electron in a neutral hydrogen atom is ionized at energies of $E \geq 13.6$ eV, which corresponds to a rest wavelength of $\lambda \leq 0.1216\mu$m. In the frame of an early galaxy, all emission at wavelengths shorter than 0.1216μm is truncated. This spectral feature, know as the *Lyman-break*, is redshifted to the near infrared in the observational frame as $\lambda_{obs} = (1 + z)\lambda_{emitted}$. Once the surrounding neutral hydrogen is permanently ionized due to the overall reionization of the universe, emitted photons of all wavelengths travel freely and the galactic spectrum is no longer suppressed.

Although observational data provide the redshift at which reionization of the universe is complete ($z \sim 7$) [36], the precise timing of this process is unknown. Observations of the wavelength of this spectral suppression feature in EBL measurements thus provide new constraints on the timing of reionization. Table 1.1 shows the redshifted observational wavelengths of this spectral suppression feature for different redshifts of the completion of the reionization process.

Table 1.1: Early galactic emission prior to the reionization of the universe is suppressed due to absorption by neutral hydrogen. In the rest frame, this suppression occurs at 0.1216μm, which is redshifted to the far optical or near infrared wavelength bands, depending on the precise timing of reionization.

Redshift, z	λ_{obs} [μm]
10	1.338
9	1.216
8	1.094
7	0.973
6	0.851

This spectral suppression feature motivates EBL observations in the near-infrared over other wavelength bands. Multiple observations spanning the predicted range of suppression wavelengths allows for comparative measurements on both sides of the suppression feature. This both increases confidence in identification of the wavelength of the spectral suppression feature and additionally provides another means of EBL component separation. The amplitude of the intensity of EBL measurements at higher wavelengths can be compared to the amplitude of lower

wavelength EBL measurements below the identified suppression feature to isolate the EBL contribution from early galaxy emission. In this way the spectral suppression feature supports early galaxy observations while simultaneously illuminating an important epoch in cosmic history. Finally, including the process of reionization in EBL modeling introduces additional constraints that increase the fidelity of physical models.

Generation of Theoretical Near-Infrared EBL Power Spectrum. The intensity and spatial distribution of emission from the early universe prior to reionization at a redshift $z > 6$ can be simulated by combining models of the underlying cosmological matter distribution with astrophysical models of stellar luminosity and nebular emission. Requiring consistency with cosmological measurements of the universe, such as redshift for complete reionization of the universe ($z \sim 7$) and optical depth to electron scattering, results in predictions for the maximum intensity of early near-infrared EBL contributions νI_ν of order ~ 1 nW/m^2/sr. Corresponding power spectrum fluctuations amplitudes (C_ℓ) are of order one tenth of intensity values, with amplitudes below ~ 0.1 nW/m^2/sr. These low signal levels demand observations with very well characterized foregrounds to facilitate accurate early galaxy component separation, optimized for fluctuations measurements focused at the expected angular separation of galaxy clusters (multipoles of a few thousands, $1000 < \ell < 5000$, corresponding to a degree-scale field of view).

1.3.3   EBL Components and Foregrounds

The EBL is comprised of all photons emitted throughout cosmic history in a particular wavelength range. In addition to emission associated with structure formation in the early universe ($z > 6$), the near-infrared EBL contains contributions from all galaxies up to the current time ($z < 6$). Measurements of this emission also contain photons from luminous processes within the Milky Way galaxy, including stars, dust emission, and local emission from the solar system. Finally, these measurements contain signal from the measuring instrument itself, and may be affected by the local environment of the instrument. The EBL signal can be isolated (within some confidence interval) by careful spectral decomposition, where foregrounds are identified and removed from the EBL signal. This tentative EBL signal must be shown to be of statistical significance, and must be proven to be extragalactic and isotropic, to be considered a definitive EBL measurement. This is true for both intensity and fluctuation measurements. Finally, identification of the early galaxy contribution to the EBL signal may occur by comparison of measurements from

multiple wavelength bands on either side of the spectral suppression feature present prior to complete reionization of the universe.

The measured EBL signal received by a detector, $\lambda I_{\lambda_{meas}}$, consists of contributions from the desired EBL signal, $\lambda I_{\lambda_{EBL}}$; foreground galactic contributions, $\lambda I_{\lambda_{FG}}$, and contributions from the instrument and local environment, $\lambda I_{\lambda_{I,E}}$:

$$\lambda I_{\lambda_{meas}} = \lambda I_{\lambda_{EBL}} + \lambda I_{\lambda_{FG}} + \lambda I_{\lambda_{I,E}}. \qquad (1.71)$$

The non-EBL contributions are astrophysical and technical foregrounds, $\lambda I_{\lambda_{FG}}$ and $\lambda I_{\lambda_{inst}}$ respectively. Each of these categories of contribution can be broken up into more detailed contributions.

$$\lambda I_{\lambda_{meas}} = \underbrace{\lambda I_{\lambda_{z>6}} + \lambda I_{\lambda_{IGL}}}_{\text{EBL}} + \underbrace{\lambda I_{\lambda_{DGL}} + \lambda I_{\lambda_{ISL}} + \lambda I_{\lambda_{ZL}}}_{\text{Galactic foregrounds}} + \underbrace{\lambda I_{\lambda_{AG}} + \lambda I_{\lambda_{inst}}}_{\text{Inst \& Env foregrounds}} \qquad (1.72)$$

Integrated Galactic Light. The EBL signal, $\lambda I_{\lambda_{EBL}}$, includes emission from the early universe, $\lambda I_{\lambda_{z>6}}$, and discussed extensively in the previous subsection. It also includes emission from all other extragalactic luminosity sources, including all galaxies up to the present day, extragalactic dust, stars outside of traditional galaxy boundaries, and any other sources. These $z < 6$ sources are grouped together with the label Integrated Galactic Light and indicated as $\lambda I_{\lambda IGL}$.

Galactic light produced after reionization is a dominant EBL component. Galaxy formation peaked during recent redshifts, at $1.5 < z < 2$, producing the largest galaxy emission contribution to EBL. Catalogs of galaxies out to $z \sim 5$, such as SDSS [104] are used to predict the EBL intensity contribution. Recent works predict the fluctuation of this population [33]. The data from current extensive galaxy surveys can be used to model total emission and spatial fluctuation contributions. Helgason et al 2012 reconstructed emission histories of 233 galaxies with near-IR observations up to $z < 5$, then extended the luminosity functions to high redshifts and faint magnitudes. A Λ-CDM galaxy clustering power spectrum was produced including both the known and extrapolated populations, then the contributions from galaxies up to a limiting magnitude (consistent with the magnitudes of the known galaxies) removed. Excess fluctuations above this limiting magnitude then cannot arise from known galaxy populations. The total contributions from the known galaxies calculated in models as in Helgason can be removed from EBL fluctuations measurements as part of the data reduction process.

IHL. EBL fluctuations can also arise from intrahalo light (IHL)[16, 106] generated by diffusely distributed stars expelled from galaxies during structure formation at

$0 < z < 2$. Emission from IHL is expected to have a spectral shape that peaks near 1.5 μm and slowly decreases, in contrast to the sharp cutoff expected in the spectral features of early galaxies. Intrahalo light comes from diffuse component, such as fields of tidally stripped stars beyond the boundaries of galaxies as typically defined. This is expected to have a relatively flat shape in these units, indicating a scale-invariant spectrum.

Galactic Foregrounds. The galactic foreground signal from emission within the Milky Way, $\lambda I_{\lambda_{FG}}$, can be similarly decomposed into components. Diffuse Galactic Light (DGL), $\lambda I_{\lambda_{DGL}}$, is due to scattering of the interstellar radiation field from dust in the galaxy. At high galactic latitudes, DGLt has a spatial power spectrum proportional to a negative power law in these units ($C_l \propto l^{-3}$) following the structure of the interstellar dust emission.

Integrated Star Light (ISL), $\lambda I_{\lambda_{ISL}}$, comes from all the stars within our galaxy. As stars are approximately randomly distributed, they contribute Poisson (shot) noise, which looks like a rising power law in Fourier space.

Additional scattered light in the solar system, known as zodiacal light (ZL) and represented as $\lambda I_{\lambda_{ZL}}$, provides another strong foreground, at levels much greater than other astrophysical sources. Each of these foregrounds is many times the brighter than the desired early galaxy signal; tens or hundreds of times brighter. Although a large signal when measuring the absolute intensity, the fluctuation power of ZL is spatially smooth due to the physical distribution of dust in our solar system and is at most a few percent of its average power.

Instrumental and Environmental Foregrounds. Signal from the instrument is also included as $\lambda I_{\lambda inst}$. Thorough lab calibration and testing allow for characterization of this signal such that it can be removed from the data while only introducing as small errors as possible.

In addition, ground-based observational measurements incur an additional, extremely dominant foreground within the Earth's atmosphere. Airglow, $\lambda I_{\lambda_{AG}}$, from hydroxyl molecules (OH) is several thousand times the desired EBL signal, and has a time varying signature that makes it difficult to correct with such technologies as Adaptive Optics. Whenever possible, instrumental design for EBL observations in the near-infrared requires measurements from above the atmosphere to avoid airglow contamination.

The indistinguishability of photons makes it challenging to identify respective com-
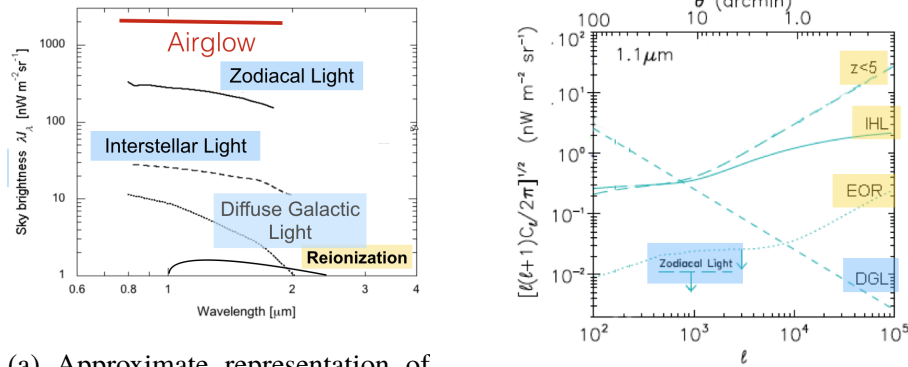
(a) Approximate representation of intensity of EBL components and foregrounds as a function of wavelength.

(b) Approximate representation of spatial fluctuation amplitudes of EBL components and foregrounds at a single wavelength.

Figure 1.10: EBL components and foregrounds represented in absolute intensity and spatial fluctuations. Foregrounds that are much brighter in intensity than EBL signal have distinct spatial power spectra that makes them easier to remove.

ponent contributions to absolute intensity measurements of the EBL. Fortunately, most EBL contributions and foregrounds have unique spectral signatures in Fourier space that aid in component separation. Additionally, many foregrounds which are overwhelming in absolute intensity have small fluctuations amplitudes in Fourier space, minimizing the impact of their removal on the assessment of the final signal.

Measurements of the sky contain EBL emission as well as galactic and instrumental emission. Understanding the components that make up the measured signal allows for prediction of their respective contributions, which can be accounted for in experimental design. It also guides accounting for these contributions in the data analysis process, in order to generate a robust final EBL measurement.

1.3.4 Early Universe Signal Discrimination in NIR EBL

In their seminal review paper post-*COBE*, Hauser and Dwek [30] state clear requirements for definitive EBL signal detection:

> [There are] three necessary conditions for detection of the CIB, i.e., that the signal is significantly positive, that it is of extragalactic origin, and that it is isotropic.

Many steps are required to move from raw sky observations to definitive claims of EBL signal detection. To begin, sky images undergo reduction and processing

to convert an astronomical image into a power spectrum plot describing observed fluctuations. Careful removal of instrumental and galactic foregrounds generates a signal expected to be extragalactic in origin, which can then be compared across multiple fields to prove isotropy and claim detection of a true extragalactic background. Additional analysis allows isolation of the contribution above that expected from known extragalactic sources, using information about individually resolved galaxies out to $z \sim 5$. A series of tests is needed to confirm the robustness of fluctuations in excess above predicted levels, most notably cross correlation of the power spectrum at one wavelength interval with a power spectrum in another wavelength interval of the same field. Positive, extragalactic, and isotropic signals are then compared to astrophysical models to predict the sources responsible for measured excesses, using observations to extend our knowledge of the physical processes producing emission throughout the evolution of the universe.

Observing Paradigm. EBL measurements begin with careful selection of observational fields. Whenever possible, selection of fields with previous observations is desirable. If multiple observations can be made separated in time, it is ideal to take observations of the same fields six months apart to control for the line of sight through the interplanetary dust cloud.

Low-level Data Analysis. Calibrated, flat-field corrected, astrometrically-aligned images are required prior to power spectrum estimation.

First, raw data is converted to sky images by conversion of raw digital units to working units, such as electrons per second, typically through a slope fitting method of the pixel photocurrent. A dark current correction is applied, generally by subtracting the dark current average determined by dark images of the detector. A flat field correction is applied, which corrects for pixel-to-pixel response across the detector. Sky or lab images can be used, depending on the instrument design. Images are aligned using a method of astrometric registration.

The point spread function (PSF) is calibrated against reference astronomical sources, in addition to preliminary laboratory measurements, again depending on the details of instrumentation. PSF calibration is followed by surface brightness calibration, where the measured photocurrent is referenced to the source flux of a known reference source, usually in a specified magnitude bin, which provides a flux conversion factor. Similar to the PSF, this is usually a complementary measurement to laboratory flux calibrations through other means. Taken together, this process results in science-quality images in configuration space. An additional masking step is

needed prior to power spectrum estimation.

Image-space Mask Generation. Before calculating the power spectra, power from detector errors and known astrophysical sources is removed. A detector mask is generated for non-responsive or hot pixels, as well as for transient features such as cosmic rays. An astronomical mask is generated to remove known stars and galaxies up to a pre-determined magnitude, with the goal of reducing Poisson fluctuation contributions to the power spectrum that arise from known galaxy populations. The astronomical mask requires a reference astronomical catalog, such as UKIDSS for stars and SDSS for galaxies, and requires a detailed knowledge of the instrument PSF. Generally, instrument-specific simulations are required to determine a balance between deepest magnitude galaxies that can be masked while maintaining a maximum number of pixels available for power spectrum estimation (generally around fifty per cent).

The introduction of image space masks generates irregularities in the power spectrum, which generally manifest as mixing power between modes in Fourier space, which results in changes in amplitude and a smoothed shape of the generated power spectrum compared to its true shape. To account for this, a deconvolution is required in the generation of power spectrum estimation.

Power Spectrum Estimation. The next step in the process is to convert from image space to Fourier space, as outlined in Section 1.3.1, using Equation 1.67. For an ideal measurement with full sky coverage and no noise, this equation produces an unbiased estimate of the underlying theoretical power spectrum [35], limited only by cosmic variance. However, actual measurements do contain noise and other error and artifacts that must be explicitly accounted for in data analysis. Quadratic estimators are used to convert observed data maps into the sky power spectrum, $\langle C_{\ell'} \rangle$ as mentioned in Section 1.3.1, which is related to the actual power spectrum $\tilde{C}_\ell$ by a mode-coupling matrix. Tailored methods allowing faster calculation of the power spectrum, such as maximum likelihood approaches used extensively in WMAP analysis and direct spherical harmonic transform approaches underlying the MASTER formalism [74] for Boomerang and BICEP CMB analysis, have been shown to produce consistent results with methods that evaluate Equation 1.67 directly.

CIBER experiments use the MASTER formalism developed for CMB analysis [74, 106], so this discussion addresses power spectrum preparation specific to that method. In the MASTER formalism, the true sky power spectrum $\tilde{C}_\ell$ is related to the raw power spectrum from the observed image $\langle C_{\ell'} \rangle$ by a noise bias $N_{\ell'}$, a mode

coupling matrix $M_{\ell\ell'}$, and a beam transfer function $B_{\ell'}$ as

$$\tilde{C}_\ell = \sum_\ell \frac{M_{\ell\ell'}^{-1}(\langle C_{\ell'}\rangle - N_{\ell'})}{B_{\ell'}^2}. \tag{1.73}$$

The noise bias is computed from a detailed model of the noise properties of the instrument, including read noise in the detector and readout, and shot noise from the random variation in photons at the detector. The beam transfer function is calculated from the measured PSF. The mode coupling mask corrects for Fourier mode mixing introduced by the image space masking.

The auto-power spectrum is calculated by using only one map for both the un-primed and primed and contributions, $a_{\ell m}$ and $a_{\ell'm'}$, so that the calculated $\langle C_{\ell'}\rangle$ is proportional to the sum of the square:

$$\langle C_{\ell'}\rangle \propto \sum_m |a_{\ell m}|^2. \tag{1.74}$$

Two independent maps may be compared with a cross-power spectrum, where

$$\langle C_{\ell'}\rangle \propto \sum_m a_{\ell m} a_{\ell'm'}^*. \tag{1.75}$$

Cross-correlation is an extremely useful means to isolate contributions due to noise present in only one of the two contributing maps. This is a powerful means of identifying excess fluctuations that are not biased by noise of a specific type. For example, this is used to remove contributions from interplanetary dust (zodiacal light) by cross-correlation of maps at the same wavelength band but observed at different times, or noise present in one detector or one instrument by cross-correlation of maps from a different detector or experiment. In this way, cross-correlations demonstrate that observations meet the required criteria of positive significance, extragalactic origin, and isotropy required for definitive identification of EBL signal. Importantly, this is also a means to identify the magnitude and timing of early galaxy EBL contributions by cross-correlation between wavelength bands on either side of an identified Lyman-break feature.

Angular power spectrum results are generally reported as plots of the normalized angular power spectrum at each wavelength band, either for individual or aggregated observational fields. Values of the fluctuation power, $\delta(\nu I_\nu)$ or $\delta(\lambda I_\lambda)$ are reported at various angular intervals (multipole separations, often displayed as ℓ ranges) for a given wavelength. These values are also often reported as root-mean-sqaure fluctuation power, $C_\ell^{1/2}$. The electromagnetic spectrum for estimates of multiple

wavelength observations may be displayed for a specific angular separation (or multipole ℓ). Finally, the power spectrum may be integrated to provide an estimate of total power, or compared to models to provide the estimated intensity νI_ν or λI_λ.

Astrophysical Interpretation of Results. Excess signals in angular auto- and cross-power spectra above the level predicted by galaxy surveys are an important observational goal, but identification of excess spatial fluctuations does not provide complete information about physical processes generating the emission. The shape, magnitude, and angular range of the normalized angular power spectrum plotted as $f(\ell) = \frac{\ell(\ell+1)C_\ell}{2\pi}$ may provide constraints on likely astrophysical sources, and may rule out other possibilities. It is most likely that extensive modeling of a complete signal, including instrumental and astrophysical foregrounds as well as known galaxies emission components, is needed to speculate about possible astrophysical sources. If early galaxy contributions to EBL are expected, additional modeling of the physics of the early sources is also needed. A model with these estimated contributions must be created that mimics aspects of the observations to justify stated astrophysical interpretations. Generally, observations are not definite but instead suggest additional measurements (for example, across additional wavelength bands or with greater sky coverage) needed to verify the proposed interpretation.

1.3.5   Infrared EBL Anisotropy Measurements

Measurements of spatial fluctuations of the EBL began in earnest with DIRBE in the mid-1990s, and continued with data from other satellites and dedicated EBL instruments. Fluctuations measurements are provoking heated discussion within the literature and community about the astrophysical interpretations the measurements and the underlying physics the measurements represent.

1.3.5.1   Ground based EBL Measurements.

The first infrared EBL fluctuations observations came from measurements with a ground-based telescope at 2.2 μm using sky chopping observational techniques [6], though these measurements were used to constrain models of early galaxy formation rather than place numerical limits on measured infrared EBL emission. Most measurements after this initial attempt were made from above the atmosphere, to minimize contamination from atmospheric foregrounds.

1.3.5.2 Satellite Observations

COBE: DIRBE, FIRAS. DIRBE images underwent re-analysis with a finding of positive signal from a sources clustered in a manner similar to galaxies [41]. This signal was expected to be on order of $\delta(\nu I_\nu)$ and was 5-10% of the intensity of the reported absolute emission. Importantly, these results showed galactic star light dominated at 1.25, 2.2, and 3.5 μm, continuing the legacy of early measurements identifying significant foregrounds. The authors masked discrete sources in the fields and removed linear gradients to obtain upper limits on spatial fluctuations. Isotropy was not evident as the various fields had different values for fluctuations. Intensity values ($\delta(\nu I_\nu$) were reported based on the defined model for conversion.

The authors extended these measurements into the far infrared, using DIRBE maps at wavelengths up to 100 μm [39]. Interplanetary dust (IPD) was removed with the Kelsall model, discrete sources masked, and the varying background removed to determine amplitude of spatial fluctuations in each field. Again, there was disagreement between fields, but broad agreement with previous reported values at 1.25, 2.2, and 3.5 μm. New upper limits were reported on fluctuations from 4.9-100 μm.

The DIRBE maps were revisited again in 2000 [40]. The authors found the overall fluctuations present in masked maps had a functional form of $\csc(|b|)$ with a positive offset, and did not appear to depend on foregrounds such as instrument noise, galactic sources, or data reduction methods, and claimed this result as infrared EBL detection. This analysis also provided updated values of previous DIRBE fluctuation upper limits using this analysis method.

Wright et al [103] used an external galaxy catalog (2MASS) to remove galactic stars in DIRBE data at 1.25 and 2.2 μm. This analysis resulted in lower spatial fluctuation upper limits than previous works in these wavelength bands.

FIRAS data was analyzed by Burigana and Popa [10]. Submillimeter fluctuations were found to have similar values in several fields at high galactic latitudes, which were presented as evidence for extragalactic origin of the fluctuations and claimed to be upper limits on EBL in these wavelength bands.

IRTS. Matsumoto looked for two kinds of fluctuations in IRTS data [65]. In an analysis of fluctuations of sky brightness, after removal of significant read out noise

at $\lambda > 2.6$ μm and removal of expected fluctuations from faint galactic stars, the authors identified excess fluctuations consistent with values reported by Kashlinsky and Odenwald with DIRBE. This analysis also looked for spatial fluctuations in a wavelength range of 1.4 - 2.1 μm, reporting clustering on the scale of $1°$ $-$ $2°$, consistent with expected scales of $z < 6$ galaxy clustering and thus likely extragalactic in origin, indicating EBL emission.

Infrared Space Observatory. The *Infrared Space Observatory* mission contained the ISOPHOT instrument. Spatial fluctuation analysis of a $30' \times 30'$ field at 170 μm by Lagache and Puget [52] showed a fluctuation profile dominated by Galacitc cirrus for wavemodes $k < 0.2$ arcmin^{-1}, based on the fluctuation shape of $P \propto k^{-3}$, which is the expected shape of the cirrus from other observations. Again, this indicates identification of an important foreground component to the EBL spatial fluctuations which must be accounted for. Excess fluctuations after removing an estimated cirrus contribution was identified as extragalactic and claimed as EBL. Although this result was of a single field and thus did not demonstrate isotropy required of definitive EBL detections, the measurement was broadly consistent with values reported previously by Kashlinsky and Odenwald [40].

Spatial fluctuation analysis of two different $44' \times 44'$ fields at at 90 and 170 μm by Matsuhara et al [63] showed a bright and flat power spectrum, interpreted by the authors as extragalactic emission from $z < 6$ star forming galaxies. In contrast to the previous ISOPHOT observations, these observations had little galactic cirrus foreground due to field selection. These results were used to place limits on source counts below detection limits and to estimate associated EBL intensity.

AKARI. AKARI observations of the North Ecliptic Pole (NEP) with the IRC instrument measured excess spatial fluctuations. The IRC has an instantaneous field of view of $10' \times 10'$ and a pixel scale of $1''.5$, and images of 14 observations between 2006 September and 2007 March were pre-processed and stacked to form circular, masked sky maps for spatial fluctuations analysis at 2.4, 3.2, and 4.1 μm [66]. The authors report significant excess fluctuation at angular scales larger than $100''$ not attributable to zodiacal light, diffuse galactic light, shot noise of faint galaxies, or clustering of low-redshift galaxies. The excess fluctuations, on the order of 1-3 nW/m^2/sr, are found to be consistent with contemporaneous *Spitzer* results, and interpreted as arising from star formation from early, $z > 6$ galaxies.

An *AKARI* FIS far-infrared spatial fluctuations analysis of mosaic sky images with a $2° \times 6°$ field of view [70] measures fluctuations of extragalactic origin and attributes them to star forming ultra-luminous infrared galaxies (ULIRGs) at redshifts up to $z \sim 2$. The authors calibrate the images, remove resolved galaxies up to specified flux, subtract zodiacal light according to both the Kelsall [47] and Wright [102] models, and correct for galactic cirrus in order to measure spatial fluctuations. After considering the short noise fluctuations of unresolved galaxies, the authors determine the level of shot noise is low enough to be attributable to unresolved galaxies alone. The authors find their power spectrum to be overall consistent with known extragalactic sources, and attribute a small excess at the intermediate scale of 0.03-0.1/arcmin to clustering of star-forming galaxies. In contrast to *AKARI* measurements at lower infrared wavelengths, these angular power spectra measurements in the far-infrared do not find unexplained excess fluctuations.

Hubble Space Telescope.   Spatial fluctuation analysis of two fields observed by the Near Infrared Camera and Multi-Object Spectrometer (NICMOS) instrument on the Hubble Space Telescope (HST) at 1.1 μm on scales out to 80″ conclude that low redshift, $z < 7$ populations below the 2MASS detection limit but easily detectable in the high signal-to-noise HST NICMOS Ultra Deep Field imageS are able to generate the near-infrared EBL fluctuations observed in the images. This analysis argues that older populations of stars (Population II and III) are not needed to explain the measured fluctuations, and in fact would have difficulty generating the large amount of flux. A similar conclusion is reached for diffuse Lyα emission. The authors strongly conclude that faint galaxies at redshifts of $0.5 < z < 1.5$ are responsible for the observed fluctuations of amplitudes of 0.4 nW/m^2/sr at a scale of 80″.

Spitzer Space Telescope.   The *Spitzer* Infrared Array Camera [24] at 3.6 and 4.5 μm identified the first excesses in EBL fluctuations above the intensity expected from known galaxies. Kashlinsky et al used a 5×5 arcminute field of view, in which they detected departure from Poisson noise on scales of 1-5 arcminutes after removing foregrounds from zodiacal light, galactic sources, and local galaxies [45]. Later work obtained similar results over a 10×10 arcminute field of view [43]. In 2012, this work was extended to $1° \times 1°$ by creating a mosaic image from multiple IRAC observations [44]. The authors attribute all observed excess fluctuations to early

galaxies or other redshift $z > 6$ sources. This was backed up by modeling supporting early galaxy emission as a source. However, this astrophysical interpretation of the cause of the excess fluctuations is not yet the consensus interpretation across the field.

Cooray et al extended prior models of galactic emission to incorporate non linear clustering (e.g. the 2-halo component of dark matter halo models) for early $z > 6$ galaxies [15, 17]. They were not able to reproduce the observed excess fluctuations with their model if they constrained the optical depth to electron scattering (the number of ionizing photons per baryon present at reionization) to be consistent with values observed by WMAP ($\sim$ 2.5 ionizing photons per baryon); in order to reproduce the observed levels of excess fluctuation, their models required a factor of ten times more ionizing photons ($\sim$ 30). Due to this, the authors conclude the observed excesses cannot be entirely attributed to early $z > 6$ galaxies, and instead are likely due to diffuse emissive components at lower redshifts of $z \sim 2$.

The lack of consensus over the astrophysical interpretation of the measured excess cannot be resolved with existing data. Additional measurements across lower near-infrared wavelength are necessary, ideally spanning the Lyman-break feature for component discrimination. CIBER-1 and CIBER-2 are designed to make such spatial fluctuation measurements.

1.3.6 CIBER-1 Results

The first Cosmic Infrared Background ExpeRiment, CIBER-1, was a suite of four instruments optimized for near-infrared EBL measurements [107]. CIBER-1 contained two degree-scale infrared cameras at 1.1 and 1.6 μm to measure spatial fluctuations, a low resolution spectrometer (LRS) designed to measure the spectrophotometric properties of the EBL in the range $0.7 \leq \lambda \leq 2.1$ μm, and a narrow band spectrometer (NBS) designed to characterize the absolute brightness of the zodiacal Light. All CIBER-1 instruments were evacuated and cryogenically cooled to liquid nitrogen temperatures, and each instrument included a dedicated cold shutter for precise determination of the zero-point signal. CIBER-1 used a sounding rocket-borne platform to provide data collection above the overwhelming airglow foreground. CIBER-1 flew four times between 2009 and 2013. The remainder of this section focuses on the spatial fluctuations measurements of the CIBER-1 Imagers.

The CIBER-1 imaging instruments measured fluctuations in extragalactic back-

ground in $\delta\lambda/\lambda = 0.5$ bands centered at 1.1 and 1.6 μm using two 11 cm telescopes each with a 2° by 2° field of view. Teledyne PICNIC detector arrays with 1024×1024 pixels captured the spatial fluctuations data, which was telemetered to the ground during flight for later analysis. The 2010 and 2012 flights of CIBER-1 produced exciting power spectra results, as described by Zemcov et al 2014 [106] and summarized below.

CIBER-1 selected observational fields with strong antecedent observations, including Lockman Hole, ELAIS-NI, Boötes A and B, and NEP [3]. Fields were observed during multiple sounding rocket flights to check reliability and observe through different patches of the zodiacal Llight. Additionally, detector arrays were rotated by 90° between flights to reduce array-dependent artifacts in the data.

CIBER-1 data undergoes preparation to convert raw data into science quality images, as described in Section 1.3.4. After dark current removal, flat field correction, and astrometric registration, the science-quality image map undergoes translation to Fourier space using a tailored variation of the MASTER formalism. The image mask developed for each frame has a corresponding mode coupling matrix, which is deconvolved from the observed Fourier map along with the noise model and beam transfer function per Equation 1.73.

Figure 1.11 displays the CIBER-1 auto- and cross-power spectra for the 1.1 and 1.6 μm bands. The panel in the top left shows the 1.1 μm auto-spectrum plotted in blue, with the 1.6 μm auto-spectrum overplotted in green. Specific foregrounds for each wavelength band are plotted in corresponding colors, generated using the methodology described in Sections 1.3.2 and 1.3.2 and references [106] and [17]. The data points and error bars are also plotted as solid circles. The solid band is a fitted total that includes all of the astrophysical foregrounds plus a bounded systematic error contribution from flat-field variations. Significantly, between $500 < \ell < 5000$, there is a signal level of ~ 1.5 nW/m^2/sr in both wavelength bands after foreground removal and above what is expected from known galaxy populations ($z < 5$) [33]. The increase is present in two separate instruments with independent light paths and independent detectors. This level of detected signal implies there are additional sources of light at this angular separation beyond what is contributed by local stars and galaxies alone.

The panel in the top right shows the cross-power spectrum of the 1.1×1.6 μm wavelength bands. Foregrounds are similarly plotted in this panel. Again, a positive excess is signal is detectable between $500 < \ell < 5000$.
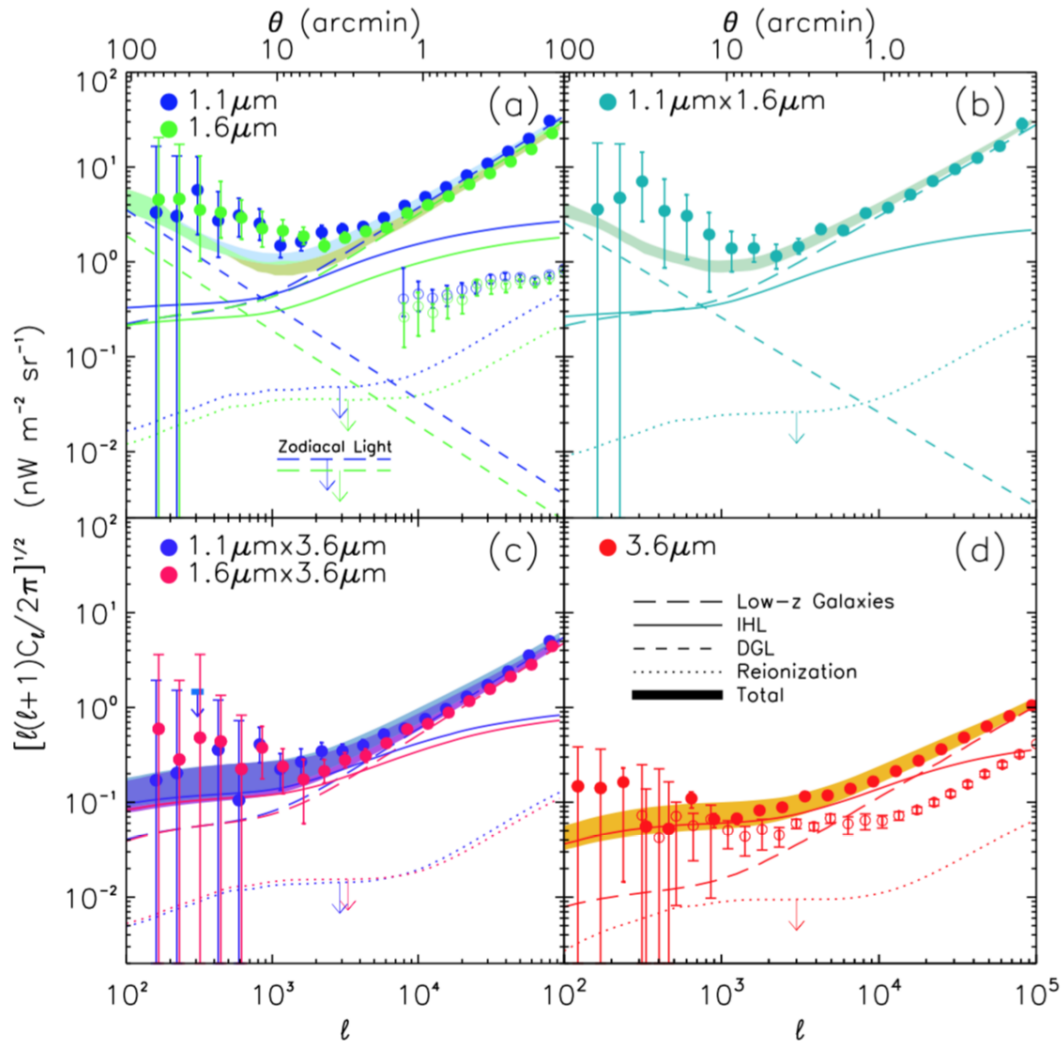
Figure 1.11: CIBER-1 (1.1 and 1.6 μm) and *Spitzer* (3.6 μm) auto- and cross-power spectra [106]. Auto-spectra are shown in panels (a) and (d), while cross-spectra are shown in panels (b) and (d). Data points are shown as filled circles. Previous measurements are shown as open circles, while multiple foregrounds (IHL, DGL) are shown in relation to various components of the EBL signal (low-z galaxies, simulated $z > 6$ reionization contribution, with the total expected emission (EBL and foregrounds) shown as solid bands in each panel. Note the excess at $\ell \sim 10^3$ between the data and dashed line of low-z galaxies, exceeding even the predicted total, indicating an excess fluctuations measurement at this angular separation not accounted for in current models.

The panel on the bottom left shows images from the InfraRed Array Camera (IRAC) on the *Spitzer* satellite. This is based on images at 3.6 μm that overlap with 2 of the 5 CIBER-1 fields. The open red circles are a plotting of the original Cooray et. al 2012 published results [17]. The solid red circles are the same data set processed with the CIBER-1 pipeline; specifically, the CIBER-1 image mask was scaled to 3.6 μm and applied to the data. As the *Spitzer* mask is much deeper, it suppresses the power at high mulitpoles in the expected manner (masking additional foreground galaxies up to a higher magnitude, and thus removing more high-ℓ power resulting in a lower overall amplitude with the expected rising shape). Some mid-ℓ power is also suppressed by this mask. Even with the deeper masking, excess fluctuations are still evident between $500 < \ell < 5000$.

Finally, the last panel shows the cross-spectra between each CIBER-1 wavelength band and *Spitzer* at 3.6 μm, with the excess fluctuations evident. The excess fluctuations at $\ell < 5000$ being clearly present in all plots across multiple fields and completely independent experiments suggests that CIBER-1 observed light from a source *other* than post-reionization, $z < 5$, galaxies. Due to the level of the excess, it is not likely that the entire excess signal comes from emission from the $z > 6$ early universe, as the expected contribution from those sources based on current astrophysical models is several orders of magnitude too low (< 1 nW/m^2/sr as described previously). Some contribution from early sources is likely present, but the level is not clear from these measurements alone. It is instructive to plot data from the power spectra on an electromagnetic spectra for reference.

Figure 1.12 shows the CIBER-1 power spectra data at a single ℓ value plotted with fluctuation amplitude as a function of wavelength, alongside HST and *Sptizer* data points and the early $z > 6$ emission predictions previously discussed. The CIBER-1 data points at 1.1 and 1.6 μm show a much more significant departure from the early universe model predictions. It would be difficult for reionization to generate a signal of the strength detected by CIBER-1; many, many photons would be required, at a level clearly not consistent with optical depth to electron scattering as measured by WMAP. In Figure 1.12, a range of amplitudes of modeled early universe emission fluctuations is shown in orange. All of these data points approximately follow a Rayleigh-Jeans spectrum (thick line) as you would expect for stellar emission, with some deviation. The 1.1 μm CIBER-1 data point has a 2σ deviation from the Rayleigh-Jeans spectrum, which suggests the possibility of a deviation from Rayleigh-Jeans at short wavelengths. Note that there is no strong Lyman-break

signal detected, which would be indicated as a suppression (at some level) of the 1.1 μm signal in comparison to the 1.6 μm signal.

Much effort went into understanding the source of these excess fluctuations. Zemcov et al [106] describe the process of developing theoretical models that are physically realizable and match the observed the spectra; some model variations include changes to the number density and physical assumptions of populations of low metallicity stars (Pop II and III), changes to the underlying dark matter distribution, and even inclusion of additional hypothetical early emission sources such as direct-collapse black holes. However, none of these matched the observed fluctuation amplitude and electromagnetic spectrum intensity that was observed. Addition of late time ($z < 2$) diffuse stellar emission associated with dark matter halos but outside of the traditional (masked and modeled) galaxy boundaries was the only model alteration that generated theoretical spectrum with notable similarities to the observational spectra. This rogue stellar emission is known as intra-halo light and is not well studied in astrophysics due to its diffuse nature. Based on this reconciliation modeling effort, the CIBER-1 data supports a conclusion that there are large, unanticipated and un-modeled foregrounds in the local universe that contribute significantly to the near-infrared EBL. Additional EBL fluctuation experiments with high sensitivity spanning both the near-infrared and optical wavelength bands are needed to further characterize this unexpected signal while continuing to probe for the emission attributable to early galaxies. CIBER-2 is a follow-on experiment to CIBER-1 that is designed to do just this.

1.4   Chapter Summary

Extragalactic background light is key to constraining observations of the earliest luminous objects in the universe, which are faint and difficult to individually resolve. While absolute intensity measurements of the EBL can be challenging to calibrate appropriately, spatial fluctuations measurements of the EBL are able to measure the amplitude of fluctuations while providing information about the angular separation of contributing objects. The intensity and distribution of these early objects is important to constrain numerical models of the early universe, when the universe transitions from a homogenous and isotropic field described by analytic cosmological models to a non-linear state with bound objects that give rise to the complexity observed in late times. Properties of these early objects were determined by prior cosmological conditions such as the scale of density fluctuations determined by inflation, the metal composition of baryons established during pri-
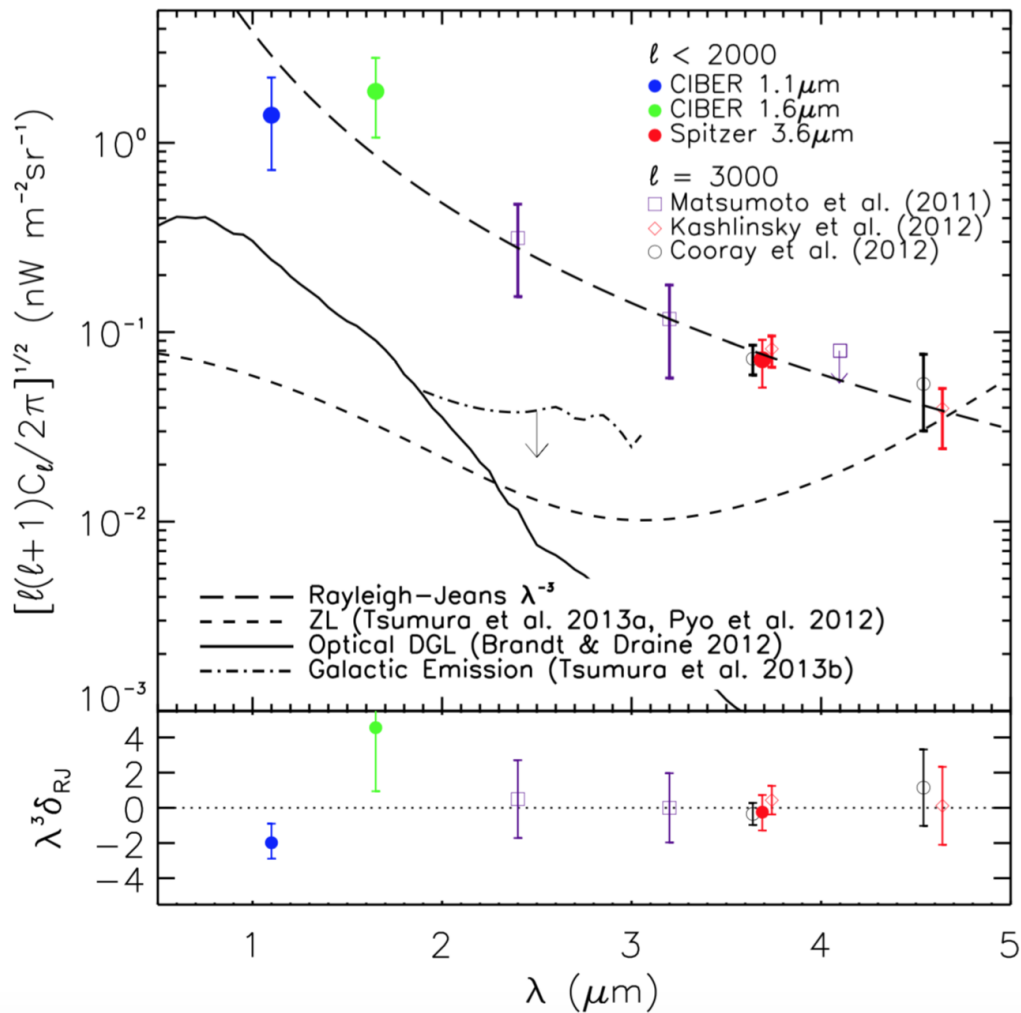
Figure 1.12: CIBER-1 electromagnetic spectra from [106]. The CIBER-2 and *Spitzer* measurements of fluctuation power (averaged between $500 < \ell < 2000$) are shown as solid circles. Previous measurements, with deeper masking thresholds, are shown as open circles. Shot-noise measurements of known, unmasked galaxies have been removed from the data, which are fitted with a Rayleigh-Jeans spectrum. Estimates for foregrounds (DGL and ZL) used in the fitting are shown. The data largely fit a Rayleigh-Jeans spectrum, with a 2-σ deviation of the 1.1 μm observation. This indicates the challenges of a simple astrophysical interpretation of the existing EBL data, and underscores the need for more data at lower wavelengths. Additionally, the lower panel shows the residual from the best-fitting Rayleigh-Jeans spectrum.

mordial nucleosynthesis, the timing of decoupling of cold dark matter and baryons from plasma, and the timing and process of reionization. Additional multiband, infrared, degree-scale spatial fluctuations measurements are an important step in understanding this important period in the history of the universe.

C h a p t e r   2

THE CIBER-2 INSTRUMENT

2.1   Introduction

The Cosmic Infrared Background ExpeRiment 2 (CIBER-2) is an instrument designed to measure extragalactic background light (EBL) fluctuations to identify emission from early galaxies ($z > 6$) prior to the reionization of the universe while also producing enhanced measurements of exciting new foreground emission at $z \sim 2$.

To this end, CIBER-2 is a wide field, degree-scale camera in a sounding rocket payload specifically designed for EBL spatial fluctuations measurements in six near-infrared and optical wavelength bands. In a short sounding rocket flight, CIBER-2 has sufficient sensitivity to probe to the faint signal level predicted for early, $z > 6$ galaxies. CIBER-2 is a collaboration between multiple institutions in the US, Japan, and Korea. This chapter presents the design of the CIBER-2 hardware in relation to the science questions that prompt the design.

2.2   High-Level CIBER-2 Design

The observation goals of CIBER-2 define a set of science drivers that set broad constraints on the instrument design.

2.2.1   Science Drivers

As discussed in detail in Chapter 1, measurements of the angular power spectrum produced by spatial fluctuations in the EBL emission provide advantages for EBL component separation over direct measurements of the absolute intensity of the EBL. Spatial fluctuations measurements require a wide field of view on the scale of a degree or more on a side to capture the clustering properties of underlying galaxy populations on scales of particular interest ($500 < \ell < 3000$) for the $z > 6$ emission of early luminous objects needed to constrain assumptions about this population. Multiple observations of different wavebands from the optical to near-infrared ($0.5 - 2.0$ μm) allow for observation of the redshifted peak of early galaxy emission and identification of the Lyman-break spectral feature in early galaxy emission, aiding in the identification of the EBL contribution from early galaxies and constraining the timing of the completion of the reionization of the universe.

Design requirements for CIBER-2 flow from the science drivers of spatial fluctuation imaging in multiple optical to near-infrared wavelength bands. A reflecting telescope with three detectors and additional band-defining filters provides the basis for detailed design. Details of the fluctuation analysis and astrophysical component separation further constrain the optical design, setting the field of view, etendue, and pixel scale. Selection of an infrared detector with cryogenic operating requirements adds telescope design constraints. Additionally, the need to make observations above emission from the earth's atmosphere restricts the vessel of the telescope; in the case of CIBER-2, a sounding rocket provides housing for the telescope assembly and facilitates observations above the undesired atmospheric foreground. Finally, observational field selection requirements impact the observation strategy but have no effect on telescope design. These science drivers and design features are summarized in Table 2.1. *CIBER-2 accommodates this design guidance by deploying a Cassegrain telescope with multiple Teledyne H2RG detectors on a sounding rocket platform that can observe multiple regions of the sky in a single flight.*

Table 2.1: CIBER-2 Design Drivers

Science Driver	Design Feature
Separation of local astrophysical foregrounds.	Spatial fluctuations measurements at degree angular scales, observed above the atmosphere.
Masking foreground galaxies.	$4''$ x $4''$ pixel size, so that the image of galaxies is small compared to a pixel.
Component separation.	Simultaneous multi-band observations spanning the optical and near-infrared.
Comparison to previous datasets.	Observational fields selected to overlap with previous measurements.

The CIBER-2 instrument consists of an evacuated sounding rocket skin encasing the telescope assembly, imaging optics and focal plane assemblies, cryogenics, and associated electronics as shown in Figure 2.1. This design meets the science drivers outlined in Table 2.1, and introduces additional engineering constraints that are discussed in the remainder of the chapter.

2.2.2 CIBER-2 Optical Layout and Focal Plane Assemblies

In order to maximize optical sensitivity and collecting area, CIBER-2 employs a reflecting Cassegrain optical design, with imaging optics separating the initial light path into three similar optical arms to achieve multi-band observations. The primary mirror is 28.5 cm with a 14 cm secondary mirror, with the size of the mirror set by the sounding rocket envelope. The primary mirror is attached to a support plate
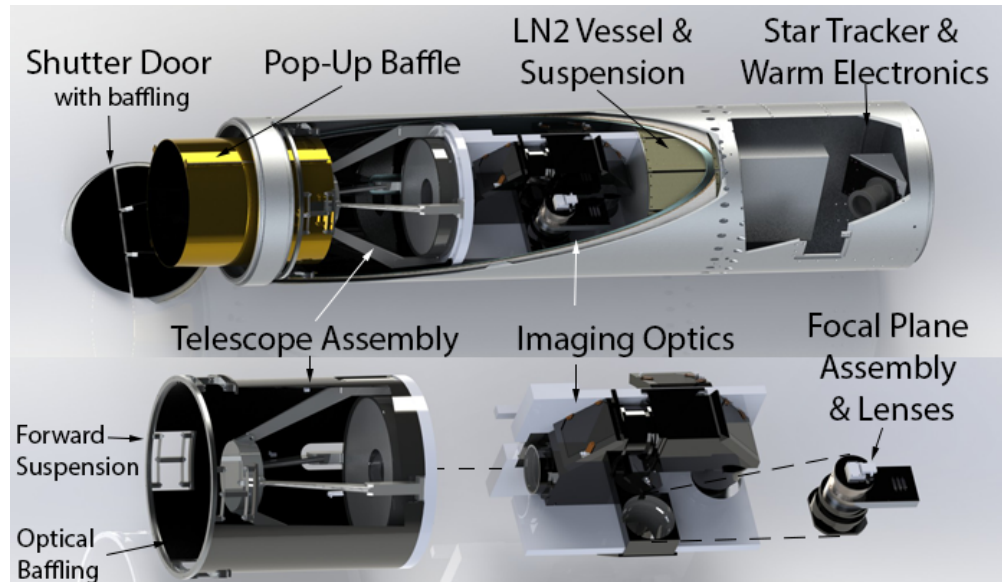
Figure 2.1: Solid model of the CIBER-2 instrument. A 28.5 cm Cassegrain telescope directs light into the imaging optics, where beam splitters divide the light into three optical paths. Each optical path travels to one of three focal plane assemblies, where a broadband filter subdivides the light into two wavelength bands which are both recorded by a single detector array for a total of six band. A small segment of each detector array is also covered linear-variable filter. The imaging optics are mounted to an optical bench that connects the Cassegrain telescope assembly to a liquid nitrogen cryostat. Radiative shielding is provided by a radiatively-cooled door liner and cryogenically-cooled pop-up baffle that extends during observations. A section forward of the instrument section contains an electronics box and a star tracker.

with flexures, and the secondary mirror is held up by a support spider that mounts to the support plate.

The imaging optics are mounted to an optical bench that connects the primary mirror support plate and the cryogenic tank. Light from the secondary mirror passes through the Cassegrain hole to the imaging optics section, where it is focused by a field lens. Two beam splitters direct the incoming light into three paths. Each path consists of additional lens elements and a focal plane assembly. Additional filtering splits the light into two wavelength bands per focal plane assembly, resulting in a total of six distinct wavelength bands spanning the range of $0.5 < \lambda < 2.0 \mu$m.

Each of the three light paths is very similar, consisting of a beam splitter, bend mirror(s), a collimator lens, a band pass filter, a camera lens, and a focal plane assembly that contains a detector array and final band defining filters, which are described in more detail in Section 2. Figure 2.2 shows a representative ray tracing
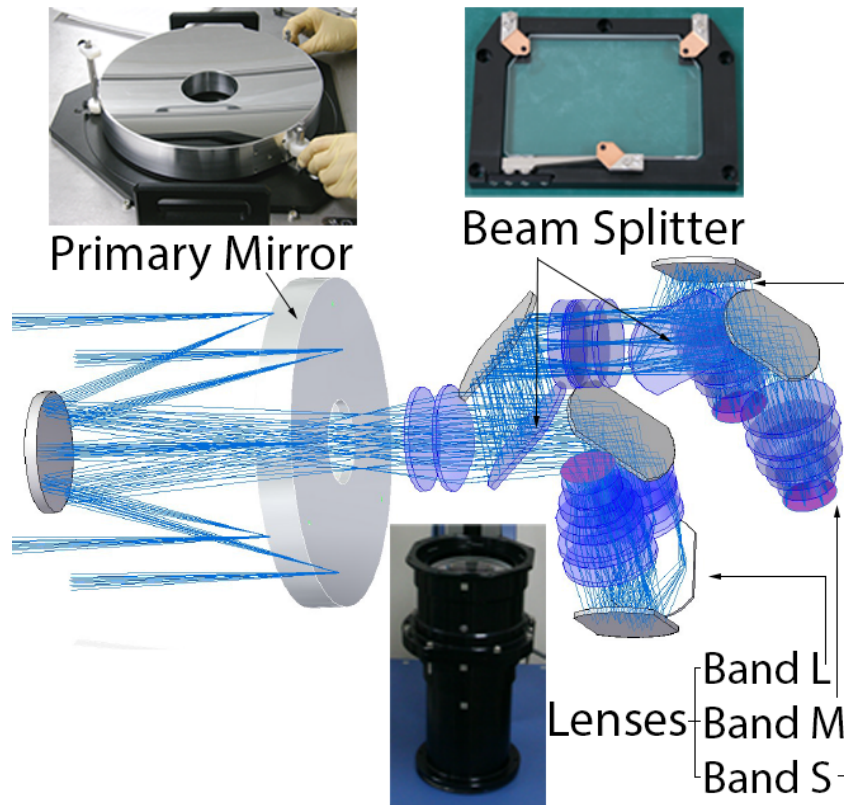
Figure 2.2: Three dimensional representation of the CIBER-2 light paths, contained within the conical sounding rocket envelope. Incoming light is split into three light paths using two dichroic beam splitters. Bend mirrors, a collimator lens, a band pass filter, and a camera lens direct the light to a focal plane assembly that contains a detector array. Photographs of fabricated components are also shown.

diagram including all of the optical components.

The design of the optical chain and selection of the detector guide the design of the focal plane assembly. Broadly, the focal plane assembly (FPA) must couple the detectors to the remainder of the optical chain. Each FPA also includes the final optical elements of the optical chain: a filter defining the final wavebands for the imaging observations as well as a linear-variable spectrograph optic that allows for spectroscopic measurements of the EBL. Each FPA must also provide housing for the H2RG detector, as well as housing for the H2RG readout cables, circuit board, and connectors in a manner robust to electronic shocks and thermal and vibrational stress.

The CIBER-2 optics were designed to achieve the target sensitivity for CIBER-2. Sensitivity is a measure of the relationship between the astrophysical signal and the noise from all sources. As CIBER-2 is observing the diffuse sky brightness,

not individual resolved objects, the signal reference is thus the specific intensity (multiplied by frequency) of the sky.[1]. A minimum required sensitivity is chosen, which in this case is a multiplicative factor (1.5×) of the diffuse sky brightness measured by DIRBE at the North Ecliptic Pole (NEP) [47], resulting in a minimum sensitivity of $\nu I_\nu = 374$ nW/m^2/sr at 1.25 μm. The required sensitivity for CIBER-2 drives the selection of resolution per pixel (pixel size), etendue selection, and observational strategy.

As in point source observations, characteristics of the detector and the observing object of interest combine to determine the expected sensitivity of the imaging instrument [29]. Read noise[2] and photon noise[3] are the dominant noise sources of most measurements, and CIBER-2 is designed to be dominated by photon noise. Photon noise depends on the brightness of the object to be observed and the observing area of the telescope, which are optimized to make this the dominant noise. Other types of noise, such as amplifier and quantization noise, are assumed to be much smaller and are not considered.

The predicted instrument sensitivity [27, 29], in units of [nW/m^2/sr], is

$$\delta \lambda I_\lambda = \delta i_{total} \left(\frac{h\nu}{(\Delta\lambda/\lambda)\eta A\Omega} \right) \tag{2.1}$$

where νI_ν is the sky brightness, δi_{total} is the quadrature sum of the photon noise and read noise, $h\nu$ is the average energy per photon, $\frac{\Delta\lambda}{\lambda}$ is the fractional bandwidth, $A\Omega$ is the observing area (etendue), and η is the total optical and quantum efficiency of the instrument. The quantity in parens provides a conversion between the detector signal, δi_{total}, in units of [e-/s] and the surface brightness in [nW/m^2/sr].

This minimum required sensitivity for CIBER-2 determines the other properties to which the instrument must be designed. The fixed diameter of the telescope places constraints on the maximum diameter of the primary mirror, setting limits on the etendue. The foreground discrimination requirement that a single galaxy fit within a pixel determines the pixel size of 4 square arcseconds, which limits the focal length f of the telescope (assuming a fixed pixel pitch for a given detector, here 18 μm for the H2RG detector). An approximate range of optical parameters can be scoped

---

[1]Note that the specific intensity is often a background noise level in point source observations, whereas for power-spectrum measurements it is the signal of measure

[2]Read noise is a property of the detector and describes the additional electrons introduced per pixel for each readout of the detector.

[3]Photon noise, also referred to as shot noise, arises from the quantized nature of light and the Poisson statistics that describe the variation in sky photons per pixel.

from these constraints. Additional assumptions about observing strategy (based on CIBER-1 data) constrain reasonable observation times from a sounding rocket, here assumed to be 70 seconds per field. Initial ranges for all parameters determine feasibility of basic instrument design. These are then iterated with optical engineers to determine final instrument parameters. Table 2.2 lists the final optical parameters of the telescope, along with sensitivities and spectral band information.

Table 2.2: CIBER-2 Instrument Parameters, assuming a diffuse sky brightness 1.5 times the brightness observed by DIRBE at the north ecliptic pole, including all detector and photon noise contributions assuming line fitting to constant radiance array reads, and allocate 35 seconds per integration, times two roll angles, for a total integration time of 70 seconds per field.

Parameter	CIBER-2						Units
Aperture	28.5						cm
Pixel Size	4						arcsec
Array	HgCdTe						
Format	2048 x 2048						
Field of View	1.1 x 2.2 for imager bands, 0.4 for LVF						degrees
Dark Current	<0.1						e-/s
Read Noise (CDS)	12						e-
Band	1	2	3	4	5	6	
λ	0.600	0.800	1.030	1.280	1.550	1.850	μm
$\frac{\delta\lambda}{\lambda}$	0.33	0.25	0.24	0.20	0.20	0.16	
Array QE	0.90	0.80	0.83	0.81	0.82	0.82	
Optics QE	0.75	0.73	0.81	0.85	0.87	0.87	
Photocurrent	9.5	6.8	8.1	7.8	7.7	3.8	e-/s
νI_ν (sky)	525	450	400	380	320	224	nW m^{-2} sr^{-1}
$\delta\nu I_\nu$ (1σ/pixel)	38.0	44.8	33.9	30.6	25.0	23.0	nW m^{-2} sr^{-1}
δF_ν (3σ)	21.5	21.1	21.0	21.0	21.0	20.9	AB mag

These sensitivities are overlaid on an electromagnetic spectrum plot in Figure 2.3 to illustrate CIBER-2 wavebands and projected sensitivities for one and three flights. CIBER-2 is designed with much greater sensitivity than CIBER-1 which, coupled with the additional wavebands, allows for exceptional component separation to distinguish the foreground contributions to the measured excess signal from the early galaxy contributions. CIBER-2 wavebands and expected errors are shown as the red bands. CIBER-2 will span both sides of the redshifted Lyman break feature in the infrared spectrum, providing additional means to discriminate the early galaxy ($z > 6$) component.
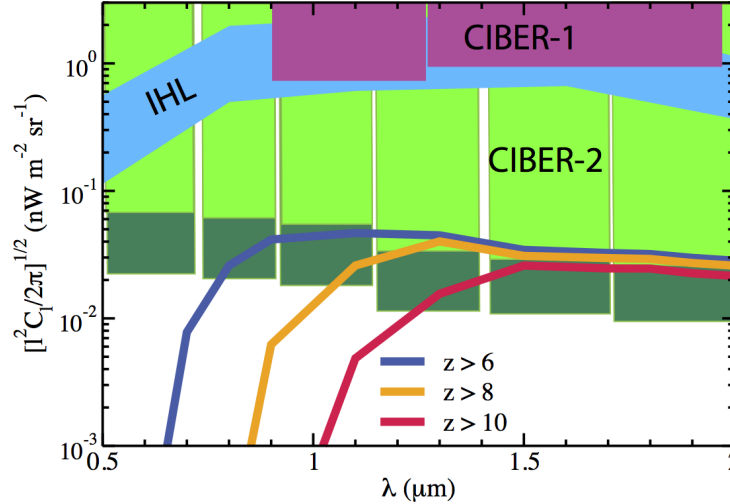
Figure 2.3: Depth of CIBER-2 fluctuation measurements in six wavelength bands from 0.5-2.0 μm at a particular angular scale. Light green indicates the depth achieved by CIBER-2 in a single flight in one field. Dark green indicates depth from all data in four flights. The light blue band indicates the predicted level of IHL across the wavelength range [106]. The three thin lines show the expected contribution to EBL fluctuations from early galaxies assuming different reionization histories, with the dark blue line (left) for $z > 6$, yellow line (middle) for $z > 7$, and red line (right) for $z > 8$. Also shown in purple is the depth from the second and third flights of CIBER-1 in each of its two wavelength bands for comparison.

2.2.3 CIBER-2 Detector Selection

Infrared detectors facilitate observations of redshifted emission of the earliest luminous objects. CIBER-2 utilizes the Teledyne Hawaii-2RG HgCdTe infrared detectors [89], capable of observations at wavelengths of $0.5 < \lambda < 2.0$. These detectors add additional design considerations to the CIBER-2 instrument design; H2RG detectors are designed to work at cryogenic temperatures to minimize noise, and as such the entire CIBER-2 experiment payload is cryogenic and evacuated.

Additionally, CIBER-2 detectors have thermal and electrical isolation requirements that impact the design of the focal plane assembly that houses the detector and preliminary read-out electronics. H2RG detectors are designed to withstand a limited rate of temperature change (2 K/min), and so focal plane assemblies that house the detectors must provide the appropriate level of thermal control. H2RG detectors are also sensitive to static shock and require well controlled voltages and currents, which impacts the design of read out electronics and requires the focal plane assembly to provide electrical isolation.

2.2.4 CIBER-2 Sounding Rocket Environment

Selection of a sounding rocket vehicle to satisfy the science driver to avoid ground-based foregrounds brings a host of environment requirements regarding size, weight, and vibration as specified by NASA [96].

The outer envelope of the cylindrical sounding rocket skin is a fixed 17.26 inches (438.4 mm) in diameter, and the experiment payload has a maximum diameter of 16.22 inches (412 mm). All telescope components, support structures, optics, cold readout electronics, and cryogenics must fit within this diameter.

Sounding rockets are subject to harsh environments upon launch, with high levels of vibration, variations in external temperature, and potential for electronic surges. NASA requires all sounding rocket payloads to pass stringent environmental tests, as outlined in the NASA Sounding Rocket Handbook [96].

Additionally, on-board electronics in sounding rocket payloads are powered by batteries during flight, so power needs for instrument operation must be carefully predetermined. As the rocket trajectory is set by the launch vehicle, weight of the rocket, and total fuel, the total amount of time above the emitting atmospheric layer is finite and predefined. This limits the total observation time available to CIBER-2, which limits the number of observational fields and total integration time per field. Field selection, field integration time, and field observation order must be determined prior to flight and cannot be changed during flight.

2.2.5 CIBER-2 High Level Design Summary

Taken together, the science drivers provide the overall design of CIBER-2 as a wide field, degree-scale camera in a sounding rocket payload specifically designed for EBL spatial fluctuations measurements in six near-infrared and optical wavelength bands. The telescope assembly, imaging optics, and other subassemblies that support such an instrument in an evacuated, cryogenic sounding rocket envelope are described in detail in the next section.

2.3 Detailed CIBER-2 Design

The general design of CIBER-2 as a multi-band, infrared, Cassegrain telescope aboard a sounding rocket leads to additional design constrains addressed in the detailed design of CIBER-2. This section summarizes the detailed design of the CIBER-2 instrument, with emphasis on fundamental physics and the constraints on subsystem design that flow from the high level design. For additional reference,

Appendix A includes a complete look at the specific design and assembly of each CIBER-2 component.

2.3.1 Imaging Optics

The CIBER-2 optical chain begins with Ritchey-Chrétien Cassegrain mirrors with a concave hyperbolic 28.5-cm-diameter primary mirror and a convex hyperbolic 14-cm-diameter secondary mirror to reduce off-axis optical errors. While a reflecting Cassegrain design is inherently free from spherical and chromatic aberrations, the selection of the Ritchey-Chrétien Cassegrain design avoids coma aberrations as well, optimizing it for the larger field of view required for CIBER-2 observations [88]. Additionally, the Ritchey-Chrétien design minimizes field curvature aberrations by generating a flat focal plane, which is also preferable for large fields of view so that all pixels on the detector (edges and center) can be focused simultaneously. Astigmatism, the final of the five types of optical aberrations, is minimized with careful optical design and fabrication (e.g. by controlling lens and mirror symmetry), and by the inclusion of additional lenses in the camera optics portions of the optical chains for each of the imaging arms. The primary and secondary mirrors are made of aluminum (AL 6061-TS) with a silver-titanium dioxide (Ag-TiO_2) coating to increase reflectance and prevent corrosion.

Optical analysis was performed on several possible mechanical designs for the secondary mirror supports. The final design includes four mechanical arms, mounted to the baseplate that supports the primary mirror. The secondary support arms are mounted outside of the diameter of the primary mirror, and have a very thin profile when viewed in the line of sight of the light path. The supports are constructed from anodized aluminum (AL 6061-TS) to reduce stray light.

The CIBER-2 imaging optics begin with a common field lens element that focuses the single beam. A beam splitting lens element next separates the light into two beams. The beam splitting element is a quartz prism with dichroic optical coatings set at a 45° angle relative to the flat plane of the light path, so that the single beam is split into two light paths (transmitted and reflected). The non-incidence surface of the element also has an antireflective (AR) coating. Each of the two light paths passes through a set of collimator optics designed to align each beam. One path is focused immediately into camera optics and onto the detector, denoted as Arm-L (1.5-2.0 μm). The other path is then divided again after the collimating optics by an additional beam splitting element, where the resulting second and third

paths, Arm-M (1.0-1.4 μm) and Arm-S (0.5-0.9 μm), are each directed into a set of camera optics and onto respective detectors. Figure 2.4 shows a schematic of the geometrical separation of the light path, while Figure 2.5 shows more clearly the optical elements in the individual light path of each arm, where the telescope and field lens (labeled G1) are common to all arms.

The camera optics include an order sorting filter, as well as beam limiting and refocusing optics to reduce the spatial cross section of the beam to fit within the physical area of the detector. The glass elements are common among all three cameras, except for a single element that is made of a different glass type tailored to the wavelength band of each arm. The camera optics also include a final filter set, close to the surface of the detector, that includes one dual windowpane filter with two filtering segments that further subdivides the final image on the detector into two adjacent, rectangular images of different wavelength bands each $1.1° \times 2.0°$, as well as an additional linear variable filter that records a third, perpendicular, $R = 20$ spectroscopic image on the remaining $1.2° \times 0.3°$ portion of the detector. This is shown in Figure 2.6.

Additionally, bend mirrors are used to redirect the light paths to keep them within the conical envelope set by the sounding rocket skin. The bend mirrors are silicon dioxide (silica, SiO_2) with the same silver-titanium dioxide coating as the primary mirrors. These optical elements are not represented in Figures 2.4 and 2.5, but can be seen as gray elements in Figure 2.2, in contrast to the purple lens elements.

The imaging optics and mirrors are manufactured to the specifications of the science team by Genesia Corporation of Japan. A collaboration of science team members and Genesia staff developed the optical ray layout and performed analysis necessary to generate distortion plots, aberration diagrams, spot diagrams, and encircled energy plots for each arm to converge on a final design. Additionally, all of the optical components are supported by flexures or spring retainers to handle the thermal compression stress in cooling and to maintain optical alignment against vibration and shock during launch. Finite element analysis (FEA) was performed as necessary.

The CIBER-2 optical chain was designed to accommodate the simulated focus locations of the final optical design. The focal plane assembly is nominally designed to hold the detector surface at the predicted focus location under cryogenic conditions. However, there is some flexibility in focusing, on both the coarse (millimeters) and fine (tens and hundreds of microns) scales. The focus can be readjusted at two locations: by adding or removing course or fine spacers to the interface between the

```
                        ┌─────┐
                        │ G8  │
                        │ G9  │
                        │ G10 │
                        └─────┘
                      ArmM (0.9−1.4micron)
```
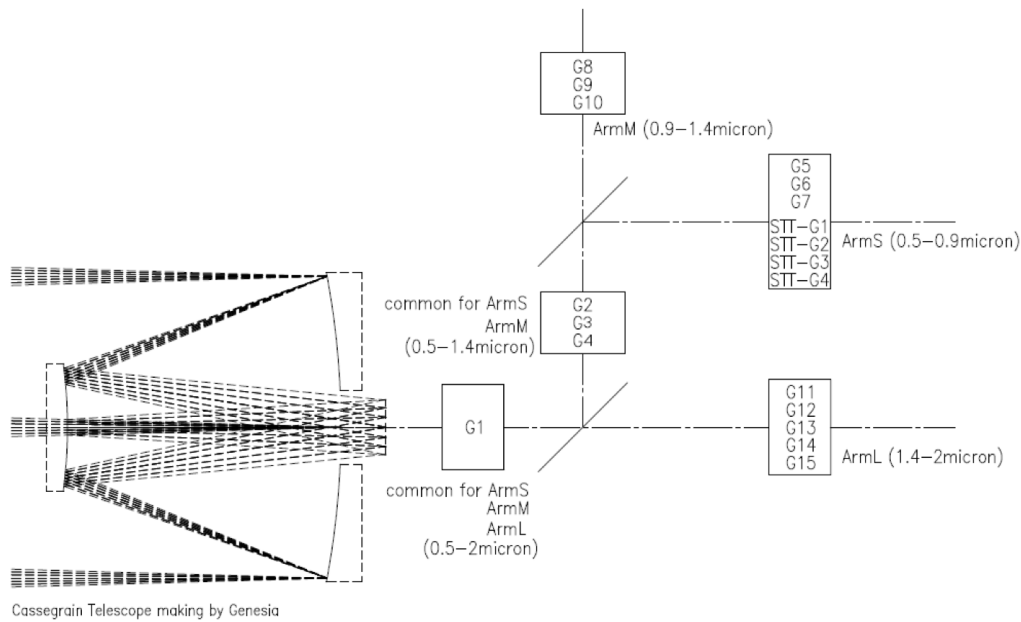
Configuration of CIBER−2 Optics

Figure 2.4: Schematic diagram of the three CIBER-2 optical paths that highlights the use of a two 45° dichroic prisms to split the light into three paths, Arms-L, -M, and -S. Optical elements are not shown individually but are represented by the letter G followed by a numerical index. The wavelength bands at various parts of the optical chain are indicated on the diagram.

lens barrel and FPA, or by adding fine spacers to one or more legs of the detector at the location at which the detector mounts to the supporting component in the FPA. In this way, precise optical focusing can be adjusted for each arm, including axis adjustment. However, the instrument must be at room temperature, pressurized, and disassembled for focus adjustments; no cold or in-flight focus adjustments are possible.

2.3.2 Focal Plane Assembly

The design of the optical chain and selection of the detector guide the design of the focal plane assembly. Broadly, the focal plane assembly (FPA) must couple the detectors to the remainder of the optical chain. The overall FPA design must provide mechanical support and thermal isolation for the detectors; be flexible enough to accommodate the predicted final focus position of each optical arm; provide a mechanism for in situ focusing; and interface to the mechanical supports of the
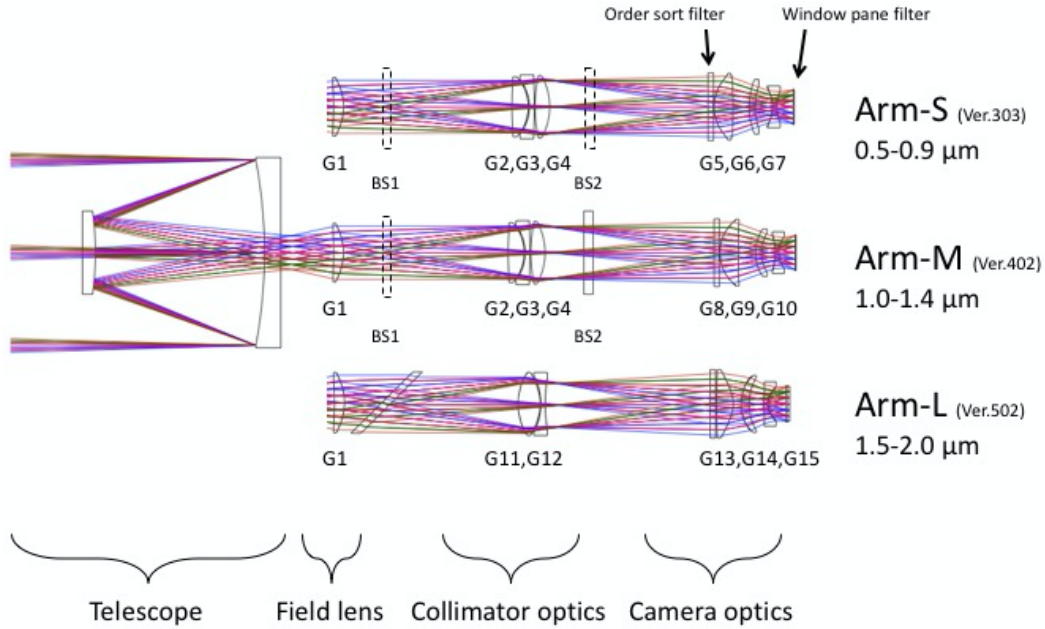
Figure 2.5: Diagram of the CIBER-2 optical paths highlighting optical elements of each optical arm, with the subcomponents of the optical chain indicated (telescope, field lens, collimator optics, camera optics).
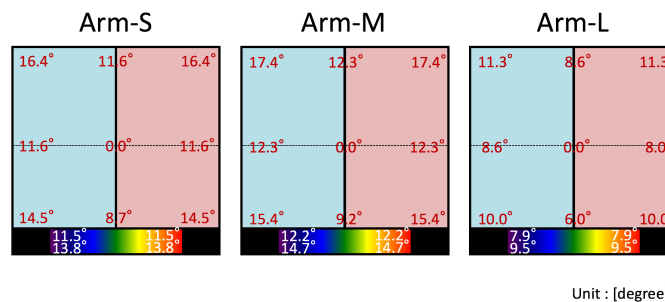
Figure 2.6: Simplified representation of final imaging on detector surface, with adjacent windowpane filters for images and perpendicular spectroscopic imaging section. The numbers indicated the predicted angle of incidence across the detector surface for each optical path, in degrees.

optical chain. The FPA must also incorporate the final filters in the optical chain, as they are designed to reside very close to the detector surface to minimize reflected images. The overall envelope of the FPA must fit within the limited envelope of the sounding rocket experiment payload section, and meet vibration requirements provided in the NASA Sounding Rocket Handbook [96].

The CIBER-2 FPA must provide mechanical support for the detector, cables, circuit board, and connectors. The H2RG detectors are read out by a cable provided by Teledyne that functions in a cryogenic environment. This cable couples to a cold circuit board for initial readout, which uses custom Manganin cables from Tekdata to transmit data and housekeeping information through the cryogenic environment to the warm section of the instrument for additional signal processing. This mechanical design must also accommodate the 2 K/min thermal rate of change requirement imposted by the detectors; CIBER-2 does this though a mechanical thermal circuit rather than relying on heating elements for temperature control. Finally, the FPA works to maintain a constant temperature once cooled to cryogenic temperatures by having direct thermal connection to the cryostat.

The full focal plane assembly for each of the three optical arms includes the H2RG detector and detector interface, the filter assembly that places the filters at the correct distances from the detector surface, the housing that supports the electronics for detector read out, and the interface components that mount to the rest of the optical chain and provide a coarse focus mechanism. These pieces can be seen together in Figure 2.7, along with a cutaway model view showing the internal parts in Figure 2.8.

The initial CIBER-2 design planned for three identical flight FPAs to be fabricated for the three optical arms of the CIBER-2 payload. This allows for lower-cost fabrication and easier assembly. However, this assumes the image projected onto the detector has the same alignment relative to the detector position, which was not the case in the final design of the optical chain. To resolve the image misalignment issue, a mechanical solution was implemented that rotates the detectors so that sky images are aligned in the same way on each detector such that the first pixel read out on each detector views the same portion of the sky, and the LVF filter and windowpane filters view the same portions of the sky. This required adaptations to the FPA circuit boards and housing envelopes to accommodate the new detector alignment without violating the spatial constraints of the sounding rocket. Final FPA designs to correct for the image misalignment can be seen in Figure 2.9.
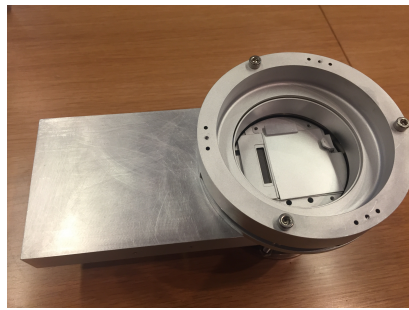
(a) Full FPA with interface pieces included. Bright square in the center is aluminum prototype of quartz window pane filter that sits directly above detector.
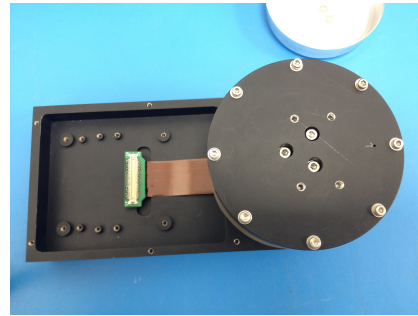
(b) Underside of detector housing with lid removed. Cold circuit board mounts to the black standoffs around the exposed cable and connects to the detector readout cable.

Figure 2.7: Two views of aluminum FPA prototype with focal plane interface pieces.
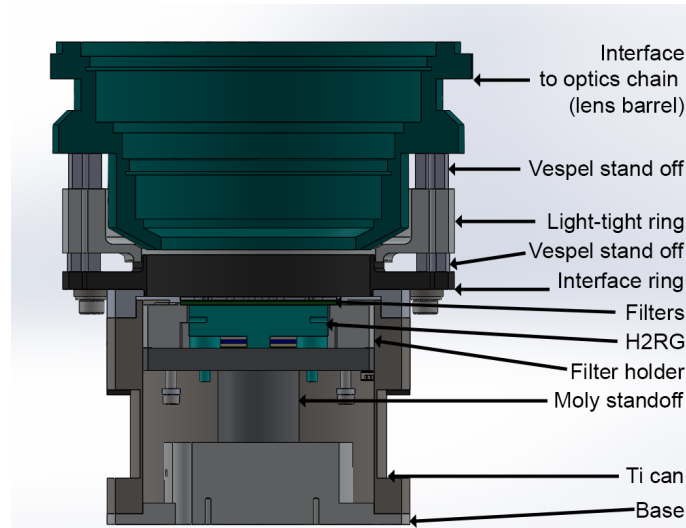
Figure 2.8: Cutaway model view of the full FPA, with labels for component parts. A final set of optical filters sit within the FPA just above the surface of the detector array. The FPA interfaces to the last component of the optics chain (lens barrel, shown in blue) and provides thermal separation and coarse and fine mechanical focus elements.
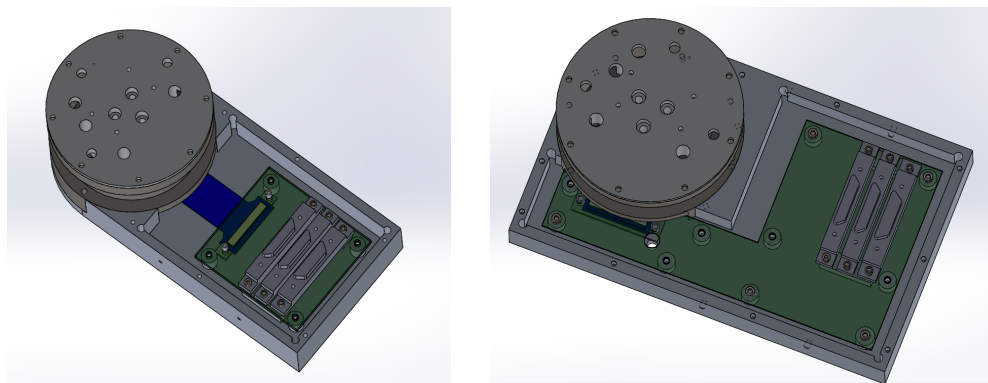
(a) Nominal FPA design that fits within (b) Rotated FPA design to accommodate
original FPA envelope.   image with 90-degree rotation.

Figure 2.9: Multiple versions of the FPA are needed to correct for image misalignment. The image misalignment is corrected by orienting the detector to observe the same patch of the sky relative to pixel readout, and the FPA circuit board and housing were redesigned to accommodate the rotated detector while remaining within the sounding rocket envelope. Here, two of three unique circuit board designs are shown.

2.3.3   Rocket Envelope and Suspension

The CIBER-2 sounding rocket has a fixed diameter within which the instrument payload must fit. The skin has an outer diameter of 17.26 inch (438.4 mm) and is 0.25 inches (6.35 mm) thick in most places, as shown in Figure 2.10a. The skin length is specified by the experiment, and for CIBER-2 is 48.47 inches (1231 mm). There is also an internal support rib to provide additional structural support to compensate for the length, located near the middle of the skin length. The skin is mated at either end to hermetic bulkheads, with a specialized mating flange that functions as an opening for insertion of the CIBER-2 experiment payload that sets the experiment payload outer diameter to 16.22 inches (412 mm).

The telescope assembly, imaging optics, and cryostat are housed in an evacuated segment of the rocket. This payload section is capped at the aft end of the rocket, toward the motors, by a door that opens to the telescope aperture. The shutter door is operated to open when the rocket is above the atmosphere, and to close again before atmospheric re-entry, while maintaining a vacuum tight seal during re-entry. The open closed positions of the shutter door are shown in Figure 2.11. To deflect infrared radiation emitted by the cooling shutter door from entering the optical path of the telescope, an anti-reflective shield of anodized aluminum (Al 6061-TS) is stood off from the face of the open shutter door with thermally-isolating Vespel
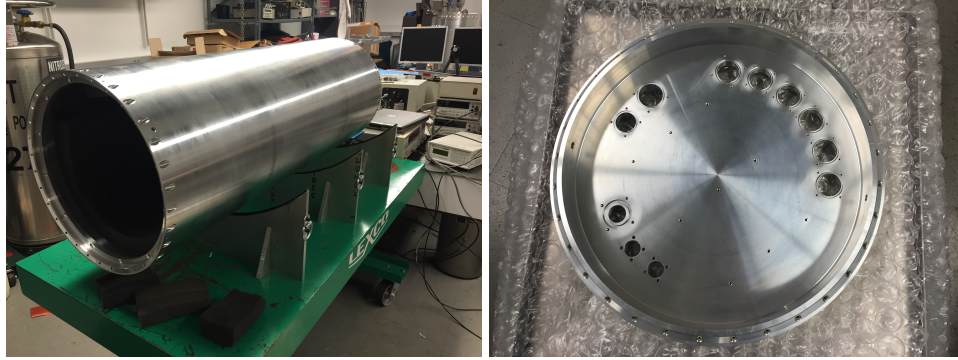
(a) CIBER-2 skin, prior to experiment payload insertion. (b) Fore face of bulkhead, toward warm section.

Figure 2.10: Rocket skin and aft vacuum bulkhead.

cylinders [20].
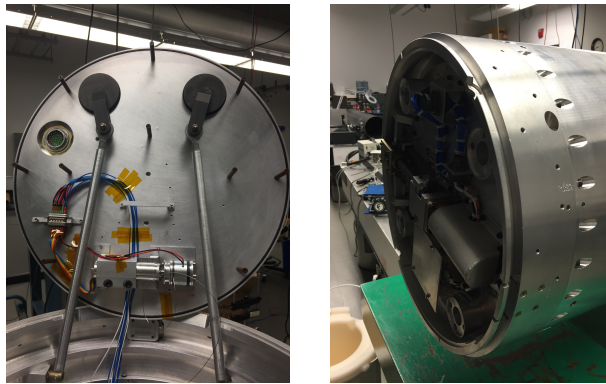
Figure 2.11: Shutter door, in open and closed positions. In-flight control wiring not shown in the open position (lab operation utilizes external power source). Additional wiring and motor mechanism on lower half of door panel for pop-up baffle control. Mechanisms for opening and closing the shutter doors visible on the outside of the door in closed position.

The opposing end of this payload section is capped with a vacuum bulkhead with hermetic cutouts for wires, vacuum equipment, and cryostat fill lines, shown in Figure 2.10b. The skin, shutter door, and hermetic bulkhead are provided by the NASA Sounding Rocket Program (NSRP), with modifications specific to the CIBER-2 project.

The CIBER-2 experiment payload interfaces to the rocket skin at fore and aft ends. At the aft end, the experiment payload interfaces with the skin via an aluminum ring

that mounts to the inside surface of the skin. Shock absorbing and thermally isolating titanium flexures mount to this ring and attach to the optical baffle, a main structural component of the telescope assembly. At the fore end, the experiment is mounted to the vacuum bulkhead using thermally insulating pieces of G-10 fiberglass that mount the cryostat directly to the bulkhead.

The aluminum (AL 6061-TS) skin-interface ring and flexures are designed to allow the experiment payload to absorb shocks from contact with the ground upon descent. Experience with CIBER-1 suggests this ring may become misshapen upon re-entry, necessitating the use of an easily replaceable ring rather than mounting the flexures directly to the rocket skin. This ring also facilitates easier installation of the experiment into the skin, as it is more convenient to guide a ring through the narrow skin opening than unattached sets of flexures. The ring is shown attached to the flexures at the bottom of Figure 2.12b.

Three sets of titanium (Ti 6Al-4V) flexures interface between the skin ring and the optical baffle, as shown in Figure 2.12. The flexures are designed to provide compressibility in the direction along the length of the rocket skin, with extensive modeling to converge on an appropriately stiff, yet pliable, design. The compressibility of the flexures provides a mechanism for the complete experiment payload to accommodate the change in size that occurs with metal pieces cooled to cryogenic temperatures, as well as to absorb shocks. Finally, the flexures also provide a thermal break between the rocket skin and cryogenic experiment payload.
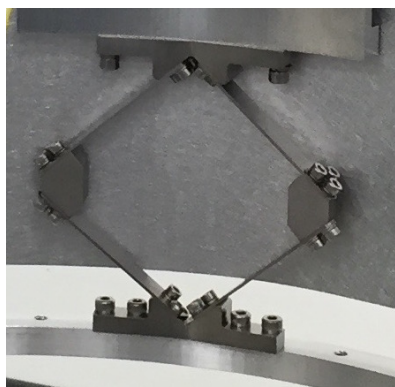
(a) Titanium flexures.

(b) Flexures in an intermediate stage of CIBER-2 assembly. The skin ring is visible at the bottom of the image.

Figure 2.12: Titanium flexures, close up and in the CIBER-2 assembly.

2.3.4 Telescope Assembly and Baffling

The CIBER-2 Telescope Assembly consists of the Cassegrain mirrors, support structures and radiation-blocking baffles.

Telescope Assembly.

The primary mirror is attached to a support plate ("baseplate") with flexures designed to absorb thermal and mechanical stresses while maintaining alignment. The secondary mirror is suspended over the primary mirror by four supporting legs in the traditional spider arrangement. These spiders also mount to the telescope baseplate. The optical baffle also mounts to the aft face of baseplate. The telescope baseplate acts a dividing interface between the aft telescope assembly and the fore optical chain. Light passes through a central hole in the baseplate to the rest of the optical chain, as can be seen in Figure 2.13a. The optical bench, optical shutter, and cold star tracker mount to the fore face of the baseplate.
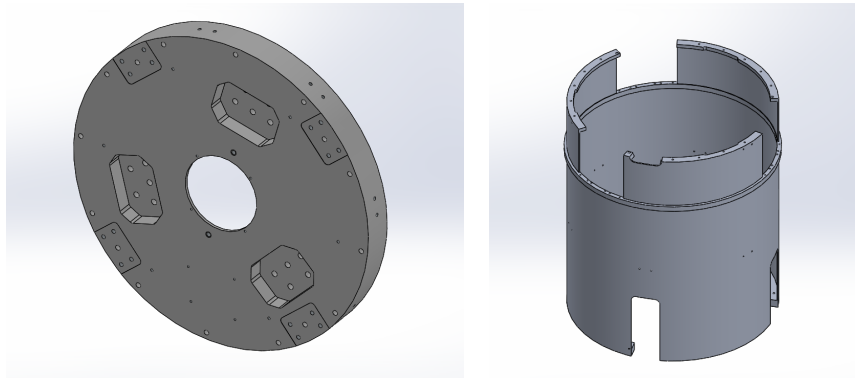
(a) The telescope baseplate is the support plate for the primary and secondary mirrors. On the aft side it attaches to the fixed optical baffle, and on the fore side it mates with the optical bench.

(b) The fixed baffle is a cylindrical optical baffle that provides both structural support and light blocking. It interfaces between the titanium flexures and the support plate for the telescope mirrors

Figure 2.13: Telescope baseplate and optical baffle.

A cylindrical optical baffle is designed to be the main supporting structure of the telescope assembly. It interfaces between the telescope baseplate and the titanium support flexures. It also provides light blocking functionality. The overall design is a cylinder of anodized aluminum (Al 6061-TS) with cutouts and other modifications for various interfaces, shown in Figure 2.13b. The modifications include ribbed cutouts for mounting of the titanium flexures at the aft end; arched cutouts for the

spider supports of the secondary mirror at the fore end; interfaces for the pop-up baffle rods; and threaded holes around the exterior surface for mounting of the radiation shield fiberglass (G10) supports, which provide mechanical support and a thermal break between the radiation shield and the optical baffle.

An electromagnetic optical shutter is attached to the underside of the telescope support plate for calibration of light levels. It allows for measurement of the dark current before and during flight. The cold shutter design is based upon a successful shutter in CIBER-1, described in detail in [95]. The shutter consists of an anodized aluminum blade, counterbalanced by a weight and permanent magnet at the back end, that is mounted on a flexural pivot. The shutter housing contains two powered electromagnets, one on either side of the shutter blade, which become polarized when power is applied and attract the weighted end of the shutter blade. In this way, the shutter can be moved between open and closed positions reliably and repeatedly in a cryogenic environment.
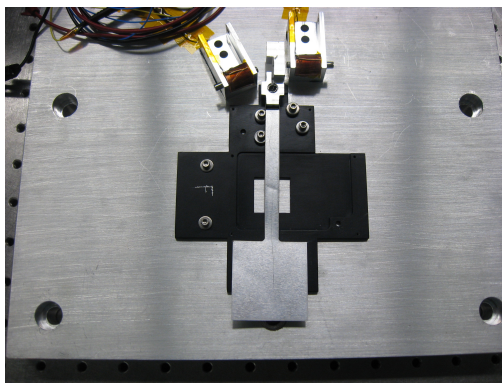
Figure 2.14: Optical shutter in vibration testing configuration. Prototype shutter blade, counterweight, pivot, control magnets and associated electronics are shown; flight housing not included in this configuration. The shutter has two active positions, open and closed (shown), which were successfully operated during and after extensive vibration testing.

Additionally, other calibration lamps are placed behind the secondary mirror. An optical fiber carries the light from the calibration lamp assembly, through the telescope baseplate, and up to a mounting point near the center of the secondary mirror. These lamps and fibers are used to illuminate the light path with a known, fixed brightness for reference observational frames used to track the relative gain of individual detectors.

Baffling.

A pop-up baffle extends upon deployment to block stray light from the skin and open shutter door. Heat from the rocket skin is radiated into the optical path, in the same infrared waveband as the science observations. Much of the radiation from the inside cylinder of the skin is blocked by the internal radiation shield. However, the radiation from the lip of the rocket skin and from the shutter door is not blocked by the internal radiation shield, and can enter the light path, potentially overwhelming the faint EBL signal CIBER-2 will observe. A solution is required to provide the necessary light blocking, while not interfering with the telescope light cone. A cylinder that can extend above the rocket skin is a natural solution.

The pop-up baffle is a movable hollow cylinder stowed inside the optical baffle during ascent and descent and deployed to extend outside the rocket skin during observation. Several prototypes were developed and tested before settling on the final design shown in Figure 2.15. The final cylindrical design extends within most of the available space inside the telescope assembly when stowed, with cutouts at the fore end of the pop-up baffle to accommodate the spider supports. Sets of guide rods keep the cylinder aligned during deployment and retraction, which is controlled by springs and motor mechanism.

The baffle extends during observations using a small motor mechanism, and retracts using spring tension and motor control. The stepper motor is located on the shutter door on a mount with a bobbin of thin metal wire that threads through the telescope aperture and attaches to the fore end of the pop-up baffle cylinder. The stepper motor turns a shaft that causes the string to wind up on the bobbin, pulling the baffle into the extended position, at which point a magnetic brake is applied to hold the motor steady and prevent the string from release. The pop-up baffle stays deployed during the duration of flight observations. It must be retracted at the end of observations prior to closure of the shutter door. To retract the pop-up baffle, the magnetic brake is released, the motor mechanism engages in reverse to unwind the string, and a set of compressed springs provide compression force to push the baffle back inside the skin envelope. Extensive testing was performed to verify motor operation in cryogenic conditions. The stowed and extended positions are shown in Figure 2.15.

While the pop-up baffle is required for flight, it is not required for lab testing and calibration of the experiment payload. These tests also require other components

| (a) Stowed position. | (b) Extended position. |
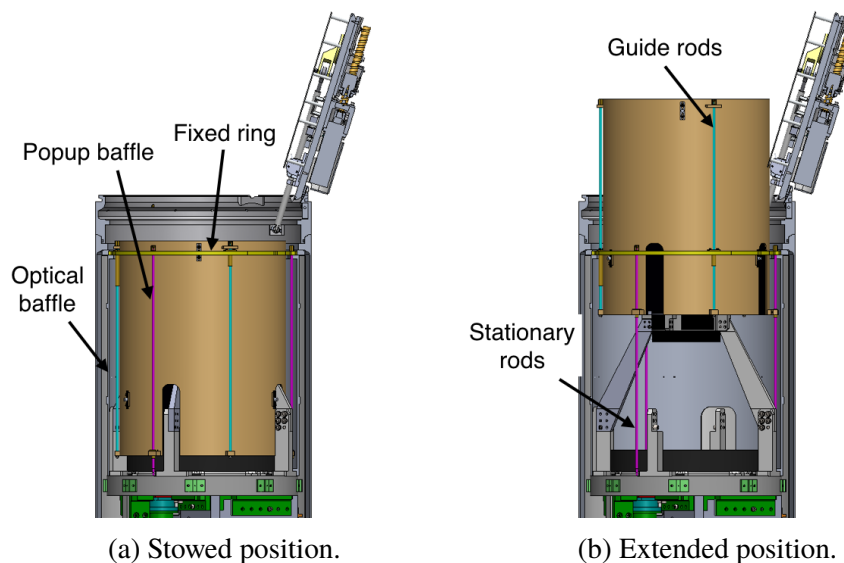
Figure 2.15: The pop-up baffle is stowed upon deployment and re-entry, and extended during observations to block thermal radiation from the skin and shutter door that would otherwise enter the light path and add noise to the science observations. Note the fixed optical baffle is not shown.

that are incompatible with the pop-up baffle. This suggests design of a pop-up baffle assembly as a stand-alone unit that is easily removed to prepare the experiment payload for the lab testing configuration and easily installed to prepare the flight configuration. A ring and rod assembly interfaces the pop-up baffle to other components in the experiment payload.

The optical baffle also performs light-blocking functions during observation. The optical baffle and deployed pop-up baffle form a long cylinder with a blackened and irregular inner surface that absorbs and redirects stray light away from the primary optical path. The cutout portions of the pop-up baffle overlap with the optical baffle when the pop-up baffle is in the deployed position, so that there are no paths for the infrared-radiating rocket skin to introduce photons into the optical path. Once light passes through the primary mirror aperture into the imaging optics chain, baffling is performed by the lens enclosures which are made of anodized aluminum and form a light-tight path to the detectors.

2.3.5 Cold Star Tracker

To improve upon the precision of the pointing of the observational path of CIBER-2 relative to the side-looking star tracker provided by NSRP, CIBER-2 includes a star

tracking assembly located in the experiment payload. This cold star tracker provides active tracking information to the NSRP-provided Altitude Control System (ACS), which is combined with the side-looking NSRP warm star tracker data for more accurate station keeping.

The cold star tracker consists of a CMOS detector at the end of a small optical chain diverted from the main CIBER-2 optical path. A pickoff mirror is located adjacent to the optical shutter blade and directs light into a dedicated optics column consisting of bend mirrors, filters, corrective aspheric optical elements, and the CMOS detector, shown in Figure 2.16a. The CMOS detector housing mounts to the forward face of the telescope support plate. A prototype of this detector and housing is shown in Figure 2.16b.
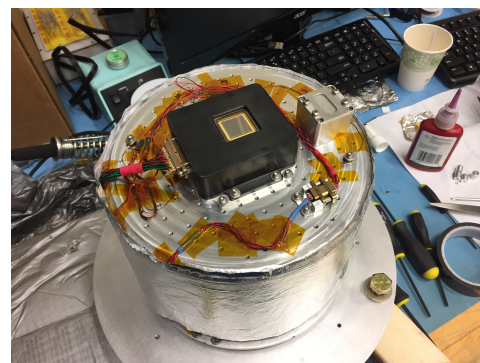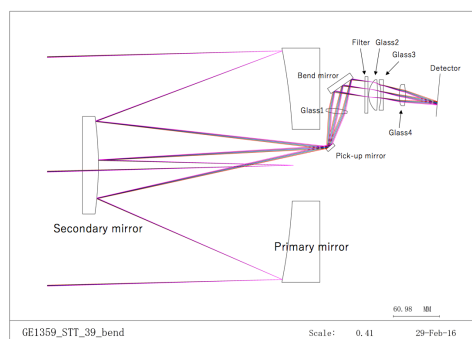
(a) Zeemax model of cold star tracker optical path.

(b) Lab testing of CSTARS, a prototype CIBER-2 cold star tracker.

Figure 2.16: The cold star tracker gets light from a pick off at the optical shutter, passes the light it through an independent optical path, and records the images on a cryogenically-tested CMOS detector to provide precision focus information to mission control.

2.3.6 Cryogenics and Thermal Shielding

Thermal Physics for Cryogenic Environments. Cryogenic environments impose additional considerations on imaging systems [101]. Low temperature environments change the thermal, electrical, and mechanical properties of many materials, and cause many non-metal materials to become brittle and outgas. As such, metals are used as much as possible, and use of plastics, fiberglass, epoxies, and other common materials is minimized. Low temperatures also cause metals to decrease in size, on the order of one part in a million (1×10^{-6}), with the exact factor determined

by the coefficient of thermal expansion. Design at both cryogenic temperatures of 77 K and room temperature of 300 K must be considered, as well as the transition period during temperature change where dissimilarities of coefficients of thermal expansion of materials have the most impact.

Thermal expansion of materials is an important consideration in design of a cryogenic instrument. Materials change size in a nonlinear manner with temperature [101, 58]. Lengths change as

$$\Delta L = L_0 \alpha \Delta T, \tag{2.2}$$

where L_0 is the original length of the material, ΔL is the change in length of material due to thermal expansion (or contraction), α is the coefficient of thermal expansion of the material, and ΔT is the change in temperature (for CIBER-2 generally from room temperature of $T_0 = 277$ K to liquid nitrogen temperatures near $T_f = 77$ K). Similarly, for small areas of contact, the areal expansion changes as

$$\Delta A = 2 A_0 \alpha \Delta T, \tag{2.3}$$

where A_0 is the original small area of the material and ΔA is the change in length of material due to thermal expansion (or contraction). Coefficients of thermal expansion for materials commonly used in CIBER-2 are listed in Table 2.3. For component assemblies that need precise assembly when cryogenic, pre-loaded springs are often used with screw fixtures so that correct positioning can be achieved after thermal contraction.

Table 2.3: Coefficients of thermal conductivity and expansion for common CIBER-2 materials.

Material	Conductivity [W/mK]	Expansion [10^{-6} m/mK]
Aluminum 6061-TS	205.0	24
Invar FeNi36	10.4	1
Molybdenum	138	5.35
Titanium 6AL-4V	6.7	8.6
Vespel SP-1	0.35	45
Quartz SiO2	1.38	0.55

An additional aspect of thermal physics important to cryogenic experiments are the processes of heat transfer [101, 58]. Conductive heat transfer is heat transfer due to molecular motion within a material without motion of the entire material, and often applies to two or more surfaces in direct contact. For materials in a

geometric configuration of adjacent layers in contact, conductive heat transfer can be approximated as a linear process where the rate of heat transfer per unit time, $\dot{q}$ [W/t] is approximated as a function of the coefficient of thermal conductivity of the material κ [W/m K], the area of contact A [m^2], the temperatures at either side of the material T_{high} and T_{low} [K], and the thickness L [m] of the material:

$$\dot{q} = \frac{\kappa A (T_{high} - T_{low})}{L}. \tag{2.4}$$

For a series of materials in thermal contact, this can be approximated as a series of such approximations:

$$\dot{q} = \frac{\kappa A (T_{high} - T_{n-1})}{L} + \frac{\kappa A (T_{n-1} - T_{n-2})}{L} + \dots = \sum_{i=1}^{n} \frac{\kappa_i A_i (T_n - T_{n-1})}{L_i} \tag{2.5}$$

This is similar to an electrical circuit with resistors in series where $\dot{q} = \sum \Delta T / R_i$. For geometries where there are multiple, parallel heat paths, the thermal circuit equation looks like an electrical circuit equations for resistors in parallel:

$$\dot{q} = \frac{(T_{high} - T_{low})}{\frac{\kappa_1 A_1}{L_1} + \frac{\kappa_2 A_2}{L_2}}. \tag{2.6}$$

This can be similarly expanded to included additional parallel heat paths.

Thermal expansion and conductivity are important considerations in detailed part design of a cryogenic instrument. Taken together, they allow for assemblies that fit and function as desired at cryogenic temperatures after fabrication and assembly at room temperatures. Additionally, radiative heat transfer plays an important thermal role in a cryogenic instrument. Radiative heat transfer adds additional heat to the instrument in a room temperature environment, as the outer shell of the instrument is always exposed to a non-cryogenic environment which will then radiate into the inner parts of the cooled instrument. For CIBER-2, during flight the skin is heated to higher temperatures which then re-radiates as it cools, adding additional radiative heat load. Additionally, during CIBER-2 testing, radiative load is also added through the hermetic viewing window during instrument testing and calibration, which necessitates a test-only configuration of the CIBER-2 instrument that includes mitigation of this additional heat load. In the simplest case of two gray, planar surfaces with absorption and emission (but no transmittance through to the outside), the radiative heat transfer between the layers is

$$\dot{q}_{net} = \frac{\sigma (T_{high}^4 - T_{low}^4)}{\frac{1}{\epsilon_{high}} + \frac{1}{\epsilon_{low}} + 1}. \tag{2.7}$$

Compared to a warmer first surface with T_{high}, the second surface will come to a radiative equilibrium with a lower temperature; adding additional layers of material reduces the final temperature of the final layer. This allows for construction of shielding layers of radiation shields and superinsulation blankets made of multiple layers of aluminized Mylar around the conical CIBER-2 instrument that shield the instrument from the warmer skin temperature. The radiative load added from optical testing is decreased by a combination of shielding and conductive heat paths to colder surfaces to aft keep components at lower temperatures.

CIBER-2 Cryogenic and Thermal Design. The CIBER-2 cryogenic system is a duplicate of the successful cryogenic system used in CIBER-1 [107]. This system consists of a 7 liter liquid nitrogen vessel filled with an open-cell aluminum foam that ensures thermal contact between liquid and metal in zero-gravity conditions. The optical bench supporting the imaging optics are mounted directly to the cryostat. Cryostat fill and vent tubes hermetically pass through the vacuum bulkhead and are accessible from the fore side of the evacuated experiment payload. The cryostat itself mounts to raised hexagonal blocks on the vacuum bulkhead through thermally-isolating fiberglass (G10) supports, as shown in Figure 2.17. The cryostat is wrapped
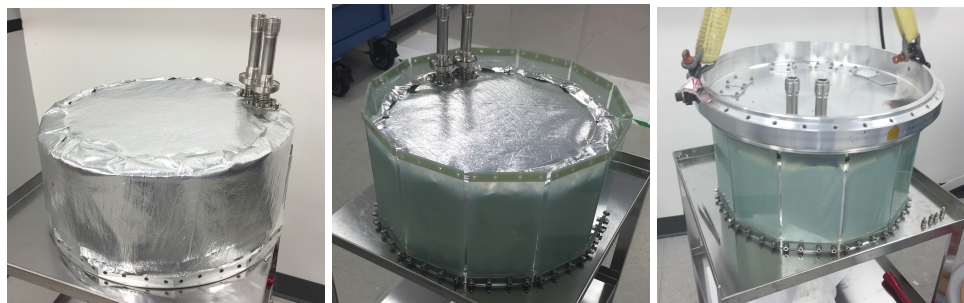
(a) Cryostat with fill and vent tubes installed, wrapped in Mylar

(b) G10 panels mounted to cryostat.

(c) Cryostat mounted to bulkhead via G10 interface panels.

Figure 2.17: CIBER-2 cryostat in various stages of assembly. The cryostat is a container filled with metal foam; fill and vent tubes for the LN_2 were assembled in the lab. Fiberglass (G-10) panels interface between the cryostat and vacuum bulkhead of the rocket, providing flexible mechanical support and thermal isolation.

in layers of aluminized Mylar prior to installation for additional thermal insulation to increase hold time. The desired hold time for the cryostat is at least 4 hours; while the scientific observation time is less than 20 minutes, the CIBER-2 instrument will

be on the rocket pad for at least two hours prior to launch with no opportunity to refill. The anticipated hold time was calculated using assumptions of the steady state thermal load under flight and test conditions, and comparing to the heat capacity of liquid nitrogen [101]. Actual steady state hold time under no loading was on the order of 8 hours; an automated means of filling the cryostat is utilized in the laboratory environment based on tracking of the internal experiment temperature.

The telescope assembly, imaging optics, and cryogenic system are enclosed in a radiation shield made of Aluminum 1100, mounted to the cryostat for cooling. The purpose of the radiation shield is twofold: it buffers the cryogenically cooled instruments from thermal radiation from the skin while simultaneously providing a cold path for portions aft of the instrument far from the cryostat. Al 1100 is chosen as it has a coefficient of thermal conductivity suited for the radiative load while maintaining some of the stiffness of aluminum. The thickness of the radiation shield was chosen after extensive modeling of the thermal loading of the system in assumed flight and test configurations. The assembled radiation shield is wrapped in a four-layer blanket of aluminized Mylar prior to insertion in the rocket skin to further reduce the radiative load from the skin. An additional heat blocking window is installed during laboratory testing to direct the excessive thermal load generated by the room-temperature laboratory testing environment directly to the cryostat, to minimize the incidental radiation into the instrument. This window has multiple copper (Cu) heat sinks mounted directly to the radiation shield to provide a thermal path for the test window to transfer the heat through conduction to the radiation shield rather than through re-radiation into the CIBER-2 instrument.

2.3.7 Warm Electronics and Detector Readout

The CIBER-2 electronics chain carries signals between the detectors, the experiment housekeeping, and the rocket telemetry system. It is made up of the cryogenic circuit boards located near the detectors in the focal plane assemblies and three other board types located in the warm star tracker section of the rocket, forward of the experiment section: data acquisition boards, array processing and housekeeping boards, and data storage boards.

CIBER-2 has three H2RG detectors, each of which is biased and read out by custom electronics on the colocated focal plane boards. The 2048 columns of the detector array are divided into 32 channels, which are read out in "slow" mode to reduce readout time and noise [73]. As the pixel voltages have a large offset, an external
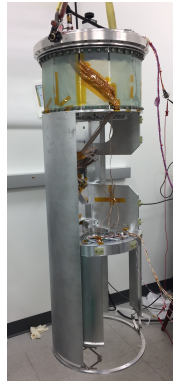
(a) Half of two-piece cylindrical radiation shield affixed.

(b) CIBER-2 with full radiation shield preparing for insertion into skin.

Figure 2.18: Views of the radiation shield. The radiation shield is two overlapping half cylinders that affix to various parts of the experiment payload through T-shaped G10 standoffs. It insulates the cryogenic CIBER-2 experiment from thermal radiation from the (much warmer) rocket skin.

reference voltage close to the average pixel voltage is used to remove the offset. A reference pixel row will be read out periodically during the full detector array readout, providing a method of 1/f noise mitigation similar to [73]. This reduction in 1/f noise is especially important for power spectrum analysis, as correlated noise in the amplifier chain of the Hawaii-I detectors used in CIBER-1 [3] affected the large-scale Fourier modes, increasing the error precisely on the scales of sky separation angles of scientific interest. The referencing techniques available for the H2RGs will allow for separation of the noise from correlated drift of the readout from the sky signal, improving the sensitivity at these angular separations.

Two data acquisition boards per detector array digitize the read out voltages. The signals from both data acquisition boards are passed to a single array processing and housekeeping board, shown in Figure 2.19a, which temporarily stores the data locally before passing it to the data storage board for permanent storage. The array processing and housekeeping boards also perform clocking and command functions for the detector array, pass housekeeping and status data to a NASA telemetry system, and respond to signals from external NASA systems.

The data rate required for three detectors exceeds the capabilities of the NASA ground telemetry systems. Instead of transmitting all data and housekeeping down to the ground station, CIBER-2 stores flight data on-board and transmits only a
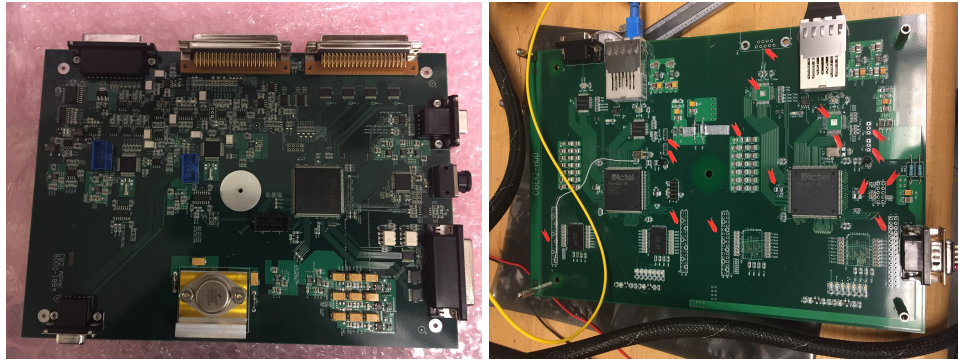
(a) Housekeeping and processing board.   (b) Data storage board board.

Figure 2.19: CIBER-2 electronics boards. Data flows from the experiment payload through hermetic connectors on the vacuum bulkhead to the large connectors on the long side of the boards. Data between boards and out to other rocket systems flows from other connectors. These boards are housed in a metal enclosure in an ambient rocket segment on the fore side of the vacuum bulkhead.

small fraction for diagnostic purposes. Each detector array requires one data storage board with two 128 GB solid-state flash memory chips, shown in Figure 2.19b. The data is retrieved from these storage devices after the completion of the sounding rocket flight. All CIBER-2 electronics boards are housed in a single metal enclosure mounted to the fore side of the vacuum bulkhead, as shown in Figure 2.20.
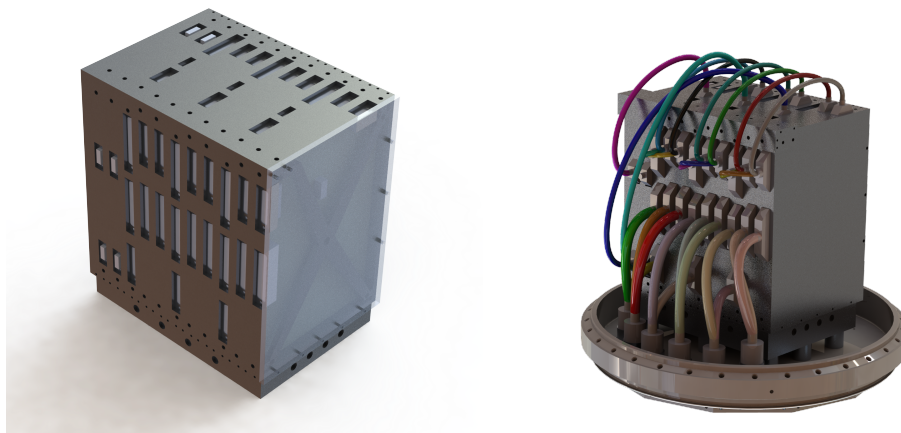
(a) Electronics housing box.   (b) Electronics housing box with wiring harnesses.

Figure 2.20: CIBER-2 electronic box models, shown alone and mounted to the vacuum bulkhead with wiring harnesses.

2.4   Full CIBER-2 Experiment Payload

CIBER-2 is designed to leverage the successes of CIBER-1 while addressing the additional science specifications needed to better characterize the Extragalactic Background Light and probe for the signal of the earliest galaxies. CIBER-2 utilizes a sounding rocket to get above the atmosphere; Teledyne HAWAII-2 RG HgCdTe detectors well suited for intensity mapping; a larger, single telescope design coupled to these large detectors to obtain degree-scale images; and an optics design with multiple filters to obtain six wavebands that span the optical into the near-infrared, 0.5 to 2.0 microns. The verification of the CIBER-2 design is discussed in the following Chapter.

Chapter 3

LAB CHARACTERIZATION AND EQUIPMENT

3.1 Introduction

Instrument verification is necessary to demonstrate that an instrument meets the science goals and requirements identified during instrument design. Verification is a process that includes evaluation of results from many tests. Such tests are intended to characterize the instrument as a whole and to demonstrate that the instrument is capable of performing the desired scientific observations.

The verification process for CIBER-2 includes optical and environmental tests of the complete, integrated, CIBER-2 experiment payload, as well as preparatory subassembly testing. Table 3.1 summarizes the verification of the science drivers described in Chapter 2. The verification process culminates in a prediction of expected sensitivity to be compared to the design sensitivity for each wavelength band, specified in Table 2 of Chapter 2; as an example, the design sensitivity at 1.25 μm is $\nu I_\nu = 374$ nW/m^2/sr .

Table 3.1: CIBER-2 Design Verification

Science Driver	Verification
Separation of local astrophysical foregrounds.	Instrument meets design sensitivity; noise is well characterized; meets environmental requirements for flight.
Masking foreground galaxies.	4$''$ x 4$''$ pixel size with focused & characterized PSF.
Component separation.	All wavelength bands demonstrate acceptable optical performance and sensitivity.
Comparison to previous datasets.	Requires flight for verification.

The prediction of the expected instrumental sensitivity for the CIBER-2 spatial fluctuations measurements requires characterization of the instrument noise and estimation various astrophysical foregrounds.[1] Characterization of the instrument noise is done through laboratory testing prior to scientific observations, and includes measurement of detector characteristics of read noise, dark current, and total optical and quantum efficiency across all detectors. Optical characteristics such as the point-spread function of each optical camera is determined. Other characteristics

---

[1]The actual instrument noise during flight, as well as the calculated astrophysical foregrounds, require analysis of the measured flight data.

of the instrument are determined from subassembly testing and other testing of the integrated instrument, such as environmental response.

Details of the current and planned CIBER-2 testing and verification are discussed in this chapter.

3.2 Laboratory Characterization and Equipment

The CIBER-2 instrument is characterized prior to flight using specialized equipment.

3.2.1 CIBER-2 Optical Testing Configuration

Characterization of CIBER-2 requires specialized instrumentation not present during flight. In flight, the CIBER-2 shutter door opens to vacuum to record data, and blocks external light and keeps the experiment payload segment evacuated when closed. However, for testing purposes while in the lab, a means of introducing light into the telescope while preserving vacuum and cryogenic temperature is necessary: a special bulkhead fitted with a circular quartz window. A light-tight cover can be placed over the quartz window for dark testing. In this testing configuration, the pop-up baffle is removed and an additional set of heat-reducing thermal quartz lenses are introduced into the telescope assembly.

The temperature of the laboratory conditions imposes additional thermal loading on the CIBER-2 experiment during lab testing as compared to flight observations. This causes a temperature difference between the cryogenically cooled experiment components and the rocket skin at ambient temperature, leading to radiative loading on the telescope assembly of ~20 W. Radiative optical loads cause the optical components to heat in the center, while the edges remain cooler as they are thermally coupled to the cooler cryogenic components. This causes the focus of the instrument to change, and focusing the telescope while in these conditions will cause the telescope to be out of focus during flight. The radiative loading must be mitigated to maintain conditions closer to flight to allow for correct focusing and permit other characterization in near-flight conditions.

To reduce the laboratory radiative loading, additional quartz windows are included in the telescope assembly, on aluminum mounts thermally coupled to the radiation shield. These cold windows have no contact with the rocket envelope, allowing them to reach lower temperatures than the window on the bulkhead. Direct thermal contact of the cold windows with the cryogenically-cooled radiation shield allows the cold windows to direct the radiative loading directly to the cryostat through conduc-

tion, preventing re-radiation of the power onto the optical components. Extensive calculations determined the need for two cold windows.

These windows can be seen on the bench in Figure 3.1, and installed in the payload in Figure 3.2. In this configuration, ~ 5 W of power is radiated from the cold windows onto the telescope optics. Based on the experience with CIBER-1, this is close enough to the ~ 3 W of power experienced in flight to allow good focus determination. This assumption will be verified with the first flight.
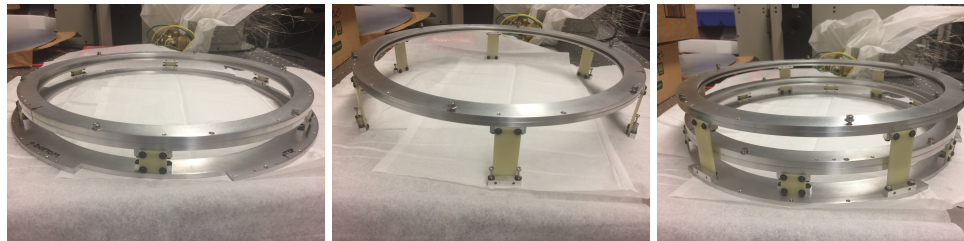
| (a) Bottom cold window. | (b) Top cold window. | (c) Full assembly. |

Figure 3.1: Cold window assembly. The bottom and top window assemblies are put together independently, with metal rings clamping the glass for thermal cooling and G10 legs standing the glass assemblies off the mounting ring that rests on the warmer fixed optical baffle. Not shown are copper heat straps connecting the metal rings to the cryogenically cooled radiation shield to allow a path for heat flow, minimizing radiation onto the instrument optics below.

3.2.2 Optical Focus Determination

The optical focus of each optical arm of CIBER-2 is determined using a collimating telescope to simulate an astronomical object, similar to the sources that will be observed in flight. A point source object is placed in the focal plane of the collimating telescope which generates a ray at the focus center. The image of this optical input on each detector array is tracked as the pinhole of the collimating telescope is moved around the estimated focus position, and the location of the collimating telescope pinhole that corresponds to the smallest point spread function (PSF) on the detector array determines what adjustments are needed to the focal plane assembly to achieve focus. The collimating telescope position shift Δl_{col} is related to the required change in detector array location Δl_{inst} through the thin lens approximation:

$$\Delta l_{inst} = \left(\frac{f_{inst}}{f_{col}}\right)^2 \Delta l_{col}, \tag{3.1}$$

where f_{inst} and f_{col} are the focal lengths of the instrument and collimating telescope, respectively. CIBER-2 uses the same collimator as CIBER-1, an $f/9.5$ off-axis
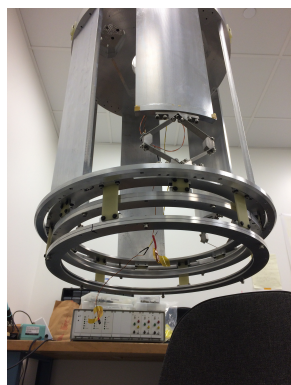
(a) Fit check of window assembly installed directly onto the test experiment payload, without insertion into the skin.
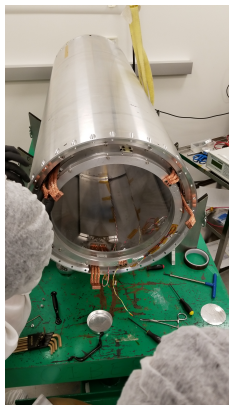
(b) Standard installation of window assembly onto the experiment payload after payload has been inserted into skin.
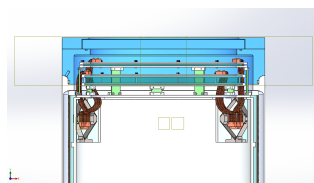
(c) Cut view of CAD model, showing windows mounted to fixed optical baffle and residing below the test bulkhead. Copper heat straps can be seen mounting to the radiation shield through the cut outs for the flexures.

Figure 3.2: Cold window assembly installed in experiment payload. The panel on the left shows the window assembly mounted to the test payload. The center panel shows installation of window assembly after the experiment is inserted into the rocket skin, which is the expected test installation procedure. The conductive copper straps designed to offload the radiation are visible. The right panel is a cutaway view of a CAD model of the cold window assembly showing how the copper straps mount to the windows and to the radiation shield.

Newtonian telescope with a focal length of 172 cm, fabricated in-house using a primary mirror ground by DGM optics [107]. Note that the final PSF values for point sources and extended sources will be calibrated based on observational data during post-flight data analysis.

Estimates for the focus distance of each FPA are predicted through simulations, but final focus distances must be determined experimentally under flight conditions in the laboratory (cryogenic temperature, evacuation). Since the focus of each CIBER-2 detector array is set mechanically and cannot be changed during flight, an iterative focusing process is utilized. The focus position is first set based on simulations, then measured with the collimating telescope during a cold test, when the experiment payload is cooled to liquid nitrogen temperatures and held under vacuum pressure; next the instrument is warmed, the FPA positions adjusted accordingly via shims, and the instrument is cooled down again and the focus remeasured. This process is repeated iteratively until all FPAs have achieved focus. The focus of each optical arm will be determined once the CIBER-2 optics have been integrated.

3.2.3 Flat Field Determination

Determining the flat field of each CIBER-2 detector array requires characterization of the detector array spectral performance in response to diffuse sources which fill the entire etendue of the telescope. This type of diffuse source simulates the extragalactic background light for which CIBER-2 is designed to observe, and relative response of each pixel to the uniform illumination is recorded as the flat field. Generation of a field-filling source requires coupling a quartz-tungsten halogen lamp, which is filtered to produce a spectrum that mimics a solar spectrum, to the optical fiber input of an integrating sphere. CIBER-2 uses the same integrating sphere as CIBER-1, a commercial integrating sphere produced by Labsphere, Inc., with a 20" diameter and 8" exit port [107]. Additionally, a cryogenic vacuum sphere is needed to allow for flat field determination in vacuum, which removes water vapor and reduces the thermal loading on the detector array. CIBER-2 uses the vacuum sphere built for CIBER-1 [107]. This configuration will be used to determine the flat field of each optical arm once the CIBER-2 optics have been integrated. This laboratory flight field may not be used in final data analysis, as in-flight flat field will be created from averages of multiple observed sky fields. However, it is useful in preliminary wavelength band sensitivity calculations and to check for systematic error.

3.2.4 Monochromatic Spectral Response

The spectral performance of each of the CIBER-2 optical arms is characterized in the laboratory environment with a commercial monochromator system. CIBER-2 uses the same monochromator system as CIBER-1, a Newport Corporation Oriel Monochromator and Spectrograph, model number MS257, coupled to a Newport Corporation Apex 50 W quartz-tungsten-halogen lamp light source [107]. The monochromator has two prisms; one with a blaze wavelength of 0.750 μm and ruling of 1200 lines/mm, and a second with a blaze wavelength of 1.20 μm and ruling of 400 lines/mm. The spectral band for each performance test is determined by including a slit of a fixed width into the test setup, while the wavelength is determined by the angle of incidence of the light source on the prism grating. This testing allows for determination of the uniformity of detector array response to light of varying wavelengths for power-spectral imaging, and for calibration references for the LVF spectrometer measurements.

3.2.5 Stray-Light Response

CIBER-2 leverages the lessons learned from CIBER-1 to minimize stray light issues [3]. This includes a large fixed baffle in the telescope assembly and a deployable pop-up baffle that blocks radiation from the rocket skin, as described in Chapter 2. Additionally, all interior surfaces of components in the light path are anodized to minimize reflectance. Thermal stability is maintained through inclusion of direct thermal contact between components and the cryostat or radiation shield through copper blocks and braids to minimize heat-based infrared radiation of internal components.

3.2.6 Detector array Characterization

The H2RG detector arrays undergo testing to verify design of the readout electronics, to optimize the data reduction pipeline, and to characterize the detector array characteristics.

Preliminary testing of detector array read out is done not with a flight array, but with an analog detector array, a Teledyne HAWAII-2RG readout integrated circuit (ROIC), that has an identical physical footprint and electrical readout but does not include the light-sensitive HgCdTe surface coating of the flight detector array. To verify the implementation of command and read out of the detector arrays, a prototype circuit board is connected to a ROIC that is set up in a cooled and evacuated cryostat, as shown in Figure 3.3a. The board is controlled by a computer program that also records the ROIC response. An example of a detailed waveform response is shown in Figure 3.3. Once appropriate voltages and currents for communication with the board were established, the noise characteristics of the ROIC at cryogenic temperatures were investigated across different settings of the CB2TB electronics board. Some results are shown in Figure 3.4.

A full read out of the array for an 8-frame exposure with no resets is shown in the left in Figure 3.5, with a line fit of a single pixel shown on the right. The striping is due to the readout pattern of the detector array, and has been optimized in later work.

The conversion of raw detector array units to units of electrons per second [e-/s] is determined in software by fitting a slope and offset to the measured output voltage of each pixel [27]. Per the manufacturer, the expected conversion is expected to be on the order of 4 μV/e-, with saturation above $\sim 100,000$ electrons. In flight observations are planned to be 35 second integrations, so this value is used as a
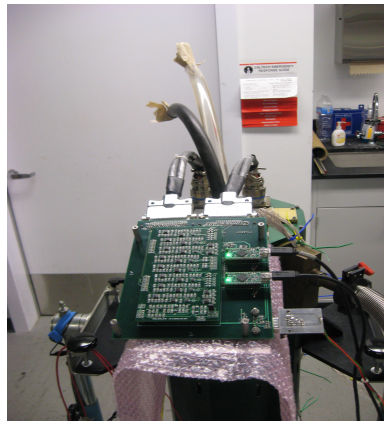
(a) Preliminary electrical testing of detector arrays using the HAWAII-2RG readout integrated circuit (ROIC). Shown here is a prototype command board connected to the ROIC installed in an evacuated and cryogenically dewar (ROIC not visible).
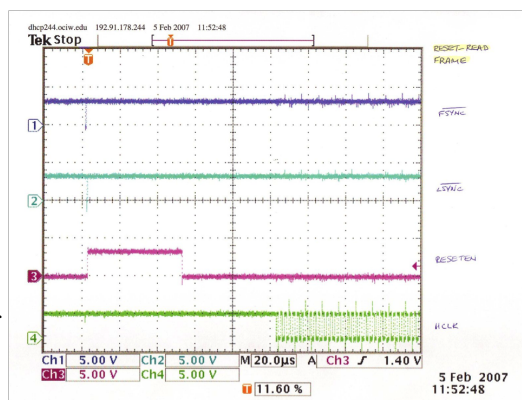
(b) Recorded ROIC waveforms.

Figure 3.3: Test setup and results of preliminary electrical testing of the H2RG readout integrated circuit (ROIC)
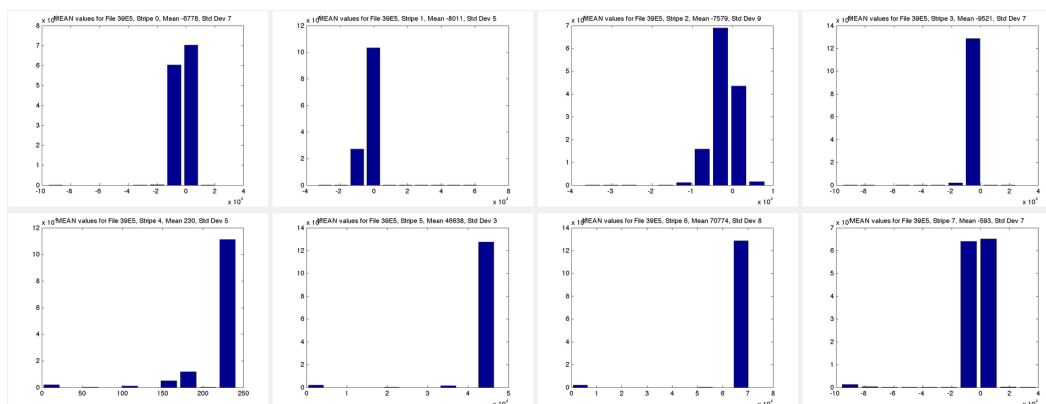
Figure 3.4: Preliminary results of voltage responses of the ROIC for different commands of the CB2TB electronics board.
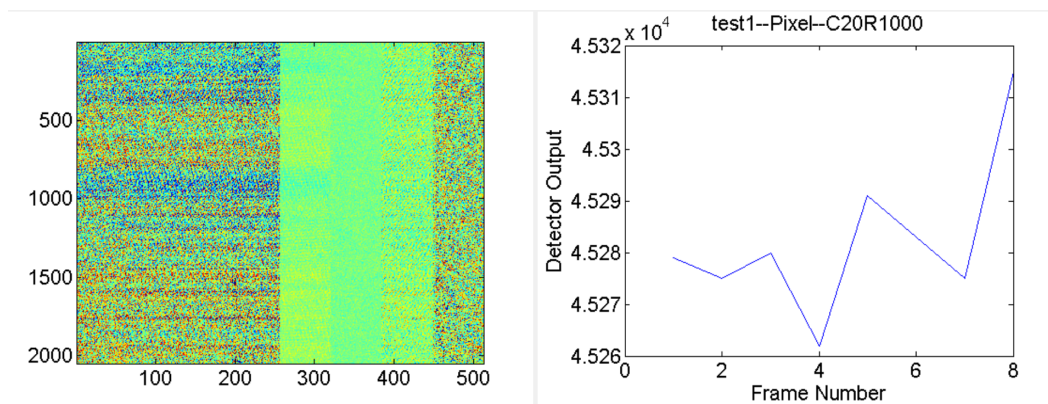
Figure 3.5: Preliminary results of noise characteristics of the ROIC at cryogenic temperatures for different settings of the CB2TB electronics board. A line fit image of the entire array for an 8-frame exposure is shown on the right, in raw units per frame.

reference in signal-to-noise estimations.

The read noise of one H2RG detector array is measured using the correlated double sampling technique designed to reduce correlated noise associated with HgCdTe detector arrays [73], which reduces correlated noise in the amplifier chain by measuring a reference pixel and subtracting that value from the measured signal for each pixel. This correlated noise arises from $1/f$ noise on the array reference and bias voltages, as well as $1/f$ noise in the multiplexer readout and other pickup. The read noise measured from the detector array using all manufactured FPA circuit boards was consistently below the predicted value of 10-12 electrons provided by the manufacturer. This method will be repeated on all detector arrays prior to flight to characterize their specific dark current values.

As the correlated noise introduces a bias with specific structure in Fourier space that mimics astrophysical signal on large angular scales, reduction of the correlated noise is an important means of decreasing error in sky measurements. Utilization of the correlated double sampling technique reduces this structured noise, as shown in Figure 3.7 for different sampling rates of the reference pixel. For all sample rates, the amplitude of the power spectra in the referenced measurements shows lower noise than the unreferenced measurements. Additional characterization of all detector arrays will allow for determination of a optimized sampling rate.

The dark current of each detector array will be determined through readout of the detector array data with the cold shutter closed, once the full optical chain is
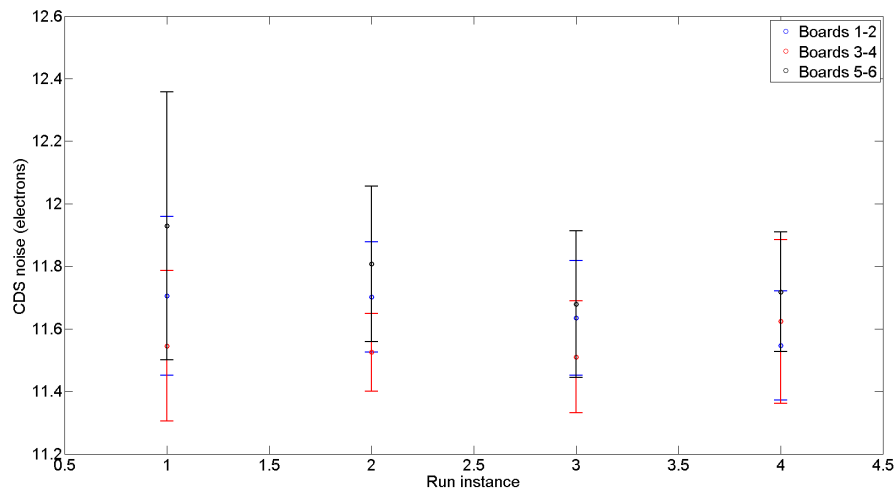
Figure 3.6: Correlated double sampling read noise of one H2RG detector array read out by multiple FPA circuit boards. The measured values are below the read noise of 12 electrons provided by the supplier.

integrated and the instrument is evacuated and cooled. The dark current is expected to be < 0.1 e-/s as indicated by the detector array manufacturer. Similarly, the quantum efficiency of each detector array is characterized by the manufacturer as between $81 - 83\%$, which will also be verified in the laboratory environment.

The read noise, dark current, and quantum efficiency (determined from flat field measurements) of each detector array will be systematically recharacterized for all detector arrays in their flight configurations prior to flight.

3.3 Subsystem Characterization and Equipment

Each of the broad CIBER-2 subsystems is subjected to functionality testing to ensure proper operation before integration into the overall experiment payload. Brief descriptions of testing of all subsystems is included here. Detailed testing information is provided for select subsystems.

3.3.1 Subsystems Testing Overview

The sounding rocket envelope is verified to successfully hold vacuum; the skin, shutter door vacuum bulkhead, and populated and sealed fore vacuum bulkhead were pumped down to and held a pressure of 10^{-8} Torr on the first attempt. Next, characterization of the cryostat to determine the hold and warm up times occurs, with the rocket envelope evacuated, the cryostat filled with liquid nitrogen (LN_2),
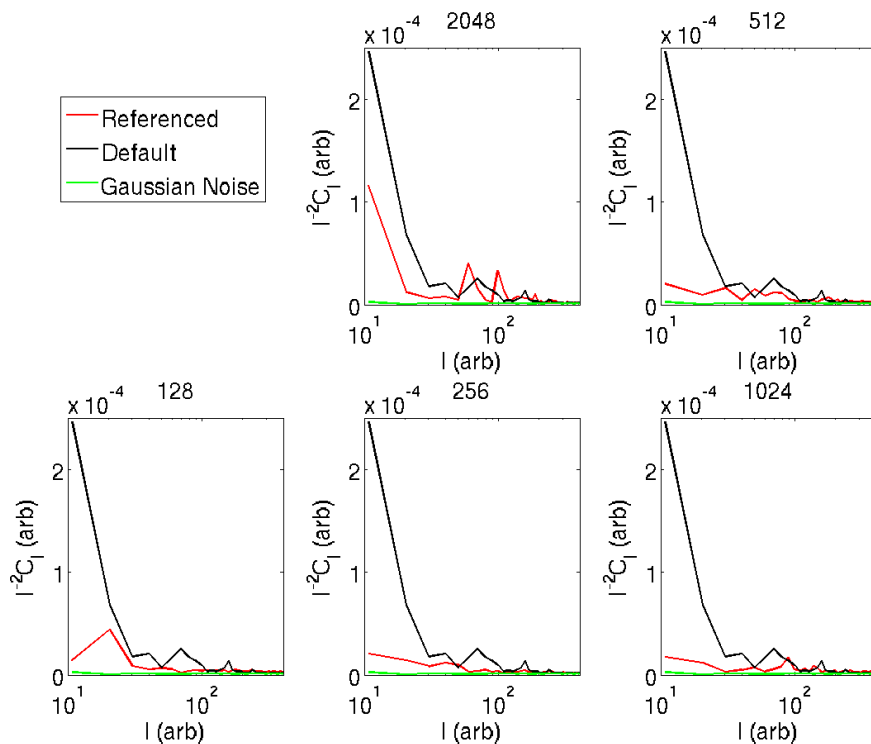
Figure 3.7: Detector array power spectra with and without correlated doubling sampling technique are displayed. Each plot includes unreferenced noise measurements (black), referenced noise measurements (red), and Gaussian noise (green) for measurements with different reference sampling rates per frame, which are indicated by the number above the plot (e.g. the first plot samples the reference pixel 2048 times before each 50-second frame is complete). For all reference sampling rates, the utilization of referencing improves the amplitude of the measured noise in the power spectrum.

and the temperature is recorded as a function of time via a number of calibrated resistance thermometers mounted inside the rocket envelope. Figure 3.8 shows results of the initial cryostat testing, with the initial hold time of $\sim$ 5 hours. This hold time represents a maximum, as it will take less time to utilize the LN_2 when additional experiment components are installed in the envelope, or when additional power sources are incident upon the instruments during testing. The time to fully warm up to room temperature, when it is permissible to release the vacuum and open the experiment, is $\sim$ 75 hours as shown in Figure 3.9. Additional cryogenic tests performed to determine temperature performance with the radiation shield recorded a longer hold time for the configuration that includes the radiation shield compared to the configuration without the radiation shield.
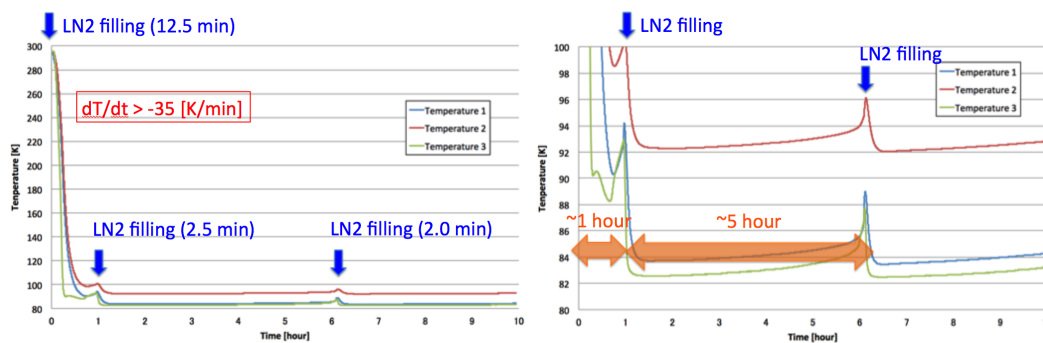
Figure 3.8: Temperature profile of cryostat cooling test.
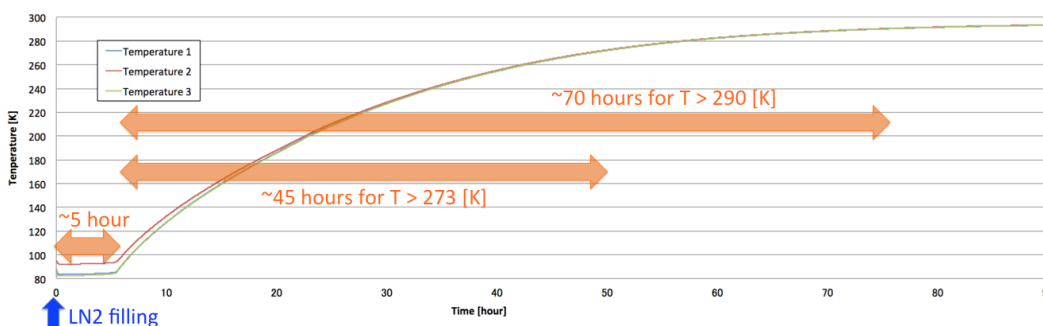
Figure 3.9: Temperature profile of cryostat warming to room temperature.

The telescope assembly does not undergo isolated subsystem testing and will instead be vibration tested as part of the entire the CIBER-2 payload preliminary testing at a NASA facility (due to the large size of the experiment section). The suspension at the aft and fore ends of the rocket leverages successful CIBER-1 designs and underwent extensive modeling, and so is assumed to be at low risk of failure. The telescope baffle tube does not require subsystem testing. The telescope baseplate and Cassegrain mirrors underwent testing that resulted in redesign of the supports of the primary mirror to better withstand required vibrations; other components such as the secondary support spiders required no change. The pop-up baffle assembly underwent thorough laboratory testing in a warm environment with a gravity vector, as it is too big to test cold and is not accommodated by other cryogenic and evacuated testing configurations. However, the pop-up baffle motor and brake mechanisms underwent successful repeated cryogenic operation.

The electromagnetic cold shutter, mounted to the telescope baseplate before the imaging optics, successfully operated during and after vibration testing to verify functionality after being subjected to vibration levels specified by the NASA Sound-

ing Rocket Handbook. The neck of the blade proved to be significantly reinforced so as not to break under launch conditions, which was a concern due to the length and thinness of the material.

Individual optical components were subject to preliminary screening by the supplier prior to delivery to determine each lens functions as designed. Optical integration testing was performed during assembly at Caltech of each optical arm of the camera optics. Comprehensive optical testing of the instrument to verify science performance is described in the optical testing section of this chapter.

3.3.2 Detailed Focal Plane Assembly and H2RG Detector Testing Discussion

The CIBER-2 focal place assemblies were subject to a number of thermal, vibrational, and preliminary focus tests before integration into the full optical chain.

The thermal design of the FPA is tested by collecting data about the temperature of various locations on the FPA during a cool down of the assembly from room temperature (300 K) to the intended operating temperature of 77 K. To test this, a subset of the FPA component parts are assembled and mounted to the work surface of a small dewar, as shown in Figure 3.10a. Resistance temperature detectors (RTDs) [28] are attached at various points on the FPA, including the mounting surface of the detector. The read out cables for the RTDs, visible in Figure 3.10a, are read out by Lake Shore 218 Temperature Monitors [72] and recorded in a data file. The cryostat is closed up, connected to a vacuum pump and pumped down, then cooled by adding liquid nitrogen to the dewar. This setup is shown in Figure 3.10b. The temperatures at all RTD locations are recorded prior to adding liquid nitrogen to the time all components have reached a stable final temperature.

Additionally, the LVF is subjected to thermal cycling to test the epoxy. A similar set up is used where the LVF holder is mounted to the work surface of a cryostat as shown in Figure 3.13a. The LVF itself is mounted to the LVF holder using special epoxy as described in Appendix A. The cryostat is then closed up, pumped out, and cooled down for several cycles. The cryostat is then opened up, shown in Figure 3.13b, and the surface examined under the metrology microscope. As can be seen in the metrology images in Figure 3.14, no cracks are visible. Note that the wavering surface indicates epoxy migrated to the surface of the LVF during installation. A new installation procedure was subsequently developed to prevent this in further assembly which includes application of epoxy to only the thin edges of the LVF and redesign of the Invar LVF holder component to include epoxy wells
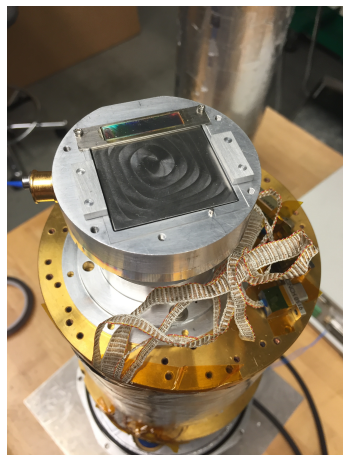
(a) Detector support and mock detector (aluminum) mounted to the cryostat work surface (gold).
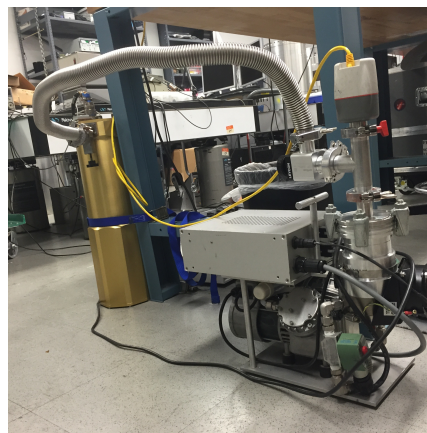
(b) Dewar (gold cylinder) connected to vacuum pump (foreground) for thermal testing of FPA.

Figure 3.10: Preliminary thermal testing of the temperature gradient of the support assembly for the H2RG detectors. Support parts are mounted directly to the surface of the cryostat, with calibrated resistance thermometers placed at multiple parts in the assembly. Recorded temperatures were compared to predicted temperatures to show the rate of change at the detector mounting surface is less than the required minimum (2 K/min).

around the LVF recess. This procedure kept the epoxy from interfering with the LVF faces. The LVF and epoxy withstood multiple thermal cycles.

A specialized metrology microscope measures the distance between CIBER-2 components to the hundreds of microns. This allows for the precise measurements needed for each CIBER-2 FPA: 100 μm separation between H2RG surface and window pane filer (roman numerals); 800 μm separation between H2RG surface and LVF; and focus distance, indicated by the separation of the detector array surface relative to the lens barrel (alphabetic indices).

Figure 3.15 shows the measurements taken of FPA components. Due to the physical limitations of the microscope, it is not possible to measure the separation between the detector surface and the windowpane filter directly. Instead, one measures the height of each detector relative to the Molybdenum mount, then separately measures the height of the filter holder on which the window pane filter rests, and finally infers the separation between the filter and the H2RG surface from the difference of these measurements. These are indicated by the red lines in Figure 3.15 labeled with roman numerals and catalogued in Table 3.2. Note the filter holder is designed to

(a) Linear scale.　(b) Logarithmic scale.　(c) Derivative of each data set.
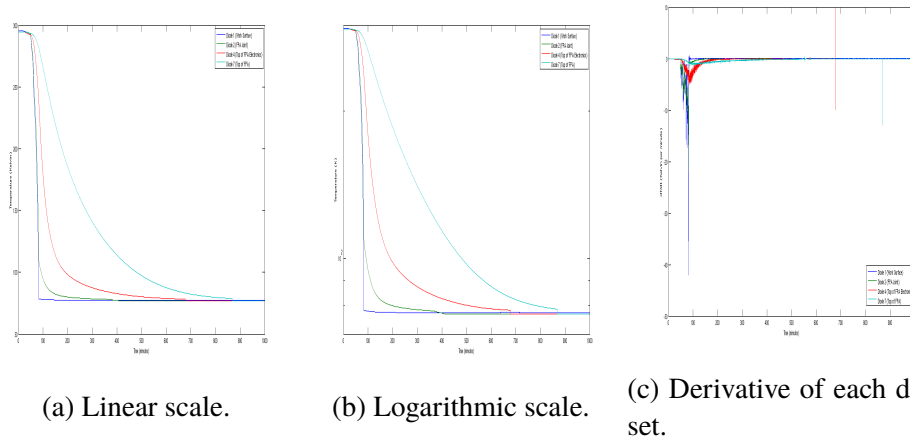
Figure 3.11: Temperature test results showing the temperature (Kelvin) as a function of time (minutes) during a cool down from room temperature (300 K) to liquid nitrogen temperature (77 K) at multiple locations within the cryostat: work surface of the cryostat (dark blue); joint of the mounting plate (dark green); top of the electronics housing (red); and mounting surface of the detector (cyan). The cyan line has a significantly reduced slope compared to the cryostat work surface, demonstrating that the mechanical thermal circuit is indeed insulating the detector from thermal shocks. Inspection of the derivative of the temperature of the work surface demonstrates a cooling rate of < 2 K/min as designed.
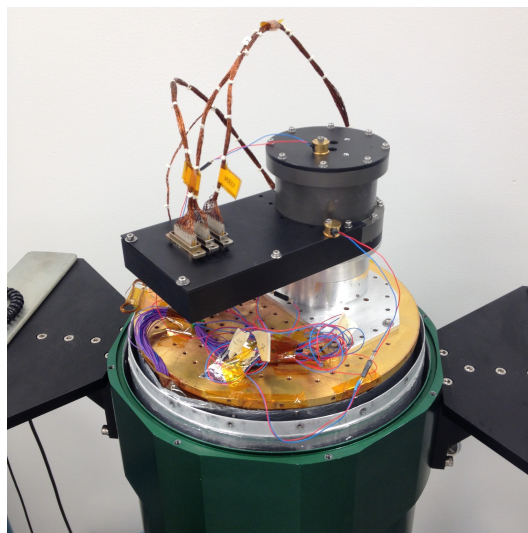
Figure 3.12: Preparation for thermal and electrical tests of the FPA.
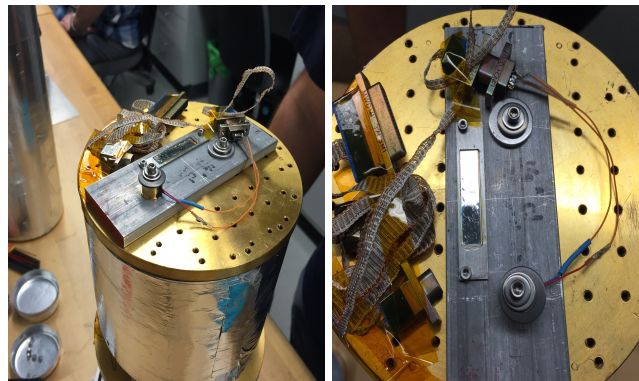
(a) Before thermal cycling. (b) After thermal cycling.

Figure 3.13: LVF mounted to cryostat work surface before and after thermal testing.

(a) Edge.   (b) Center.

Figure 3.14: Views of the LVF after thermal testing, from the metrology microscope.

have a maximum tolerance shorter than the minimum height of the filter, and the final height adjusted by the addition of shims. The shimmed filter holder is then installed over the corresponding detector mounted to a Moly standoff.

Table 3.2: Measurements to determine separation distance between detector surface and window pane filter. Science requirement is $100\mu m$ separation when cryogenically cooled, which is estimated to be 100.6 μm at room temperature.

	Predicted from CAD model [mm]	Prototype (with shims) [mm]
I. Filter Holder height	13.00	12.98 (13.093)
II. Detector height	13.0048	12.987
Separation (I-II)	-0.0048	-0.007 (+0.106)
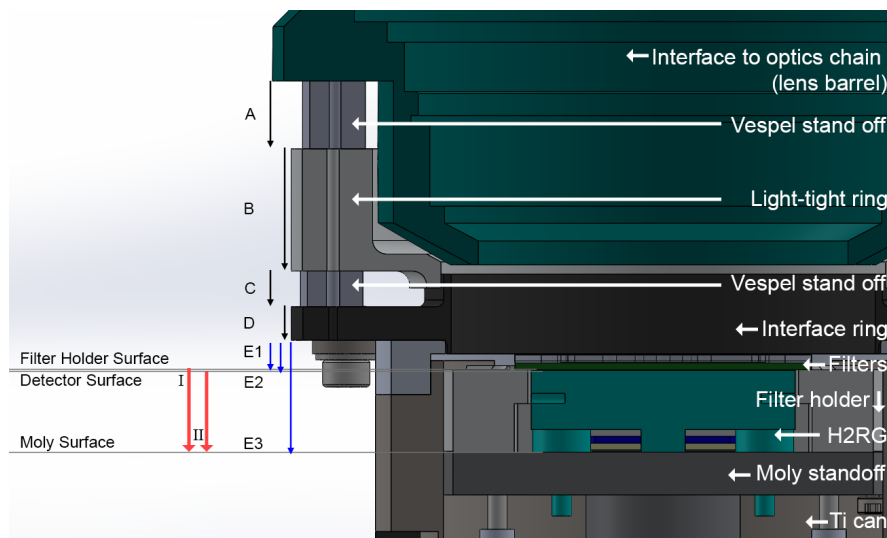
Figure 3.15: Cutaway view of CAD model of focal plane assembly, with component parts labeled. Vertical arrows indicate components measured for filter installation and focus distance.

Finally, the FPAs are assembled to accommodate the predicted focus distance for each optical arm. Precise focus position cannot be determined a priori, as final focus occurs when the experiment is cryogenically cooled. The predicted cold focus distance from the lens barrel to the surface of each detector is converted to room temperature (~300K) values. FPA components are measured individually then built up with shims to achieve the predicted warm focus distance. Component part measurements and warm predicted focus lengths are summarized in Table 3.3, corresponding to the alphabetic indices and thin black vertical arrows shown in Figure 3.15. Final focus position is achieved by the iterative cold focus test followed by warming the instrument and adjusting the fine focus of a detector by shimming as described elsewhere in this document.

FPA circuit board housing does not require precise measurement to achieve focus. However, there is some risk to electrical connection stability and circuit board integrity due to the environmental conditions imposed by the sounding rocket environment. To test this, an entire FPA assembled with the housing, circuit board, and electrical connections undergoes vibration testing. In additional to testing electrical components, this vibration testing also verifies the ability of the FPA design to keep the filters in precise alignment after thermal cycling and vibration, and to verify that the thin windowpane filter (1 mm thickness) located close to the face of the detector (100 μm above detector surface) does not make contact with the detector nor

Table 3.3: Arm-S measurements (mm) to determine focus distance.

Heights (mm)	Predicted from CAD model
A. Vespel stand off	10.0
B. Light-tight ring	18.0
C. Vespel stand off	5.25
D. Interface ring	4.93
E_1. To filter surface	4.36
E_2. To detector surface	4.458
E_3. To moly stand off	16.50
Focus distance (A+B+C+D+E_2)	42.658
Optical model predicted focus distance at 300K	42.57

fracture under stress. Electrical check out and metrology performed after thermal cycling and vibration testing increases confidence in expected FPA performance during flight and reduces risk.

3.4 NASA Sounding Rocket Testing Overview

This section describes the NASA testing required by the NASA Sounding Rocket Handbook [96]. The Handbook contains specific design requirements for experiment payloads, as NASA requires each payload to successfully complete a series of environmental tests that evaluate the ability of the experiment payload to withstand the flight environment.

The sounding rocket payload must achieve the scientific objectives of the instrument while functioning within the mechanical, electrical and environmental parameters of a sounding rocket, which are often hostile and drastically different from the controlled environments for instruments in the laboratory. To verify functioning, NASA requires integration and testing of new payloads, usually conducted at Wallops Flight Facility (WFF) in Wallops Island, Virginia.

Once a scientific instrument arrives at WFF for evaluation, the experiment payload is subject to Payload Integration. This is a complete assembly of the scientific instrument payload with all other parts of the rocket payload in launch configuration. At this time, aspects of design and operation are checked, such as mechanical fit and operation and telemetry and electrical systems operation. Sequence tests are also performed.

After successfully completing Payload Integration, the assembled payload is taken to

the Test and Evaluation (T&E) Laboratory where it is subjected to acceptance tests. Acceptance tests simulate some of the conditions the payload is likely to encounter in flight. Payload sub-systems that are required to operate in flight are demonstrated during the acceptance tests. Every system must confirm the ability to survive flight conditions through completion of its intended function. The tests include physical properties determination; magnetic calibration; and vibration, shock, structural loads (bending), spin-deployment, dynamic balancing, and vacuum testing.

Note that many of these tests focus on the entire payload and are less important to verify at the individual instrument sub assembly level (e.g. the bend test). However, a few tests, especially vacuum testing and vibration, are very important to verify for individual subassemblies and are therefore pre-tested prior to Payload Integration at WFF, as described in the previous Section.

3.4.1   Vibration Testing

Vibration testing is the process of applying a controlled amount of vibration to a test specimen, usually for the purposes of establishing reliability or testing to destruction. In practice the test article is securely mounted on a shaker table or actuator, which may be operated by electro-dynamic or hydraulic force; typically hydraulic force is used at very low frequencies because of the large displacements involved, and electro-dynamic force is used where higher frequencies are involved.

Vibration testing applies specific vibration pattern to an object under test, in order to determine reliability or functionality under such stress, or to determine at what level the object is no longer functional. The object being tested is mounted to a shaker table or actuator and the vibration is applied. The testing pattern usually attempts to mimic the actual environment in which the object will be functioning. The two main pattern sets for vibration testing are Swept-Sine and Random test patterns. In the Swept-sine approach the frequency is swept back and forth with amplitudes corresponding to the desired test levels. In Random testing the frequency spectrum of a noise source is shaped to represent the environment in which the object will operate.

Sine testing is requires the frequency to be swept back and forth between a lower limit and an upper limit at a pre-determined, logrithmic rate. The same testing profile is applied to all axes. NASA requires a sine testing sweep rate of 4 octaves per minute (meaning the frequency will double 4 times per minute of sweep while increasing and halve 4 times per minute when decreasing) where the frequency is

Table 3.4: Sine testing parameters

Mode	Acceleration	Frequency
Displacement Limit	3.84 in./s	5-24 Hz
Velocity Limit	1.53 g	24-110 Hz
Acceleration Limit	3.50 g	110-800 Hz
Acceleration Limit	10.0 g	800-2000 Hz

Table 3.5: Random testing parameters

Acceleration	Frequency	Notes
0.01 g^2/Hz	20 Hz	
0.10 g^2/Hz	1000 Hz	
0.10 g^2/Hz	1000-2000 Hz	Roll off rate of 1.8 db/oct. slope

swept according to the Test Profile in Table 3.4. The force applied is actually an acceleration, measured in units of the acceleration of gravity, g = 9.8 N/kg.

Swept-Sine testing has different modes based on the frequency of vibration. For low frequencies, the displacement is very large for a given acceleration level, often equal to the system displacement limit, and so sine testing is performed subject to displacement limits and the acceleration is instead specified as peak-to-peak displacement. Intermediate frequencies are tested at the velocity limit, constrained by the maximum output voltage of the amplifier but specified as g-force.

Random testing is not actually random, but tries to duplicate a noise output that has been spectrally-shaped to match actual conditions. The same testing profile is again applies to all axes, for a duration of 10 seconds per axis. The random vibration test profile is displayed in Table 3.5.

Subassemblies are subjected to vibration testing as needed in the laboratory environment (using private contractors) to reduce risk upon integration of the full experiment. The full experiment payload is subject to formal NASA vibration testing at Wallops Flight Facility prior to launch.

3.4.2   Other Testing

Mass properties determination includes measurement of the weight, center of gravity, roll moment of inertia, pitch, moment of inertia of the complete flight payload.

This information is provided to the NASA Guidance, Navigation, and Control group for such calculations as an updated flight trajectory. Static and Dynamic tests determine which payload configurations must be balanced in order to ensure successful completion of the scientific objectives and overall mission. If necessary, balancing weights are placed throughout the payload. Dynamic spin balance is determined by a bend test, where the tip deflection of the aft end of the payload is measured while the aft end is subjected to a predetermined load; the resulting bend measurements are included in the flight profile analysis.

Once the testing and qualification process is complete, NSROC conducts launch operations at the planned flight time and launch site. For CIBER-2, in the launch site for the first flight will be White Sands Missile Range, New Mexico. Additional Flight Plan information for CIBER-2 is described in Chapter 4.

3.5 Testing and Verification Summary

The CIBER-2 experiment payload is ready for scientific observation after verification of ability to meet the science objectives and NASA sounding rocket requirements. To verify the CIBER-2 instrument meets the science drivers outlined in Table 3.1, CIBER-2 optical testing is performed to determine the optical focus, spectral performance, diffuse source response, flat field characterization, and detector characterization. Individual subsystems within the CIBER-2 experiment are subjected to tailored testing to ensure proper function and to reduce risk upon integration. These include characterization and environmental tests. Finally, CIBER-2 must meet NASA sounding rocket environmental guidelines governing vibration and thermal response. Upon successful verification of all testing, CIBER-2 is ready for launch and scientific observations.

C h a p t e r   4

CIBER-2 IN FLIGHT

4.1 Future Rocket Payload

The NASA Sounding Rocket Program is described in Reference [96]. The Sounding Rocket program provides standardized systems for launch, payload separation, active pointing during flight, real time telemetry, and parachute recovery. CIBER-2 is designed to launch on the NASA Black Brant IX vehicle system, consisting of a Mark 70 Terrier booster stage and a Black Brant sustainer. These motors make up the aft end of the rocket. Moving forward from the motors, the entire rocket consists of a payload separation system, the CIBER-2 experiment and star tracker section that contains the CIBER-2 warm electronics (described in Chapter 2), a telemetry section, an active guidance system, an attitude control system, and finally the ogive recovery system.

4.2 Future CIBER-2 Flight Profile

The CIBER-2 launch sequence closely follows the launch sequence of CIBER-1 flights 1 through 3 [107]. The Mark 70 Terrier rocket motor burns for approximately 6 seconds for launch. This segment has guide fins that cause the rocket to spin at a rate of approximately 4 Hz, providing thrust axis stability. Once burn is complete, the motor is separated from the rest of the rocket by drag. The second stage burns for approximately 30 seconds then is ejected from the remaining rocket sections by the payload separation section. Next, cables with weighted ends are released from the payload section to reduce the spin rate of the rocket to a rate of approximately 0.5 Hz. Once the lower spin rate is achieved, the cables are released. The telescope aperture opens and observations begin. Upon completion of observations and prior to re-entry, the telescope aperture is closed. Gas expelled from the attitude control system is used to increase the rocket spin rate to approximately 1 Hz. The rocket re-enters the atmosphere and the parachute deploys when the rocket reaches a height of 16,000 feet. The payload has a velocity of approximately 30 ft/s when it collides with the ground. Recovery of the payload begins several hours after completion of flight. Payload recovery is crucial for CIBER-2, as the data collected in flight will be stored on the rocket.

CIBER-2 plans two flights in the configuration described in this work. The first

flight is planned for 2019 with the second flight to follow six months later. The flights are separated by six months for consistency checks on absolute photometry measurements with the LVF spectrometer, as the Zodiacal foreground is modulated by the Earth's annual path around the sun. Two flights will also allow for cross correlation between CIBER-2 flight data to characterize and eliminate instrumental artifacts. Additional flights are planned with different optical configurations, such as modified wavebands.

4.3 Future Observing Strategy

4.3.1 Legacy Field Observations

For flights planned to be consistent with past CIBER-1 observations, CIBER-2 will observe five fields [99]. These fields are chosen to coincide with previous absolute intensity and spatial fluctuation observations [43, 44, 16] for cross correlation and point source removal. Typical candidate fields are Bootes, North Ecliptic Pole, Lockman Hole, and ELAIS-N1.

As each detector is divided into two rectangular wavelength bands through use of a windowpane filter as described in Chapter2, CIBER-2 observes each field at two different roll angles to center each of the wavelength bands on the same patch of sky. Each wavelength band is observed for 35 seconds, so that each field has a total observation time of 70 seconds per field. This time is determined by preliminary signal calculations, which suggest this length of time is necessary to achieve the desired sensitivity for component separation, as reflected in Table 2.2. Additionally, launch windows are defined so that the sun and moon are below the depressed horizon and Earthshine is not a significant contributor of emission [99].

4.3.2 COSMOS Fields

Additional flights may utilize other observational strategies. Of particular interest is a prolonged observation of the COSMOS field, which will enable cross correlation studies of matter at well-characterized redshifts [84, 61, 49]. The CIBER-1 data suggest a bright foreground, postulated to be intrahalo light (IHL) [106], as described in Chapter 1. CIBER-2 observations designed for cross-correlating with external tracers of the low-redshift dark matter distribution, which has well-characterized redshifts, will provide evidence for the redshift of the observed CIBER-1 excess fluctuations. Positive cross-correlations with observations in any of the COSMOS redshift bins between $0.5 < z < 2.5$ would provide support for the interpretation that the observed excess emission comes from a source such as IHL, while no positive

cross-correlations with observations at $z < 2.5$ redshift intervals could suggest a different origin for this emission.

To make observations of the COSMOS field, CIBER-2 observations would involve sequential, overlapping fields of view such that each segment of the windowpane filter on each detector would view the same field through sequential, stepped observations along a strip of sky in the well-documented COSMOS field. This is demonstrated in Figure 4.1.
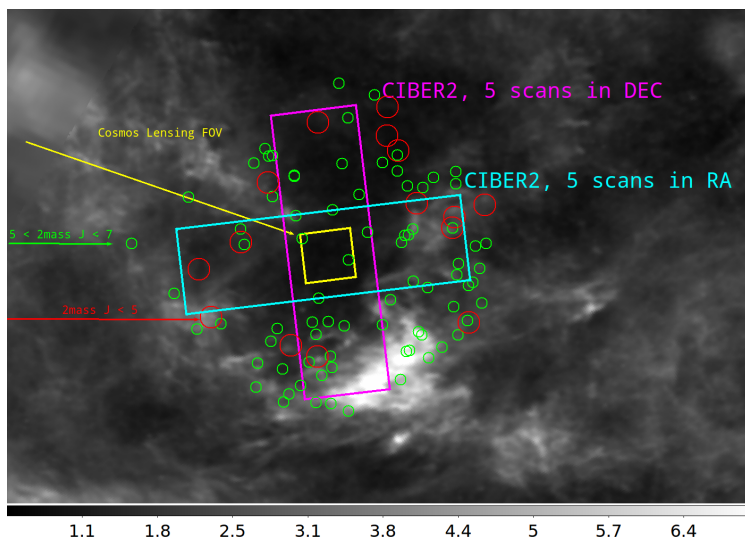
Figure 4.1: Image of COSMOS field with suggested CIBER-2 observational strips indicated as yellow and purple rectangles. These paths were selected to avoid the brightest point-sources (e.g. stars and galaxies) in the region while allowing an overlapping FOV.

4.3.3 General Observing Procedure

Per CIBER-1 data regarding atmospheric emission (airglow), observations from heights about 350 km provide the least-noisy fluctuations measurements. Thus CIBER-2 observations are planned to begin once the rocket reaches this height, at which point the rocket is oriented to the field, the shutter door opens to allow the telescope aperture an unobstructed view of the sky, the pop-up baffle extends, and data recording begins. This procedure is followed for all field observing strategies. Once the 70-second observation of a field is complete, the rocket is oriented toward the next observational field via thrusters, with some time for settling. Note that the shutter door remains open with the pop-up baffle in the extended position during reorientation of the rocket. In general, the next observation begins approximately

30 seconds after completion of the previous observation. This process repeats until observation of all fields is complete, while the rocket traces the apex portion of its trajectory. Finally, the shutter door is closed as the rocket prepares for reentry.

4.4 Preliminary Data Reduction

CIBER-2 data is processed by a custom data analysis pipeline similar to the infrastructure utilized in CIBER-1 [3, 106] and described in detail in Chapter 1 and briefly summarized here.

Although a small amount of data is telemetered down during flight, the complete data set of CIBER-2 observations is stored in a flash drive on a circuit board in the CIBER-2 experiment payload, as described in Chapter 2. The experiment payload portion of the rocket must be recovered to obtain the data by downloading it off the drive. This is data comprises the raw data in the form of photocurrent per pixel per frame for each of the three CIBER-2 detectors.

Raw data retrieved from the rocket payload is a time stream that must be converted into detector array images, separated into single-wavelength-band images (as each detector records two adjacent images with different wavelength bands) calibrated, flat-field corrected, and aligned on the sky. Pixels with poor performance are masked, as are bright astronomical sources (J-band $\sim$ 19 AB magnitude), and any residual source structure, such as diffraction spikes due to CIBER-2's secondary mirror support structures. This forms the CIBER-2 science-quality configuration-space images.

The power spectrum of a sky image is then generated. Contributions to the power spectrum from instrumental and photon noise, the beam transfer function, and the effects of mode coupling due to pixel masking are then modeled and quantified. This results in power specta for each of the CIBER-2 wavelength bands for each field observed.

As CIBER-2 observes in six spectral bands, a total of 21 auto- and cross-spectra are available for science analysis. Various contributions to the large scale EBL fluctuations will be identified from spectral decomposition of the auto- and cross-spectra. Specific results of interest are confirmation of the foreground identified in CIBER-1 to further probe the IHL interpretation. and identification of the spectral break feature that will measure the wavelength and thus constrain the redshift of reionization of the universe, and allow for constraint of emission from early, $z > 6$ galaxies.

OUTRO

The earliest galaxies in the universe are thought to be very different from galaxies formed in the last half of the lifetime of the universe, and their properties provide important constraints on our understanding of the early universe and the process of reionization. Such early galaxies are very faint due to their great cosmological distance, and are difficult to observe directly as discrete objects with current technology. Instead, the collection of photons from all such objects can be observed as a diffuse, extragalactic background. Measurements of the fluctuations of the extragalactic background provide a novel means to study these early luminous objects.

Recent advances in infrared detector technology have led to the development of CCD-like detectors for infrared imaging. These detectors have unprecedented resolution, low noise, and pixel-by-pixel readout that facilitate novel observations in the infrared waveband that complement our understanding of early galaxies, galaxy evolution, and the evolution of the large scale structure of the universe. The second Cosmic Infrared Background ExpeRiment, CIBER-2, uses one such type of detector, a 2048 x 2048 HAWAII-2RG (H2RG) HgCdTe near-IR detector array, to capture images of the diffuse extragalactic background in six optical and near-infrared wavebands.

CIBER-2 consists of a 28.5-cm Cassegrain telescope assembly, imaging optics, and cryogenics mounted aboard a sounding rocket. Images of the extragalactic background are recorded by three detector arrays at the end of an optical chain, with each detector housed in a custom Focal Plane Assembly (FPA). The large field of view and wavelength coverage of CIBER-2 makes this instrument uniquely suited to make sensitive measurements of the extragalactic background fluctuations.

The scientific motivation of CIBER-2 leads to a specific instrument design suited for fluctuation measurements from above the atmosphere. The design and development of the instrument described in this work demonstrate its readiness for comprehensive verification, where it will be tested to determine how well its performance compares to design goals. Once the optical performance is verified, CIBER-2 will undergo NASA environmental tests, and then will make observations of science fields during a short sounding rocket flight. The resulting power spectra will contribute to our knowledge of the emission of early luminous objects.

BIBLIOGRAPHY

[1]   R. Barkana and A. Loeb. "In the beginning: the first sources of light and the reionization of the universe". In: *Physics Reports* 349 (2001), 125–238.

[2]   D. Baumann et al. "Probing Inflation with CMB Polarization". In: *American Institute of Physics Conference Series*. Ed. by Dodelson, S. and Baumann, D. and Cooray, A. and Dunkley, J. and Fraisse, A. and Jackson, M. G. and Kogut, A. and Krauss, L. and Zaldarriaga, M. and Smith, K. Vol. 1141. American Institute of Physics Conference Series. 2009, pp. 10–120.

[3]   J. Bock et al. "The Cosmic Infrared Background ExpeRiment (CIBER): The Wide-Field Imagers". In: *The Astrophysical Journal Supplement Series* 207 (2013), p. 32.

[4]   N. W. Boggess et al. "The COBE mission - Its design and performance two years after launch". In: *The Astrophysical Journal* 397.420-429 (1992).

[5]   J. R. Bond, B. J. Carr, and C. J. Hogan. "Spectrum and anisotropy of the cosmic infrared background". In: *The Astrophysical Journal* 306 (1986), 428–450.

[6]   S. P. Boughn, P. R. Saulson, and J. M. Uson. "The smoothness of the 2.2 micron background - Constraints on models of primeval galaxies". In: *The Astrophysical Journal* 301 (1986), pp. 17–22.

[7]   T. D. Brandt and B. T. Draine. "The Spectrum of the Diffuse Galactic Light: The Milky Way in Scattered Light". In: *The Astrophysical Journal* 744 (2012), p. 129.

[8]   V. Bromm, P. S. Coppi, and R. B. Larson. "The Formation of the First Stars. I. The Primordial Star-forming Cloud". In: *The Astrophysical Journal* 564 (2002), 23–51.

[9]   V. Bromm and A. Loeb. "Formation of the First Supermassive Black Holes". In: *The Astrophysical Journal* 596 (2003), pp. 34–46.

[10] C. Burigana and L. Popa. "Correlation properties of the diffuse light from COBE-FIRAS maps". In: *Astronomy and Astrophysics* 334 (1998), pp. 420–426.

[11] S. M. Carroll. "Lecture Notes on General Relativity". In: *ArXiv General Relativity and Quantum Cosmology e-prints* (1997).

[12] M. Colless et al. "The 2dF Galaxy Redshift Survey". In: *Looking Deep in the Southern Sky*. Ed. by R. Morganti and W. J. Couch. 1999, p. 9.

[13] A. Cooray. "21-cm Background Anisotropies Can Discern Primordial Non-Gaussianity". In: *Physical Review Letters* 97.26 (2006).

[14] A. Cooray and R. Sheth. "Halo models of large scale structure". In: *Physics Reports* 372 (2002), pp. 1–129.

[15] A. Cooray et al. "First Star Signature in Infrared Background Anisotropies". In: *The Astrophysical Journal* 606.2 (2004).

[16] A. Cooray et al. "Near-infrared background anisotropies from diffuse intra-halo light of galaxies". In: *Nature* 494 (2012), pp. 514–517.

[17] A. Cooray et al. "The Near-infrared Background Intensity and Anisotropies during the Epoch of Reionization". In: *The Astrophysical Journal* 756 (2012), p. 15.

[18] S. Dodelson. *Modern cosmology*. Academic Press, 2003.

[19] A. Domínguez et al. "Detection of the Cosmic γ-Ray Horizon from Multiwavelength Observations of Blazars". In: *The Astrophysical Journal* 770 (2013), p. 77.

[20] DuPont. *DuPont Vespel SP-1*. Tech. rep. Du Pont, 2014.

[21] E. Dwek and R. G. Arendt. "A Tentative Detection of the Cosmic Infrared Background at 3.5 microns from COBE/DIRBE Observations". In: *The Astrophysical Journal* 508.1 (1998), pp. L9–L12.

[22] E. Dwek and R. G. Arendt. "A Tentative Detection of the Cosmic Infrared Background at 3.5 μm from COBE/DIRBE Observations". In: *The Astrophysical Journal Letters* 508 (1998), pp. L9–L12.

[23] E. Dwek and J. Slavin. "On the determination of the cosmic infrared background radiation from the high-energy spectrum of extragalactic gamma-ray sources". In: *The Astrophysical Journal* 436 (1994), 696–704.

[24] G. G. Fazio et al. "The Infrared Array Camera (IRAC) for the Spitzer Space Telescope". In: *The Astrophysical Journal Supplement* 154 (2004), pp. 10–17.

[25] E. R. Fernandez and E. Komatsu. "The Cosmic Near-Infrared Background: Remnant Light from Early Stars". In: *The Astrophysical Journal* 646.703-718 (2006).

[26] D. J. Fixsen et al. "The Spectrum of the Extragalactic Far-Infrared Background from the COBE FIRAS Observations". In: *The Astrophysical Journal* 508 (1998), pp. 123–128.

[27] J. D. Garnett and W. J. Forrest. "Multiply sampled read-limited and background-limited noise performance". In: *Proc. SPIE*. Society of Photo-Optical Instrumentation Engineers (SPIE) Conference Series 1946 (1993). Ed. by A. M. Fowler.

[28] *Germanium RTDs*. Lake Shore Cryotronics. 2017.

[29] I. S. Glass. *Handbook of Infrared Astronomy*. Ed. by R. Ellis et al. Cambridge University Press, 1999.

[30] M. G. Hauser and E. Dwek. "The Cosmic Infrared Background: Measurements and Implications". In: *Annual Review of Astronomy and Astrophysics* 39 (2001), pp. 249–307.

[31] M. G. Hauser et al. "IRAS observations of the diffuse infrared background". In: *The Astrophysical Journal Letters* 278.L15-L18 (1984).

[32] M. G. Hauser et al. "The COBE Diffuse Infrared Background Experiment Search for the Cosmic Infrared Background. I. Limits and Detections". In: *The Astrophysical Journal* 508.1 (1998), pp. 25–43.

[33] K. Helgason, M. Ricotti, and A. Kashlinsky. "Reconstructing the Near-IR Background Fluctuations from known Galaxy Populations using Multiband Measurements of Luminosity Functions". In: *The Astrophysical Journal* 752.2 (2012), p. 18.

[34] H.E.S.S. Collaboration. "Measurement of the extragalactic background light imprint on the spectra of the brightest blazars observed with H.E.S.S." In: *Astronomy and Astrophysics* 550 (2013), A4.

[35] G. Hinshaw et al. "First-Year Wilkinson Microwave Anisotropy Probe (WMAP) Observations: The Angular Power Spectrum". In: *The Astrophysical Journal Supplement* 148 (2003), 135–159.

[36] G. Hinshaw et al. "Nine-year Wilkinson Microwave Anisotropy Probe (WMAP) Observations: Cosmological Parameter Results". In: *The Astrophysical Journal Supplement* 208 (2013).

[37] N. Kaiser. "On the spatial correlations of Abell clusters". In: *The Astrophysical Journal Letters* 284 (1984), pp. L9–L12.

[38] A. Kashlinsky. "Cosmic Infrared Background and Early Galaxy Evolution". In: *Physics Reports* 409 (2005), pp. 361–438.

[39] A. Kashlinsky, J. C. Mather, and S. Odenwald. "Clustering of the Diffuse Infrared Light from the COBE DIRBE Maps: an All-Sky Survey of C(0)". In: *The Astrophysical Journal Letters* 473 (1996), L9.

[40] A. Kashlinsky and S. Odenwald. "Clustering of the Diffuse Infrared Light from the COBE DIRBE Maps. III. Power Spectrum Analysis and Excess Isotropic Component of Fluctuations". In: *The Astrophysical Journal* 528 (2000), 74–95.

[41] A. Kashlinsky et al. "Clustering of the Diffuse Infrared Light from the COBE DIRBE Maps. I. C(0) and Limits on the Near-Infrared Background". In: *The Astrophysical Journal* 470 (1996), p. 681.

[42]   A. Kashlinsky et al. "Detecting Population III Stars through Observations of Near-Infrared Cosmic Infrared Background Anisotropies". In: *The Astrophysical Journal* 608.1 (2004), pp. 1–9.

[43]   A. Kashlinsky et al. "New Measurements of Cosmic Infrared Background Fluctuations from Early Epochs". In: *The Astrophysical Journal* 654.1 (2007), pp. L5–L8.

[44]   A. Kashlinsky et al. "New Measurements of the Cosmic Infrared Background Fluctuations in Deep Spitzer/IRAC Survey Data and Their Cosmological Implications". In: *The Astrophysical Journal* 753.1 (2012).

[45]   A. Kashlinsky et al. "Tracing the first stars with cosmic infrared background fluctuations". In: *Nature* 438.7064 (2005), pp. 45–50.

[46]   M. Kawada et al. "A rocket-borne observation of the far-infrared sky at high Galactic latitude". In: *The Astrophysical Journal Letters* 425 (1994), pp. L89–L92.

[47]   T. Kelsall et al. "The COBE Diffuse Infrared Background Experiment Search for the Cosmic Infrared Background. II. Model of the Interplanetary Dust Cloud". In: *The Astrophysical Journal* 508 (1998), pp. 44–73.

[48]   T. Kelsall et al. "The COBE Diffuse Infrared Background Experiment Search for the Cosmic Infrared Background. II. Model of the Interplanetary Dust Cloud". In: *The Astrophysical Journal* 508 (1998), pp. 44–73.

[49]   A. M. Koekemoer et al. "The COSMOS Survey: Hubble Space Telescope Advanced Camera for Surveys Observations and Data Processing". In: *The Astrophysical Journal Supplement* 172 (2007), pp. 196–202.

[50]   E. Komatsu et al. "Seven-year Wilkinson Microwave Anisotropy Probe (WMAP) Observations: Cosmological Interpretation". In: *The Astrophysical Journal Supplement* 192 (2011), p. 18.

[51]   P. M. Korngut et al. "The Cosmic Infrared Background ExpeRiment (CIBER): the Narrow Band Spectrometer". In: *The Astrophysical Journal Supplement Series* 207 (2013), p. 34.

[52]   G. Lagache and J. L. Puget. "Detection of the extra-Galactic background fluctuations at 170 mum". In: *Astronomy and Astrophysics* 355 (2000), pp. 17–22.

[53]   G. Lagache et al. "First detection of the warm ionised medium dust emission. Implication for the cosmic far-infrared background". In: *Astronomy and Astrophysics* 344 (1999), 322–332.

[54]   G. Lagache et al. "The Extragalactic Background and Its Fluctuations in the Far-Infrared Wavelengths". In: *ISO Survey of a Dusty Universe*. Ed. by D. Lemke, M. Stickel, and K. Wilke. Vol. 548. Lecture Notes in Physics, Berlin Springer Verlag. 2000, p. 81.

[55] A. Lanz et al. "Studying extragalactic background fluctuations with the Cosmic Infrared Background ExpeRiment 2 (CIBER-2)". In: *Space Telescopes and Instrumentation 2016: Optical, Infrared, and Millimeter Wave*. Vol. 9143. Proc. SPIE. 2014, 91433N.

[56] R. B. Larson. "The Stellar Initial Mass Function and Beyond (Invited Review)". In: *Galactic Star Formation Across the Stellar Mass Spectrum*. Ed. by J. M. De Buizer and N. S. van der Bliek. Vol. 287. Astronomical Society of the Pacific Conference Series. 2003, 65–80.

[57] A. Lawrence et al. "The UKIRT Infrared Deep Sky Survey (UKIDSS)". In: *Monthly Notice of the Royal Astronomical Society* 379 (2007), 1599–1617.

[58] J.H. Lienhard IV and J.H. Lienhard V. *A Heat Transfer Textbook*. Cambridge, MA: Phlogiston Press, 2017.

[59] P. Madau and M. Dickinson. "Cosmic Star-Formation History". In: *Annual Review of Astronomy and Astrophysics* 52 (2014), 415–486.

[60] P. Madau and J. Silk. "Population III and the near-infrared background excess". In: *Monthly Notices of the Royal Astronomical Society: Letters* 359.1 (2005).

[61] R. Massey et al. "Dark matter maps reveal cosmic scaffolding". In: *Nature* 445 (2007), pp. 286–290.

[62] J. C. Mather, D. J. Fixsen, and R. A. Shafer. "Design for the COBE far-infrared absolute spectrophotometer (FIRAS)". In: *Infrared Spaceborne Remote Sensing*. Ed. by M. S. Scholl. Vol. 2019. Proc. SPIE. 1993, 168–179.

[63] H. Matsuhara et al. "ISO deep far-infrared survey in the "Lockman Hole". II. Power spectrum analysis: evidence of a strong evolution in number counts". In: *Astronomy and Astrophysics* 361 (2000), pp. 407–414.

[64] T. Matsumoto, M. Akiba, and H. Murakami. "A search for the near-infrared extragalactic background light". In: *The Astrophysical Journal* 332 (1988), pp. 575–595.

[65] T. Matsumoto et al. 2000, in preparation.

[66] T. Matsumoto et al. "AKARI Observation of the Fluctuation of the Near-infrared Background". In: *The Astrophysical Journal* 742.2 (2011).

[67] T. Matsumoto et al. "Infrared Telescope in Space Observations of the Near-Infrared Extragalactic Background Light". In: *The Astrophysical Journal* 626.1 (2005), pp. 31–43.

[68] T. Matsumoto et al. "The submillimeter spectrum of the cosmic background radiation". In: *The Astrophysical Journal* 329.567-571 (1988).

[69] S. Matsuura et al. "A rocket-borne observation of the near-infrared sky brightness". In: *Publications of the Astronomical Society of the Pacific* 106 (1994), pp. 770–779.

[70] S. Matsuura et al. "Detection of the Cosmic Far-infrared Background in AKARI Deep Field South". In: *The Astrophysical Journal* 737.1 (2011).

[71] H. J. Mo and S. D. M. White. "An analytic model for the spatial clustering of dark matter haloes". In: *Monthly Notice of the Royal Astronomical Society* 282 (1996), pp. 347–361.

[72] *Model 218 Temperature Monitor*. Rev 2.5. Lake Shore Cryotronics. 2012.

[73] S. H. Moseley et al. "Reducing the read noise of H2RG detector arrays: eliminating correlated noise with efficient use of reference signals". In: *Proc. SPIE* 7742 (2010).

[74] P. F. Muciaccia, P. Natoli, and N. Vittorio. "Fast Spherical Harmonic Analysis: A Quick Algorithm for Generating and/or Inverting Full-Sky, High-Resolution Cosmic Microwave Background Anisotropy Maps". In: *The Astrophysical Journal Letters* 488 (1997), pp. L63–L66.

[75] T. L. Murdock and S. D. Price. "Infrared measurements of zodiacal light". In: *The Astronomical Journal* 90 (1985), 375–386.

[76] J. F. Navarro, C. S. Frenk, and S. D. M. White. "The Structure of Cold Dark Matter Halos". In: *The Astrophysical Journal* 462 (1996), p. 563.

[77] G. Neugebauer et al. "The Infrared Astronomical Satellite (IRAS) mission". In: *The Astrophysical Journal Letters* 278 (1984), L1–L6.

[78] M. Noda et al. "Rocket observation of the near-infrared spectrum of the sky". In: *The Astrophysical Journal* 391 (1992), pp. 456–465.

[79] *Parker O-Ring Handbook*. Parker Hannifin Corporation. Cleveland, OH, 2007.

[80] R. B. Partridge and P. J. E. Peebles. "Are Young Galaxies Visible?" In: *The Astrophysical Journal* 147 (1967), p. 868.

[81] P. J. E. Peebles. *Principles of Physical Cosmology*. Princeton University Press, 1993.

[82] P. J. E. Peebles. "The Nature of the Distribution of Galaxies". In: *Astronomy and Astrophysics* 32 (1974), p. 197.

[83] Planck Collaboration et al. "Planck 2013 results. XXIV. Constraints on primordial non-Gaussianity". In: *Astronomy and Astrophysics* 571 (2014), A24.

[84] M. Postman et al. "The Cluster Lensing and Supernova Survey with Hubble: An Overview". In: *The Astrophysical Journal Supplement* 199 (2012), p. 25.

[85] J.-L. Puget et al. "Tentative detection of a cosmic far-infrared background with COBE." In: *Astronomy and Astrophysics* 308 (1996), p. L5.

[86] M. Punch et al. "Detection of TeV photons from the active galaxy Markarian 421". In: *Nature* 358 (1992), p. 477.

[87]   M. R. Santos, V. Bromm, and M. Kamionkowski. "The contribution of the first stars to the cosmic infrared background". In: *Monthly Notice of the Royal Astronomical Society* 336 (2002), 1082–1092.

[88]   D. J. Schroeder. *Astronomical optics*. 2nd ed. Academic Press, Inc, 2000.

[89]   Teledyne Imaging Sensors. *Teledyne Imaging Sensors HAWAII-2RG Visible and Infrared Focal Plane Array*. Brochure.

[90]   S. Serjeant. *Observational Cosmology*. Cambridge University Press, 2010.

[91]   S. A. Shectman. "Clusters of galaxies and the cosmic light". PhD thesis. California Institute of Technology, 1974.

[92]   M. B. Silva et al. "Intensity Mapping of Lyα Emission during the Epoch of Reionization". In: *The Astrophysical Journal* 763 (2013), p. 132.

[93]   R. F. Silverberg et al. "Design of the diffuse infrared background experiment (DIRBE) on COBE". In: *Infrared Spaceborne Remote Sensing*. Ed. by M. S. Scholl. Proc. SPIE. 1993, pp. 180–189.

[94]   M. F. Skrutskie et al. "The Two Micron All Sky Survey (2MASS)". In: *The Astrophysical Journal* 131.2006 (), 1163–1183.

[95]   I. S. Sullivan. "CIBER: A Near-Infrared Probe of the Epoch of Reionization". PhD thesis. California Institute of Technology, 2011.

[96]   *The NASA Sounding Rocket Program Handbook*. NASA Sounding Rockets Program Office.

[97]   R. I. Thompson et al. "Constraints on the Cosmic Near-Infrared Background Excess from NICMOS Deep Field Observations". In: *The Astrophysical Journal* 657 (2007), 669–680.

[98]   M. Trodden and S. M. Carroll. "TASI Lectures: Introduction to Cosmology". In: *ArXiv Astrophysics e-prints* (2004).

[99]   K. Tsumura et al. "Observations of the Near-infrared Spectrum of the Zodiacal Light with CIBER". In: *The Astrophysical Journal* 719 (2010), pp. 394–402.

[100]   K. Tsumura et al. "The Cosmic Infrared Background ExpeRiment (CIBER): The Low Resolution Spectrometer". In: *The Astrophysical Journal Supplement Series* 207 (2012), p. 33.

[101]   J. G. Weisend. *Handbook of cryogenic engineering / edited by J.G. Weisend II*. Philadelphia, PA : Taylor and Francis, 1998.

[102]   E. L. Wright. "Angular Power Spectra of the COBE DIRBE Maps". In: *The Astrophysical Journal* 496 (1998), pp. 1–8.

[103]   E. L. Wright. "DIRBE minus 2MASS: Confirming the Cosmic Infrared Background at 2.2 Microns". In: *The Astrophysical Journal* 553 (2001), pp. 538–544.

[104]   D. G. York and SDSS Collaboration. "The Sloan Digital Sky Survey: Technical Summary". In: *The Astrophysical Journal* 120 (2000), 1579–1587.

[105]   B. Yue et al. "Infrared background signatures of the first black holes". In: *Monthly Notices of the Royal Astronomical Society: Letters* 433 (2013), pp. 1556–1566.

[106]   M. Zemcov et al. "On the origin of near-infrared extragalactic background light anisotropy". In: *Science* 346 (2014), pp. 732–735.

[107]   M. Zemcov et al. "The Cosmic Infrared Background ExpeRiment (CIBER): A Sounding Rocket Payload to Study the Near Infrared Extragalactic Background Light". In: *The Astrophysical Journal Supplement Series* 207 (2013), p. 31.

[108]   A. R. Zentner et al. "The Physics of Galaxy Clustering. I. A Model for Subhalo Populations". In: *The Astrophysical Journal* 624 (2005), 505–525.

A p p e n d i x   A

DETAILED CIBER-2 DESIGN

A.1 Introduction

CIBER-2 is designed to measure spatial fluctuations in the extragalactic background light with a rocket-borne, multi-band, infrared instrument. This appendix complements the design overview provided in Chapter 2. Additional detail of most mechanical subassemblies is provided. Note that there is some duplication of information from Chapter 2 for completeness.

A.1.0.1 Sounding Rocket Environment Constraints

Preliminary design selections to satisfy science drivers described in Chapter 2 bring additional requirements that apply to all components of the CIBER-2 experiment payload. Specifically, selection of a sounding rocket vehicle to satisfy the science driver to avoid ground-based foregrounds brings a host of environment requirements regarding size, weight, and vibration as specified by NASA. Also, selection of infrared detectors to satisfy the science driver to observe the reionization signature in observed galactic spectra requires the use of liquid nitrogen to keep the detector noise low enough to satisfy the sensitivity requirements. The sounding rocket and cryogenic environments apply to most CIBER-2 mechanical subsystems.

Sounding rockets have limited spatial volumes and strict weight requirements. Additionally, sounding rockets are subject to harsh environments upon launch, with high levels of vibration, variations in external temperature, and potential for electronic surges. NASA requires all sounding rocket payloads to pass stringent vibration tests, as outlined in the NASA Sounding Rocket Handbook [96]. Robust subsystem development processes include subjecting individual subsystems to tests at the levels required of the overall experiment.

A.1.0.2 Cryogenic Environment Constraints

Cryogenic environments impose additional considerations on imaging systems [101]. Low temperature environments change the thermal, electrical, and mechanical properties of many materials, and cause many non-metal materials to become brittle and outgas. As such, metals are used as much as possible, and use of plastics, fiberglass,

epoxies, and other common materials is minimized. Low temperatures also cause metals to decrease in size, on the order of one part in a million (1×10^{-6}), with the exact factor determined by the coefficient of thermal expansion (discussed in more detail in Chapter 2). Design at both cryogenic temperatures of 77 K and room temperature of 300 K must be considered, as well as the transition period during temperature change where dissimilarities of coefficients of thermal expansion of materials have the most impact.

A.1.1 CIBER-2 Payload Overview

CIBER-2 is a wide field, degree-scale camera in a sounding rocket payload specifically designed for EBL spatial fluctuations measurements in six near-infrared and optical wavelength bands. The basic design of CIBER-2 is illustrated in Figure A.1. CIBER-2 consists of an evacuated, cryogenic sounding rocket envelope within which is contained a telescope assembly, imaging optics and detectors, and a cryogenic system. Additional electronics are contained in an adjacent section of the sounding rocket. These subassemblies are described in detail below.

A.2 Sounding Rocket Envelope

The CIBER-2 sounding rocket has a fixed diameter within which the instrument payload must fit. The telescope assembly, imaging optics, and cryostat are housed in an evacuated segment of the rocket. This payload section is capped at the aft end of the rocket, toward the motors, by a door that opens to the telescope aperture. The opposing end of this payload section is capped with a vacuum bulkhead with hermetic cutouts for wires, vacuum equipment, and cryostat fill lines.

A.2.1 Skin

The CIBER-2 experiment payload is housed in a cylindrical skin provided by the NASA Sounding Rocket Program (NSRP), with modifications specific to the CIBER-2 project. The skin has an outer diameter of 17.26 inch (438.4 mm) and is 0.25 inches (6.35 mm) thick in most places for an internal diameter 17.01 inches (432 mm) [96]. The skin length is specified by the experiment, and for CIBER-2 is 48.47 inches (1231 mm). Each end has specialized flanges for mating to hermetic bulkheads and an opening of fixed diameter, which sets the maximum outer diameter of the experiment to be inserted into the skin. The fore end aperture is 16.26 inches (413 mm) in diameter, setting the maximum CIBER-2 experiment payload outer diameter to 16.22 inches (412 mm). The fabricated CIBER-2 skin is pictured in
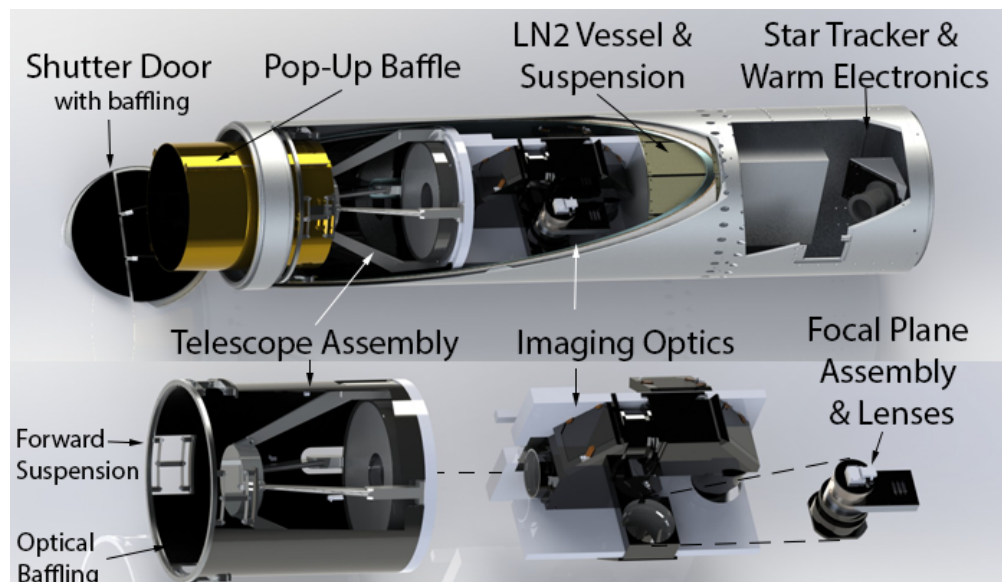
Figure A.1: Solid model of the CIBER-2 instrument. A 28.5 cm Cassegrain telescope directs light into the imaging optics, where beam splitters divide the light into three optical paths. Each optical path travels to one of three focal plane assemblies, where a broadband filter subdivides the light into two wavelength bands which are both recorded by a single detector array for a total of six band. A small segment of each detector array is also covered linear-variable filter. The imaging optics are mounted to an optical bench that connects the Cassegrain telescope assembly to a liquid nitrogen cryostat. Radiative shielding is provided by a radiatively-cooled door liner and cryogenically-cooled pop-up baffle that extends during observations. A section forward of the instrument section contains an electronics box and a star tracker.

Figure A.2.

In addition to these standard features, the CIBER-2 skin also has an internal support rib to provide additional structural support to compensate for the length. This rib is located near the middle of the skin length and has a diameter slightly larger than the fore aperture diameter so as not to obstruct the experiment payload. The rib also has a cutout, or flanged portion back to the internal skin surface, to allow for passage of the thick, 12-gauge wires that extend to the aft shutter door for shutter door power and motion control.

A.2.2   Shutter Door

An electrically operated vacuum shutter door is provided by NSRP to fit to the skin. The shutter door opens an aperture of approximately 15 inches diameter at
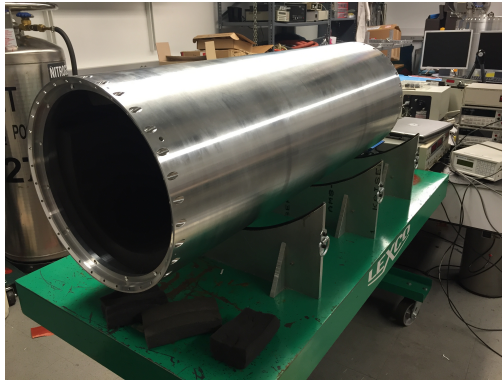
Figure A.2: CIBER-2 skin, prior to experiment payload insertion.

the aft end of the payload. The shutter door is operated to open when the rocket is above the atmosphere, and to close again before atmospheric re-entry, while maintaining a vacuum tight seal during re-entry. Due to this electronic control, the flight configuration of the door includes a wiring harness, hermetic seal, and motor mechanism. The lab configuration of the door includes an external control box with switches to control opening and closing of the shutter door. This external control box requires an external power supply for operation. The shutter door is added to the payload after the experiment is inserted into the skin, usually as the last step in assembly prior to testing or flight.
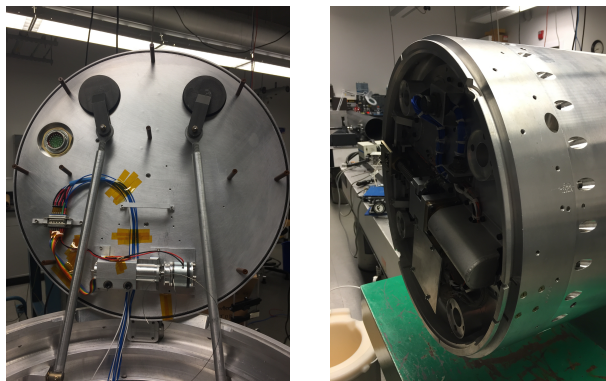
Figure A.3: Shutter door, in open and closed positions. In-flight control wiring not shown in the open position (lab operation utilizes external power source). Additional wiring and motor mechanism on lower half of door panel for pop-up baffle control. Mechanisms for opening and closing the shutter doors visible on the outside of the door in closed position.

Along with the skin, the shutter door heats up as it travels through the atmosphere. It radiates this heat once it leaves the atmosphere and begins cooling. This radiation is

emitted in the infrared range and could be picked up by the detectors, adding noise to the science observations. To minimize this, an anti-reflective shield of anodized Al 6061-TS is stood off from the face of the open shutter door with thermally-isolating Vespel cylinders [20]. This radiation shield emits less heat into the optical path and redirects the bulk of the cooling radiation from the shutter door. The Vespel supports can be seen as gray posts on the face of the open door in the left panel of Figure A.3. These cylinders are affixed to the face of the door with screws. The panel mounts to the shield with screws that thread into the other end of the Vespel posts. The outer radius and cutout of the shield is selected to not interfere with the shutter door opening upon movement, and to clear the pop-up control mechanisms. The height of the Vespel posts is set by the arms that control the shutter door motion and the height of the pop-up control mechanisms, while being not so tall as to make contact with any elements inside the experiment payload when in the closed position.

The shutter door is designed to hold vacuum, as the experiment is evacuated prior to launch. Once the experiment is above the atmosphere in the vacuum of low space, the shutter door is opened for science observations. After all observations, the shutter door is closed prior to atmospheric re-entry.

A.2.3   Bulkhead

An additional vacuum bulkhead is provided by NSRP to cap the fore end of the cryogenic portion of the experiment payload. The AL 6061-TS bulkhead, shown in Figure A.4, has special joints to mate to the rocket skin. The other bulkhead interface is similarly designed to mate with another skin segment that is part of the overall rocket envelope supporting CIBER-2 in flight.

NSRP allows cutouts and other details such as threads to be added to the bulkhead per customer request. The CIBER-2 bulkhead has cutouts for many hermetic connectors, along with accompanying O-ring [79] recesses cut directly into the fore face of the bulkhead[1]. The bulkhead also has cutouts to accommodate the cryostat fill tubes and the vacuum port and O-ring groove. These cutouts are described in Figure A.4b. The fore face of the bulkhead also has screw threading for mounting the housing that will contain the readout and housekeeping electronics, whose rectangular footprint is visible in Figure A.5. The aft face has a raised hexagonal structure with screw holes for mounting the cryostat support structures (visible in Figure A.4b). The aft

---

[1]The size of the O-ring is determined by the associated through-hole. The recesses for the O-rings have dimensions and surface roughnesses required for the O-ring size.
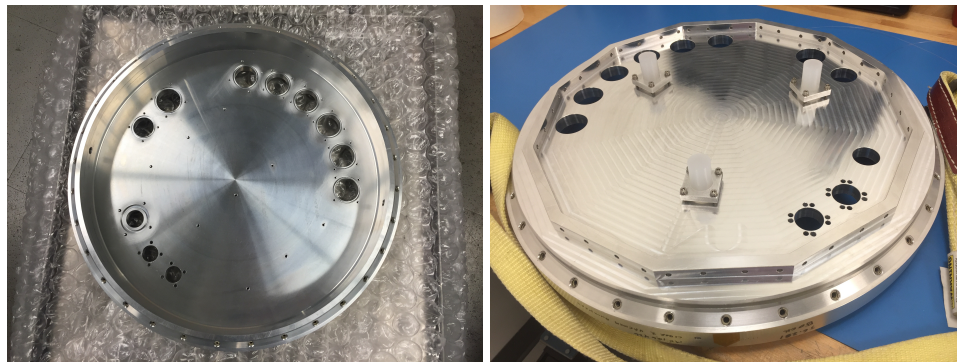
(a) Fore face of bulkhead, toward warm
section.

(b) Aft face of bulkhead, toward evacu-
ated experiment payload section.

Figure A.4: Two views of aft vacuum bulkhead.

face also has 3 sets of 4 threaded screw holes for mounting compressible, shock-absorbing, silicone cylinders that sit under the cryostat.
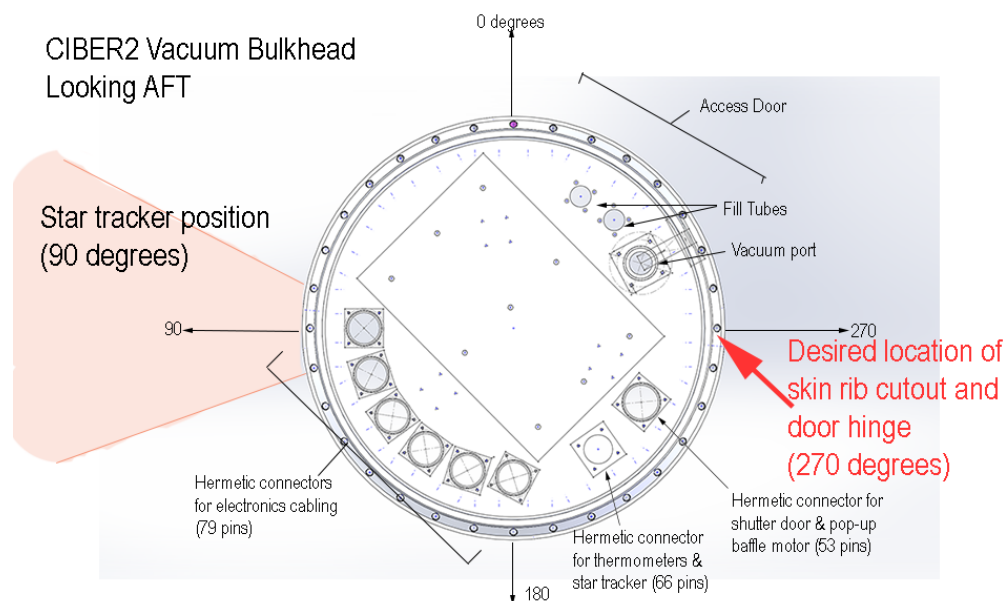
Figure A.5: Vacuum bulkhead, looking aft down rocket skin. Warm section not shown. Hermetic connectors into evacuated section shown with labels. The rotated rectangle represents the footprint of the warm electronics box.

Unfortunately, NSRP provided a bulkhead with cutouts that did not match the requested specifications, and so some additional machining was needed to compensate. Specifically, the clocking for the mounting screws of the cryostat fill ports was incorrect, and required machining of a new set of threaded holes with the correct

clocking, as can be seen in Figure A.6. The corrected bulkhead is also visible in the right hand panel of Figure fig:bulkhead, as there are double sets of screw holes around these cutouts. As the hole threads are *inside* the O-ring seal of the cryostat tubes, the unfilled incorrect holes do not break the vacuum seal. Also, one of the hermetic connectors was machined to a too-large size, and so a conversion plate with an O-ring groove was made to correct this (not shown).

Figure A.6: Corrected clocking of the fore bulkhead cryostat fill tube mounting holes. Here, the cryostat fill tubes were successfully installed.

The vacuum bulkhead also has a custom set of blanks for all hermetic connections, so that the rocket can be cooled and evacuated with no hermetic connections. Hermetic connections can be added as desired for various testing configurations. A few configurations are shown in Figure A.7.
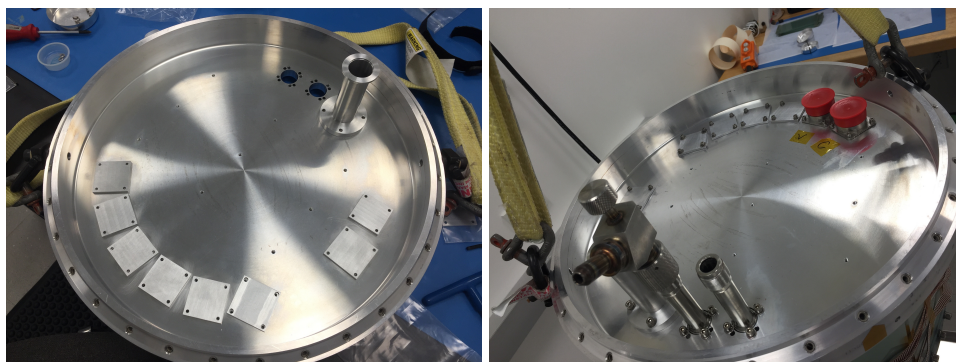
(a) Bulkhead with all hermetic blanks and vacuum port installed, prior to cryogenic fill line installation (open holes).

(b) Bulkhead with some hermetic blanks, 2 hermetic connectors (red caps), vacuum port, and cryogenic fill tubes.

Figure A.7: Aft vacuum bulkhead in various configurations.

A.3 Telescope Assembly

The CIBER-2 Telescope Assembly consists of the Cassegrain mirrors, support structures and radiation-blocking baffles. The CIBER-2 Cassegrain telescope has a 28.5 cm primary mirror and 14 cm secondary mirror. The primary mirror is attached to a support plate with flexures. The secondary mirror is held up by a support spider that mounts to the support plate. A cylindrical optical baffle that provides both structural support and light blocking is also attached to the support plate. Titanium flexures fix the optical baffle to a mounting ring that is attached directly to the rocket skin. These flexures relieve mechanical stress and provide a thermal break between the rocket skin and the telescope assembly. A pop-up baffle extends upon deployment to block stray light from the skin and open shutter door. An electromagnetic optical shutter is attached to the underside of the telescope support plate for calibration of light levels. Additionally, other calibration lamps are placed behind the secondary mirror.

A.3.1 Interface to Rocket Skin

The CIBER-2 experiment payload interfaces to the NSRP rocket skin at fore and aft ends. At the aft end, the experiment the Telescope assembly interface with the skin via a ring that mounts directly to the underside of the inner lip of the skin. Shock absorbing and thermally isolating titanium flexures mount to this ring and attach to the optical baffle, a main structural component of the telescope. At the fore end, the experiment is mounted to the vacuum bulkhead using thermally insulating pieces of G-10 fiberglass that mount the cryostat directly to the bulkhead, as described in more detail in Section A.

The AL 6061-TS "skin ring" and flexures are designed to allow the experiment payload to absorb the shock that occurs upon contact with the ground when the sounding rocket returns. Experience with CIBER-1 suggests this ring may become misshapen upon re-entry, necessitating the use of an easily replaceable ring rather than mounting the flexures directly to the rocket skin. This ring also facilitates easier installation of the experiment into the skin, as it is more convenient to guide a ring through the narrow skin opening than unattached sets of flexures. The ring is shown attached to the flexures at the bottom of Figure A.8b.

Three sets of titanium flexures interface between the skin ring and the optical baffle. Each consists of four titanium short legs, mounted onto triangles to form a diamond shape. The top and bottom ends of the diamond shape mount to fixtures that attach

to the interface pieces. The diamond is slightly curved to match the radius of the rocket. An individual flexure and the set of three flexures can be seen in Figure A.8.
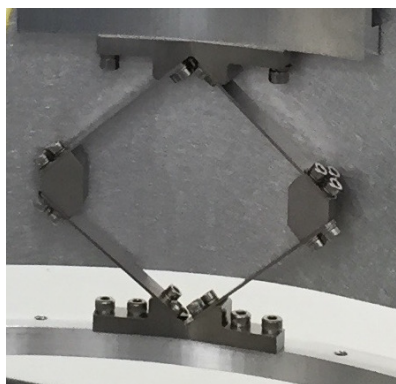
(a) Titanium flexures.

(b) Flexures in an intermediate stage of CIBER-2 assembly. The skin ring is visible at the bottom of the image.

Figure A.8: Titanium flexures, close up and in the CIBER-2 assembly.

The flexures provide compressibility in the direction along the rocket skin. This is necessary for the overall experiment to have a mechanism to accommodate the change in size that occurs with metal pieces cooled to cryogenic temperatures, as well as to absorb shocks that occur during landing. These requirements guided the detailed design of the flexures.

The flexures also provide a thermal break between the rocket skin and cryogenic experiment payload. Although some heat is transferred from the skin to the skin ring and into the flexures, the amount of surface area in contact between each set of pieces of the assembly is very small, minimizing conductive heat transfer. Additionally, the coefficient of thermal conductivity is moderate for titanium, further reducing heat transfer[2].

A.3.2 Cassegrain Optical Design

CIBER-2 is designed around the maximum optics that would fit within the rocket skin. Using a common light source and dividing the beam among multiple detectors is very different than in CIBER-1, where the rocket skin housed four independent instruments sharing only structural supports and a cryostat [107]. A single telescope in the rocket skin allows much greater photon collection, which is used for our science purposes to increase sensitivity rather than resolution (as is usually the drive

---

[2]Considerations of thermal heat transfer are described in Chapter 2.

behind larger apertures). CIBER-2 balances its resolution with the science driver of keeping foreground galaxies much smaller than a single pixel on the detectors to aid the masking of these foreground galaxies for power spectra analysis. Instead, we utilize the larger aperture to increase sensitivity, allowing for deeper sky images to be taken in exposure times similar to CIBER-1. This is outlined in the sensitivity calculation in Section A.

The CIBER-2 Cassegrain telescope has a 28.5 cm primary mirror and 14 cm secondary mirror. The primary mirror is attached to a support plate ("baseplate") with flexures designed to absorb thermal and mechanical stresses while maintaining alignment. The secondary mirror is suspended over the primary mirror by four supporting legs in the traditional spider arrangement. These spiders also mount to the telescope baseplate. Light passes through a central hole in the baseplate to the rest of the optical chain.

The telescope baseplate acts a dividing interface between the aft telescope assembly and the fore optical chain. The primary mirror, secondary mirror support spiders, and optical baffle mount to the aft face of the baseplate. The interface holes and recesses for the primary mirror flexures can be seen in Figure A.9a. The optical bench, optical shutter, and cold star tracker mount to the fore face of the baseplate. The recess for the optical shutter can be seen in Figure A.9b. The baseplate is also an ideal mechanical part to provide intermediate support for the radiation shield that extends most of the length of the skin and encloses the experiment payload in two half-cylinders of Al 1100. The cylindrical face of the telescope baseplate contains threaded holes for T-shaped G10 mounts that provide a thermal break between the radiation shield and the cryogenically-cooled telescope baseplate.

A.3.3 Optical Baffle

The optical baffle is designed to be the main supporting structure of the telescope assembly. It interfaces between the telescope baseplate and the titanium support flexures. It also provides light blocking functionality. The overall design is a cylinder of Al 6061-TS with cutouts and other modifications for various interfaces, shown in Figure A.10a.

Instead of mounting to the top of the optical baffle, the titanium flexures mount to ribbed cutouts on the optical baffle, shaped as three square cutouts in the aft end of the baffle. The fore end of the optical baffle has a lip for mounting to the telescope baseplate. Four arched cutouts allow additional space for the legs of the spider
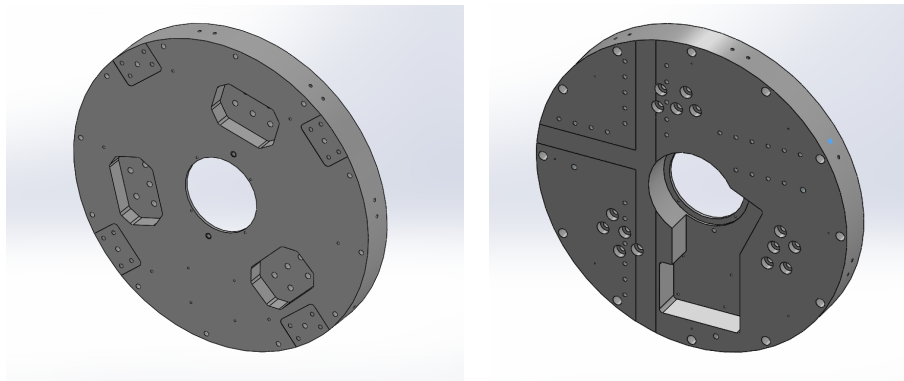
(a) Aft face of telescope baseplate, to which the primary mirror attaches.

(b) Fore face of telescope baseplate, to which the optical bench attaches.

Figure A.9: The telescope baseplate is the support plate for the primary and secondary mirrors. On the aft side it attaches to the fixed optical baffle, and on the fore side it mates with the optical bench.

supports of the secondary mirror.

Additionally, the optical baffle serves as the aft anchor point of the radiation shield. The outer surface of the optical baffle is studded with threaded holes for mounting G10 supports that provide thermal breaks between the radiation shield and the optical baffle. Finally, the set of three stabilizing rods of the pop-up baffle thread into three holes distributed around the fore lip of the baseplate.

A.3.4   Pop-up Baffle

Heat from the rocket skin is radiated into the optical path, in the same infrared waveband as the science observations. Much of the radiation from the inside cylinder of the skin is blocked by the internal radiation shield. However, the radiation from the lip of the rocket skin and from the shutter door is not blocked by the internal radiation shield, and can enter the light path, potentially overwhelming the faint EBL signal CIBER-2 will observe. A solution is required to provide the necessary light blocking, while not interfering with the telescope light cone. A cylinder that can extend above the rocket skin is a natural solution.

The pop-up baffle is designed to block all stray light that can enter the light path. To this end, the cylinder is designed to impede emission from the skin lip and the open shutter door. It must be smaller than the lip of the rocket skin so as to be deployable. It is thin radially so as to not interfere with the light path. It is long enough to block light that would travel from the top of the shutter door to the support spider at the

(a) Isometric view of the cylindrical optical baffle.

(b) View of the fore lip of the optical baffle that mounts to Ti flexures. 3 cutouts for the Ti flexures are visible as thinner rectangular cutouts.

(c) View of the aft lip of the optical baffle that mounts to the telescope baseplate. 4 cutouts for the support spiders are visible as thinner rectangular cutouts.
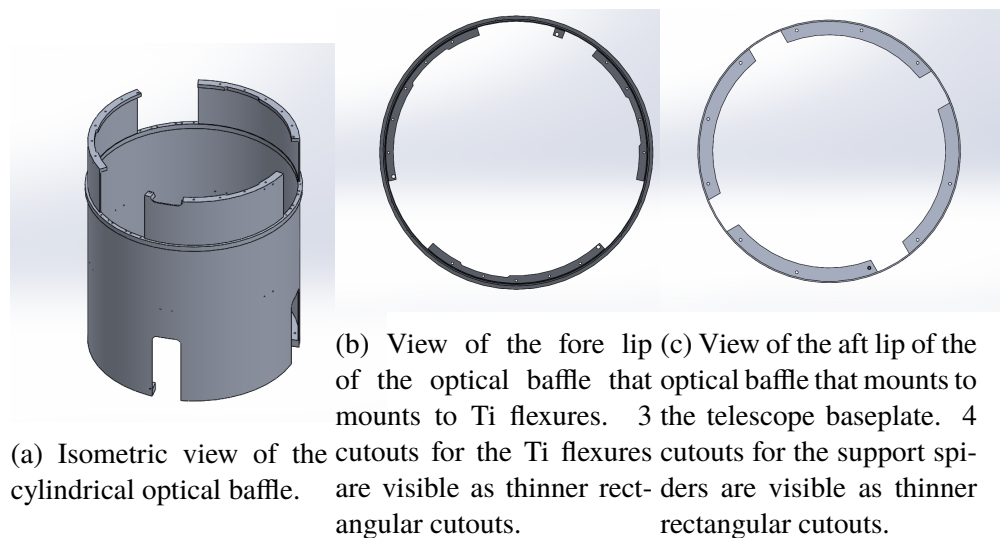
Figure A.10: Fixed baffle design. The fixed baffle is a cylindrical optical baffle that provides both structural support and light blocking. It interfaces between the titanium flexures and the support plate for the telescope mirrors.

aft end while still blocking the lip of the skin at the fore end, as illustrated in Figure A.11. However, the baffle cannot have this full height at all times, as the shutter door would not be able to close and vacuum could not be achieved. Thus a design that fits entirely within the closed rocket is required, suggesting a deployable solution that can be stowed inside the rocket with a closed shutter door then ascend to the desired height for observations. At the fore end, light from the skin lip must be blocked, so the location of the deployed position is chosen to overlap with the fixed optical baffle, also shielding the flexure mounting cutouts on the optical baffle. A cylinder with radial thickness of 0.079 inches (2 mm) and a height of 17.13 inches (435 mm) forms the basic design.

While the pop-up baffle is required for flight, it is not required for lab testing and calibration of the experiment payload. These tests also require other components that are incompatible with the pop-up baffle. This suggests design of a pop-up baffle assembly as a stand-alone unit that is easily removed to prepare the experiment payload for the lab testing configuration and easily installed to prepare the flight configuration.

A ring and rod assembly interfaces the pop-up baffle to other components in the experiment payload. The basic cylindrical design of the pop-up baffle is augmented with 3 sets of tabs at the fore and aft edges of the cylinder, through which 3 sets of rods
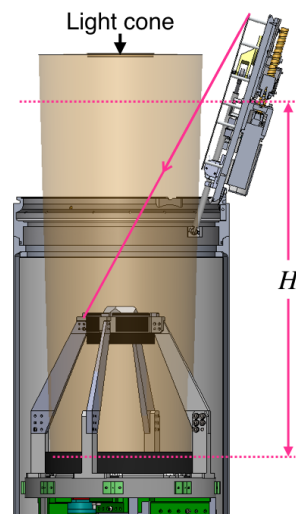
Figure A.11: Pop-up baffle design constraints: The pop-up baffle must avoid the optical light cone for CIBER-2 observations (brown) while blocking radiation emitted by the shutter door. The intersection of the light cone and ray trace of radiation from the top of the shutter door into the light path, marked as the upper horizontal dotted line, determines the maximum height needed for the baffle. The absolute lowest allowed stowed position of the baffle is indicated by the lower dotted line.

travel to extend and retract the baffle. These rods are also threaded though an external ring that in turn mounts to the aft lip of the fixed optical baffle, providing the main interface surface for the pop-up baffle. Extensive prototype testing demonstrated that in the lab test environment, where the experiment payload is on its side and gravity is a dominant force, the pop-up baffle tends to have alignment issues during test deployment and retraction. To resolve this, a second set of rods on the fore end of the baffle is added for guidance, with an additional set of 3 tabs at the fore end of the baffle and aligned threaded holes added for these rods in the bottom lip of the fixed optical baffle. The two sets of rods can be seen in different colors in Figure 2.15, with blue deployment rods and pink stationary guidance rods.

The length of the pop-up baffle is problematic when stowed, as it interferes with the legs of the support spider that hold up the secondary mirror. Cutouts are added to the fore end of the pop-up baffle to accommodate the spider supports. The stowed and extended positions are shown in Figure A.12.

Several prototypes were developed and tested before settling on the final design shown in Figure A.12. Prototype testing is described in Section 3. The baffle extends during observations using a small motor mechanism, and retracts using

(a) Stowed position.   (b) Extended position.
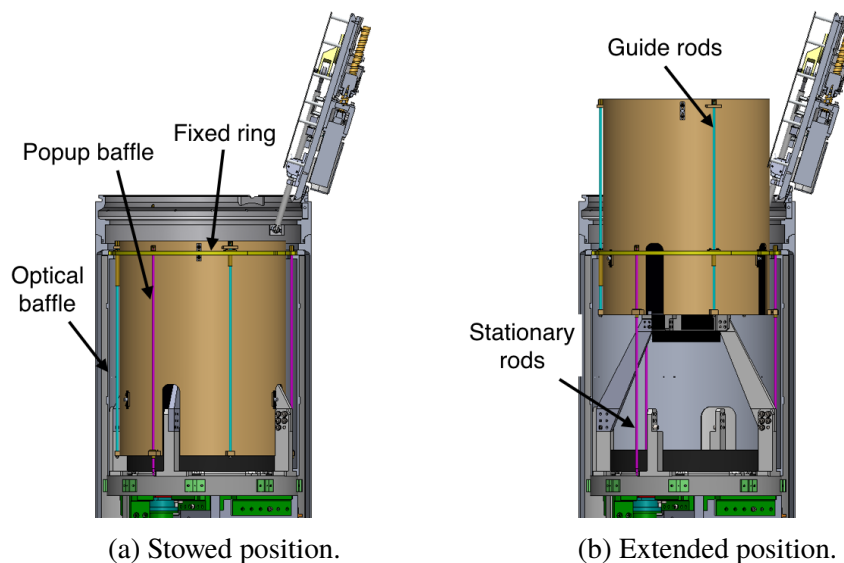
Figure A.12: The pop-up baffle is stowed upon deployment and re-entry, and extended during observations to block thermal radiation from the skin and shutter door that would otherwise enter the light path and add noise to the science observations. Note the fixed optical baffle is not shown.

spring tension and motor control. The stepper motor is located on the shutter door on a mount with a bobbin of thin metal wire that threads through the telescope aperture and attaches to the fore end of the pop-up baffle cylinder. The stepper motor turns a shaft that causes the string to wind up on the bobbin, pulling the baffle into the extended position, at which point a magnetic brake is applied to hold the motor steady and prevent the string from release. The pop-up baffle stays deployed during the duration of flight observations. It must be retracted at the end of observations prior to closure of the shutter door. To retract the pop-up baffle, the magnetic brake is released, the motor mechanism engages in reverse to unwind the string, and a set of compressed springs provide compression force to push the baffle back inside the skin envelope.

A.3.5   Cold Shutter and Calibration Lamps

For calibration purposes, the payload also contains a cold shutter and calibration lamps. The cold shutter is mounted to the forward face of the primary mirror support plate. It allows for measurement of the dark current before and during flight. The cold shutter design is based upon a successful shutter in CIBER-1, described in detail in [95]. The shutter consists of an anodized aluminum blade, counterbalanced

by a weight at the back end, that is mounted on a flexural pivot. The weighted end of the shutter blade has a permanent magnet. This blade and flexural pivot are encased in a housing that contains two powered electromagnets, one on either side of the shutter blade. Providing power to one housing magnet causes it to become polarized, attracting the weight and moving the shutter blade. In this way, the shutter can be moved between open and closed positions reliably and repeatedly in a cryogenic environment, where the open position removes the shutter blade from the light path and actively holds the blade in this position, and the closed position moves the blade into the light path, also under active control. This active control of positions allows the blade to remain in a known, reliable location while undergoing vibration and controlled motion that are part of the sounding rocket environment.

For CIBER-2 the cold shutter design must be scaled up to accommodate the larger light cone in CIBER-2 as compared to CIBER-1. The overall blade size and blade arm length are increased. The pivot location is designed to be the same, requiring additional counterweighting to balance the increased mass and longer footprint of the blade. Analytic and model-based calculations were performed to optimize the center of mass to be at the correct coordinates for the pivot. The housing requires redesign to accommodate the larger counterweight and new positions of the controlling magnets, as well as to interface to the telescope support plate while keeping the shutter blade at the correct location in the optical path. The resulting design was fabricated and tested for electronic control, ability to continue operation after extensive vibration, and cryogenic operation, as described in Section 3. The optical shutter in the vibration test configuration is shown in Figure A.13.

CIBER-2 has additional optical calibration lamps in the telescope assembly. The calibration lamps are housed within an assembly attached to the optical bench. An optical fiber carries the light from the calibration lamp assembly, through the telescope baseplate, and up to a mounting point near the center of the secondary mirror. These lamps and fibers are used to illuminate the light path with a known, fixed brightness for reference observational frames used to track the relative gain of individual detectors.

A.4 Imaging Optics

The imaging optics are mounted to an optical bench that connects the primary mirror support plate and the cryogenic tank. Light from the secondary mirror passes through the Cassegrain hole to the imaging optics section, where it is focused
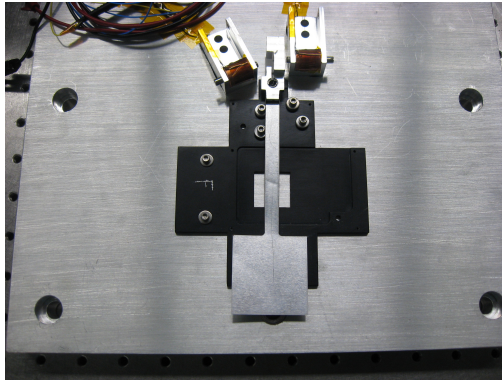
Figure A.13: Optical shutter in vibration testing configuration. Prototype shutter blade, counterweight, pivot, control magnets and associated electronics are shown; flight housing not included in this configuration. The shutter has two active positions, open and closed (shown), which were successfully operated during and after extensive vibration testing.

by a field lens. Next, two beam splitters direct the incoming light into three paths, each with an H2RG detector array. Additional filtering splits the light into two wavelength bands per detector array, resulting in a total of six distinct wavelength bands spanning the range of $0.5 < \lambda < 2.0\mu$m.

Each of the three light paths is very similar, consisting of a beam splitter, bend mirror(s), a collimator lens, a band pass filter, a camera lens, and a focal plane assembly that contains a detector array. Figure A.14 shows a representative ray tracing diagram including all of the optical components.

The imaging optics and mirrors are manufactured to the specifications of the science team by Genesia Corporation of Japan. All of the optical components are supported by flexures or spring retainers to handle the thermal compression stress in cooling and to maintain optical alignment against vibration and shock during launch.

A.5   Focal Plane Assembly

Broadly, the focal plane assembly[3] (FPA) must couple the detectors to the remainder of the optical chain. The overall FPA design must provide mechanical support and thermal isolation for the detectors; be flexible enough to accommodate the predicted final focus position of each arm; provide a mechanism for in situ focusing; and interface to the mechanical supports of the optical chain. The FPA must also incorporate the final filters in the optical chain, as they are designed to reside very

---

[3]This section is described in additional detail commensurate to the recent project focus.
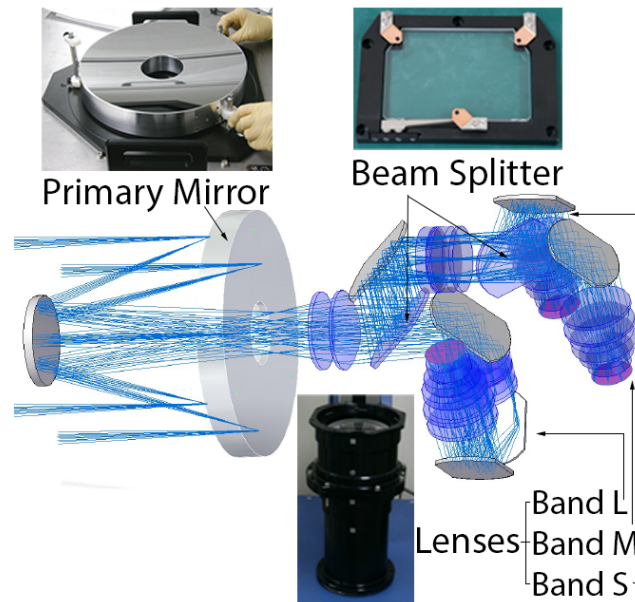
Figure A.14: Schematic representation of the CIBER-2 light paths. Incoming light is split into three light paths using two dichroic beam splitters. Bend mirrors, a collimator lens, a band pass filter, and a camera lens direct the light to a focal plane assembly that contains a detector array. Photographs of fabricated components are also shown.

close to the detector surface to minimize reflected images. The overall envelope of the FPA must fit within the limited envelope of the sounding rocket experiment payload section. The selection of the H2RG detector brings additional design considerations.

H2RG detectors are designed to work at cryogenic temperatures to minimize noise [89], and as such the entire CIBER-2 experiment payload is cryogenic. The detectors are read out by a cable provided by Teledyne that functions in a cryogenic environment. This cable couples to a cold circuit board for initial readout, which uses custom Manganin cables from Tekdata to transmit data and housekeeping information through the cryogenic environment to the warm section of the instrument for additional signal processing. The CIBER-2 FPA must provide mechanical support for the detector, cables, circuit board, and connectors. The CIBER-2 FPA must also accommodate the limited rate of temperature change that H2RG detectors are designed to withstand (2 K/min).

Finally, the CIBER-2 FPA must also meet vibration requirements provided in the NASA Sounding Rocket Handbook [96].

Thus the focal plane assembly must interface with the remainder of the optical chain,

provide housing for the H2RG detector, and provide housing for the H2RG readout cables, circuit board, and connectors in a manner robust to vibrational stress. The schematic in Figure A.15 summarizes these constraints.
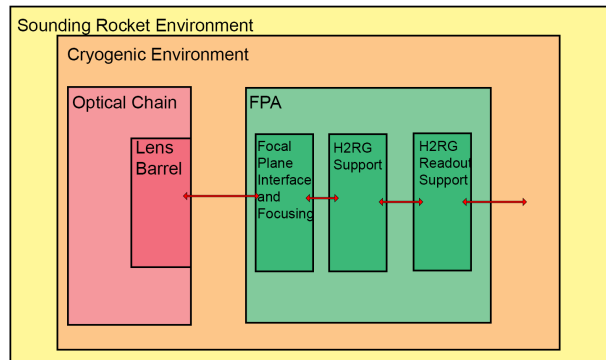
Figure A.15: Schematic diagram illustrating general functions of the CIBER-2 Focal Plane Assembly and its mechanical and electrical relationships to interface components including the optical chain, the cryogenic environment, and the greater sounding rocket environment.

A.5.1   Design Constraints

A.5.1.1   Optical Interface Constraints

The terminal optical chain component to which the FPA interfaces is the lens barrel, pictured in Figure A.16 with the specified interface for the FPA indicated. The CIBER-2 FPA is coupled to the lens barrel through three M4 screws at a diameter of 101 mm, with an optical keep out zone of 70 mm in diameter.
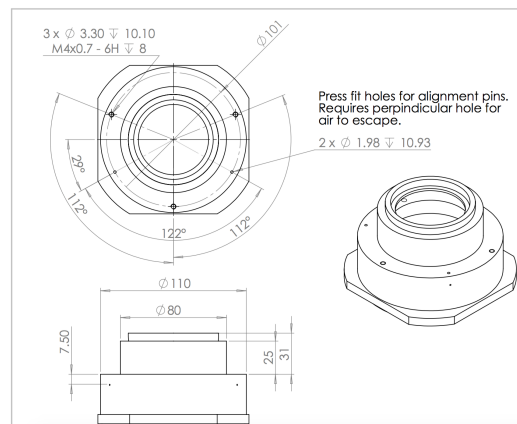
Figure A.16: Interface envelope to Genesia lens barrel.

The final focus position at 77 K for each arm is between 41 and 43.5 mm from the contact surface of the lens barrel, as shown in Figure A.17. The surface of the H2RG detector in each arm must be located at the specified position, with the distance at 77K shown first and the distance at 300K shown in parens.
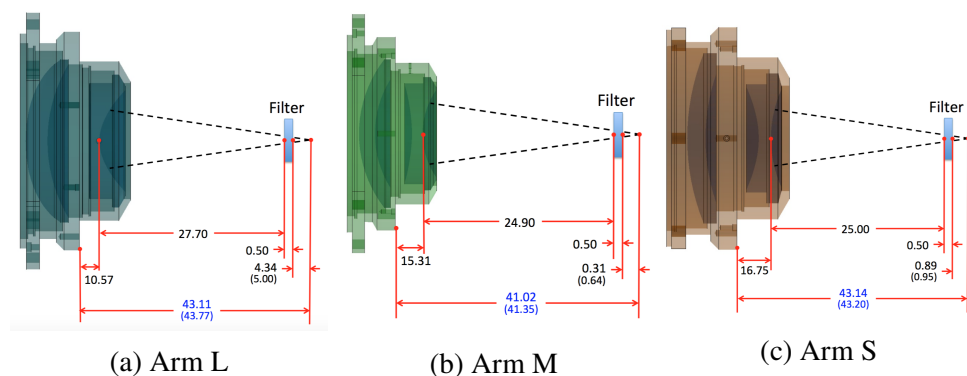
Figure A.17: Expected focus distances for each optical arm (L, M, S), measured from the mounting surface of the lens barrel.

A.5.1.2   Detector Interface Constraints

Teledyne provides documentation describing the interface requirements for the H2RG detectors. Included in this documentation are instructions for safe electrostatic handling of the devices, mechanical interface requirements, and thermal guidelines.

Extreme care is required in handling of the H2RG detectors. A humidity-controlled environment, electrostatic protection (antistatic mats and wrist straps), and single-use gloves are required for all handling of the device. In addition, the detector cannot be touched directly, and comes with a special handling tool. The focal plane assembly design must accommodate installation using the handling tool, and overall FPA assembly must include appropriate protection precautions.

Mechanically, the H2RG detector has three threaded legs with concentric shoulders that allow mounting of the detector to flat surface. The detector is held in place with washers and nuts applied to the threaded legs at the other side of the interface part, clamping the mating surface in place. Surface roughness is quite small at the shoulder surface to allow for a very parallel mounting surface relative to the image plane. This suggests that the surface of the mated part have a similar value for surface roughness, likely requiring lapping or similar finishing process.

H2RG detectors are designed for cryogenic operation at liquid nitrogen temperatures (77 K). However, the detectors are designed to withstand temperature changes of less than 2 K/min. The FPA design must include some mechanism to provide a controlled temperature change at the detector surface, both during the cool down and warm up processes and during operation, where heat load from the optics may vary as well.

Data is transmitted from the detectors through a proprietary, flexible cable provided by Teledyne. The initial readout of the detectors is handled by a circuit board colocated on the FPA. The circuit board connects to cryogenic cables that transmit data to the warm, non-cryogenic segments of the rocket that house later segments of the signal processing electronics, including data storage. The FPA must encompass the detector, readout cable, circuit board, and connectors.

A.5.1.3 Environment Constraints

Sounding rockets have limited spatial volumes and strict weight requirements. The FPAs reside in the optical subdivision of the experiment payload. As the optical chain is rather complicated, branching into three arms using multiple beam splitters and reflecting mirrors, the remaining spatial envelope for the FPAs must be as compact as possible and fit within the maximum payload radius.

The FPA must also demonstrate it alone can withstand the vibration requirements levied by NASA, and that all subcomponent parts will remain functional. In addition, it is preferable that filters remain within 2 pixels of initial calibrated positions to facilitate desired image processing analysis (removal of point sources, point spread function matching, etc). The FPA must also be designed with appropriate cryogenic considerations.

A.5.2 Mechanical subsystems design and description
A.5.2.1 Detector Interface

The H2RG detector is mounted to a surface that meets that flatness requirements put forth by Teledyne, with access to securing the legs of the detector tightly to this surface. As such, a round disc with a central conical protrusion is designed to be the primary interface piece, with the outer diameter of the cylindrical support smaller than the diameter of the feet so that the feet protrude through the mating surface for clamping. The material of this component was chosen as part of a broader thermal

circuit analysis. This Molybdenum support is shown in the right hand side of Figure A.18.

Figure A.18: Detector support pieces; from left, Titanium can, Molybdenum support mounted to anodized Aluminum base (black). In center, a cup for screws used during assembly.

A.5.2.2 Filter assembly

The filter assembly mates to the Molybdenum support and provides mounting for the final filters that sit closest to the detector. The bulk of the detector is covered by imaging filters, which are two bandpass filters on a single pane of quartz designed to reside 100 μm above the detector surface. The filter assembly also supports a linear variable filter (LVF), which is another piece of quart designed for spectroscopy. As this LVF does not span the detector surface, it is epoxied into an Invar holder along the sides of the LVF. This allows a means of fastening the LVF to the FPA assembly that maximizes the observing area, so no part of the LVF is taken away for mechanical supports such as clamps. Invar was chosen as the interface material for the LVF as it has thermal expansion properties that closely match that of the LVF quartz. Additionally, care was taken to select an epoxy suitable for cryogenic use, with little outgassing, matching coefficients of thermal expansion, which is also transparent in our waveband (in case any epoxy covers the optical surface of the LVF). An aluminum prototype of the filter assembly is shown in Figure A.19.

A.5.2.3 Interface to other optics

The interface components to the Genesia optics have three purposes: provide a light-tight mechanical interface between the last component of the optical chain (the lens barrel, manufactured by Genesia) and the housing of the FPA; provide a
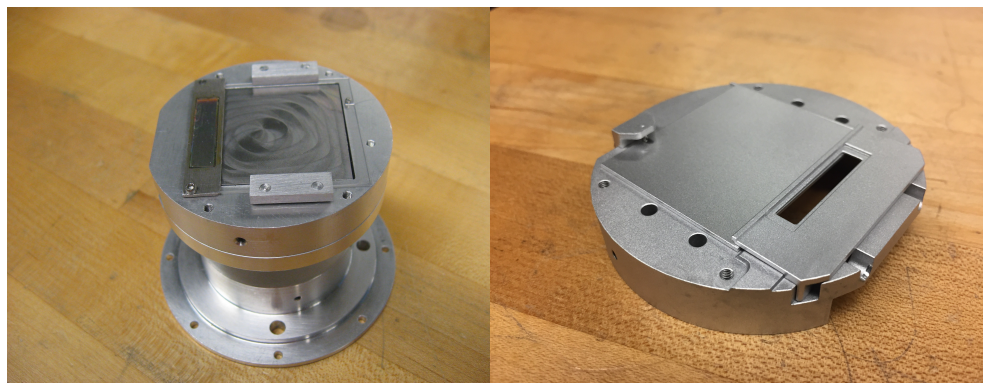
(a) Previous prototype version of filter assembly shown with quartz filter held in place with spring clamps. Previous LVF version shown.

(b) Updated version of filter holder prototype shown with aluminum dummy piece in place of quartz filter. Updated LVF holder shown.

Figure A.19: Aluminum prototype of filter assembly, with the cylindrical base the filter holder, the large rectangle a stand-in for the quartz imaging filter, and the smaller rectangle of the linear variable filter holder.

thermal break between the optics, which are expected to be fairly warm, and the detector, which is required to be as close to 77 K as possible; provide a focusing mechanism that is coarsely adjustable (2 mm) to accommodate the exact focus position predicted for each arm as well as provide a means for fine adjustment (100 μm) within each arm.

The interface mechanism between the lens barrel and FPA housing was specified early in the design process. The FPA must mount to the lens barrel using a pattern of three M4 screws located at a diameter of 101 mm. Press-fit pins are also included to allow for a more precise mating. An aluminum interface ring was designed to mate to the FPA housing on one side and the lens barrel interface on the other. Standoffs of an insulating material, Vespel SP-1, are designed to provide a thermal break between the warm optical chain and the FPA, in order to keep the detector temperature as low as possible. Two sets of blocks of Vespel are used in place of rings due to the high cost of the material, and secured in place by screws and slip-fit holes to receive the press-fit pins. An additional aluminum ring is added to this assembly to provide a light-blocking function, keeping stray light out of the beam. These components are shown in Figure A.20.

The precise height of the Vespel standoffs is determined by the envelope of the lens barrel and the focus distance. The height of the set of Vespel blocks between the lens
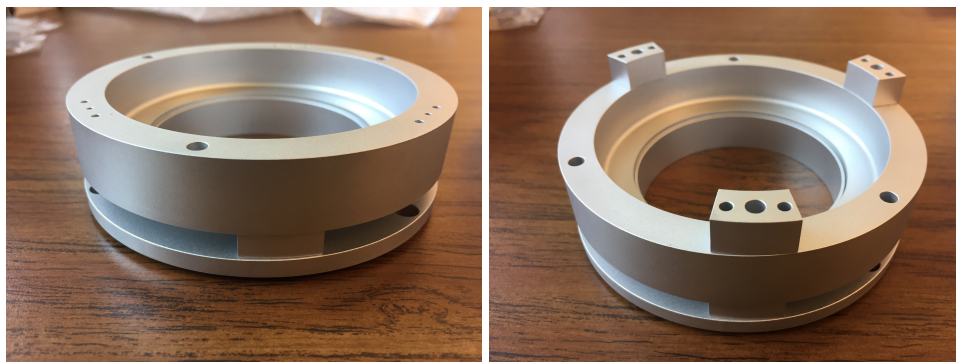
Figure A.20: Multiple views of the prototype interface between the optical chain and the main body of the FPA. Several interface rings are stood off from standoffs of an insulating material (small blocks shown here in prototype aluminum).

barrel and the intermediate light-tight ring is determined by the shape of the lens barrel and set at 10 mm. The height of the second set of Vespel blocks is designed to be coarsely configurable to match the specific focus distance of each of the three arms of the CIBER-2 instrument. While the overall FPA was designed for a target focus distance of 42.4 mm between the lens barrel mounting surface and the surface of the detector, the final predicted focus positions for each arm varies slightly due to the specific lenses used in each arm. For the target focus distance, a reference block height of 6 mm is assumed. The base height for the Vespel blocks tailored to the predicted focus distance of each arm are outlined in Table A.1.

Table A.1: Distance in millimeters [mm] from mounting surface of optical lens barrel to focus distance at detector surface for each optical arm of CIBER-2. The height of a set of a Vespel blocks can vary to accommodate the different focus distances for each arm, both as predicted and in the event of changes to the actual focus distance or the final heights of machined components.

Height	Design	Arm-L	Arm-M	Arm-S
Focus distance at 300K (77K)	42.57 (42.40)	43.282 (43.11)	41.184 (41.02)	43.310 (43.14)
Lens Barrel Vespel at 300K (77K)	10.0 (9.920)	10.0 (9.920)	10.0 (9.920)	10.0 (9.920)
Vespel for predicted focus at 300K	6.0	5.8	3.75	5.8
Manufactured Vespel at 300K	n/a	5.25	3.0	5.25

Assuming the predicted focus distance is correct and the parts are made to the specified height values, the values listed in the Focus Vespel row of Table A.1 will be appropriate. For fine focusing, washers with thicknesses of 10, 40, and 100 μm can be placed under any of the three Focus Vespel blocks to increase

the position or focus distance on scales of less than 1 mm. In the event that the tolerances or actual focus distance result in smaller focus distances, the set of Vespel blocks manufactured for each arm are shortened by at least 0.5 mm as listed in the Manufactured Vespel row of the table, with the expectation that the actual focus distance will achieved with the fine focus washers.

A.5.2.4 Full Focal Plane Assembly

The full focal plane assembly includes all the subassemblies that work together to meet all design constraints and provide a detector surface at the precise focus distance for optimized images. These include the detector and detector interface, the filter assembly that places the filters at the correct distances from the detector surface, the housing that supports the electronics for detector read out, and the interface components that mount to the rest of the optical chain. These pieces can be seen together in Figure A.21, along with a cutaway model view showing the internal parts in Figure A.22.
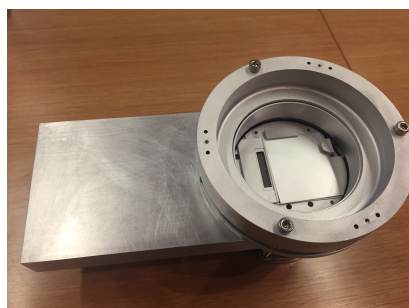
(a) Full FPA with interface pieces included. Bright square in the center is aluminum prototype of quartz window pane filter that sits directly above detector.
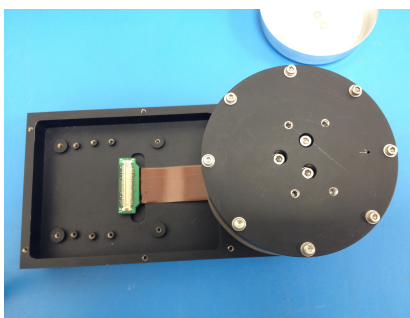
(b) Underside of detector housing with lid removed. Cold circuit board mounts to the black standoffs around the exposed cable and connects to the detector readout cable.

Figure A.21: Two views of aluminum FPA prototype with focal plane interface pieces.

The initial CIBER-2 design planned for three identical flight FPAs to be fabricated for the three optical arms of the CIBER-2 payload. This allows for lower-cost fabrication and easier assembly. However, this assumes the image projected onto the detector has the same alignment relative to the detector position, which was not the case in the final design of the optical chain.
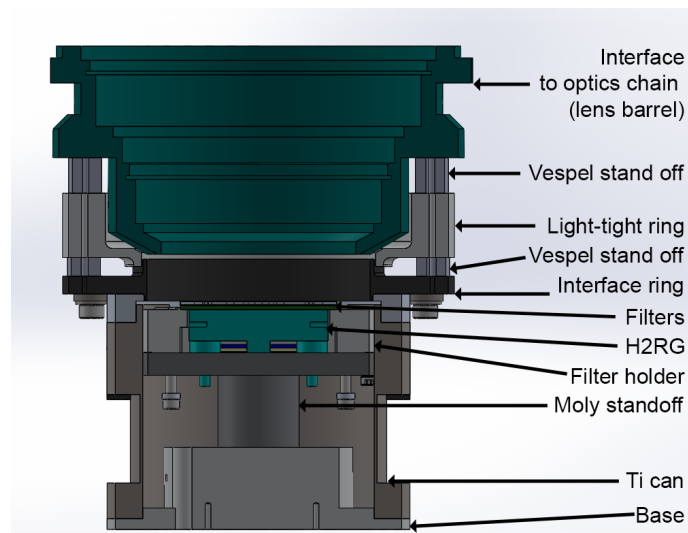
Figure A.22: Cutaway model view of the full FPA, with labels for component parts.

A.5.3   Optical Issue Analysis and Resolution

A.5.3.1   Desired alignment of CIBER-2 images

In order to obtain sky images optimized for cross-correlation and spectroscopic analysis, the image of the sky observed by each detector must be aligned such that the same portion of the sky is recorded on the same physical location of each detector. This allows for dithering or stepping in the observation strategy that moves images of the sky across the detectors in a consistent manner, maximizes area of images used for intensity mapping and cross-correlation analysis, and aligns the spectroscopic images.

The image recorded by each detector is divided into a sky map portion and a spectroscopic portion. The sky map portion is further subdivided into two wavebands. These are oriented such that a band of 600 pixels across the full 2048 pixels of the detector width at one end of the detector is allocated to spectroscopic imaging, and the remaining 1448 rows of pixels are dedicated to two imaging rectangles. The imaging rectangles are oriented such that the rectangles form two columns under the spectroscopic portion, with the dividing portion of the images perpendicular and centered relative to the spectroscopic portion, as shown in Figure A.23. This begets two imaging rectangles that are 1448 pixels along one side and 1024 pixels along the other.

The CIBER-2 observation strategy calls for the sounding rocket to point at a desired sky field (such as Bootes or the North Ecliptic Plane), record an image for ~30
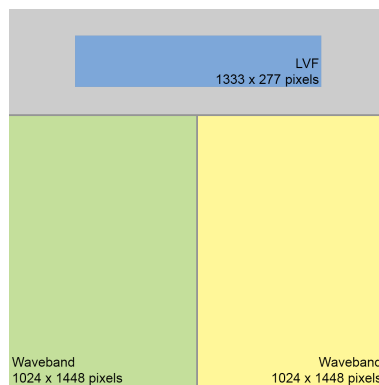
Figure A.23: Allocation of the 2048 x 2048 pixels of the H2RG detector into two infrared wavebands (with windowpane quartz filter) for fluctuation imaging and a spectroscopic portion (with a linear variable filter (LVF).

seconds, then step the rocket by 1.2 degrees[4] along the 90-270 plane of the rocket coordinate system to record the same sky image on the other half of the detector in the other imaging waveband (for cross-correlation of images). As each detector is divided into two imaging segments and a spectroscopic imaging segment as shown in Figure A.23, the corresponding area of each of these types of images must be aligned in order to compare images across the different wavebands provided by each detector.

A.5.3.2 Misaligned images issue

Ideally, the images recorded on each detector would be aligned by the optics in each of the three arms of the CIBER-2 optical chain. However, this is not the case in the CIBER-2 optical chain. An inspection of the optical models at the conclusion of initial FPA design and a concurrent investigation of rocket observation strategy revealed that the images recorded by each detector in each of the three arms of the CIBER-2 optical chain were all aligned differently. One image was rotated by 90 degrees relative to the other two images, and the remaining two images were vertically aligned but mirrored. This can be seen in Figures A.24 and A.25, where a projection of a non-symmetric shape[5] propagated through the optical chain is recorded on each detector.

---

[4]1.2 degrees is the size of the FOV of an image in a single waveband.

[5]A non-symmetric shape has no mirror images when reflected across either set of perpendicular axes centered on the spatial extent of the image. Here, the number "2" was used as the reference non-symmetric shape.
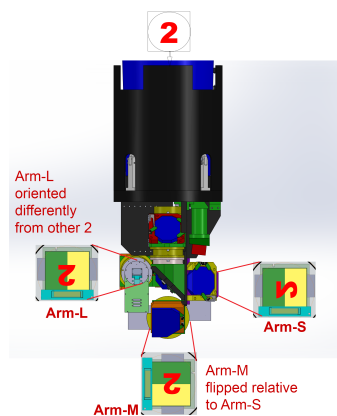
Figure A.24: Alignment of images as mapped onto each arm of the three-arm CIBER-2 optical chain (Arms-L, -M, -S).
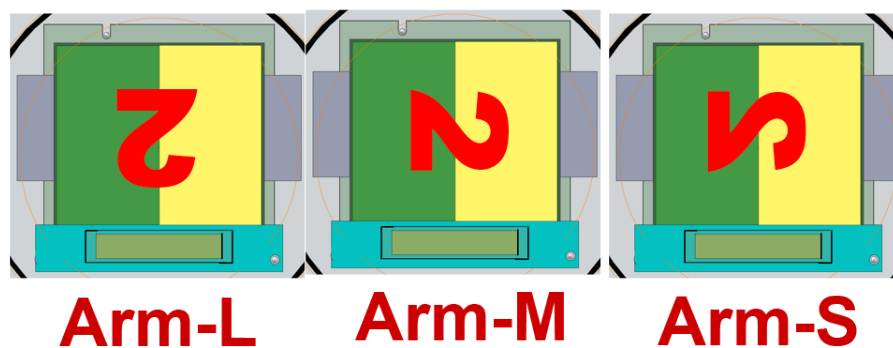
Figure A.25: [
Orientation of a simulated non-symmetric object on each detector.]Orientation of a simulated non-symmetric object projected onto the sky as observed by each CIBER-2 optical arm and recorded on the initial alignment of detectors in the FPA. Clearly, the images are misaligned. A mechanical (as opposed to optical) solution was implemented.

The images in each arm clearly reach the detectors with different orientations, resulting in misalignment that would lead to spectroscopic and intensity mapping data that is not suitable for comparative spectroscopic or imaging cross-correlation analysis. An optical solution to this issue was untenable for programmatic reasons (schedule, cost), and so mechanical solutions were pursued with the goal of having filters oriented the same relative to sky images to obtain sky images optimized for cross-correlation and spectroscopic analysis. A secondary optimization parameter was detector orientation; having the same portion of the detector oriented the same relative to sky images would ensure that the images were read out of the detector in the same manner , facilitating simpler noise modeling and identification of detector anomalies in the data streams.

A.5.3.3 Mechanical solutions to image misalignment

In a ground based instrument, or other instrument where total volumetric footprint was not restricted, a possible solution would be to simply rotate the entire FPA assembly to obtain the desired image alignment. However, due to the space constraints imposed on CIBER-2 by the sounding rocket environment, rotation of FPAs by 90 or 180 degrees would violate the sounding rocket envelope and thus was not a viable solution. Additionally, senior engineers advised keeping the challenging parts of the assembly as similar as possible to reduce the cost of fabrication and minimize the chances of human error during the assembly process.

These constraints suggest mechanical solutions that resolve the image alignment by changing the alignment of the location of the circuit board relative to the detector. The original optics model included an FPA envelope that fit within the experiment payload, so altering the FPA envelope as little as possible will result in solutions that fit (as opposed to leaving FPA design intact but installing the entire FPA in a rotated position, which violates the experiment payload). This mechanical solution has two components: aligning the detector can stack (including H2RG detector, read out cable, and filters) to align all images and redesigning the circuit board and circuit board housing to interface with the new location of the H2RG read out cable while keeping the original location of the connectors that transmit data to the warm side.

Solutions are also impacted by the observation strategy of the CIBER-2 experiment. The position of the sounding rocket on the sky and the way in the rocket moves to execute a dither pattern are coupled to the orientation of the filters. While either the observing strategy or the filter orientation can be said to be unconstrained, since

they are coupled, the selection of either of these impacts the other. NASA engineers advised that the rocket can step in pitch (0-180 degree plane) or yaw (90-270 degree plane), and that motion along yaw uses less fuel. Thus we set the CIBER-2 rocket step direction in the 90-270 plane, which sets the filter orientation in a particular way to obtain the desired images for analysis.

A.5.3.4   Final engineering solutions

Image alignment is narrowed down to selection of mechanical alignment options that provide the desired observing pattern. For cross-correlation analysis, subsequent images on the sky must move in such a way as to move an observed object from one rectangular window pane filter band pass into the other, while keeping the portion of the sky observed by the LVF continuous. This constraint removes the option of aligning all arms with Arm-L from Figure A.25. Other physical constraints on the FPA envelope determine the solution uniquely.

Arm-L has few limitations on expanding the housing within 5 cm in any direction. The housing for Arm-M can expand to the sides of the nominal circuit board design, but cannot extend housing past the nominal rounded edge of the Titanium detector enclosure due to interference with the optical spine. The housing for Arm-S can expand out on only one side due to interference with other components in the optical chain, and can also expand beyond the Titanium detector enclosure. This constrains the solution set to a single solution that accommodates the observing strategy and fits within the experiment payload envelope.

The implemented solution is to make Arm-M the nominal FPA, with Arm-L having a rotated filter holder and detector such that the housing is expanded to one side and the circuit board is redesigned to have an L-shape, and Arm-S having a mirrored configuration compared to the nominal design where the filter holder and detector are rotated 180 degrees relative to their nominal positions and the circuit board redesigned to have a six-shape. This reorients the detectors, windowpane filters, and LVFs such that a sky image falls the same way relative to these components for each arm.

Resolution of the image misalignment results in 3 FPA designs with identical detector stacks and focal plane interfaces and tailored variations in only the detector read out circuit board and circuit board housing. After ensuring that images are aligned across detectors, it is important to set up the experiment to avoid drift that would
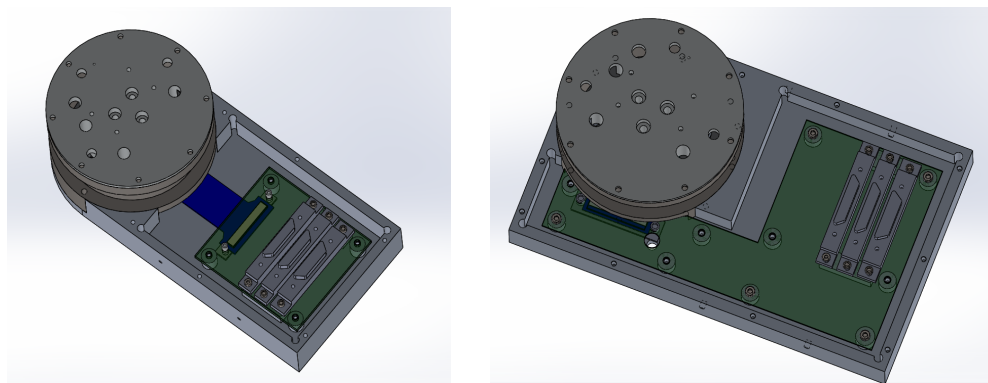
(a) Nominal FPA design that fits within original FPA envelope.

(b) Rotated FPA design to accommodate image with 90-degree rotation.

Figure A.26: Multiple versions of the FPA are needed to correct for image misalignment.

degrade the science images. The addition of a cold star tracker to the overall CIBER-2 experiment payload performs this pointing monitoring function.

A.6 Cold Star Tracker

To improve upon the precision of the pointing of the observational path of CIBER-2 relative to the side-looking star tracker provided by NSRP, CIBER-2 includes a star tracking assembly located in the experiment payload. This cold star tracker provides active tracking information to the NSRP-provided Altitude Control System (ACS), which is combined with the side-looking NSRP warm star tracker data for more accurate station keeping.

The cold star tracker consists of a CMOS detector at the end of a small optical chain diverted from the main CIBER-2 optical path. A pickoff mirror is located adjacent to the optical shutter blade and directs light into a dedicated optics column consisting of bend mirrors, filters, corrective aspheric optical elements, and the CMOS detector, shown in Figure A.27a. The CMOS detector is mounted directly onto a circuit board contained in a housing unit installed up against the forward face of the telescope support plate. A prototype of this detector and housing is shown in Figure A.27b.

The circuit board performs basic power functions for the CMOS detector and passes the data from the CMOS to wires guided along the CIBER-2 optical bench to a dedicated hermetic connector on the vacuum bulkhead. Warm wires on the fore side of the bulkhead hermetic connector bring the data to a dedicated circuit board
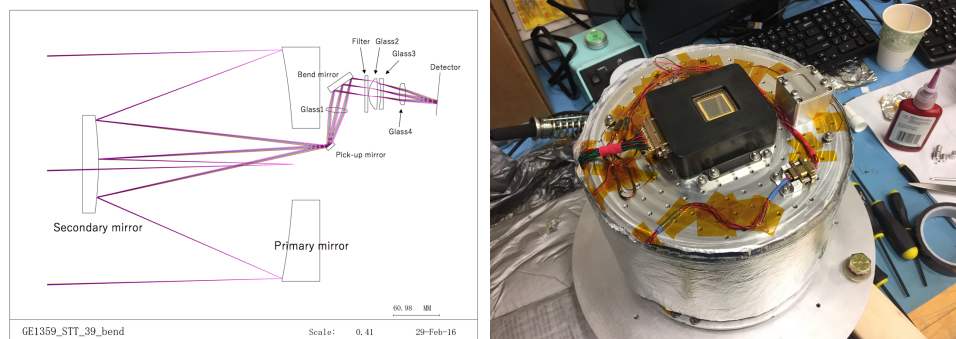
(a) Zeemax model of cold star tracker optical path.

(b) Lab testing of CSTARS, a prototype CIBER-2 cold star tracker.

Figure A.27: The cold star tracker gets light from a pick off at the optical shutter, passes the light it through an independent optical path, and records the images on a cryogenically-tested CMOS detector to provide precision focus information to mission control.

housed in the secondary warm electronics box, where preliminary image processing is performed. Information about changes in star location of CMOS images from one frame to the next is passed out to the NSRP ACS. The ACS contains an algorithm to determine if the drift indicated in the images is within predetermined parameter values; if these drift values are exceeded, the ACS will correct the pointing of the CIBER-2 rocket to stay on target.

A.7   Cryostat, Suspension, and Shielding

The CIBER-2 cryogenic system is a duplicate of the successful cryogenic system used in CIBER-1 [107]. This system consists of a 7 liter liquid nitrogen vessel filled with an open-cell aluminum foam that ensures thermal contact between liquid and metal in zero-gravity conditions. The optical bench supporting the imaging optics are mounted directly to the cryostat, using a grid of threaded holes. Cryostat fill and vent tubes hermetically interface with the vacuum bulkhead as in Figure A.28a and are accessible from the fore side of the evacuated experiment payload. The cryostat itself mounts to raised hexagonal blocks on the vacuum bulkhead through thermally-isolating G10 supports, as shown in Figure A.29. The cryostat is wrapped in layers of Mylar prior to installation for additional thermal insulation.

Shock-absorbing bumpers are mounted to the aft side of the vacuum bulkhead prior to cryostat installation, as shown in Figure A.28b. These bumpers are cylindrical pieces of Silicon with a small lip fitted into an Al 6061-TS ring that bolts to the
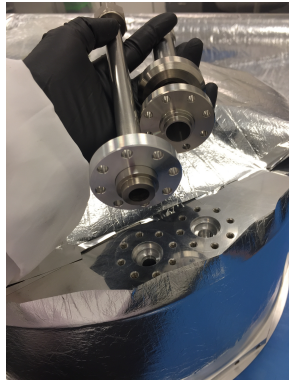
(a) Vent and fill tubes must be hermetically sealed to the cryostat.
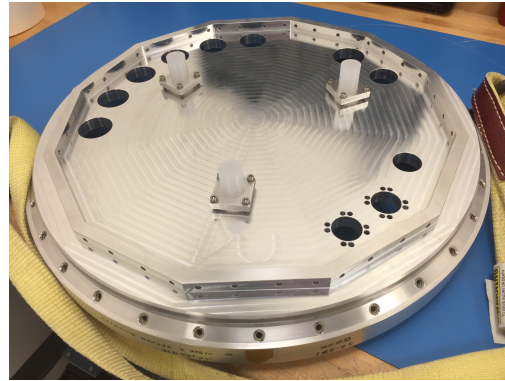
(b) Silicon bumpers mated to the bulkhead under the cryostat body absorb shocks upon rocket landing that may otherwise damage the cryostat.

Figure A.28: Preparation for CIBER-2 cryostat assembly.The cryostat itself must be assembled, and the vacuum bulkhead prepared for cryostat mounting.

bulkhead. The aluminum mounts are heated to increase in size and fitted to the silicone without adhesive or fasteners. The combination of close sizing and lip keep the silicon in place. The bumpers are designed to absorb shock upon rocket landing, preventing the cryostat from contacting the bulkhead directly. The G10 plates are somewhat flexible and may bend or break upon landing, and are easily replaced for future flights.
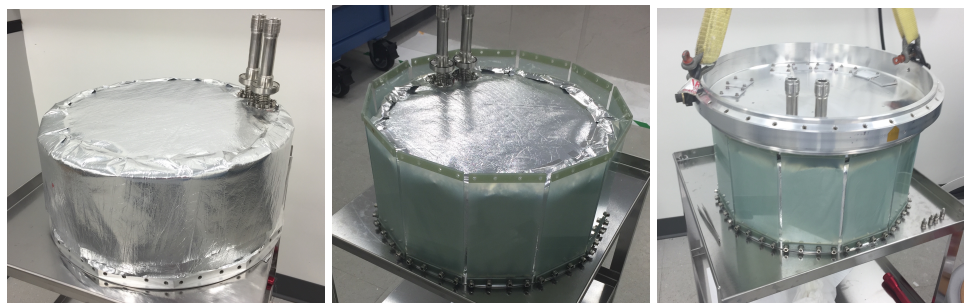
(a) Cryostat with fill and vent tubes installed, wrapped in Mylar

(b) G10 panels mounted to cryostat.

(c) Cryostat mounted to bulkhead via G10 interface panels.

Figure A.29: CIBER-2 cryostat in various stages of assembly. The cryostat is a container filled with metal foam; fill and vent tubes for the LN_2 were assembled in the lab. G-10 panels interface between the cryostat and vacuum bulkhead of the rocket, providing flexible mechanical support and thermal isolation.

The telescope assembly, imaging optics, and cryogenic system are enclosed in a radiation shield made of Aluminum 1100, mounted to the cryostat for cooling. The radiation shield buffers the cryogenically cooled instruments from thermal radiation from the skin. Al 1100 is chosen as it has a coefficient of thermal conductivity suited for the radiative load while maintaining some of the stiffness of aluminum. It is a "clamshell" design, with two overlapping cylindrical halves that extend from a mount ring affixed to the cryostat work surface at the aft end of the cryostat to a few millimeters from the aft end of the optical baffle. It is affixed to the experiment payload at various locations along the optical bench, telescope support plate, and optical bench using small T-shaped G-10 mounts. Fabrication of the radiation shield is difficult as it requires sheets of Al 1100 to be rolled to the precise radius. However, all mounting holes and a small overlap region for closing the assembly must be machined prior to rolling of the baffle. The assembled radiation shield is wrapped in a Mylar blanket prior to insertion in the rocket skin to further reduce the radiative load.
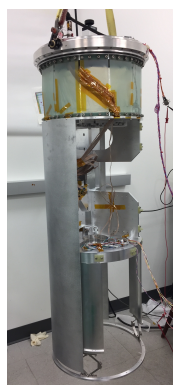
(a) Half of two-piece cylindrical radiation shield affixed.

(b) CIBER-2 with full radiation shield preparing for insertion into skin.

Figure A.30: Views of the radiation shield. The radiation shield is two overlapping half cylinders that affix to various parts of the experiment payload through T-shaped G10 standoffs. It insulates the cryogenic CIBER-2 experiment from thermal radiation from the (much warmer) rocket skin.

A.8   Warm Electronics

The CIBER-2 electronics chain carries signals between the detectors, the experiment housekeeping, and the rocket telemetry system. It is made up of the circuit boards located near the detectors in the focal plane assemblies described in Section A and

three other board types located in the star tracker section of the rocket, forward of the experiment section: data acquisition boards, array processing and housekeeping boards, and data storage boards.

CIBER-2 has three 2048 x 2048 HAWAII-2RG (H2RG) detector arrays, which are second-generation commercial HgCdTe near-IR detectors manufactured by Teledyne Scientific and Imaging Corporation. Each detector is biased and read out by custom electronics on the focal plane boards. The 2048 columns of the detector array are divided into 32 channels, which are read out in "slow" mode to reduce readout time and noise. As the pixel voltages have a large offset, an external reference voltage close to the average pixel voltage is used to remove the offset. A reference pixel row will be read out periodically during the full detector array readout, providing a method of 1/f noise mitigation [73].

A.8.1   Array Processor and Housekeeping Boards

Two data acquisition boards per detector array digitize the read out voltages. Each data acquisition board handles 20 channels; 16 channels for detector output and 4 channels for associated housekeeping output. The signals from both data acquisition boards are passed to a single array processing and housekeeping board, shown in Figure A.31a, which temporarily stores the data locally before passing it to the data storage board for permanent storage. The array processing and housekeeping boards also perform clocking and command functions for the detector array, pass housekeeping and status data to a NASA telemetry system, and respond to signals from external NASA systems.

A.8.2   Data Storage Boards

The data rate required for three detectors exceeds the capabilities of the NASA ground telemetry systems. Instead of transmitting all data and housekeeping down to the ground station, CIBER-2 stores flight data on-board and transmits only a small fraction for diagnostic purposes. Solid-state storage is required to withstand the physical environment experienced in flight. Each detector array requires one data storage board with two 128 GB flash memory chips, shown in Figure A.31b. This data storage board receives the digitized detector array output data from the array processing and housekeeping board and stores a primary and backup copy on each of the flash memory chips. Housekeeping data and a single channel of flight data are transmitted via rocket telemetry systems to the ground station. Raw rocket telemetry received by the ground system is forwarded to custom ground station
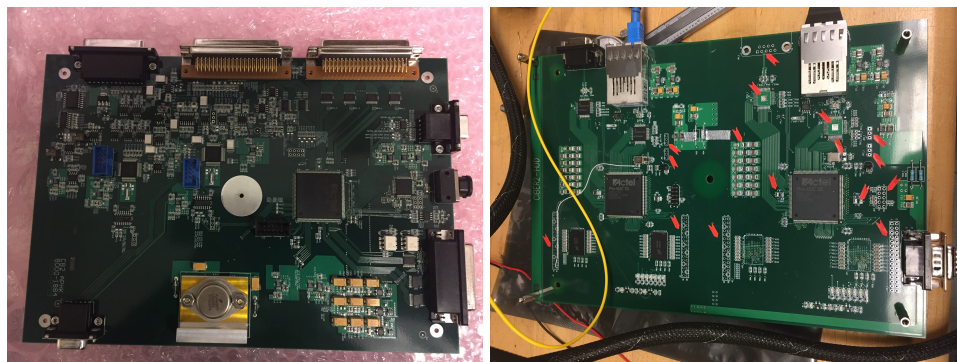
(a) Housekeeping and processing board.   (b) Data storage board board.

Figure A.31: CIBER-2 electronics boards. Data flows from the experiment payload through hermetic connectors on the vacuum bulkhead to the large connectors on the long side of the boards. Data between boards and out to other rocket systems flows from other connectors. These boards are housed in a metal enclosure in an ambient rocket segment on the fore side of the vacuum bulkhead.

elections (GSE) which displays the data in real time. The GSE system is also used during testing.

A.8.3   Electronics Housing

The CIBER-2 electronics boards are housed in a metal enclosure mounted to the fore side of the vacuum bulkhead. The housing is designed to accommodate the 11 total boards and wiring harness in the tight space constraint provided by the rocket envelope. It is also designed to make access to and removal of individual boards as simple as possible. It has an L-shaped backing with individual stalls for each board, and separate face and top plates with cutouts for connectors. The boards are large enough (10 x 7 inches (254 x 188 mm)) that mounting at the edges may not be enough to suppress drumming modes induced by vibration. An exoskeleton of aluminum is designed to fit each individual board so that they can also be clamped down at other locations on the board to prevent the drumming mode and decrease the chance of fatigue failure of any board. The electronics housing board is shown in Figure A.32, while the exoskeleton and housing mount are shown in Figure A.33.

A.9   Full CIBER-2 Experiment Payload

CIBER-2 is designed to leverage the successes of CIBER-1 while addressing the additional science specifications needed to better characterize the Extragalactic Background Light and probe for the signal of the earliest galaxies from the Epoch
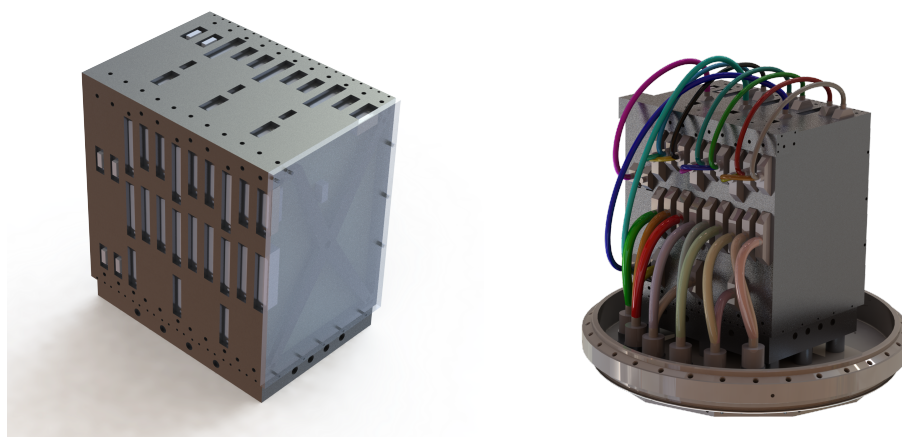
(a) Electronics housing box.

(b) Electronics housing box with wiring harnesses.

Figure A.32: CIBER-2 electronic box models, shown alone and mounted to the vacuum bulkhead with wiring harnesses.
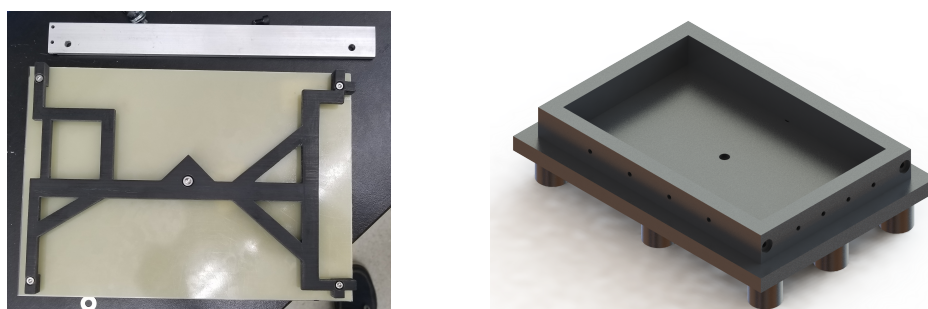
(a) Individual board exoskeletons.

(b) Electronics housing board mount.

Figure A.33: CIBER-2 electronics box details. The large electronics boards are subject to vibrational modes and must be stabilized with exoskeletons. The larger electronics housing box interfaces to the rocket skin by the mount shown here.

of Reionization. CIBER-2 utilizes a sounding rocket to get above the atmosphere; Teledyne HAWAII-2 RG Mercury Cadmium Telluride detectors well suited for intensity mapping; a larger, single telescope design coupled to these large detectors to obtain degree-scale images; and an optics design with multiple filters to obtain six wavebands that span the optical into the near-infrared, 0.5 to 2.0 microns.

A p p e n d i x B

MECHANICAL DRAWINGS

Figure B.1: Mechanical drawing for flight version of the CIBER-2 focal plane assembly detector holder (Moly standoff).
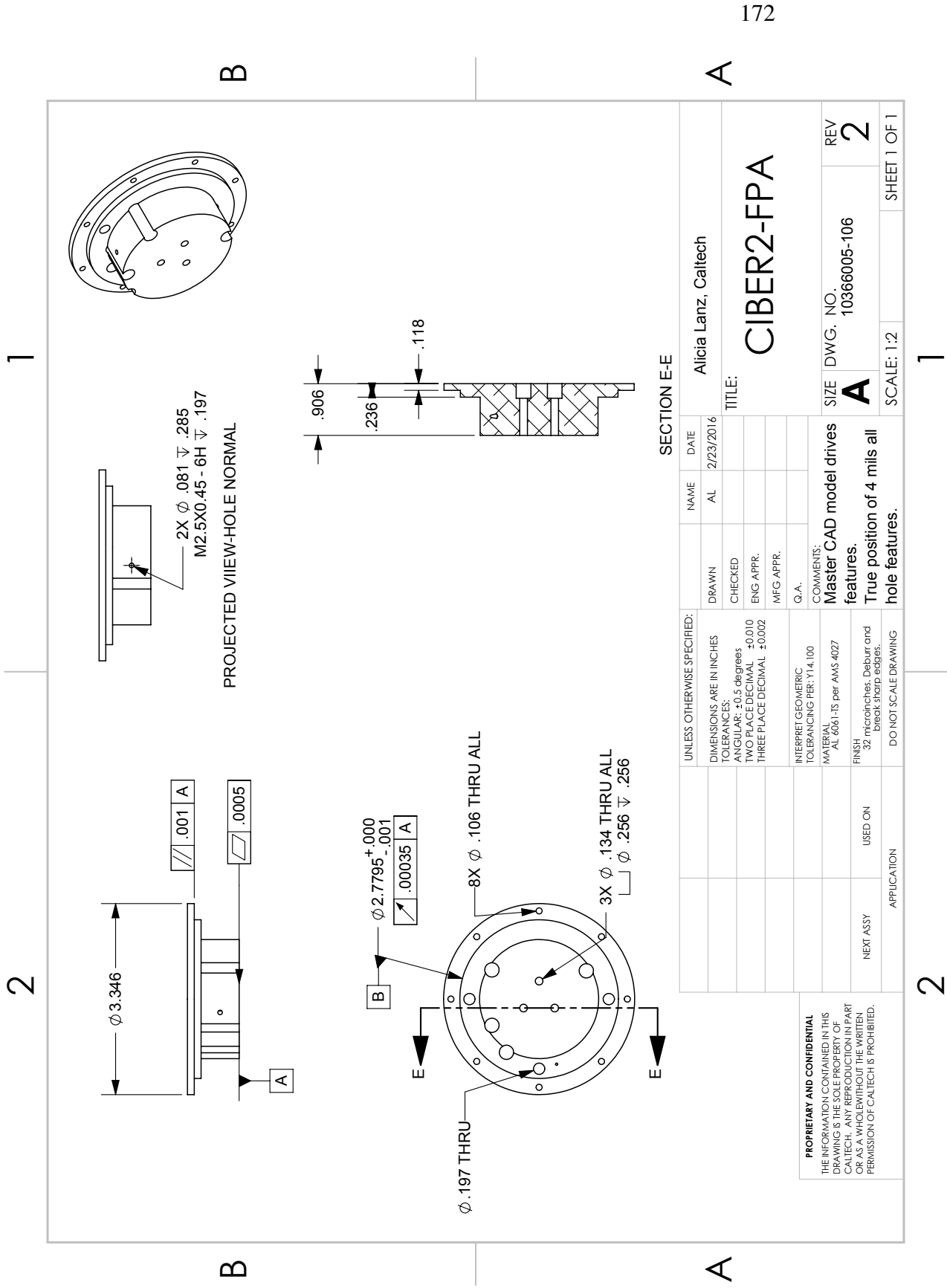
Figure B.2: Mechanical drawing for flight version of the CIBER-2 focal plane assembly base.
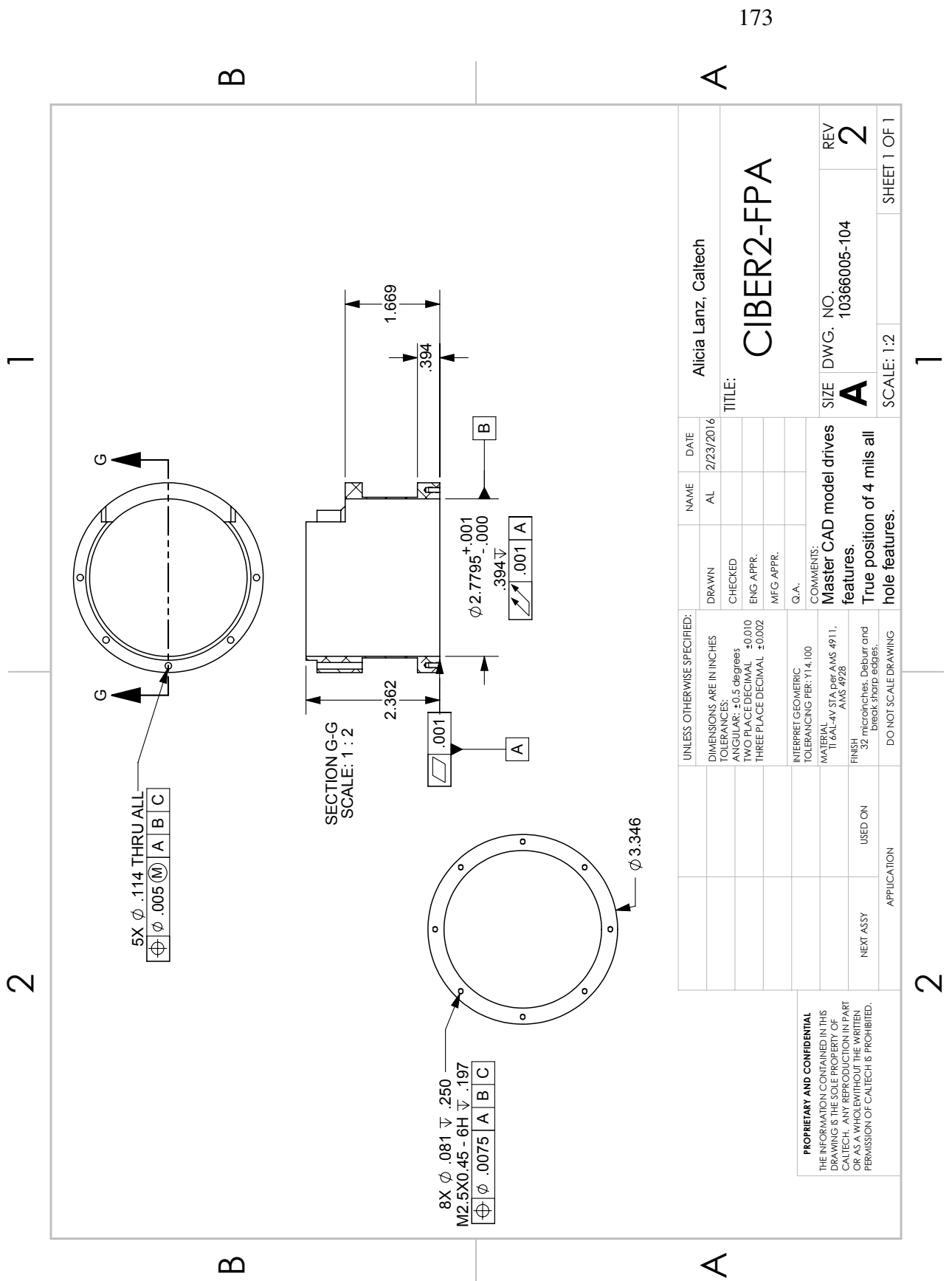
Figure B.3: Mechanical drawing for flight version of the CIBER-2 focal plane assembly titanium can.
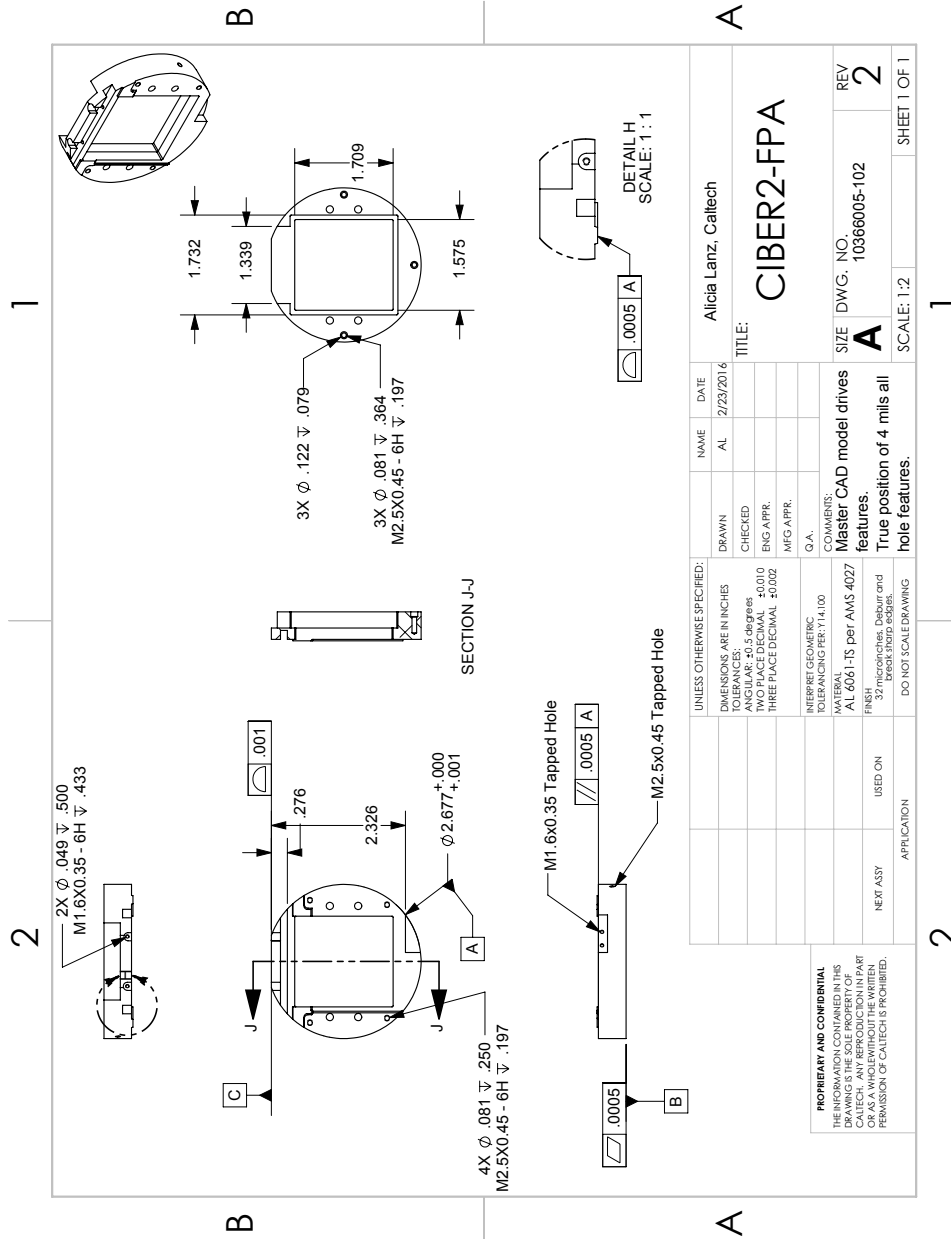
Figure B.4: Mechanical drawing for flight version of the CIBER-2 focal plane assembly filter holder.

Figure B.5: Mechanical drawing for flight version of the CIBER-2 focal plane assembly filter holder shim.
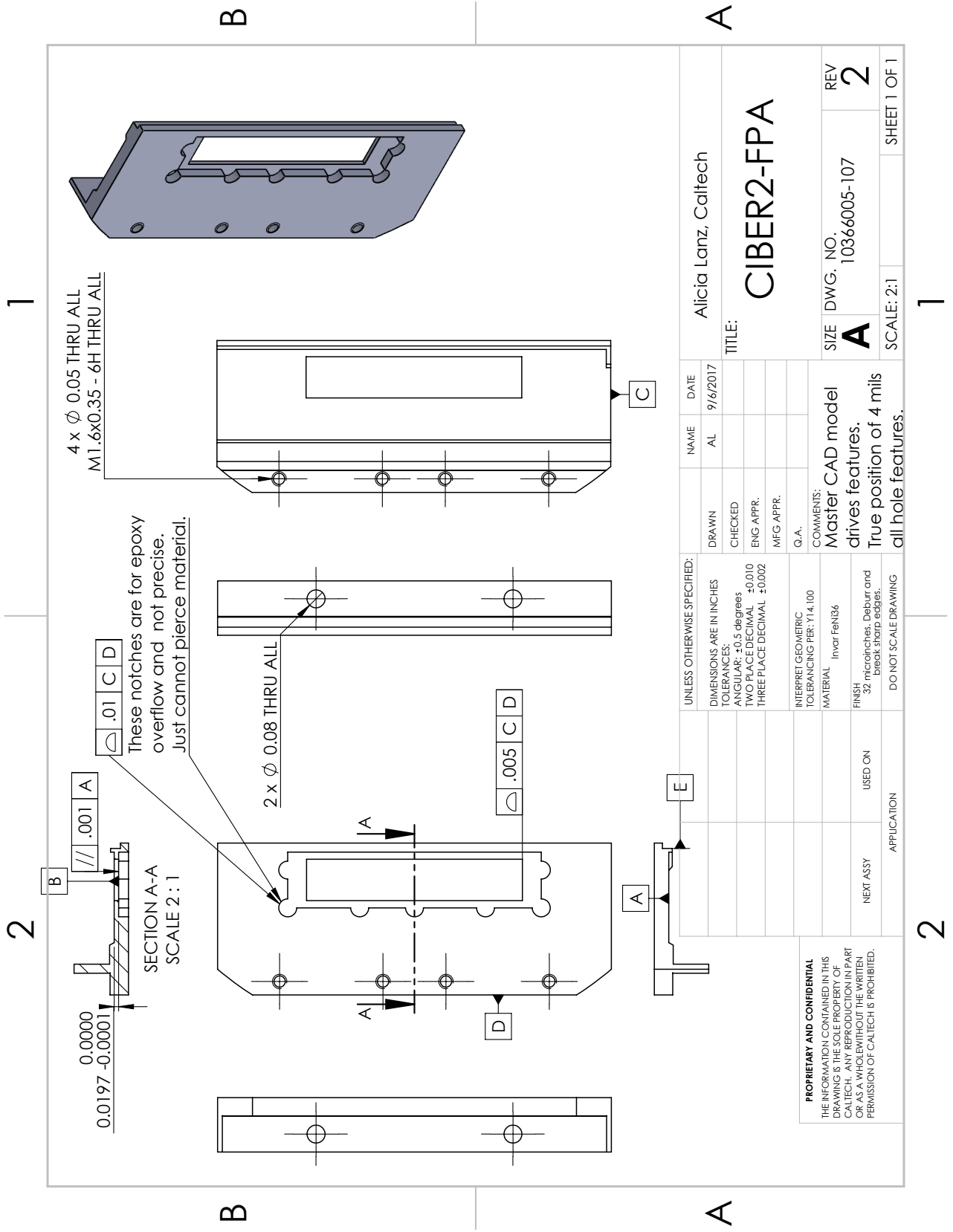
Figure B.6: Mechanical drawing for flight version of the CIBER-2 focal plane assembly linear variable filter holder.
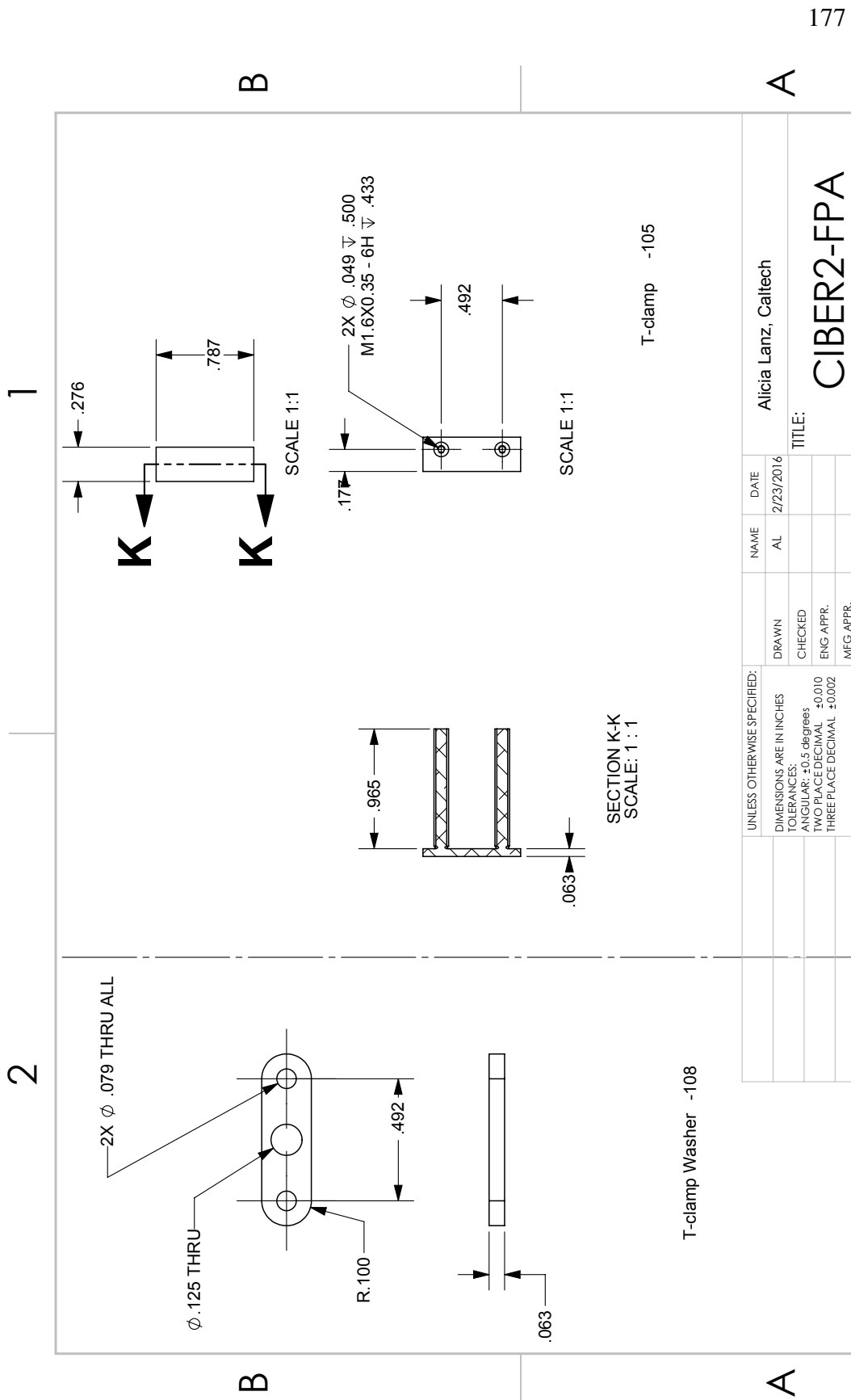
Figure B.7: Mechanical drawing for flight version of the CIBER-2 focal plane assembly filter spring clip and T-washer.

Figure B.8: Mechanical drawing for flight version of the CIBER-2 focal plane assembly window pane filter.

Figure B.9: Mechanical drawing for flight version of the CIBER-2 focal plane assembly pin holder.

Figure B.10: Mechanical drawing for flight version of the CIBER-2 focal plane assembly assembly shield.

Figure B.11: Mechanical drawing for flight version of the CIBER-2 focal plane assembly light-tight mask.

Figure B.12: Mechanical drawing for flight version of the CIBER-2 focal plane interface light-tight ring.
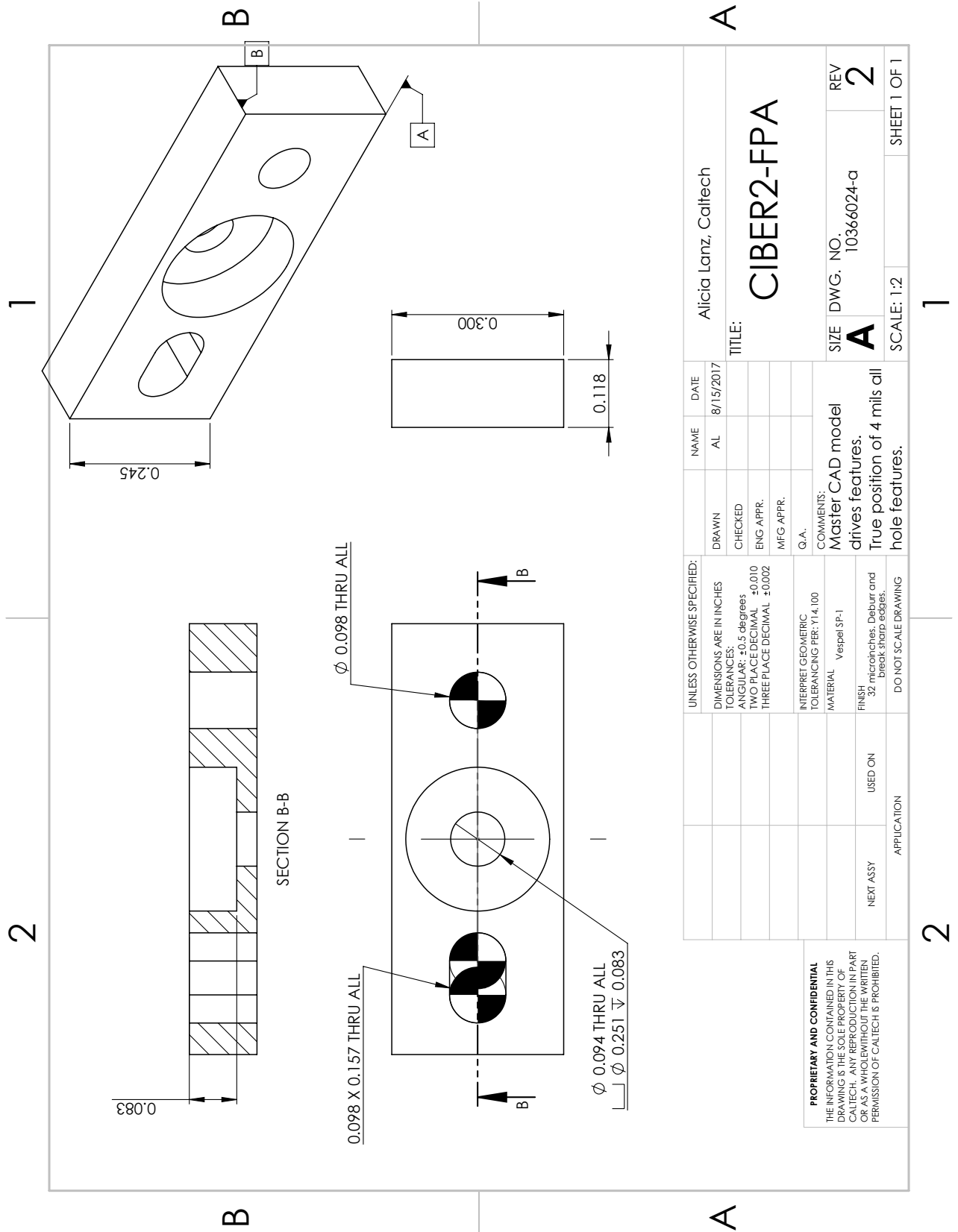
Figure B.13: Mechanical drawing for flight version of the CIBER-2 focal plane interface Vespel blocks for Arm-M (short focus distance).

B

A

1

2

0.300

0.207

0.245

0.113

SECTION B-B

Ø 0.098 THRU ALL

0.098 X 0.157 THRU ALL

Ø 0.094 THRU ALL
⌴ Ø 0.251 ▽ 0.113

B

B

A

		NAME	DATE
	DRAWN	AL	8/15/2017
	CHECKED		
	ENG APPR.		
	MFG APPR.		
	Q.A.		

UNLESS OTHERWISE SPECIFIED:

DIMENSIONS ARE IN INCHES
TOLERANCES:
ANGULAR: ±0.5 degrees
TWO PLACE DECIMAL ±0.010
THREE PLACE DECIMAL ±0.002

INTERPRET GEOMETRIC
TOLERANCING PER: Y14.100

MATERIAL   Vespel SP-1

FINISH
32 microinches. Deburr and
break sharp edges.

DO NOT SCALE DRAWING

COMMENTS:
Master CAD model
drives features.
True position of 4 mils all
hole features.

Alicia Lanz, Caltech

TITLE:

CIBER2-FPA

SIZE | DWG. NO.
A | 10366024-b

REV
2

SCALE: 1:2   SHEET 1 OF 1

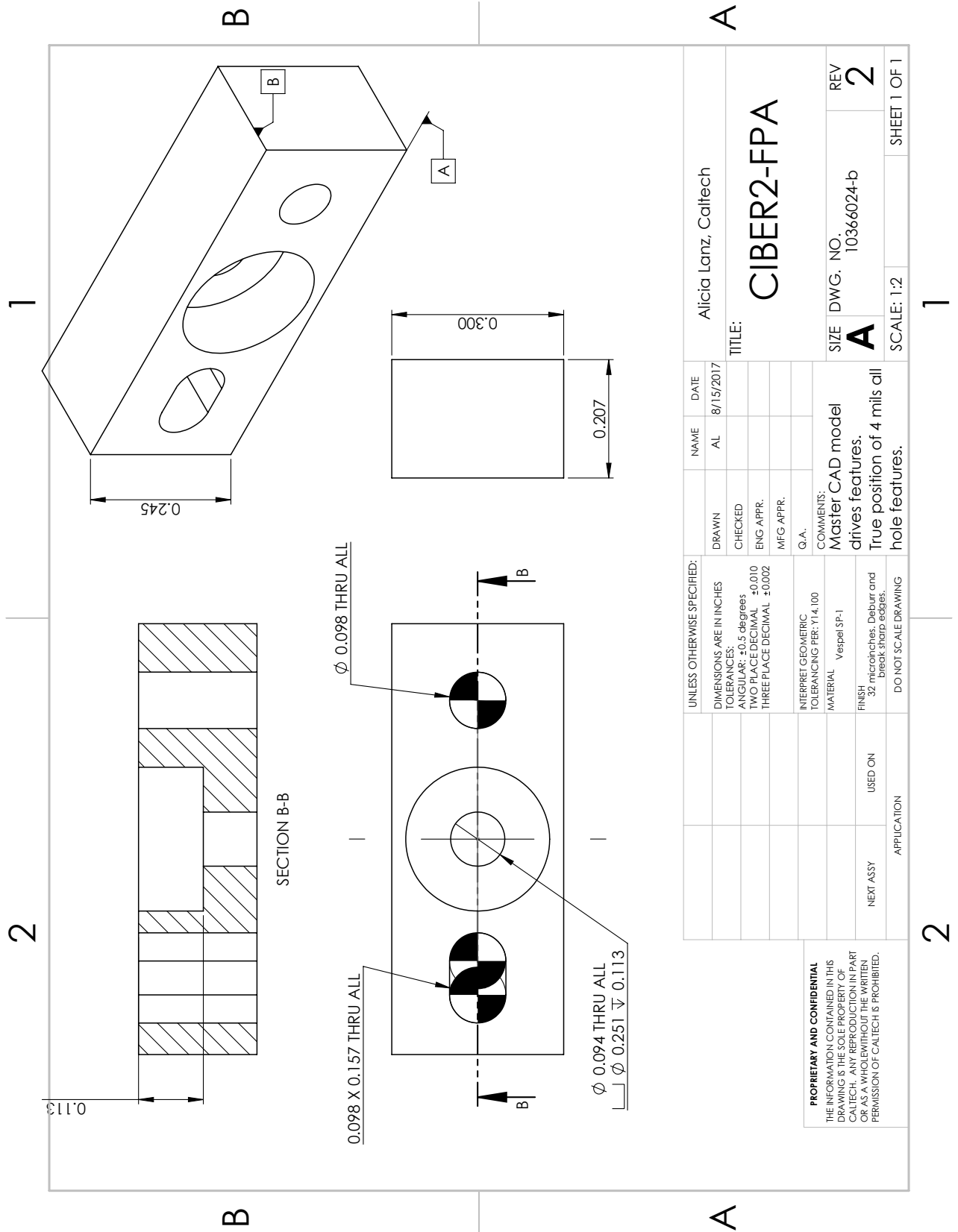NEXT ASSY   USED ON

APPLICATION

Figure B.14: Mechanical drawing for flight version of the CIBER-2 focal plane interface Vespel blocks for Arms-L and -S (longer focus distance).
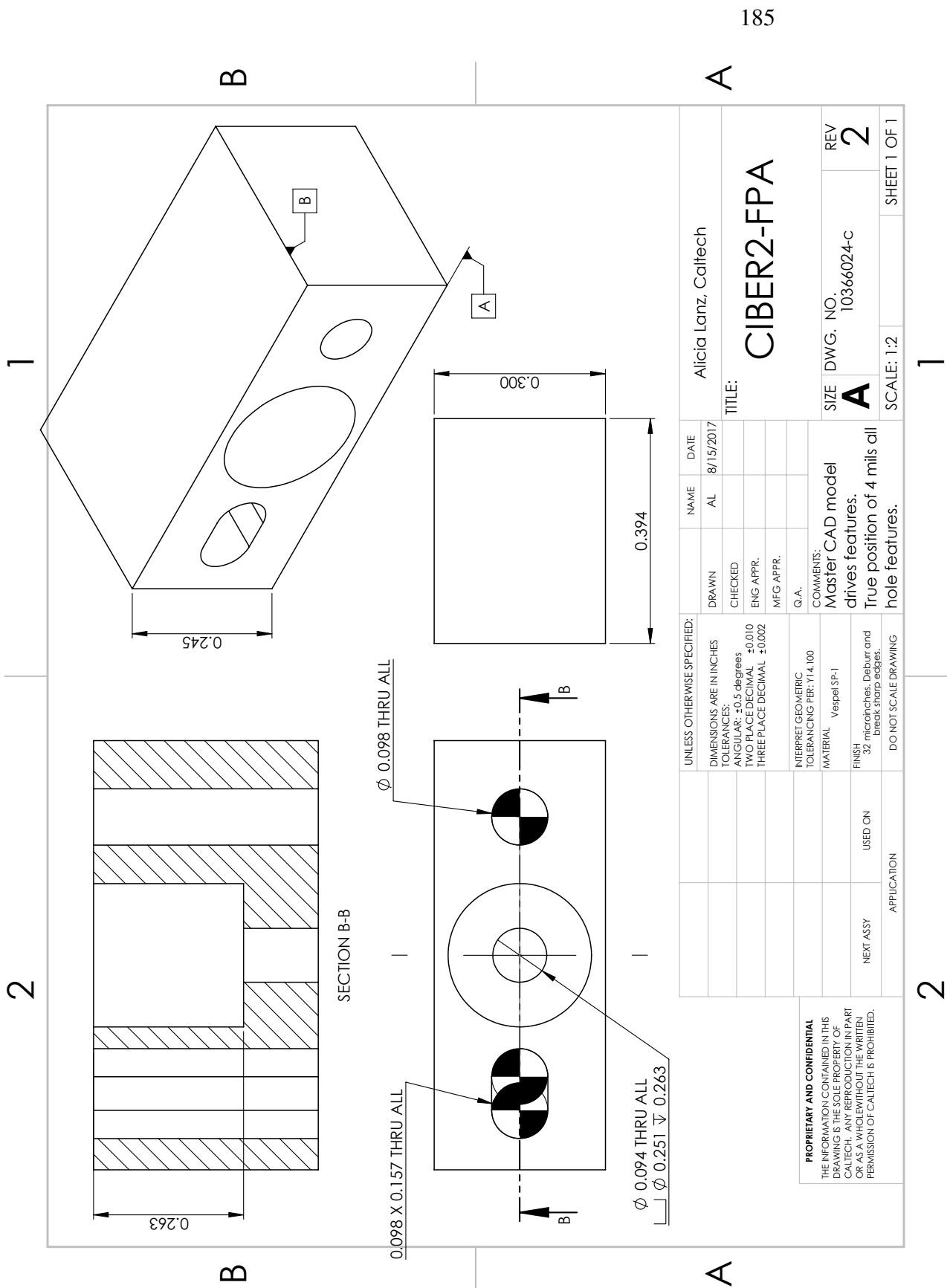
Figure B.15: Mechanical drawing for flight version of the CIBER-2 focal plane interface Vespel blocks (all configurations; sets distance between lens barrel and interface ring).
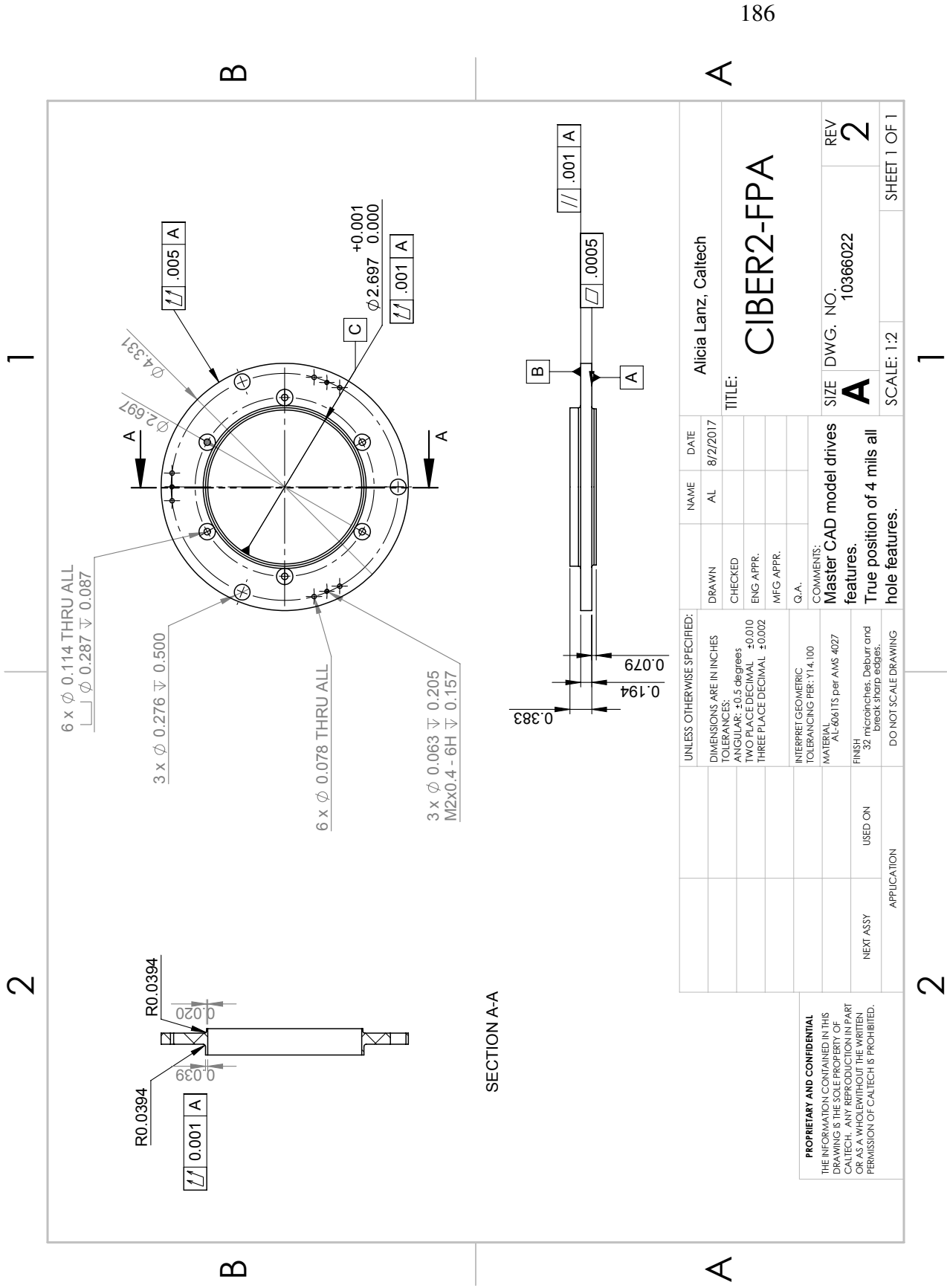
Figure B.16: Mechanical drawing for flight version of the CIBER-2 focal plane interface interface plate to the FPA housing.
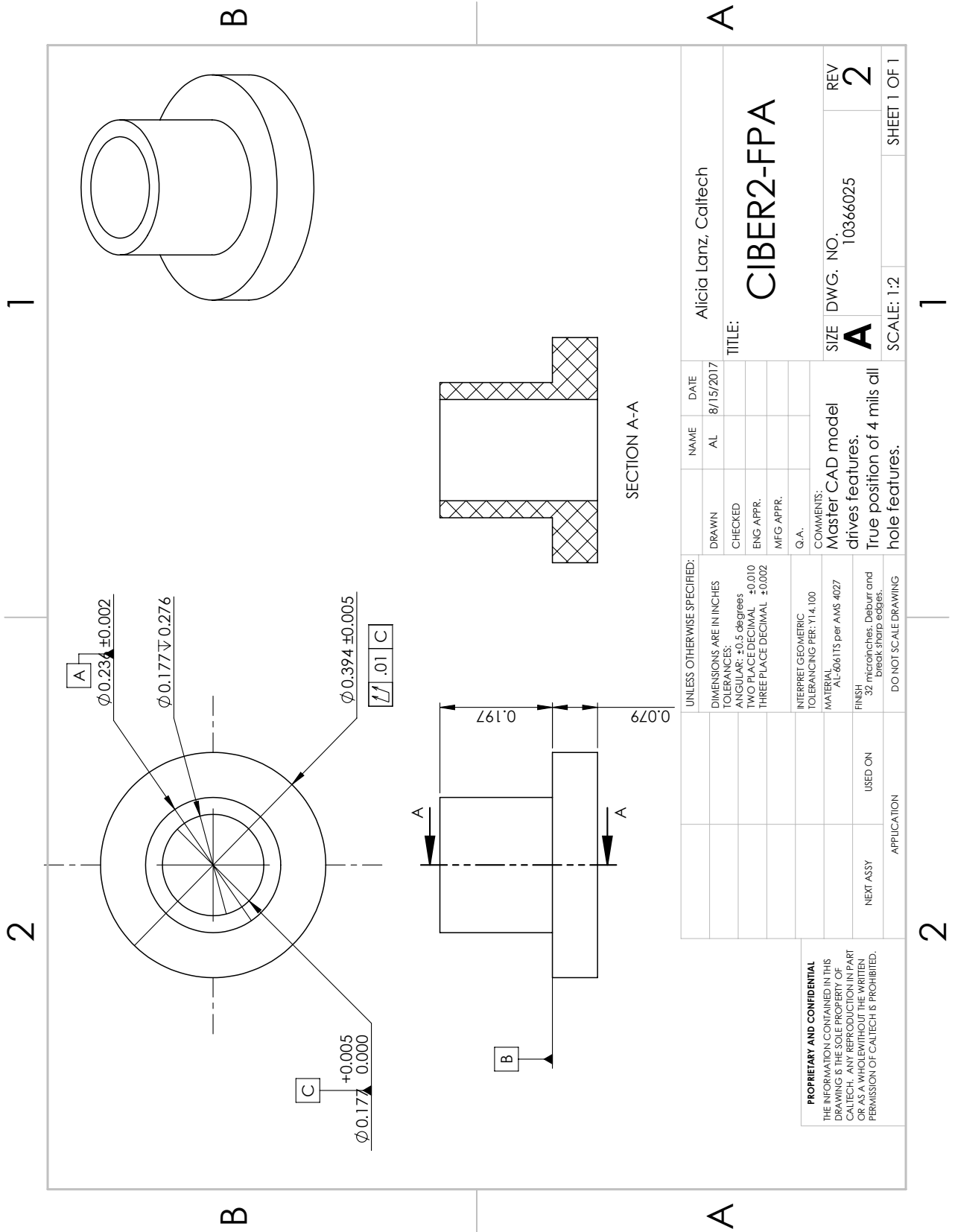
Figure B.17: Mechanical drawing for flight version of the CIBER-2 focal plane interface Vespel plug for thermal isolation.
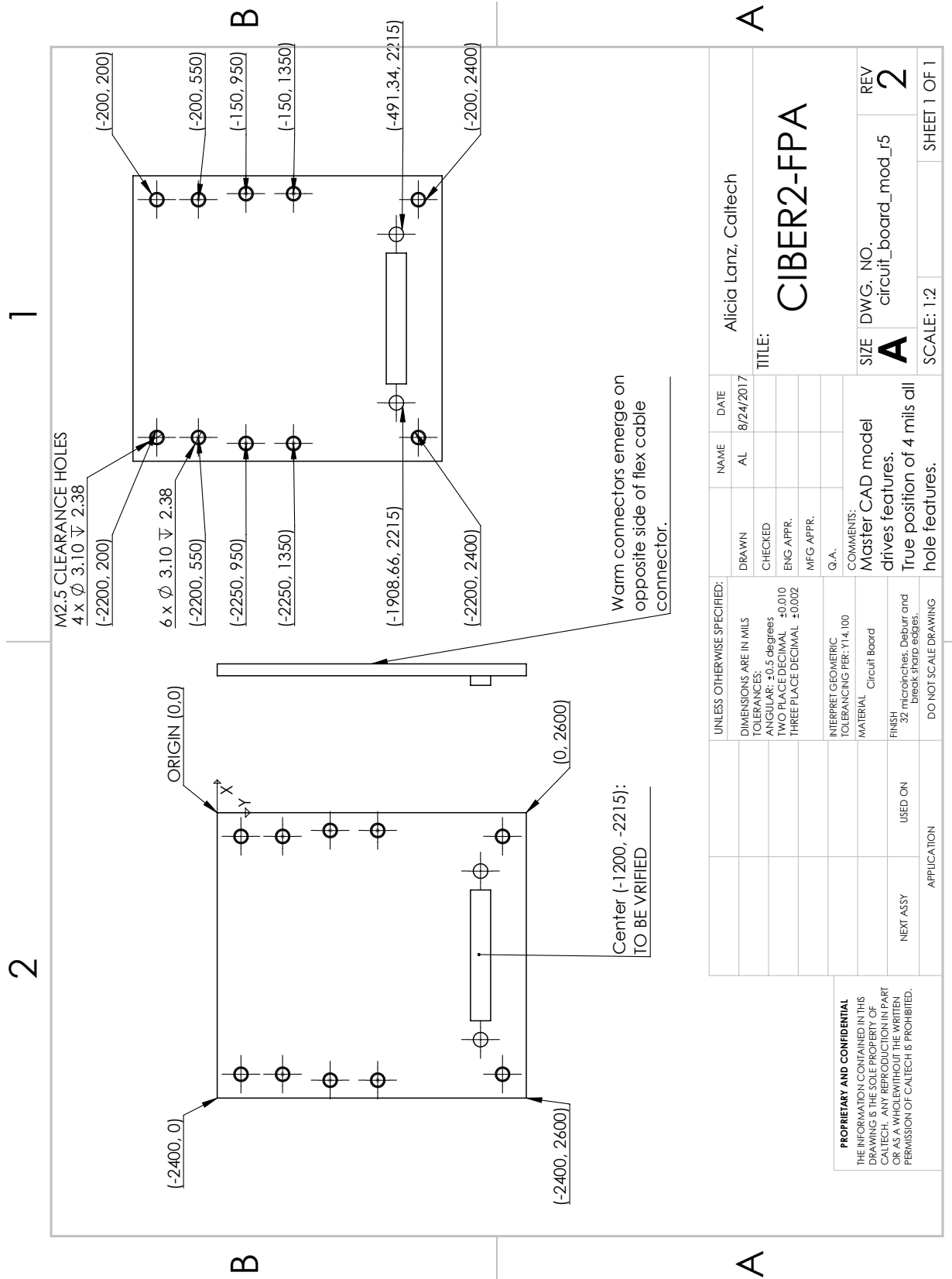
Figure B.18: Mechanical drawing for flight version of the CIBER-2 focal plane assembly detector readout circuit board (nominal configuration).